

AD-A063 558

MICHIGAN UNIV ANN ARBOR ELECTRON PHYSICS LAB

F/G 9/5

FREQUENCY CONVERSION IN PUNCH-THROUGH SEMICONDUCTOR DEVICES.(U)

AUG 78 P J MCCLEER

DAA629-76-6-0232

UNCLASSIFIED

TR-143

ARO-13853.2-EL

NL

1 OF 3
ADA
063558



ARO 13853.2-EL

014525 1-T

LEVEL

12

AD A063558

**FREQUENCY CONVERSION IN PUNCH-THROUGH
SEMICONDUCTOR DEVICES**

TECHNICAL REPORT NO. 143

August 1978

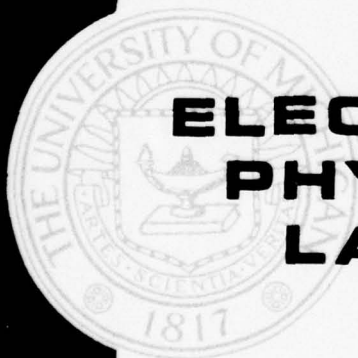


By

P. J. McCLEER

DDC FILE COPY

Approved for public release; distribution unlimited.



**ELECTRON
PHYSICS
LABORATORY**

**DEPARTMENT OF ELECTRICAL AND COMPUTER
ENGINEERING**

THE UNIVERSITY OF MICHIGAN, ANN ARBOR

GRANT WITH: U. S. ARMY RESEARCH OFFICE, RESEARCH TRIANGLE PARK,
N. C. RESEARCH GRANT NO. DAAG29-76-G-0232.

19 01 17 016

The findings in this report are not to be construed as an official Department of the Army position, unless so designated by other authorized documents.

This report has also been submitted as a dissertation in partial fulfillment of the requirements for the degree of Doctor of Philosophy in The University of Michigan, 1978.

UNCLASSIFIED

SECURITY CLASSIFICATION OF THIS PAGE (When Data Entered)

REPORT DOCUMENTATION PAGE		READ INSTRUCTIONS BEFORE COMPLETING FORM
1. REPORT NUMBER 014525 1-T	2. GOVT ACCESSION NO. 18 ARO 19 13853.2-EL	3. RECIPIENT'S CATALOG NUMBER
4. TITLE (and Subtitle) FREQUENCY CONVERSION IN PUNCH-THROUGH SEMICONDUCTOR DEVICES.	5. TYPE OF REPORT & PERIOD COVERED Interim Technical rept.	6. PERFORMING ORG. REPORT NUMBER Tech. Report No. 143
7. AUTHOR(s) Patrick J. McCleer	8. CONTRACT OR GRANT NUMBER(s) DAAG29-76-G-0232	
9. PERFORMING ORGANIZATION NAME AND ADDRESS Electron Physics Laboratory The University of Michigan Ann Arbor, MI 48109	10. PROGRAM ELEMENT, PROJECT, TASK AREA & WORK UNIT NUMBERS 13853-EL	
11. CONTROLLING OFFICE NAME AND ADDRESS U. S. Army Research Office Post Office Box 12211 Research Triangle Park, NC 27709	12. REPORT DATE August 1978	13. NUMBER OF PAGES 249
14. MONITORING AGENCY NAME & ADDRESS (if different from Controlling Office) TR-143 014525-1-T	15. SECURITY CLASS. (of this report) Unclassified	15a. DECLASSIFICATION/DOWNGRADING SCHEDULE NA
16. DISTRIBUTION STATEMENT (of this Report) Approved for public release; distribution unlimited.		
17. DISTRIBUTION STATEMENT (of the abstract entered in Block 20, if different from Report) NA		
18. SUPPLEMENTARY NOTES The findings in this report are not to be construed as an official Department of the Army position, unless so designated by other authorized documents.		
19. KEY WORDS (Continue on reverse side if necessary and identify by block number) Frequency conversion Punch-through semiconductor devices Detectors Mixers BARITT diodes Phototransistor BARITT photodetector		
20. ABSTRACT (Continue on reverse side if necessary and identify by block number) The objectives of this investigation are to study the frequency conversion properties of punch-through semiconductor devices and to establish the frequency regions of their potential application as efficient detectors and mixers of information-bearing signals. The physics of two punch-through devices are studied in detail: the three-terminal punch-through transistor and the two-terminal BARITT (barrier injection transit-time) diode. The particle current injection process for both devices is		

DD FORM 1 JAN 73 1473

EDITION OF 1 NOV 65 IS OBSOLETE

UNCLASSIFIED

SECURITY CLASSIFICATION OF THIS PAGE (When Data Entered)

20. examined and identified as simple diffusion over a potential barrier (exponential injection with respect to the barrier height). Dc and small-signal ac models for both punch-through structures are derived from standard bipolar junction transistor theory by applying a current-dependent, rather than the standard voltage-dependent, boundary condition for the minority carrier concentration at the collector edge of the low-field base region. The small-signal models include carrier transit-time effects in the diffusion-drift, reverse-biased regions of the devices by means of a transit-time factor similar to the factor used in the standard frequency domain analysis of pure saturated drift transit-time diodes. The small-signal noise properties of the BARITT diode are developed employing the same techniques used in the formulation of the BARITT diode circuit model. Both, small-signal impedances predicted by the circuit model and small-signal noise measures predicted by the noise analysis, compare very well with experimentally measured values of typical BARITT structures.

The microwave and millimeter-wave detection properties of the BARITT diode and the optical detection properties of the punch-through transistor are examined using the small-signal models. The BARITT diode is shown to be capable of efficient rectification at frequencies both within and above the region of diode negative resistance. The punch-through phototransistor is shown to be a high-speed version of the standard phototransistor; attaining its rapid response capability through its lack of charge-storage inertial effects. The device is also capable of additional quantum gain due to negative-resistance reflection-type amplification near the transit-time frequency.

An analytic large-signal model for the BARITT diode is developed based on the nonlinear exponential injection mechanism. Excellent agreement is obtained when the results of this simple model are compared with the results of higher-order numerical studies and to experimental results. Extension of the model to include harmonic power extraction is also demonstrated.

BARITT diode frequency converters are examined in two fundamentally different studies, based on two different methods of analysis: a very-low IF mixer study, applicable only to self-oscillating mixers, in which the conversion properties are obtained from a perturbation of the basic oscillator equations and a general four-frequency mixer study, in which an equivalent linear network is developed to describe the pumped diode and its circuit environment. The minimum detectable signal of the very-low IF mixer is shown to be comparable to the AM noise of the diode oscillator itself and the optimum noise figure of the general mixer is shown to be comparable, particularly at millimeter wavelengths, to that obtainable from the best present-day Schottky-barrier diode mixers.

TABLE OF CONTENTS

ACCESSION for	
NTIS	White Section <input checked="" type="checkbox"/>
DDC	Buff Section <input type="checkbox"/>
UNANNOUNCED	<input type="checkbox"/>
JUS LICATION	<input type="checkbox"/>
BY	
DISTRIBUTION/AVAILABILITY NOTES	
DL	SPECIAL

	<u>Page</u>
LIST OF ILLUSTRATIONS	vi
LIST OF TABLES	xiii
LIST OF SYMBOLS	xiv
CHAPTER I. INTRODUCTION	1
1.1 Introduction	1
1.2 Basic Principles of Punch-Through Semiconductor Devices	1
1.2.1 Punch-Through Transistors	2
1.2.2 BARITT Diodes	11
1.2.3 Frequency Scaling of Punch-Through Devices	12
1.3 Frequency Conversion Applications of Punch-Through Devices	16
1.3.1 Small-Signal Detection	16
1.3.2 Four-Frequency Mixers	17
CHAPTER II. DEVICE PHYSICS AND DC SOLUTIONS	19
2.1 Introduction	19
2.2 Carrier Concentrations in Narrow-Base Diffusion Transistors and in Punch-Through Transistors	19
2.2.1 Standard Theory for Diffusion Transistors	20
2.2.2 Narrow Base Width Considerations and the Punch-Through Transistor	23
2.3 Physics of Punch-Through Injection and the BARITT Diode	29
2.3.1 Punch-Through Injection	29
2.3.2 The BARITT Diode	34
2.4 Dc Solutions for the Low-Field Region of a BARITT Diode	36

	<u>Page</u>
2.5 Dc Base Resistance in a Punch-Through Transistor	46
CHAPTER III. SMALL-SIGNAL MODELS OF PUNCH-THROUGH DEVICES AND SMALL-SIGNAL NOISE PROPERTIES OF BARITT DEVICES	50
3.1 Introduction	50
3.2 Small-Signal Transistor Models	52
3.2.1 Common-Base y -Parameter Intrinsic Diffusion Transistor Model	52
3.2.2 Narrow Base-Width Considerations	58
3.2.3 The Complete Small-Signal Model	61
3.3 Small-Signal Analysis of Punch-Through Transistors	64
3.4 Small-Signal BARITT Diode Analysis	71
3.4.1 Theory	71
3.4.2 Results	82
3.5 Small-Signal BARITT Diode Noise Analysis	87
3.5.1 Shot Noise	87
3.5.2 Diffusion Noise	89
3.5.3 Results.	91
CHAPTER IV. BARITT DIODE VIDEO DETECTORS	96
4.1 Introduction	96
4.2 Exponential Diode Detector Theory	97
4.3 BARITT Diode Detectors	100
4.4 Theoretical and Experimental Results	104
4.5 Discussion	115
CHAPTER V. OPTICAL DETECTION WITH PUNCH-THROUGH SEMICONDUCTOR DEVICES	119
5.1 Introduction	119
5.2 Optically Generated Currents and Transit-Time Effects	120
5.3 Punch-Through Phototransistors--Photo-BARITTs	122
5.4 Conclusions	128
CHAPTER VI. LARGE-SIGNAL ANALYSIS OF BARITT DIODES	130
6.1 Introduction	130
6.2 Single-Frequency Large-Signal Model	131
6.2.1 Theory	131
6.2.2 Single-Frequency Results	140

	<u>Page</u>
6.3 Multifrequency Harmonic Large-Signal Operation of BARITT Diodes	150
6.3.1 Theory	150
6.3.2 Two-Frequency Results	151
CHAPTER VII. BARITT DIODE MIXERS	162
7.1 Foreword	162
7.2 Very-Low Intermediate-Frequency Self-Oscillating BARITT Diode Mixers	162
7.2.1 System Description	162
7.2.2 Perturbation Theory	167
7.2.3 Perturbation Theory Discussion--Special Cases	174
7.2.4 Theoretical and Experimental Results for Very-Low Intermediate-Frequency Self- Oscillating BARITT Diode Mixers	182
7.3 Four-Frequency BARITT Diode Mixers	197
7.3.1 Introduction	197
7.3.2 The Frequency Conversion Process in a BARITT Diode and Frequency Converter Circuits	199
7.3.3 Determination of the Transadmittance Terms	209
7.3.4 BARITT Diode Mixer Noise Figure	212
7.3.5 Results for BARITT Diode Mixers	219
CHAPTER VIII. CONCLUSIONS AND SUGGESTIONS FOR FURTHER WORK	233
APPENDIX A. VOLTAGE AND CURRENT EARLY EFFECT	236
APPENDIX B. AN INTERPRETATION OF THE AM AND FM MODULATION OF THE RF VOLTAGE ACROSS AN OSCILLATING DIODE VERY- LOW IF MIXER	239
LIST OF REFERENCES	242

LIST OF ILLUSTRATIONS

<u>Figure</u>		<u>Page</u>
1.1	Experimental p^+np^+ Si BARITT Diode Photo I-V Characteristic.	4
1.2	Two-Dimensional p^+np^+ Transistor Structure.	7
1.3	I-V Characteristics for Experimental p^+np^+ Punch-Through Transistor.	10
1.4	Negative-Resistance Frequency Dependence on Metallurgical Base Width for p^+np^+ BARITT Diodes.	15
2.1	One-Dimensional pnp Transistor Structure.	21
2.2	Injection Point Carrier Concentration Ratio $K = p(0)/p_s$ for a p^+np^+ Si BARITT Device.	32
2.3	Lumped Representation of Carrier Concentration and Electric Field in the Low-Field Region of a BARITT Diode.	37
2.4	Ratio of Drift to Total Current as a Function of Position for a p^+np^+ Si BARITT Device. ($N_d = 5 \times 10^{15} \text{ cm}^{-3}$, $J_o = 300 \text{ A/cm}^2$ and $N = 20$)	40
2.5	Convergence of Dc Solution. ($N_d = 5 \times 10^{15} \text{ cm}^{-3}$ and $J_o = 300 \text{ A/cm}^2$)	42
2.6	Carrier Concentration and Electric Field as Functions of Position in the Low-Field Region of a p^+np^+ Si BARITT Diode. ($N_d = 1 \times 10^{15} \text{ cm}^{-3}$ and $J_o = 100 \text{ A/cm}^2$)	43
2.7	Carrier Concentration and Electric Field as Functions of Position in the Low-Field Region of a p^+np^+ Si BARITT Diode. ($N_d = 5 \times 10^{15} \text{ cm}^{-3}$ and $J_o = 300 \text{ A/cm}^2$)	44
2.8	Carrier Concentration and Electric Field as Functions of Position in the Low-Field Region of a p^+np^+ Si BARITT Diode. ($N_d = 1 \times 10^{16} \text{ cm}^{-3}$ and $J_o = 500 \text{ A/cm}^2$)	45
2.9	Effective Base Width for Majority Carrier (Electron) Current (Low-Level Injection).	48

<u>Figure</u>		<u>Page</u>
3.1	Small-Signal Common-Base Equivalent Circuit for an Intrinsic Diffusion Transistor. ($y_{11} = g_n + g_e + j\omega C_{es}$, $y_{12} = -g_c$ and $y_{22} = g_c + j\omega C_{cs}$)	57
3.2	Complete Common-Base Equivalent Circuit for Diffusion Transistor. ($y_{11} = g_n + g_e + j\omega C_{es}$, $y_{12} = -g_c$, $y_{22} = g_c + j\omega C_{cs}$)	63
3.3	Small-Signal Model of Punch-Through Transistor.	66
3.4	Base Resistance-Collector Capacitance Time Constant for Dc Maximum Power Structures.	68
3.5	Common Emitter Output Resistance for Dc Maximum Power Structures. [$R_g = r_b + r_e$, $r_e = (1/g_e)$, $J_o = 100 \text{ A/cm}^2$, $C_e/C_c = 20$ and $\delta = 0.01$]	69
3.6	Unilateral Gain for Dc Maximum Power Structures. ($L_e = 1 \text{ } \mu\text{m}$, $J_o = 100 \text{ A/cm}^2$, $\delta = 0.01$ and $C_e/C_c = 20$)	72
3.7a	Equivalent Circuit for ith Lump in BARITT Diode Drift-Diffusion Region.	78
3.7b	Complete Equivalent Circuit for the Second-Order BARITT Diode Model.	79
3.8	Simplified Equivalent Circuit for the Second-Order BARITT Diode Model.	81
3.9	Convergence of Small-Signal Model. (N = Number of Low-Field Region Lumps). ($N_d = 3.3 \times 10^{15} \text{ cm}^{-3}$, $w_B = 6.0 \text{ } \mu\text{m}$, $J_o = 50 \text{ A/cm}^2$)	83
3.10	Comparison of Small-Signal Impedance, Theory (N = 10) and Experiment. (Snapp and Weissglas ¹⁰)	84
3.11	Small-Signal Impedance for Four Dc Maximum Power Structures.	86
3.12	Equivalent Circuit Used to Find the Open-Circuit Noise Voltage $v_{ns} = v_{Fn} + v_{Bn}$ Due to Injected Shot Noise.	88
3.13	Shot Noise and Diffusion Noise Mean Square Voltages for an X-Band BARITT Diode. (p^+np^+ Si BARITT, $N_d = 3.3 \times 10^{15} \text{ cm}^{-3}$, $w_B = 6 \text{ } \mu\text{m}$ and $J_o = 50 \text{ A/cm}^2$)	92

<u>Figure</u>		<u>Page</u>
3.14	Small-Signal Noise Measure for an X-Band BARITT Diode. ($p^{+}np^{+}$ Si BARITT, $N_d = 3.3 \times 10^{15} \text{ cm}^{-3}$ and $w_B = 6 \text{ } \mu\text{m}$)	93
3.15	Comparison of Theoretical and Experimental ⁴⁶ Noise Properties of a $p^{+}np^{+}$ Si BARITT Diode. (Snapp and Weissglas ¹⁰ Device B, $N_d = 1.2 \times 10^{15} \text{ cm}^{-3}$, $w_B = 7.9 \text{ } \mu\text{m}$)	95
4.1	(a) General Exponential Diode Detector Circuit $Z_o = (g_o + j\omega C_o)^{-1}$. (b) Thevenin Equivalent Detector Circuit $V'_g = V_g / (A + CR_g)$, $Z'_g = (B + DR_g) / (A + CR_g) \equiv R'_g + jX'_g$.	98
4.2	BARITT Diode Detector Equivalent Circuit. [$V'_g = V_g / (A + CR_g)$ and $Z'_g = (B + DR_g) / (A + CR_g) \equiv R'_g + jX'_g$]	101
4.3	Normalized Detector Idealities for Dc Maximum Power Structure in Negative-Resistance Regions.	105
4.4	Drift-Diffusion Region Resistances for Dc Maximum Power Structures. ($J_o = 50 \text{ A/cm}^2$)	107
4.5	Effective Cutoff Frequencies as a Function of Bias for Dc Maximum Power Structure No. 2.	108
4.6	Experimental and Theoretical Detected Voltage Sensitivity for a K-Band BARITT Diode.	110
4.7	Swept Frequency Detector Response in Negative-Resistance Frequency Region.	111
4.8	Theoretical and Experimental Results for Video Detection at 27.44 GHz with X-Band Diode.	113
4.9	Small-Signal Resistance of X-Band BARITT Diode. ($p^{+}np^{+}$, Si, $N_d = 2 \times 10^{15} \text{ cm}^{-3}$, $w_B = 5 \text{ } \mu\text{m}$ and Area = $1.7 \times 10^{-4} \text{ cm}^2$)	114
4.10	Two-Dimensional BARITT Diode Structure.	117
5.1	Depletion-Layer Optically Generated Current as a Function of Depletion-Layer Width and Modulation Frequency.	123
5.2	Small-Signal Equivalent Circuit for a Photo-BARITT Including a Resonant Load.	125

<u>Figure</u>		<u>Page</u>
5.3	Small-Signal Impedance Plot of Punch-Through Transistor Structure. ($J_o = 100 \text{ A/cm}^2$, $\lambda = 0.7 \text{ } \mu\text{m}$, $w_c = 5 \text{ } \mu\text{m}$ and $C_c/C_e = 0.05$)	127
5.4	Magnitude of Detected Optical Current as a Function of Modulation Frequency and δ . ($J_o = 100 \text{ A/cm}^2$, $\lambda = 0.7 \text{ } \mu\text{m}$, $w_c = 5 \text{ } \mu\text{m}$ and $C_c/C_e = 0.05$)	129
6.1	Large-Signal Single-Frequency Models for Uniformly Doped BARITT Diodes.	137
6.2	Small-Signal Negative-Resistance Region Q's for the First Four Dc Maximum Power Structures of Table 3.1.	138
6.3	Saturation Characteristic of the Single-Frequency Large-Signal Injected Particle Current.	141
6.4	Large-Signal Power and Efficiency as a Function of Drive and Frequency for the Experimental Device of Kwok, ¹ Nguyen-Ba ² and Kwok et al. ⁶¹	142
6.5	Large-Signal Theoretical and Experimental Values for the Rectification Effect for Snapp and Weissglas's ¹⁰ Diode B. ($N_d = 1.2 \times 10^{15} \text{ cm}^{-3}$ and Base Width = $7.9 \text{ } \mu\text{m}$)	143
6.6	Large-Signal Theoretical and Experimental Values for Conductance Compression for Snapp and Weissglas's ¹⁰ Device B. ($G_o = \text{Small-Signal Value}$, $N_d = 1.2 \times 10^{15} \text{ cm}^{-3}$ and Base Width = $7.9 \text{ } \mu\text{m}$)	144
6.7	Theoretical Power Output and Efficiency vs. RF Voltage Amplitude for Dc Maximum Power Structure No. 1 at 10.5 GHz. (Kwok and Haddad ^{1,23})	146
6.8	Simple-Model Single-Frequency Large-Signal Results for Dc Maximum Power Structure No. 1 at 10.5 GHz.	147
6.9	Optimum Large-Signal Values for the Output Power Density and Resistance of the Dc Maximum Power Structures.	148
6.10	Two-Frequency Harmonic Large-Signal Equivalent Circuit for the BARITT Diode.	152
6.11	Large-Signal Second-Harmonic Impedance for Dc Maximum Power Structure No. 3. ($V_{F1} = 0.4 \text{ V}$)	154

<u>Figure</u>		<u>Page</u>
6.12	Large-Signal Second-Harmonic Impedance for Dc Maximum Power Structure No. 3 near Small Values of \hat{V} . ($V_{F1} = 0.4$ V, Note Scale Change from Fig. 6.11)	155
6.13	Large-Signal Fundamental and Second-Harmonic Impedances for a K-Band BARITT Diode Structure. ("Cold" Capacitive Reactances Subtracted Out, $N_d = 4 \times 10^{15} \text{ cm}^{-3}$, Base Width = 3 μm , $J_o = 400 \text{ A/cm}^2$ and $f_1 = 18 \text{ GHz}$)	159
6.14	Large-Signal Fundamental and Second-Harmonic Impedances for a K-Band BARITT Diode Structure. ("Cold" Capacitive Reactances Subtracted Out, $N_d = 4 \times 10^{15} \text{ cm}^{-3}$, Base Width = 3 μm , $J_o = 400 \text{ A/cm}^2$ and $f_1 = 18 \text{ GHz}$)	160
7.1	(a) Physical Circuit, (b) Load Variation Model and (c) Injected Signal Model.	163
7.2	LF and RF Coupled Circuit Models. ($Z = R + jX$ for all Impedance Quantities)	166
7.3	Modulation Detection Sensitivity Experiment. (a) Test Setup, (b) Phasor Diagram and (c) Experimental Results.	171
7.4	Measured Minimum Detectable Signal to Carrier Ratios for Different X-Band Devices (Adopted from Reference 11). ($f_m = 10 \text{ kHz}$)	185
7.5	Large-Signal R-X Tuning Trajectories for K-Band BARITT Diode. (Si, p^+np^+ , $N_d = 4 \times 10^{15} \text{ cm}^{-3}$, $w_B = 3.0 \mu\text{m}$ and $f = 21.3 \text{ GHz}$)	187
7.6a	RF Output Power for K-Band BARITT Diode as a Function of Drive and Bias. ($f = 21.3 \text{ GHz}$)	188
7.6b	Large-Signal Negative Resistance of K-Band BARITT Diode as a Function of Drive and Bias. ($f = 21.3 \text{ GHz}$)	189
7.7	Sensitivity of the K-Band BARITT Diode Impedance with Respect to Drive as a Function of Drive, Bias and Tuning. ($f = 21.3 \text{ GHz}$)	190
7.8a	Rectification Effect for the K-Band BARITT Diode as a Function of Bias and Tuning. ($f = 21.3 \text{ GHz}$)	191

<u>Figure</u>		<u>Page</u>
7.8b	Rectification Effect Factor β for the K-Band BARITT Diode as a Function of Drive, Bias and Tuning. ($f = 21.3$ GHz)	192
7.9	Device-Circuit Interaction Voltage V_c for the K-Band BARITT Diode as a Function of Drive, Bias and Tuning. ($f = 21.3$ GHz)	193
7.10	K-Band BARITT Diode Doppler Detector Sensitivity.	196
7.11	Small-Signal Equivalent Circuit of the Pumped BARITT Diode at the Input Signal Frequency ω_1 .	203
7.12	ABCD Parameters of Two Elements of a BARITT Diode Frequency Converter Equivalent Circuit. (a) Transadmittance Network ($A = D = 0$, $B = 1/y_{21}$, $C = y_{12}$) and (b) Linear Portion of a BARITT Diode [$A = 1 + (j\omega C/Y)$, $B = (1 - \Gamma)/Y$, $C = j\omega C$, $D = 1$].	205
7.13	Complete BARITT Diode Frequency Converter Equivalent Circuit.	206
7.14	y-Parameters for a Reduced Frequency Converter Network (Image Port Terminated).	208
7.15	Representation of a Linear Two-Port Network with all Internal Noise Sources Expressed as Equivalent Input Noise Sources \hat{V}_n and \hat{I}_n .	216
7.16	Stability Parameters for Snapp and Weissglas's Diode B. (a) Weak Pumping, $V_p/V_T = 1$ and (b) Strong Pumping, $V_p/V_T = 10$. ($f_p = 7.5$ GHz, Open Image, $J_o = 50$ A/cm ²)	221
7.17	Downconverted Noise Voltage Components (Mean Square) for Snapp and Weissglas's Diode B as a Function of Pumping Strength. ($J_o = 50$ A/cm ² , $f_s = 7.65 \times 10^9$ GHz, $f_p = 7.5$ GHz, Open Image)	223
7.18	Optimum Excess Noise Figures for Snapp and Weissglas's Diode B. (USBDC, $f_p = 7.5$ GHz, Open Image)	225
7.19	Maximum Power Structure No. 2. ($J_o = 100$ A/cm ² , $V_p/V_T = 10$, USBDC, Open Image, IF = 1.5 GHz)	227

<u>Figure</u>		<u>Page</u>
7.20	Transit-Time Effects on Open-Circuit Diffusion Noise Voltage at Input Signal Frequency of Dc Maximum Power Structure No. 2. ($J_o = 100 \text{ A/cm}^2$, $V_p/V_T = 10$, USBDC, IF = 1.5 GHz)	229
7.21	Optimum Excess Noise Figure for Dc Maximum Power Structure No. 2. ($J_o = 100 \text{ A/cm}^2$, USBDC, Open Image, IF = 1.5 GHz)	230
7.22	RF Resistance Values for Dc Maximum Power Structure No. 2. ($J_o = 100 \text{ A/cm}^2$, $V_p/V_T = 10$, USBDC, Open Image, IF = 1.5 GHz)	231

LIST OF TABLES

<u>Table</u>		<u>Page</u>
3.1	Dc Maximum Power p^+np^+ Si BARITT Structures.	85
6.1	Large-Signal Equations for Uniformly Doped BARITT Diode Diffusion-Drift Region.	135
6.2	Single-Frequency and Two-Frequency Large-Signal Results for Dc Maximum Power Structure No. 3 ($N_d = 5 \times 10^{15} \text{ cm}^{-3}$, Base Width = 4 μm , $J_o = 400 \text{ A/cm}^2$, $V_{F1} \approx 0.4 \text{ V}$, $V_{F2} = 0.093 \text{ V}$, $\psi = 321 \text{ Degrees}$, Fundamental Frequency = 20 GHz).	157
7.1	First- and Second-Order Approximations for a K-Band Diode.	211

LIST OF SYMBOLS

A	Device cross-sectional area (cm^2).
A, B, C, D	ABCD two-port network parameters.
$b, b', e, c,$	Base, intrinsic base, emitter and collector terminals of a bipolar junction transistor.
C	Linville stability factor.
C_i	Displacement capacitance of region i .
C_{es}, C_{cs}	Emitter and collector charge storage capacitances.
C_m, S_m	Real and imaginary parts of the Fourier components of the large-signal injected particle current in a BARITT diode.
D_n, D_p	Diffusion coefficients for electrons and holes (cm^2/s).
E	Electric field (V/cm).
e_H, e_L	Small-signal voltage generators used in perturbation analysis of diode oscillators.
F_c, F_e, F_n	Particle concentration boundary values used in transistor analysis (cm^{-3}).
f	Frequency (Hz).
f_c, f_{ce}	Cutoff and effective cutoff frequencies used in passive device detector analysis.
G_d	Small-signal diode conductance (mho/cm^2).
G_{F1}, G_{F2}	Large-signal conductances of the forward-biased region of a BARITT diode at the fundamental and second-harmonic frequencies (mho/cm^2).
g_i	Small-signal conductance for region i of a device (mho/cm^2).
g_m	Downconversion transconductance of a very-low IF BARITT mixer (mho/cm^2).
I_o	Dc current (A).

I_i	Current in region i of a device (A).
I_m	Modified Bessel function of order m .
I_n	Noise current (A).
I_v	Optically generated current (A).
J_o	Dc current density (A/cm ²).
J_{diff}, J_{drift}	Diffusion and drift particle current densities (A/cm ²).
J_i	Current density in region i of a device (A/cm ²).
J_m, J_{pm}	Fourier components of the large-signal injected particle current in a BARITT diode (A/cm ²).
J_n, J_p	Electron and hole particle current densities (A/cm ²).
J_t	Total, particle plus displacement, current density (A/cm ²).
K	Ratio of injected particle concentration to saturated region particle concentration in a punch-through device.
L_e	Width of the emitter stripe in a stripe geometry planar transistor (μ m).
L_n, L_p, L_n^*, L_p^*	Electron and hole real and complex diffusion lengths (cm).
LSBDC, USBDC	Lower sideband and upper sideband downconverters.
M	Ratio of particle to total current density.
M_{AM}	AM modulation sensitivity for a diode oscillator.
MDS/C	Minimum detectable signal to carrier ratio.
N	Number of subsections in the low-field region of a BARITT diode.
$(N/C)_{AM, DSB}$	Double sideband AM noise to carrier ratio.
N_d	Donor doping concentration (cm ⁻³).
NF, NF_e	Noise figure and excess noise figure.
p_s	Dc hole concentration in the saturated velocity region of a punch-through device.

Q	Quality factor, ratio of energy stored to energy dissipated.
q	Electronic charge.
R, R_d	Large- or small-signal diode resistance.
R_g, R_s	Signal source resistance.
S/N	Signal to noise ratio.
U	Unilateral gain.
V_{bi}	Built-in potential of a p-n junction (V).
V_{CB}, V_{EB}	Dc junction bias voltages in a bipolar junction transistor (V).
V_{F1}, V_{F2}	Magnitudes of large-signal voltages across the forward-biased region of a BARITT diode at fundamental and second-harmonic frequencies (V).
V_p	Magnitude of large-signal voltage across the forward-biased region of a BARITT diode mixer at the pump frequency (V).
V_{RF}	Magnitude of large-signal RF voltage across a two-terminal device (V).
V_T	Thermal voltage, 0.026 V, at room temperature.
v	Mobile carrier drift velocity (cm/s).
v_c	Device-circuit interaction voltage of an oscillating diode.
v_{ij}	Small-signal voltage drop or rise from terminal i to terminal j (V).
v_n	Small-signal noise voltage (V).
v_s	Mobile carrier saturated drift velocity (cm/s).
w, w_B	Width of metallurgical base region in a pnp, npn or MSM device.
w_c	Width of a reverse-biased junction space-charge region.
w_e	Width of a forward-biased junction space-charge region.
X_i	Reactance of region, device or circuit element i.

Y_B	Small-signal admittance of the reverse-bias of a BARITT diode.
Y_{ij}	Small-signal admittance parameters of a two-port network.
Y_m	Transadmittance term of order m in a BARITT diode frequency converter.
Z_1, Z_2	Large-signal fundamental and second-harmonic impedances of a BARITT diode.
Z_B, Z_F	Impedance of reverse-biased and forward-biased regions of a BARITT diode.
Z_i	Impedance of device or circuit element i.
α	Particle current transport factor in the base region of a bipolar transistor.
α	Optical absorption coefficient (cm^{-1}).
Γ	Transit-time factor of a diffusion-drift region.
γ	Propagation constant of particle current space-charge waves in the diffusion-drift region of a punch-through device.
γ_m	Detector ideality factor.
Δ	Lump extent in the subdivision of the low-field portion of a diffusion-drift region of a BARITT diode (cm).
δ	Ratio of base region majority carrier current to minority carrier current at the injection point.
$\delta V, \delta I, \delta \omega$	Small perturbation quantities.
ϵ	Medium permittivity (F/cm).
η	Efficiency.
θ	Transit angle (rad).
λ	Optical wavelength (μm).
μ_n, μ_p	Electron and hole mobilities ($\text{cm}^2/\text{V-s}$).
ξ	Device-circuit tuning angle (rad).
σ	Conductivity (mho/cm).

τ_n, τ_p	Electron and hole recombination lifetimes (s).
ψ	Relative phase angle of second-harmonic voltage to fundamental voltage across the forward-biased region of a BARITT diode.
ω	Angular frequency (rad/s).

CHAPTER I. INTRODUCTION

1.1 Introduction

This study is concerned with the frequency conversion and detection properties of punch-through semiconductor devices. The two principal devices that will be considered in detail are the three-terminal punch-through transistor and its two-terminal special case, the BARITT (barrier injection transit time) diode. The majority of the theory developed in this work will directly pertain to the BARITT diode only; however, with only a slight circuit complication, the addition of base lead circuitry, the results can be easily adapted to the analysis of punch-through transistor converters and detectors.

The low-noise characteristics of punch-through injection (diffusion over a potential barrier) are the principal impetus for this study. The highly nonlinear voltage-current relationship of punch-through injection and the possibility of device transit-time negative resistance further enhance the candidacy of punch-through structures as frequency converters. This discourse explores these considerations as well as circuit and material constraints and will attempt to establish the upper frequency limits of useful operation for all conversion and detection schemes presented.

1.2 Basic Principles of Punch-Through Semiconductor Devices

Although the device theory that is developed throughout this report is completely general in nature, only the

p⁺np⁺ abrupt-junction uniformly doped Si structure will be dealt with in detail. The reasons for this choice of a particular device doping profile and material are, in order of importance: (1) Si pnp base region minority carriers (holes) have a lower value of mobility than do the majority carriers (electrons). This mobility relationship simultaneously aids in the phasing of the induced current for negative-resistance applications and lowers the base lead series resistance for three-terminal operation. (2) Holes in Si have a lower ionization rate than do electrons, thus pnp structures are capable of sustaining higher avalanche-free dc input powers than their npn counterpart devices. (3) Only Si devices have been experimentally fabricated thus far. There is no overriding advantage in using the more exotic III-V materials such as GaAs or InP to construct uniformly doped punch-through structures since their high electron mobility values actually result in lower RF negative-resistance capabilities¹ and their low hole mobility values result in only incremental improvements. Tailored base region doping profiles are also not considered in this work,² however, this would represent a simple extension of the dc and small-signal theories presented in Chapters II and III, respectively.

1.2.1 Punch-Through Transistors. Punch-through transistors³ have no history except in a negative sense. The following is a quote typical of most if not all transistor textbooks:

"As the reverse-bias voltage on the collector junction increases still further, the collector space-charge penetration...increases and the effective base width is still further reduced. In some

transistors it is possible for the effective base width to be reduced to zero by this mechanism, and this condition is known as punch through. In a punch-through condition, the transistor behaves as though the emitter and collector were tied together by a fixed voltage source, and the base appears connected to both through a reverse-biased junction. Normal transistor action ceases as soon as the punch-through voltage is reached."⁴ In other words, punch through has been traditionally thought of as a breakdown condition. We counter here with the assertion that punch through is far from a breakdown mechanism and, in fact, in a low-impedance environment it is a desirable occurrence as the frequency response of the transistor actually improves when the device is punched through.

Proof of continued transistor action into punch through can be deduced from the results of an experiment that uses optical carrier generation to simulate majority carrier base current in a two-terminal p^+np^+ structure. The results of such an experiment are shown in Fig. 1.1. Here, a high-intensity microscope light was incident upon an X-band p^+np^+ Si device with a uniform base donor density of $1.6 \times 10^{15} \text{ cm}^{-3}$ and a base region width of $3.6 \text{ } \mu\text{m}$.^{*} As the bias voltage V_{ce} between the two p^+ regions is increased the structure behaves as a standard open-base phototransistor with a large Early effect due to the nonstandard doping profile.

* It should be noted that this particular device was not intended for the purposes of this experiment and was therefore fabricated with the face of the diode covered with gold to act as a contact. The quantity of light that reached the base region was thus limited to that entering via the exposed sidewalls of the device.

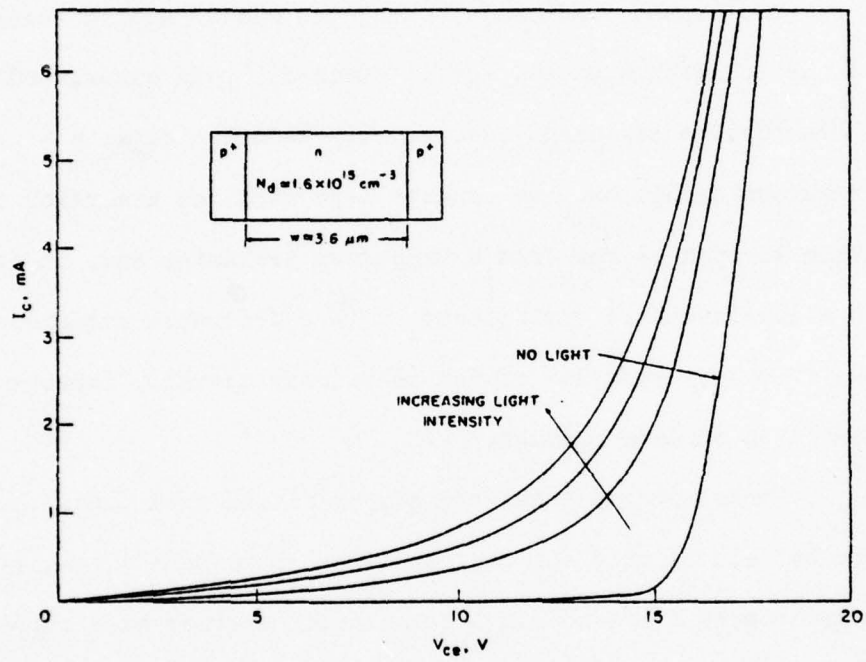


FIG. 1.1 EXPERIMENTAL p^+np^+ Si BARITT DIODE PHOTO I-V CHARACTERISTIC.

When the punch-through voltage is reached, a large collector current develops independent of the incident light. This is the punch-through current and is due to the diffusion of holes flowing across the now-lower potential barrier, i.e., forward-biased junction, between the base region and the emitting p^+ region. However, in the presence of light, differing magnitudes of light intensity can still be easily discerned even though the bias voltage is past the punch-through value. Since the punch-through mode change in the dc bias current per change in incident light intensity remains at or even increases from its pre-punch-through value, it must be true that controlled injection of minority carriers at the emitting junction continues into the punch-through mode of operation. That is, the presence of the space charge of the optically generated base region majority carriers (electrons) near the forward-biased emitter junction perturbs the barrier potential such that a greater or lesser number of minority carriers (holes) can diffuse across the junction depending upon the number of electrons generated within the depleted region of the device. For no optical generation the hole current is dependent solely on the level of punch-through bias, but with optical generation the magnitude of the hole current is modulated by the intensity of the incident light. The depth of this modulation is determined primarily by the standard transistor current gain mechanism. The direct optically generated hole current is but a small secondary effect, exactly analogous to the standard case of normal nonpunch-through photo-transistor operation. A more detailed analysis of a punch-through pnp photodetector is given

in Chapter V; a discussion of the experimental results and the basic principles of the device is included here as the basis for the fundamental premise that transistor action continues up to and into the punch-through mode.

Introduction of base region majority carriers into the quasi-neutral base region of a three-terminal junction transistor, under normal forward operating conditions, is accomplished by the simple process of base current flow. The situation is no different in the operation of punch-through transistors. Punch through reduces the effective width of the low field region through which majority carriers can flow in the transverse direction from the base contact to a spot under the emitter, but it cannot completely eliminate this region. The potential distribution from emitter to collector must include the value possessed by an undepleted majority carrier source region near the base contact; in the two-dimensional planar structure shown in Fig. 1.2, points 1 and 2 represent these two end points and the transverse path s , the equipotential surface common to both points. The dashed lines depict the extremities of the junction space charge or depletion layers for zero bias. When the bias voltages V_F and V_R are both applied with the polarities shown, the forward-biased emitter-base junction-depletion layer shrinks somewhat while the reverse-biased collector-base junction depletion layer grows and the structure is said to be under normal forward bias. If V_R is increased to a magnitude such that the edge of the collector-base depletion layer just touches the edge of the emitter-base layer, punch

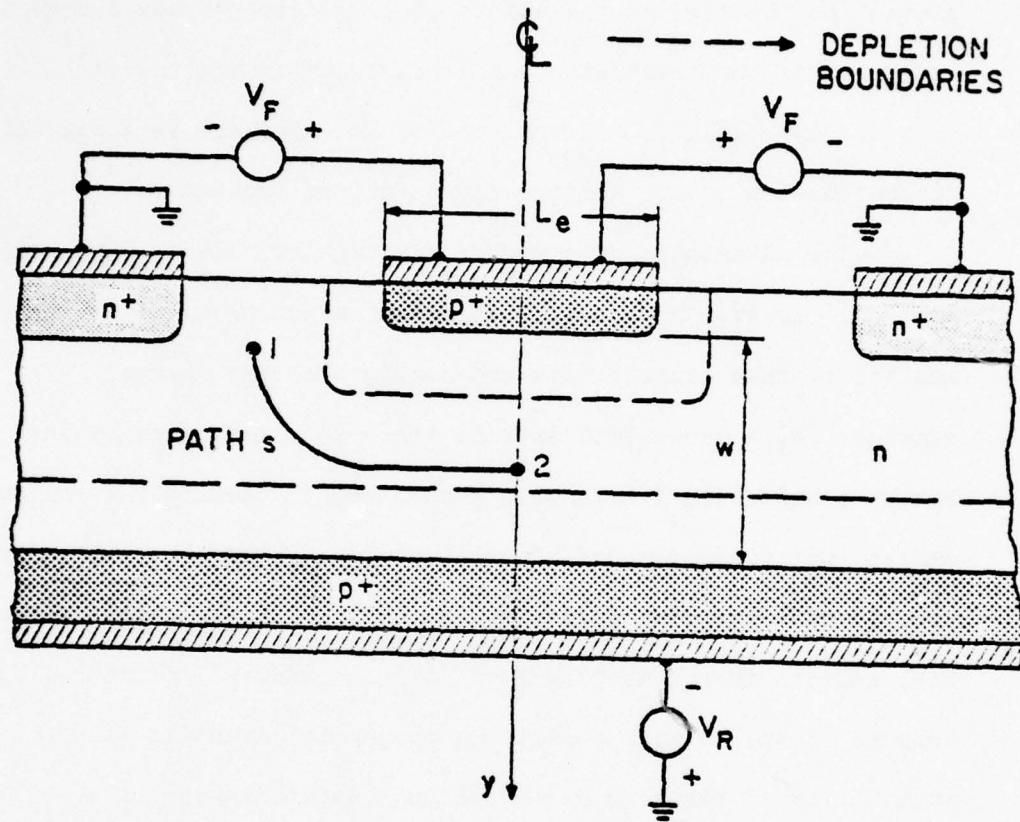


FIG. 1.2 TWO-DIMENSIONAL p^+np^+ TRANSISTOR STRUCTURE.

through occurs. Nevertheless, path s must still exist, though its longitudinal position may have shifted, and there remains a base current path continuum of majority carriers from the base contact to the edge of the emitter-base junction space-charge layer. Thus the transistor can still function and can still provide power gain if the collector load impedance is comparable to the now-low common emitter device output impedance.

The advantages of a punched-through transistor structure are: (1) an effective base width that is extremely small, thus negligible base transit time and negligible base charge storage; (2) a base width that is achieved electronically and not by a difficult fabrication procedure; (3) negligible collector series resistance because of the inverted doping profile in comparison with standard practice; and (4) the base push-out effect, Kirk effect, is not as prevalent as in a standard structure, again because of the doping profile. A potential advantage is the possibility of negative device output resistance due to transit-time effects in the collector-base space-charge layer. Given a negative output resistance, a three-terminal microwave BARITT-type oscillator can be envisioned. The presence of base region majority carriers at the minority carrier injection point in such a device would suppress the power self-limiting effects of the injected minority carrier space charge and enable a larger output RF power in comparison with that of a two-terminal device of similar longitudinal structure. Some possible disadvantages of punch-through transistors are: (1) high series base resistance due to the extremely narrow effective base width, (2) inability

to operate as a pure class B amplifier, and (3) thermal problems due to the necessarily high dc power bias point.

A prototype experimental Si p⁺np⁺ low-frequency structure (emitter stripe width = 20 μ m), similar to that shown in Fig. 1.2, was fabricated here* using diffused base and emitter contacts on epitaxial material (base region donor concentration = 1.3×10^{15} cm⁻³). A measured collector current collector-to-emitter voltage I-V curve, typical for these experimental devices, is shown in Fig. 1.3. A considerable portion of the epitaxial layer was lost to out diffusion of the substrate during the p-type isolation diffusion which accounts for the low value of the punch-through voltage at zero base current. Several devices were tested at 10 MHz as small-signal amplifiers in a 50- Ω system. In each case the forward scattering parameter S_{21} increased when the quiescent operating point was moved into the punch-through region. The specific improvement for the device shown in Fig. 1.3 was 5.5 dB in going from bias point A (S_{21} = 2.2 dB) to bias point B (S_{21} = 7.7 dB). Although these results are preliminary and far from exhaustive they do lend credence to the feasibility of the punch-through mode of operation.

Chapter II of this work contains a discussion of the detailed device physics of simple, uniformly doped punch-through transistors and a method of approximating values for the dc base resistance of a p⁺np⁺ Si version of the device. A small-signal equivalent circuit for the punch-through transistor and an estimate of the

* The structure was fabricated by T. N. Jackson.

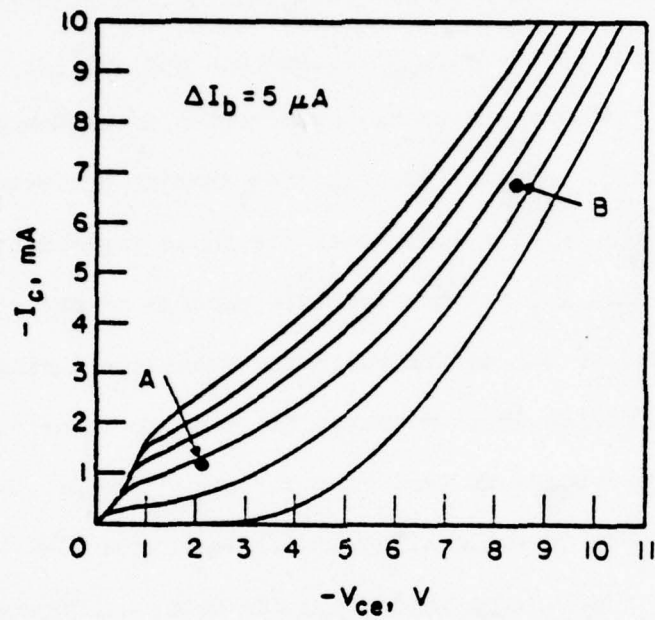


FIG. 1.3 I-V CHARACTERISTICS FOR EXPERIMENTAL p^+np^+ PUNCH-THROUGH TRANSISTOR.

high-frequency performance limitations based on the model are presented in Chapter III. Appendix A contains a discussion of a possible feedback mechanism in the punch-through transistor similar to the Early effect in standard transistors.

1.2.2 BARITT Diodes. The two-terminal three-layer punch-through structure now known as the BARITT diode was conceived by Shockley⁵ in 1954 as a means of achieving negative resistance through carrier diffusion or drift delay. Several important contributions concerning the device have appeared since (see Kwok¹ and Nguyen-Ba² for a complete history and state of the art) but the basic principles remain as originally promulgated by Shockley.

In light of the previous discussions on the punch-through transistor, a BARITT diode can most simply be described as an open-base punch-through transistor. But in the diode structure, as opposed to the transistor, base region majority carriers do not play an active role in the device physics since the diode has no prime source of majority carrier resupply. Base region minority carriers which diffuse over the emitter-base potential barrier are swept to the collector contact by the electric field of the reverse-biased collector-base junction.* The possibility of negative resistance arises when the time delay due to the minority carriers transit across the collector-base space-charge layer results in the fundamental component of the induced terminal current

* The two p-n junctions can be replaced by two back-to-back Schottky barriers,⁶ the structure of the first functioning microwave BARITT device.⁷

and the emitter-collector terminal voltage being close to 180 degrees out of phase. The BARITT diode is presently employed in microwave systems, though in relatively small numbers, as a low-noise two-terminal negative-resistance device. Unfortunately, due to the self-limiting and phase-tracking nature of its injection process the diode is also a low-power device. This one fact alone has hindered the BARITT's acceptance in the microwave design community. But for the receiver-type applications considered in this study, high power is not a prerequisite and the overall utility of the diode is reappraised.

A dc solution for the minority carrier current injection and for the low-field current transport of a uniformly doped BARITT diode is given in Chapter II. Small-signal impedance and noise models for the diode based on this dc solution are presented in Chapter III, and an approximate large-signal nonlinear model, harmonic effects included, is developed in Chapter VI. These models are used in the device-circuit analyses of frequency conversion effects in BARITT diode networks given in Chapters IV and VII.

1.2.3 Frequency Scaling of Punch-Through Devices. Simple frequency scaling rules for the design of uniformly doped punch-through devices can be derived from the following four principles:

1. BARITT diode injected minority carrier current density, dc and RF, must not approach a value that will induce excessive space-charge limiting of the injection process itself. Thus

$$J_o, J_{RF} \propto N_d, \quad (1.1)$$

where J_o is the dc current density, J_{RF} is the RF current density, and N_d is the base region doping density. This relationship also applies to the punch-through transistor but the restriction stems from a base push-out consideration rather than an injection limitation concern.

2. The magnitude of the electric field at the collector end of the metallurgical base region cannot exceed a critical maximum value; a value such that avalanche multiplication is avoided. That is, for maximum input dc power

$$N_d w = \text{const}, \quad (1.2)$$

where w is the width of the metallurgical base region.

3. The efficiency of power generation by negative-resistance transit-time oscillations is independent of frequency if skin-effect losses are neglected. Thus

$$\frac{P_{RF}}{P_{dc}} = \eta = \text{const} \quad (1.3)$$

for an optimally designed structure. This principle should be considered an assumption rather than a maxim, and at higher current densities must surely be suspect⁸ due to thermal effects.

4. The optimum frequency for negative-resistance power generation is proportional to the inverse of the metallurgical base width $f \propto w^{-1}$. Figure 1.4 is a summary of this relationship for several experimental and theoretical BARITT devices.^{9,10} Since the dc voltage across a punch-through device is approximately proportional to the product of the base region doping density and the square of the base region width

$$V_o \propto N_d w^2, \quad (1.4)$$

both the dc power density

$$\frac{P_{dc}}{A} \propto (N_d w)^2 \approx \text{const} \quad (1.5)$$

and the RF power density, reference Eq. 1.3, are independent of frequency, where A is the device cross-sectional area. Circuit design-scaling considerations require that circuit impedance levels remain constant with frequency so the device cross-sectional area A must be scaled as f^{-2} since the primary contribution to the impedance of a punched-through device is the cold capacitive reactance of the depleted base region

$$X_d \approx - \left(\frac{fA}{w} \right)^{-1}.$$

Thus the RF power generation capability of a punch-through structure follows the familiar

$$P_{RF} f^2 \approx \text{const}.$$

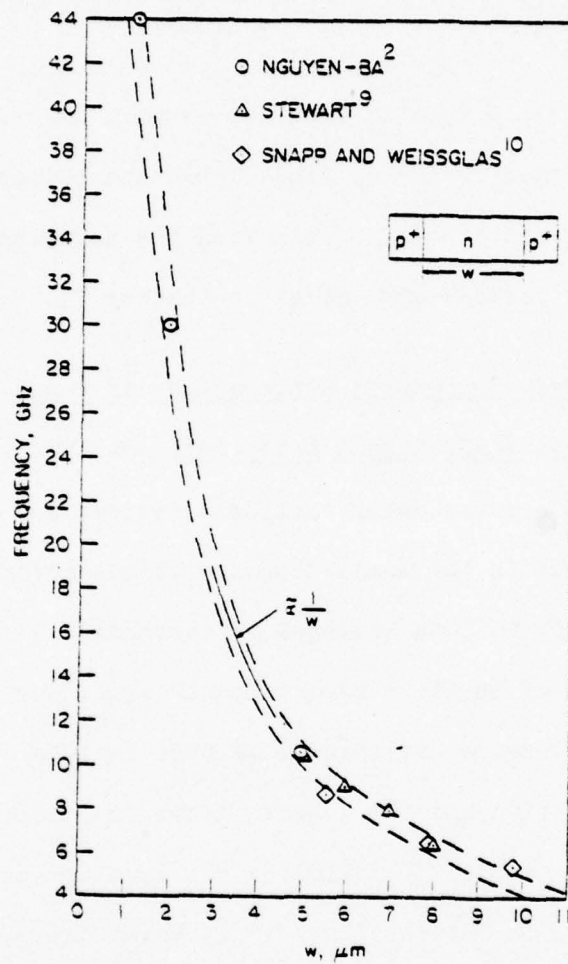


FIG. 1.4 NEGATIVE-RESISTANCE FREQUENCY DEPENDENCE ON METALLURGICAL BASE WIDTH FOR p^+np^+ BARITT DIODES.

Similarly, the magnitude of the large-signal negative resistance R_d can be shown to follow

$$R_d f^2 = \text{const} .$$

Examples of this type of behavior as well as a discussion of a realistic upper frequency limit for the application of punch-through devices are given following the development of the approximate large-signal model in Chapter VI.

1.3 Frequency Conversion Applications of Punch-Through Devices

1.3.1 Small-Signal Detection. BARITT diodes and punch-through transistors are basically nonlinear devices and as such can transfer perturbations in the small-signal voltages across their terminals to variations in bias voltages or currents. Since these devices are capable of negative resistance as well, the realization of a combined low-noise amplifier low-level detector is quite practical. This application and the general detector problem are reviewed in Chapter IV following the development of a device small-signal model in Chapter III. It is shown theoretically and experimentally that the BARITT diode in the proper circuit is a very sensitive detector of microwave signals. It is also shown that the price for such a response, not surprisingly, is bandwidth. As mentioned previously, a punched-through small-signal optical detector is described in Chapter V. The novelty of this detector is the possibility of quantum optical gain when the light modulation frequency is near the transit-time frequency of the device drift region. A gain-bandwidth trade-off exists for this "photo-BARITT" detector as does with the microwave version.

1.3.2 Four-Frequency Mixers. The paramount application for punch-through semiconductor devices espoused in this study is the four-frequency mixer, i.e., pump, primary sideband signal, image sideband signal, and intermediate frequency signal. Of the many variations of the punch-through four-frequency mixer structure perhaps the most interesting, primarily for its simplicity, is the self-pumped down-converter. The punch-through device is embedded in a circuit such that it oscillates at the pump frequency. An input signal at either a higher or a lower frequency than that of the pump is coupled to the device which in turn mixes it with the relatively large pumping waveform to create the image and a down-converted signal. Since in the right frequency range a punch-through transistor or BARITT diode can exhibit a negative resistance at any one or at all the principal frequencies of concern, the conversion process has the possibility of taking place with a net gain in power level. The total device-circuit interaction at all four frequencies governs whether any specific punch-through converter circuit has overall gain or loss. Of course, a punch-through mixer can be operated with an external pump source, the standard situation for Schottky-barrier and point-contact diodes, but this is counter to the simplicity of the self-pumped scheme. Both methods of pumping are discussed in the development of the four-frequency mixer in Chapter VII.

Punch-through transistors and BARITT diode mixers are interesting not only for their simple circuit configuration and possible gain mechanism but also for their low-noise characteristics.

The conversion noise for input signals very near the pump frequency is due primarily to the AM noise of the oscillation process. In this mode, self-oscillating BARITT diode doppler detectors have been shown to be superior, i.e., possess a lower minimum-detectable-signal capability, to their IMPATT and Gunn diode counterparts both at X-band¹¹ and above.¹² The conversion noise for input signals sufficiently far away from the pump frequency is due to the correlated and uncorrelated injection and drift noise components at the three signal frequencies and is relatively unaffected by the pump noise. Receiver single-sideband noise figures as low as 13.7 dB have been measured in this laboratory for X-band doubly-tuned BARITT diode mixers with an IF of 145 MHz.

Chapter VII of this work contains a detailed analysis of BARITT diode four-frequency mixers. For input signals very near the pump frequency a perturbation analysis^{13,14} on the large-signal model of Chapter VI is used to derive the conversion transfer function. This perturbation analysis is then shown to be a special case of the general four-frequency mixer. The general mixer itself is studied using a method very similar to Hines' work¹⁵ on instabilities in IMPATT diode networks. The noise figure of the mixer is calculated using a generalization of Strutt's method¹⁶ for simple diode mixers and is based on the small-signal impedance and noise models developed in Chapter III.

CHAPTER II. DEVICE PHYSICS AND DC SOLUTIONS

2.1 Introduction

This chapter presents a discussion of the physics of punch-through semiconductor devices, a dc solution for the drift region of a BARITT diode, and an estimate of the dc base resistance in a punch-through transistor. A current- and voltage-dependent boundary condition for the minority carrier concentration at the base edge of the collector-base depletion layer is introduced which allows a smooth transition from the classic diffusion transistor to the punch-through transistor or the BARITT diode. This transition is not possible if the standard voltage-only-dependent boundary condition for the minority carrier concentration is used to determine the current flow at the collector-base interface. Previous theories of punch-through current injection are discussed and the limitations of the theory used in this study, diffusion over a potential barrier, are detailed. A simple numerical analysis is used to solve for the minority carrier concentration in the low-field portion of the drift region in a BARITT diode and an upper bound is determined for the dc resistance to transverse majority carrier current flow in the effective base region of a punch-through transistor.

2.2 Carrier Concentrations in Narrow-Base Diffusion Transistors and in Punch-Through Transistors

The standard solution for carrier concentrations and currents in the field-free base region of a uniformly doped transistor structure

under low-level injection was first given by Shockley¹⁷ in his classic paper that introduced the junction transistor in 1949. This solution has served as the foundation for all the present-day theories of bipolar transistor operation, i.e., high injection, field-aided base transport, Webster effect, and Kirk effect. This section exposes the limitations of the standard theory under the conditions of an extremely narrow base width and punch through. The standard theory is then modified and the punch-through limit is accounted for.

2.2.1 Standard Theory for Diffusion Transistors. The one-dimensional field-free base region pnp transistor structure considered in this study is shown in Fig. 2.1. A constant base doping concentration and low-level emitter injection are assumed; thus, minority carrier transport in the quasi-neutral base region can be described by diffusion alone, that is

$$J_p = -qD_p \frac{dp}{dx}, \quad (2.1)$$

where J_p is the hole current density, D_p is the low-field hole diffusion coefficient, and q is the electronic charge. The other relationship which governs the base region hole distribution is the time-independent hole continuity equation

$$0 = \frac{p - p_n}{\tau_p} + \frac{1}{q} \frac{dJ_p}{dx}, \quad (2.2)$$

where p_n is the thermal equilibrium hole concentration and τ_p is the hole lifetime. The solution for the resulting second-order, constant coefficient, homogeneous ordinary differential equation can be expressed as

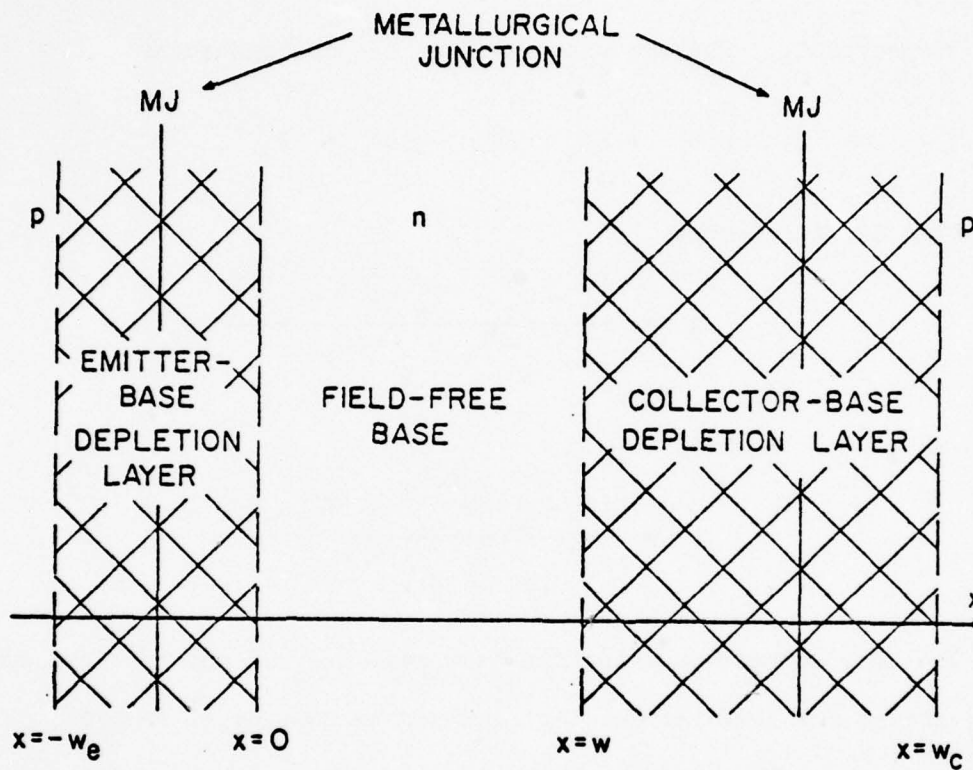


FIG. 2.1 ONE-DIMENSIONAL pnp TRANSISTOR STRUCTURE.

$$p - p_n = A e^{x/L_p} + B e^{-x/L_p},$$

where $L_p = \sqrt{D_p \tau_p}$ = the diffusion length for holes in the base and A and B are constants which must be determined by the boundary conditions at the emitter and collector edges of the base, $x = 0$ and $x = w$, respectively. These boundary values are designated as

$$p(0) = F_e \quad \text{and} \quad p(w) = F_c. \quad (2.3)$$

Thus A and B become

$$A = \frac{F_c - p_n - (F_e - p_n) e^{-w/L_p}}{e^{w/L_p} - e^{-w/L_p}}$$

and

$$B = \frac{(F_e - p_n) e^{w/L_p} - (F_c - p_n)}{e^{w/L_p} - e^{-w/L_p}}.$$

The hole current entering the base region $J_p(0)$ and the hole current exiting the base region $J_p(w)$ can now be determined from Eq. 2.1, in terms of the hole concentration boundary values, as

$$J_p(0) = \frac{qD_p}{L_p} \left[(F_e - p_n) \coth \frac{w}{L_p} - (F_c - p_n) \operatorname{csch} \frac{w}{L_p} \right] \quad (2.4)$$

and

$$J_p(w) = \frac{qD_p}{L_p} \left[(F_e - p_n) \operatorname{csch} \frac{w}{L_p} - (F_c - p_n) \coth \frac{w}{L_p} \right]. \quad (2.5)$$

To complete the description of the transistor currents the majority carrier electron currents at the emitter and collector edges of their

respective depletion layers are added to the hole currents to form the emitter and collector terminal currents, defined as positive into the terminals,

$$J_e = J_p(-w_e) + J_n(-w_e) \quad (2.6)$$

and

$$J_c = -J_p(w_c) - J_n(w_c) \quad (2.7)$$

The standard minority carrier boundary condition for the junction transistor first introduced by Shockley is

$$F = p_n e^{V_J/V_T}, \quad (2.8)$$

where V_J is the applied voltage that appears across the junction depletion layer, emitter-base or collector-base, and V_T is the thermal voltage kT/q . Application of this particular form of the minority carrier boundary condition to transistors with the emitter-base junction forward biased such that $F_e \gg p_n$, the collector-base junction reverse biased such that $F_c \ll p_n$, and with base widths greater than several Debye lengths yields a satisfactory description of transistor action. That is, a small majority carrier current in the base controls a much larger injected current into the same region. If the transport of minority carrier current through the base is efficient then there exists the possibility of a power gain mechanism.

2.2.2 Narrow Base Width Considerations and the Punch-Through Transistor. The standard solution for currents in the active region of a diffusion transistor was presented in the previous section.

In this section a solution under narrow base width conditions is considered. Specifically, the standard solution is modified to account for the punch-through limit, $w \rightarrow 0$.

A problem arises when the standard boundary condition, Eq. 2.8, is applied to the collector-base junction under the additional conditions of normal biasing, $V_{EB} > 0$ and $\exp(V_{CB}/V_T) \ll 1$, and a very small base width, $w/L_p \ll 1$. The expressions for the exiting and entering hole currents in the base region $[0, w]$ now become

$$J_p(w) \approx \frac{qD_p F_e}{w} \left[1 + \frac{1}{6} \left(\frac{w}{L_p} \right)^2 \right]^{-1} \quad (2.9)$$

and

$$\begin{aligned} J_p(0) &= \frac{qD_p F_e}{L_p} \left(\frac{L_p}{w} + \frac{w}{3L_p} \right) \\ &= J_p(w) + \frac{qD_p w}{2L_p^2} F_e, \end{aligned} \quad (2.10)$$

where the standard small argument expansions for the hyperbolic functions have been employed and the emitter-base junction boundary condition has been kept in its general form. It appears that both currents can be made arbitrarily large by a simple reduction of the base width w . Of course this is not physically possible as the emitter-base junction can only supply a finite amount of current, the ultimate magnitude of which is determined by the junction doping profile and its level of forward bias.

The requirement that the hole concentration at the base edge of the collector-base depletion layer be less than the thermal equilibrium concentration, independent of the hole current density,

is disconcerting at best. For typical base doping densities the hole thermal equilibrium concentration is approximately 10^4 to 10^6 holes/cm³ in Si. Thus the standard reverse-biased p-n junction boundary condition, Eq. 2.8, would lead to absurdly low minority carrier concentrations which could never support the transport transition from diffusion to drift current that holes must undergo in traversing the field-free base region to the high-field collector-base depletion region. Matz¹⁸ was apparently the first to consider this difficulty in detail and was able to solve for the minority carrier concentration at the collector edge of the base region by considering a two-carrier model and by using the condition that the longitudinal majority carrier current at the depletion-layer edge is zero. Kirk,¹⁹ in his study of the base-push-out effect on minority carrier transit time, required that the minority carrier charge density at the depletion-layer edge be equal to the dc collector current density divided by the scattering-limited drift velocity. Middlebrook²⁰ studied the effects of Kirk's current-dependent collector boundary condition on the behavior of the dc collector current and the dc common emitter current gain. None of these authors, however, considered the combined effects of a substantial minority carrier concentration at the base edge of the collector-base depletion layer and an extremely narrow base width.

The following empirical formula is suggested as a replacement for the standard collector edge boundary condition

$$F_c = Kp_s[1 - \exp(-p_s/p_n)] + p_n \exp(V_{CB}/V_T) \quad , \quad (2.11)$$

where $p_s = J_p(w)/qv_s$, the hole concentration that would be needed to account for a pure saturated drift current of magnitude $J_p(w)$, with v_s the saturated drift velocity ($v_s = 10^7$ cm/s in Si) and K a dimensionless constant equal to the ratio of the actual hole concentration at the base edge of the collector-base depletion layer to the saturated drift hole concentration p_s . A numerical solution for a single-carrier model of drift and diffusion current flow in a depleted region near a zero field injection point is given later in this chapter. From this single-carrier solution a lower bound on K for a two-carrier device can be determined, but it is sufficient for now to simply acknowledge the fact that for base donor concentrations less than 5×10^{16} in Si the value of K is greater than five. Note that the new boundary condition, Eq. 2.11, is a smooth transition from the standard boundary conditions, which is valid only for low collector-base bias and extremely low collector-current densities, to a new boundary value which is valid for any bias level and current density in the normal region of transistor operation. In particular, for normal biasing, $\exp(V_{CB}/V_T) \ll 1$, and current densities such that $p_s \gg p_n$, Eq. 2.11 simplifies to

$$F_c = Kp_s \quad (2.12)$$

With this simplification the hole current density at $x = w$ for the narrow-base condition $w \ll L_p$ can be solved for in closed form as

$$J_p(w) = \frac{qD_p F_e}{w \left(1 + \frac{KD_p}{wv_s} \right)} \quad (2.13)$$

Now as $w \rightarrow 0$ the current does not grow without bound and a measure of physical reality is retained. For $K = 10.0$ the base width at which the second term in the denominator of Eq. 2.13 becomes unity is $0.2 \mu\text{m}$ for holes in Si.

The concept of "punch through" in a transistor is now examined. Intuitively, a mathematical description of a transistor that is punched through should be obtainable from the standard transistor equations by taking the limit as the base width approaches zero. With the standard boundary condition for minority carrier concentration at the collector edge of the base region this is not possible, as is evidenced by Eq. 2.9. However, using the simplified form of Eq. 2.11, $F_c = Kp_s$, the limit as $w \rightarrow 0$ of the minority current density remains finite and is

$$\lim_{w \rightarrow 0} J_p(w) = J_p(0) = \frac{qv_s F_e}{K} \quad (2.14)$$

At punch through, control of the emitter injection process will be maintained if a base region majority carrier current path exists from the base terminal to a point along the base edge of the emitter-base depletion layer, $x = 0$ in Fig. 2.1. This path allows a base current to flow and provides an independent means of control over the voltage across the emitter-base depletion layer. This conduction path of majority carriers must exist since the presence of an equal potential contour for normal biasing, path s in Fig. 1.2, between an undepleted base region point, 1, and a point under the emitter stripe, 2, precludes a carrier concentration gradient along the path as there is no counter-balancing path-directed electric field along the path by definition. Thus transistor action, controlled

injection of minority carriers, will continue into the punch-through mode of operation.

A simplifying assumption that will aid in the understanding of punch-through operation without detracting from the basic physics of the mode is that carrier recombination and generation can be neglected within the transistor except in the undepleted emitter and collector bulk regions. After the complete formulation of the punch-through transistor problem, one can always return to include the effects of recombination in the forward-biased emitter-base junction and in the low-field portion of the drift region as well as generation in the reverse-biased collector-base junction,²¹ but these corrections will not be attempted in this study. Without recombination the hole current ceases to be a function of x within the depleted regions, $J_p(x) = J_p(0) = J_p$, and the collector and emitter terminal currents become

$$J_c = -J_p - J_{ns} \quad (2.15)$$

and

$$J_e = J_p(-w_e) + J_n(-w_e) = J_p + J_{nb} + J_{ns} \quad (2.16)$$

where J_{ns} is the electron reverse leakage current density of the collector-base junction, a constant for sufficient reverse bias, and J_{nb} is the emitter electron current supplied from the base terminal. It is easily shown from the electron current continuity equation at $x = -w_e$ that the total emitter electron current can be expressed as

$$J_{nb} + J_{ns} = \frac{qD_n}{L_n} (F_n - n_p) \quad (2.17)$$

where D_n and L_n are the electron diffusion coefficient and the electron diffusion length within the emitter region, respectively; n_p is the thermal equilibrium electron concentration within the emitter; and the boundary value F_n is the electron density at the emitter edge of the emitter-base depletion layer, $x = -w_e$. We have assumed that the longitudinal length of the emitter region is much greater than the electron diffusion length. Thus for no recombination throughout the active region of the device, the emitter and collector terminal currents for a punch-through transistor can be expressed in terms of the hole and the electron boundary values for the forward-biased emitter-base junction. Estimates for these values are given in the next section.

2.3 Physics of Punch-Through Injection and the BARITT Diode

2.3.1 Punch-Through Injection. Previous investigators^{22,23} attributed forward current flow in punch-through p^+np^+ devices to thermionic emission over the emitter-base barrier and solved for a no-barrier-maximum current density in terms of an effective Richardson constant. Chu et al.,²² without discussion, justified this calculation by assuming that the mean free path for momentum-randomizing collisions was greater than the base region Debye length. However, the one experimental example they present violates this assumption by more than an order of magnitude. For p^+np^+ Si devices the mean free path and the Debye length become comparable in structures with base doping densities in excess of 10^{17} donors/cm³, well above the doping concentrations of the envisioned devices discussed in Chapter I. Persky²⁴ investigated the problem of current

flow in a punch-through device and redefined the diffusion current when carrier concentration gradients in a field-free region approach values that cannot be sustained by the standard diffusion process. That is, when a carrier concentration gradient predicts a value of diffusion current greater than that of the local thermionic emission limit,

$$|J_{diff}| = \left| qD_p \frac{dp}{dx} \right| > qp v_{TE} , \quad (2.18)$$

where v_{TE} is the thermal velocity of carriers in any one particular direction, then the definition of diffusion current must be modified. Persky determined that the current definition must be altered by the addition of a saturation expression for uniformly doped p^+np^+ Si devices with $N_d > 5 \times 10^{17} \text{ cm}^{-3}$.

In this study we shall assume that the punched-through minority carrier injection in the forward-biased emitter-base junction can be described by the standard diffusion process. After calculations for carrier concentrations and gradients are completed we can check for self-consistency by using Eq. 2.18. The only field-free point within the active region of a punch-through structure is the transition point between the emitter-base and the collector-base depletion regions, termed the injection point or $x = 0$. So for self-consistency at $x = 0$ it must be true that

$$qp(0)v_{TE} > J_o ,$$

but

$$p(0) = Kp_s = K \frac{J_o}{qv_s}$$

and the diffusion self-consistency condition reduces to

$$K > \frac{v_s}{v_{TE}}.$$

A worst case value of v_{TE} was given by Berz²⁵ for a point at the border of a sink region for diffusing carriers as

$$\begin{aligned} v_{TE} &= \left(\frac{2qV_T}{\pi m^*} \right)^{1/2} \\ &= 2.25 \times 10^6 \text{ cm/s} \end{aligned}$$

for holes in Si, where m^* is the mobility effective mass of the carrier (for holes in Si $m^* = 0.38 m_0$, where m_0 is the rest mass of an electron²⁶). Thus the thermal process of diffusion can adequately describe hole injection in a pnp punch-through device if $K > 4.5$.

A numerical solution for the K value of a single-carrier model of a p⁺np⁺ Si BARITT diode as a function of base region doping density and with dc current density as a parameter is given in Fig. 2.2. This numerical solution is described in Section 2.4. As can be seen, K exceeds the self-consistency limit for $N_d \leq 6 \times 10^{16}$.

Since the slope of the electric field in the low-field region on the collector side of the injection point in a two-carrier device (a punch-through transistor) must necessarily be lower than that in a single-carrier device (a BARITT diode), diffusion current must be the dominant transport mechanism for a longer distance in the reverse-biased region of the punch-through transistor than in the BARITT diode. Therefore, for the same current density

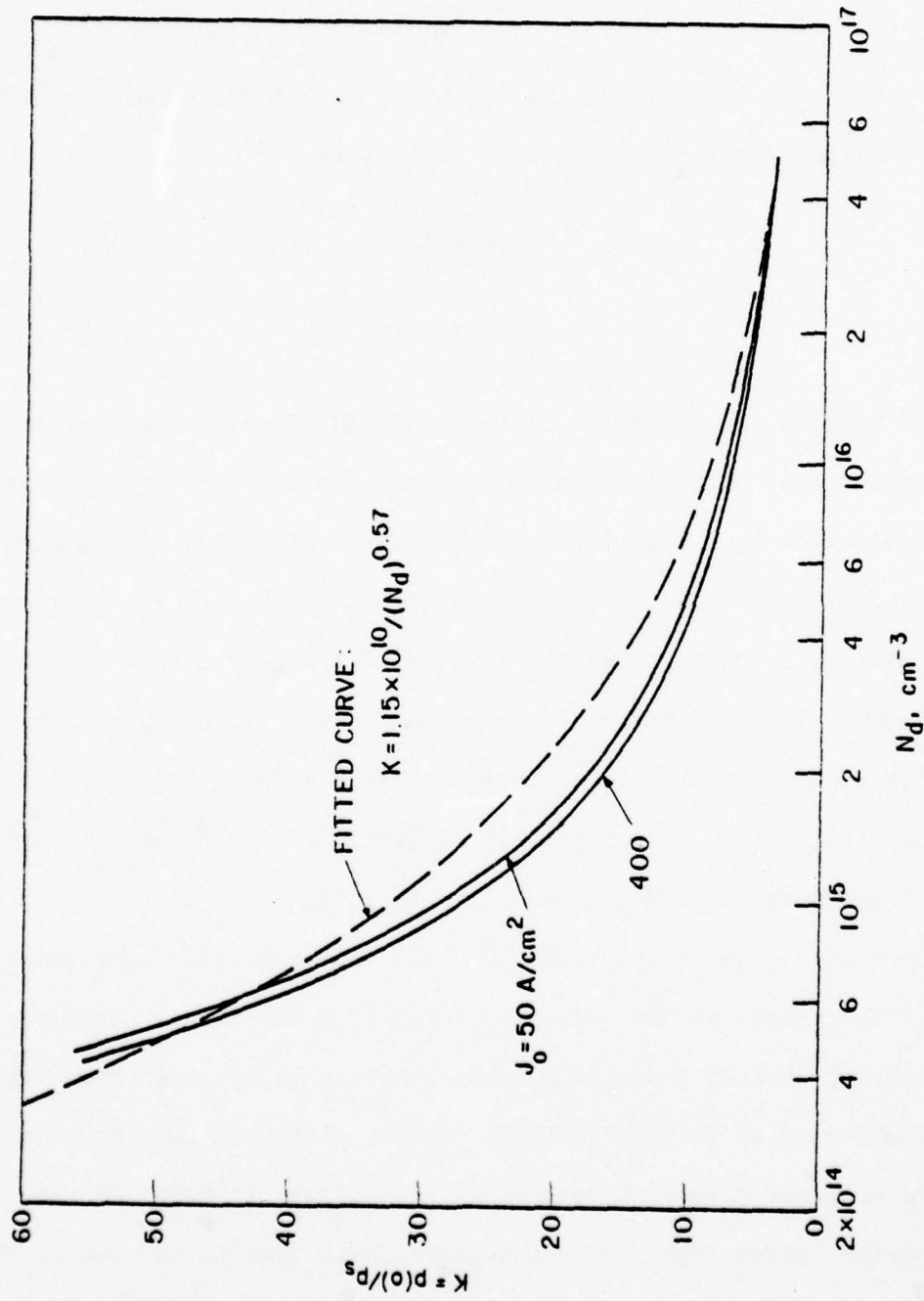


FIG. 2.2 INJECTION POINT CARRIER CONCENTRATION RATIO

$K = p(0)/p_s$ FOR A p^+np^+ Si BARITT DEVICE.

$$K_{PTT} > K_{BARITT}$$

and for devices with $N_d \leq 6 \times 10^{16}$, Fig. 2.2 assures that diffusion describes the injection process in a punch-through transistor as well as a BARITT diode.

We now make the principal assumption needed to determine the boundary values F_e and F_n , the hole and electron concentrations on the opposite sides of the emitter-base barrier. Namely, the hole and electron quasi-Fermi potentials are assumed to remain approximately constant across the extent of the barrier. This assumption is standard for low-level injection theory of a p-n junction^{27,28} and leads to the standard boundary condition, Eq. 2.8, for the forward-biased p-n junction, but it is obviously not true for the reverse-biased collector-base junction in a transistor and thus one should not expect Eq. 2.8 to lead to a viable solution for the collector current. V_e is defined as the potential at $x = -w_e$ and $V_e + V_{bi} - V_F$, the potential at $x = 0$, where V_{bi} is the built-in potential of the junction and V_F is the applied voltage across the junction depletion layer. Thus,

$$F_n = n(-w_e) = n_i e^{(V_e - \phi_{ne})/V_T}$$

and

$$n(0) = n_i e^{(V_e + V_{bi} - V_F - \phi_{ne})/V_T},$$

where n_i is the intrinsic carrier concentration of the material and ϕ_{ne} is the electron quasi-Fermi potential at $x = -w_e$. Dividing the

two equations yields F_n in terms of the electron concentration at the injection point:

$$F_n = n(0) e^{-(V_{bi}-V_F)/V_T} \quad (2.19)$$

Similarly, for holes

$$F_e = p(-w_e) e^{-(V_{bi}-V_F)/V_T}$$

However, since

$$p(-w_e) = p_n e^{V_{bi}/V_T} = (n_i^2/N_d) e^{V_{bi}/V_T}$$

we have

$$F_e = \frac{n_i^2}{N_d} e^{V_F/V_T} \quad (2.20)$$

For a transistor with quasi-charge neutrality at $x = 0$,

$$n(0) = p(0) + N_d$$

Thus

$$F_n = N_d \left[1 + \left(\frac{n_i}{N_d} \right)^2 e^{V_F/V_T} \right] e^{-(V_{bi}-V_F)/V_T}, \quad (2.21)$$

which reduces to the standard low-level form when the second term in brackets can be neglected in comparison with the first.

2.3.2 The BARITT Diode. A BARITT diode, an open-base punch-through transistor, can easily be described by the present formulation. The emitter electron current density from the base J_{nb} is zero and, since there is no recombination in the active region of the diode by assumption, the only electron current within the diode is the

constant reverse leakage current of the collector-base junction.

From Eqs. 2.17 and 2.19 we find that

$$J_{ns} = \frac{qD_n}{L_n} \left[n(0) e^{-(V_{bi}-V_F)/V_T} - n_p \right] .$$

The electron leakage current for a p-n junction is²⁹

$$J_{ns} = \frac{qD_n}{L_n} N_d e^{-V_{bi}/V_T}$$

so the electron concentration at the injection point of a symmetrically doped p^+np^+ device can be solved for and is given by

$$n(0) = 2N_d e^{-V_F/V_T} . \quad (2.22)$$

With this equation, the justification for considering the BARITT diode as a single-carrier device becomes evident. For any bias above a moderate level of forward drive the concentration of base region majority carriers, in this case electrons, can be neglected in comparison to that of the injected minority carriers. Specifically, the concentrations of holes and electrons at $x = 0$ are equal when

$$\frac{V_F}{V_T} = \ln \frac{N_d}{n_i} + \frac{1}{2} \ln 2 .$$

In Si at room temperature $n_i = 1.6 \times 10^{10} \text{ cm}^{-3}$ and for $N_d = 5 \times 10^{15} \text{ cm}^{-3}$ the level of drive needed to make the carrier concentrations equal is $V_F/V_T = 13.0$.

The hole current for a punch-through pnp BARITT device can be obtained from Eqs. 2.14 and 2.20 and is given by

$$J_p = \frac{qv_s}{K} \frac{n_i^2}{N_d} e^{V_F/V_T} . \quad (2.23)$$

The quantity $qv_s n_1^2 / KN_d$ behaves as a diode saturation current and, since K is a very weak function of J_p , the injection is exponential in nature. It should be noted that Eq. 2.23 holds for the hole current injected into a punch-through transistor as well, although the value of the saturation current will be somewhat smaller since $K_{PTT} > K_{BARITT}$.

2.4 Dc Solutions for the Low-Field Region of a BARITT Diode

An approximate but computationally simple numerical solution for the minority carrier concentration in the low electric field region on the collector side of the injection point can be obtained by assuming a piecewise linear electric field distribution. That is, the low-field region is divided into N lumps, each lump of length Δ , and within each lump the slope of the electric field is assumed to be constant, as shown in Fig. 2.3. A convenient terminating point for the solution is the distance w_s needed for the space-charge-free electric field to rise to a value E_s such that the drift velocity is one half its saturated value

$$w_s = \frac{E_s}{\frac{qN_d}{\epsilon}}, \quad (2.24)$$

where the velocity-electric field relationship is assumed to be

$$v = \frac{v_s}{E + E_s} E. \quad (2.25)$$

A further assumption is that the emitter-base junction's level of forward drive is such that the majority carriers (electrons) in the active region can be neglected in comparison with the background

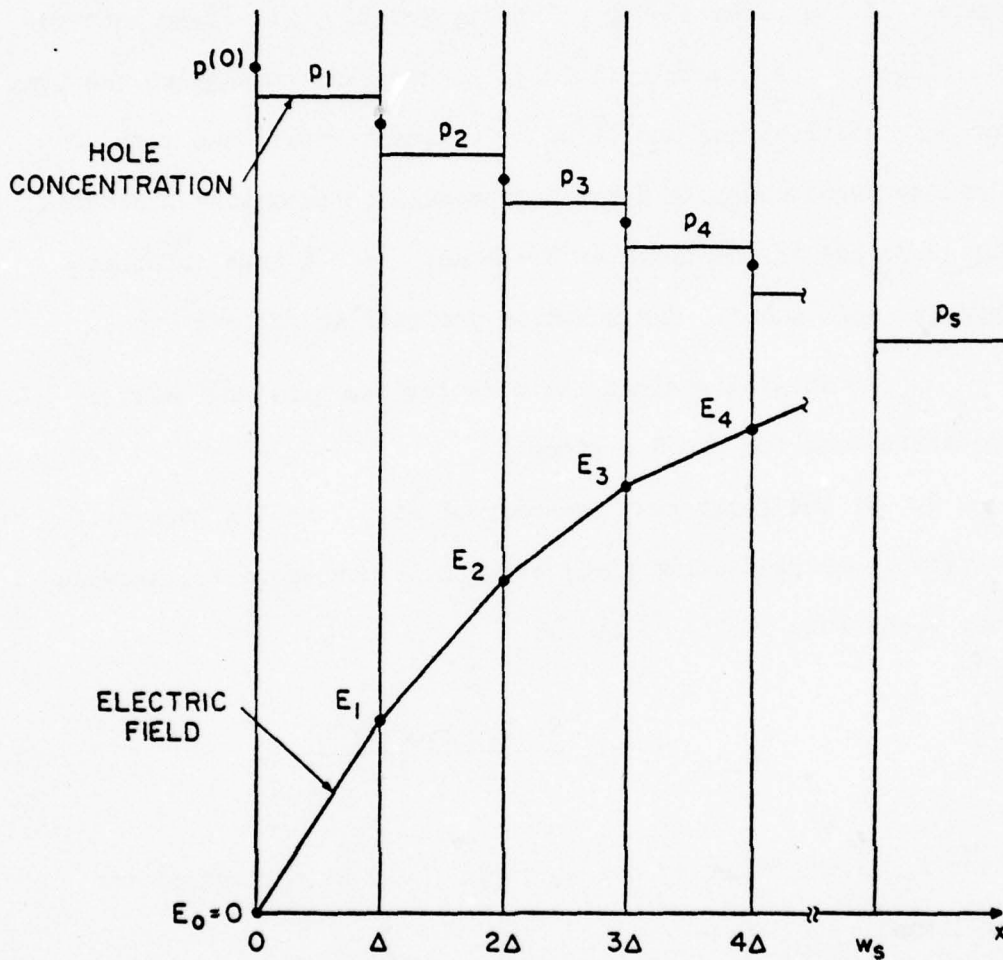


FIG. 2.3 LUMPED REPRESENTATION OF CARRIER CONCENTRATION AND ELECTRIC FIELD IN THE LOW-FIELD REGION OF A BARITT DIODE.

doping and the injected minority carriers (holes). In order to satisfy Gauss's law within each lump,

$$\frac{dE}{dx} = \frac{q}{\epsilon} (N_d + p) , \quad (2.26)$$

where ϵ is the permittivity of the material, it is clear that for the slope of the electric field to be constant throughout the lump the hole distribution must also be constant within the lump. Thus the resulting hole distribution will be piecewise discontinuous, Fig. 2.3, but in the limit as $N \rightarrow \infty$ and $\Delta \rightarrow 0$ a true solution should be approached. The solution proceeds as follows:

1. An initial estimate is made for the constant carrier concentrations for the N regions.
2. At the right most boundary of each lump i a hole drift current is defined using the average hole concentration between lump i and lump $i + 1$. That is,

$$J_{\text{drift}}^i = qv_s \frac{p_i + p_{i+1}}{2} \frac{E_i}{E_i + E_s} , \quad (2.27)$$

where E_i is the value of the electric field at the end of the i th lump,

$$E_i = E_{i-1} + \frac{q}{\epsilon} (N_d + p_i) , \quad (2.28)$$

where $E_0 = E(0) = 0$. Also a hole diffusion current is defined at the same point, depending upon the difference between the hole concentrations of the i th + 1 and i th lump,

$$J_{diff}^i = -qV_T \frac{v_s}{E_i + E_s} \frac{p_{i+1} - p_i}{\Delta} , \quad (2.29)$$

where the Einstein relation has been used to express the diffusion coefficient. The total current at $x = i\Delta$ is then

$$J^i = J_{drift}^i + J_{diff}^i .$$

For the $i = N$ case, p_{N+1} is assumed to be equal to the pure saturation velocity hole concentration p_s . In addition, this concentration is assumed to exist at $x = 10 w_s$, even if the diode is not physically this long. The spatial average for the hole concentration at $x = w_s$ then becomes

$$p_s + \frac{9w_s}{9w_s + 0.5\Delta} (p_N - p_s) ,$$

and the slope of the hole concentration at $x = w_s$ is

$$\frac{p_s - p_N}{9w_s + 0.5\Delta} .$$

The actual value of the concentration slope at this point has only a miniscule effect on the solution as well over 90 percent of the current flow at $x = w_s$ is by the drift mechanism. The ratio of the drift current component to the total current over the low-field region for a specific structure is shown in Fig. 2.4.

3. The specified current density is subtracted from each calculated current density; in vector form

$$\underline{J} - \underline{J}_0 = \underline{\Delta J} .$$

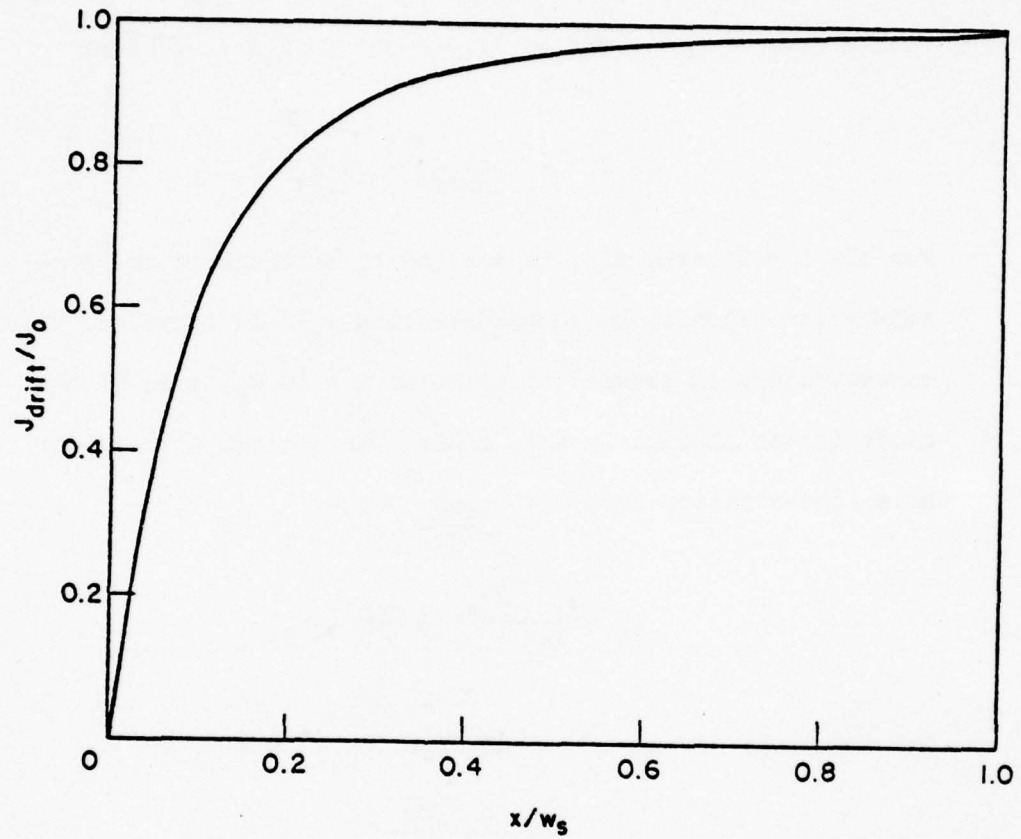


FIG. 2.4 RATIO OF DRIFT TO TOTAL CURRENT AS A FUNCTION OF POSITION FOR A p^+np^+ Si BARITT DEVICE.

($N_d = 5 \times 10^{15} \text{ cm}^{-3}$, $J_0 = 300 \text{ A/cm}^2$ AND $N = 20$)

If the magnitude of ΔJ is below a specified error, then the solution is considered converged; if not, continue.

4. The sensitivity matrix or Jacobian can be formed as

$$[JC]_{ij} = \frac{\partial J^i}{\partial p_j}.$$

In this case the differentiation can be carried out analytically from Eqs. 2.27 through 2.29.

5. A first-order Newton correction is performed:

$$\underline{p}^{new} = \underline{p}^{old} - [JC]^{-1} \Delta J.$$

The iteration starts again with Step 2 and continues.

The convergence properties of this method of solution are demonstrated in Fig. 2.5 which shows the behavior of the calculated value of K vs. the number of lumps in the low-field region for a particular structure, where

$$K = \frac{p(0)}{p_s} = \frac{p_1 + \frac{\Delta J_o}{2qD_p}}{p_s}.$$

As can be seen a satisfactory solution, within 15 percent of the limiting value, can be obtained with as few as five lumps. The error criteria, Step 2, for this study was $|\Delta J| \leq 10^{-4}$ A/cm² and the average number of Newton iterations needed to achieve this level of error was five, starting from an initial guess of $p_i = p_s$ for all i .

Typical results for the normalized hole concentration and the electric field in the low-field region are shown in Figs. 2.6 through 2.8 for structures with $N_d = 10^{15}$, 5×10^{15} and 10^{16} cm⁻³ and $J_o = 100$, 300 and 500 A/cm². Rather than present the hole concentration in stepped form as in Fig. 2.3 a straight-line

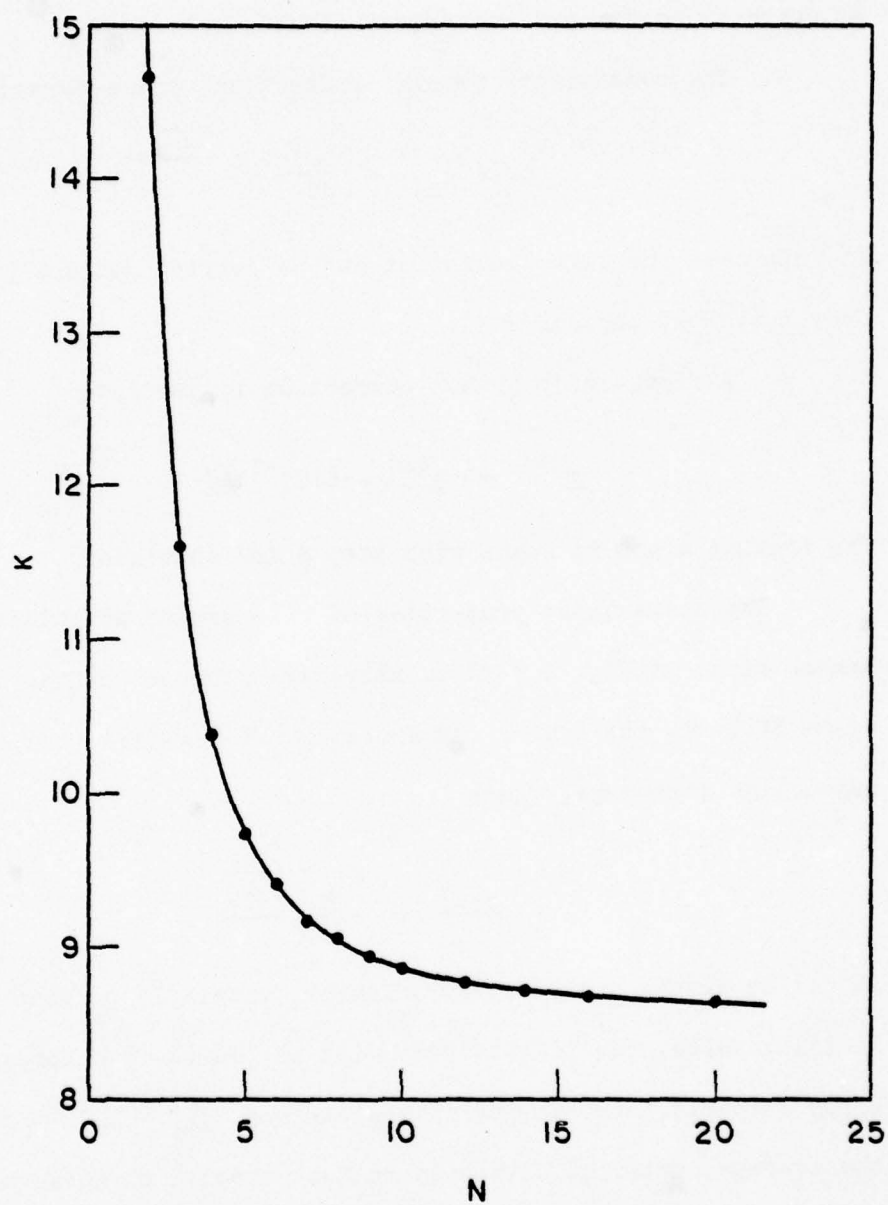


FIG. 2.5 CONVERGENCE OF DC SOLUTION. ($N_d = 5 \times 10^{15} \text{ cm}^{-3}$
AND $J_o = 300 \text{ A/cm}^2$)

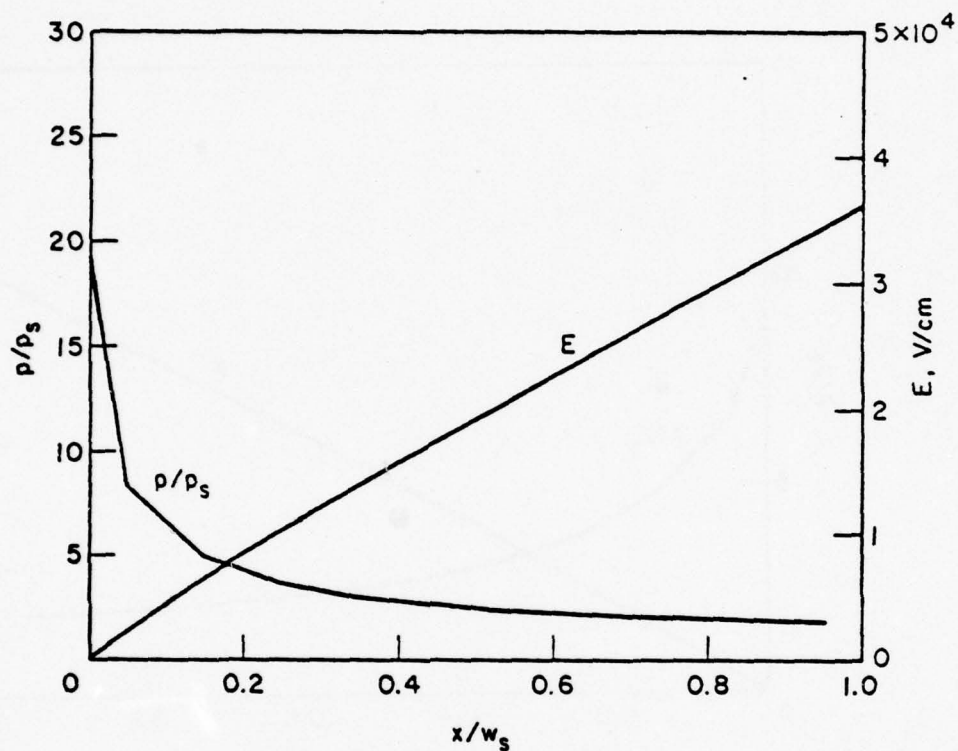


FIG. 2.6 CARRIER CONCENTRATION AND ELECTRIC FIELD AS FUNCTIONS OF POSITION IN THE LOW-FIELD REGION OF A p^+np^+ Si BARITT DIODE. ($N_d = 1 \times 10^{15} \text{ cm}^{-3}$ AND $J_o = 100 \text{ A/cm}^2$)

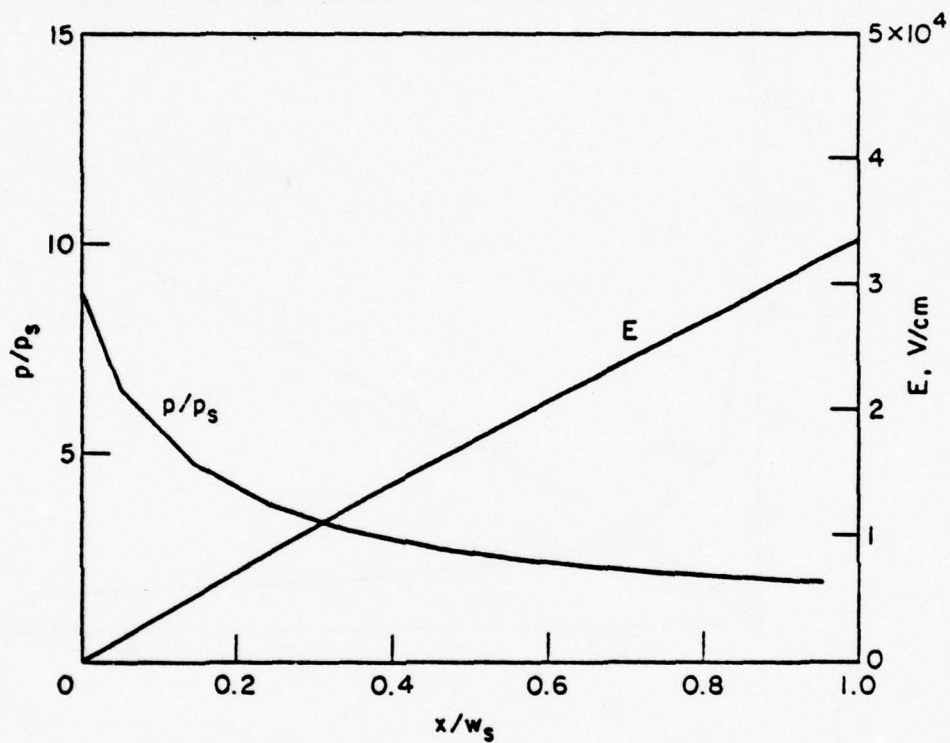


FIG. 2.7 CARRIER CONCENTRATION AND ELECTRIC FIELD AS FUNCTIONS OF POSITION IN THE LOW-FIELD REGION OF A p^+np^+ Si BARITT DIODE. ($N_d = 5 \times 10^{15} \text{ cm}^{-3}$ AND $J_o = 300 \text{ A/cm}^2$)

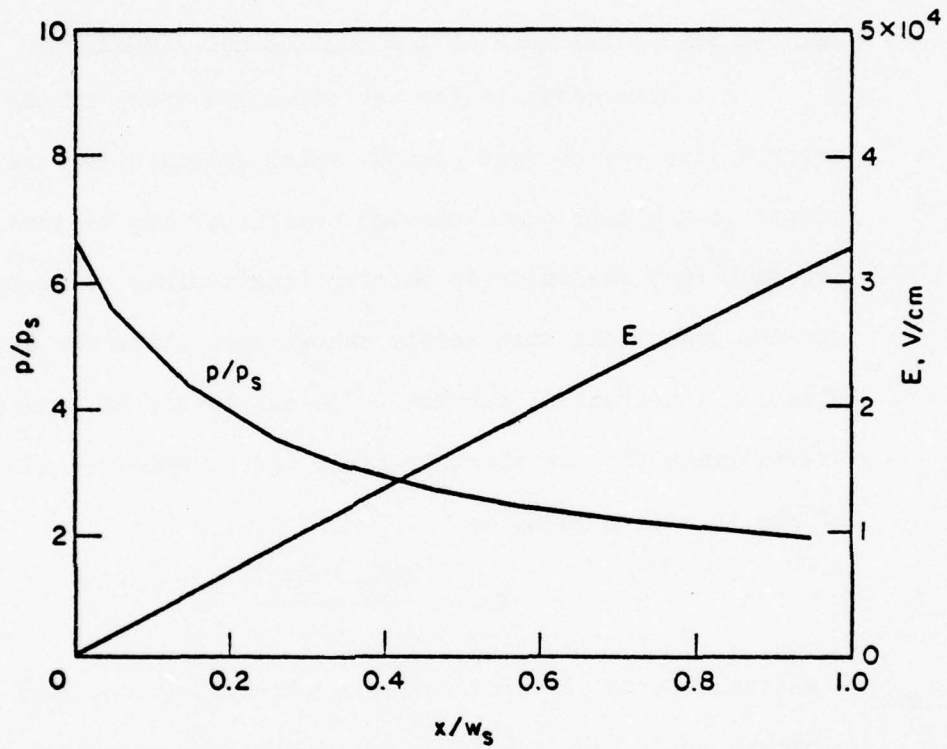


FIG. 2.8 CARRIER CONCENTRATION AND ELECTRIC FIELD AS FUNCTIONS OF POSITION IN THE LOW-FIELD REGION OF A p^+np^+ Si BARITT DIODE. ($N_d = 1 \times 10^{16} \text{ cm}^{-3}$ AND $J_o = 500 \text{ A/cm}^2$)

interpolation has been used to connect the concentrations at the midpoint of each lump. The results from this dc solution are used extensively in Chapter III in the study of the small-signal impedance and noise properties of the BARITT diode.

2.5 Dc Base Resistance in a Punch-Through Transistor

A simple estimate for the effective width of the transverse majority carrier current channel which exists under the emitter stripe in a planar punch-through transistor can be obtained by using the fact that the majority carrier longitudinal drift and diffusion current components must nearly cancel each other for a small total electron longitudinal current. For all levels of injection, an overestimate for the electric field distribution on the collector side of the injection point is

$$E \approx \frac{q(N_d + Kp_s)x}{\epsilon}$$

A suitable solution for the electron concentration, such that the electron drift and diffusion longitudinal current components exactly cancel for this assumed field distribution, is a Gaussian profile

$$n(x) \approx (N_d + Kp_s) \exp [-(x/a)^2] ,$$

where

$$a^2 = 2\epsilon V_T / q(N_d + Kp_s) .$$

Thus an upper bound for the resistance per unit length of the conducting majority carrier channel for $x \geq 0$ can now be expressed as

$$\rho_B = \left\{ h\sigma_0 \int_0^\infty \exp \left[-(x/a)^2 \right] dx \right\}^{-1}, \quad (2.30)$$

where σ_0 is the channel conductance at $x = 0$, $\sigma_0 = q\mu_n(N_d + Kp_s)$; μ_n is the low-field electron mobility; h is the length of the emitter stripe into the paper in Fig. 1.2; and the upper limit of the integration has been taken to be infinity (this should introduce negligible error as the actual base width is much larger than the Gaussian constant a). This integral can be evaluated in closed form and the result is defined as the effective channel or majority carrier base width

$$w_{\text{eff}} = \frac{a\sqrt{\pi}}{2}.$$

A plot of this effective channel width as a function of N_d for low-level injection is given in Fig. 2.9. The actual value of the base resistance for a given geometry can now be calculated as

$$R_B = \frac{1}{2} \cdot \frac{1}{2} \cdot \frac{\rho_B L_e}{3}, \quad (2.31)$$

where L_e is the emitter stripe width, one factor of one-half is due to the fact that base current only flows to the center of the emitter from each edge, the other factor of one-half is due to the presence of the two base current paths from the edges of the emitter, and the factor of one-third can be shown to arise from the fact that the transverse base current must be equal to zero at the center line of the emitter stripe.³⁰ Actual values of R_B will not be calculated for any particular structure, rather this calculation

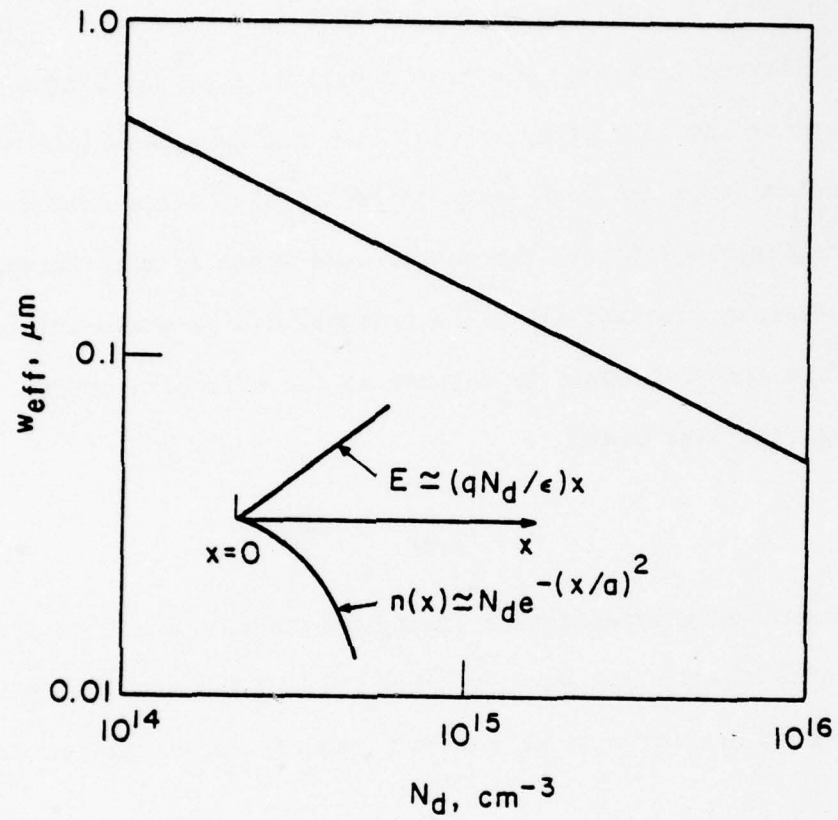


FIG. 2.9 EFFECTIVE BASE WIDTH FOR MAJORITY CARRIER
(ELECTRON) CURRENT (LOW-LEVEL INJECTION).

will serve as a basis for an estimate of the small-signal base resistance-collector capacitance time constant for a punch-through transistor.

CHAPTER III. SMALL-SIGNAL MODELS OF PUNCH-THROUGH DEVICES
AND SMALL-SIGNAL NOISE PROPERTIES OF BARITT DIODES

3.1 Introduction

The determination of the impedance/admittance or the noise properties of any semiconductor device is facilitated to a great extent by the assumption of small-signal conditions. Under this assumption dc quantities and equations are expanded in first-order Taylor series about their quiescent values and the resulting equations for the perturbation quantities are linearized. This procedure, in general, produces coupled nonlinear ordinary differential equations in phasor space for the small-signal variables of interest: particle concentrations, particle currents, terminal voltages, etc. In this chapter, however, further simplifying assumptions are introduced such that for each punch-through device studied, closed-form analytic solutions can be obtained without recourse to numerical techniques.

The chapter begins with a discussion, for background purposes, of the basis for all the small-signal models derived in this study, the common-base y-parameter model for the one-dimensional intrinsic diffusion transistor. This model is then modified to allow a smooth transition to the punch-through state, similar to the modification of the standard dc formulation for the diffusion transistor presented in Chapter II. The complete device equivalent circuit model, i.e., terminal voltage and current model, is then developed by inclusion of the transit-time effects of minority carrier flow in

the collector-base depletion layer and the junction space-charge capacitances. The small-signal characteristics of the punch-through transistor and the BARITT diode are next discussed in detail. A second-order small-signal model for the BARITT diode is presented in which the low-field portion of the drift-diffusion region immediately adjacent to the forward-biased injection region is accounted for, akin to the dc analysis of Chapter II. Finally, the small-signal noise properties of the BARITT diode are developed using the same method employed in the derivation of the small-signal diode equivalent circuit.

For reference, the small-signal equations that describe one-dimensional hole flow in semiconductors are given here:

1. The small-signal hole current density,

$$J_p = q p_0 \mu E + q v p - q D \frac{dp}{dx} , \quad (3.1)$$

where the dc drift velocity v , the small signal mobility μ , and the diffusion coefficient D are all functions of the dc field E_0 only; that is, $v = \mu_{dc} E_0$, $D = \mu_{dc} V_T$, $\mu = \mu_{dc} [1 - (v/v_s)]$, and $\mu_{dc} = v_s / (E_0 + E_s)$.

2. The total current density,

$$J_t = J_p + j \omega \epsilon E . \quad (3.2)$$

3. Gauss's law,

$$\frac{dE}{dx} = (q/\epsilon) p . \quad (3.3)$$

4. The hole continuity equation,

$$\frac{dJ_p}{dx} = - q \left(\frac{1}{\tau_p} + j \omega \right) p . \quad (3.4)$$

In these four equations and throughout the remainder of this work all symbols which represent currents, voltages, electric fields and particle concentrations will be understood to be in phasor notation unless they possess a zero subscript which will indicate unperturbed dc values.

3.2 Small-Signal Transistor Models

3.2.1 Common-Base y -Parameter Intrinsic Diffusion Transistor Model. To establish a common notation and a basis for the device models of this chapter, the theory of the one-dimensional common-base y -parameter model³¹ for the intrinsic diffusion transistor is outlined in this section.

The differential equation governing the distribution of the small-signal hole concentration in the field-free base region of the p^+np^+ transistor structure of Fig. 1.2 can be derived from Eqs. 3.1 and 3.4 in a manner similar to the derivation of the dc equation (Eq. 2.2) and can be expressed as

$$\left(\frac{d^2}{dx^2} - \frac{1}{L_p^*} \right) p = 0 , \quad (3.5)$$

where L_p^* is the complex diffusion length

$$L_p^* = \frac{L_p}{\sqrt{1 + j\omega\tau_p}} .$$

Completely analogous to the dc solution of the transistor the solutions to Eq. 3.5 can be used to express the small-signal hole current density at the emitter and collector edges of the base region as (c.f., dc Eqs. 2.3 and 2.4)

$$J_p(0) = \frac{qD_p}{L_p^*} \left[f_e \coth \frac{w_0}{L_p^*} - f_c \operatorname{csch} \frac{w_0}{L_p^*} \right] \quad (3.6)$$

and

$$J_p(w_0) = \frac{qD_p}{L_p^*} \left[f_e \operatorname{csch} \frac{w_0}{L_p^*} - f_c \coth \frac{w_0}{L_p^*} \right], \quad (3.7)$$

where the hole concentration boundary values f_e and f_c are the small-signal counterparts to the dc values F_e and F_c and can be expressed as first-order perturbations of these same dc values; that is,

$$f_e = \left. \frac{\partial F_e}{\partial V_{EB}} \right|_{V_{EBO}} v_{eb}' \quad (3.8)$$

and

$$f_c = \left. \frac{\partial F_c}{\partial V_{CB}} \right|_{V_{CBO}} v_{cb}', \quad (3.9)$$

where v_{eb} , and v_{cb} , are the small-signal phasor voltages across the emitter-base and the collector-base junctions, respectively.

If the Early effect³² is present, i.e., the position w of the collector edge of the base region is a function of the collector-base bias, then $w = w_0 + w_{ac}$ and*

$$\begin{aligned} f_c &= \left[\left. \frac{\partial F_c}{\partial V_{CB}} \right|_{V_{CBO}} - \left. \frac{\partial p_0}{\partial x} \right|_{w_0} \left. \frac{\partial w}{\partial V_{CB}} \right|_{V_{CBO}} \right] v_{cb}' \\ &= \left[\left. \frac{\partial F_c}{\partial V_{CB}} \right|_{V_{CBO}} \right]' v_{cb}' \end{aligned} \quad (3.10)$$

* Appendix A contains a detailed derivation of the Early effect correction, Eq. 3.10.

The total small-signal emitter current density must contain a term due to electrons (base region majority carriers) that are injected from the base into the emitter. This contribution can be derived from an expansion of dc Eq. 2.17 and in phasor space is given by

$$J_n(-w_e) = \frac{qD_n}{L_n^*} \frac{\partial F_n}{\partial V_{EB}} \bigg|_{V_{EBO}} v_{eb}', \quad (3.11)$$

where L_n^* is the complex diffusion length of electrons in the emitter region.

Thus for no recombination in the emitter-base junction space-charge region the y-parameter form for the emitter current density is

$$\begin{aligned} J_e &= J_n(-w_e) + J_p(0) \\ &= y_{11}v_{eb}' + y_{12}v_{cb}', \end{aligned}$$

where

$$y_{11} = \frac{qD_n}{L_n^*} \frac{\partial F_n}{\partial V_{EB}} \bigg|_{V_{EBO}} + \frac{qD_p}{L_p^*} \frac{\partial F_p}{\partial V_{EB}} \bigg|_{V_{EBO}} \coth \frac{w_o}{L_p^*} \quad (3.12)$$

and

$$y_{12} = - \frac{qD_p}{L_p^*} \frac{\partial F_p}{\partial V_{CB}} \bigg|_{V_{CBO}} \operatorname{csch} \frac{w_o}{L_p^*} \quad (3.13)$$

with it being understood that $(\partial F_c / \partial V_{CB})|_{V_{CBO}}$ is replaced by $((\partial F_c / \partial V_{CB})|_{V_{CBO}})'$ if the Early effect is present. At $w = w_o$ the y-parameter form of the collector current density is

$$J_c = -J_p(w_o) = y_{21}v_{eb}' + y_{22}v_{cb}'$$

where

$$y_{21} = - \frac{qD_p}{L_p^*} \frac{\partial F_e}{\partial V_{EB}} \bigg|_{V_{EBO}} \operatorname{csch} \frac{w_o}{L_p^*} \quad (3.14)$$

and

$$y_{22} = \frac{qD_p}{L_p^*} \frac{\partial F_c}{\partial V_{CB}} \bigg|_{V_{CBO}} \coth \frac{w_o}{L_p^*} \quad (3.15)$$

Again, $\left(\frac{\partial F_c}{\partial V_{CB}} \right) \bigg|_{V_{CBO}}$ would replace $\left(\frac{\partial F_c}{\partial V_{CB}} \right) \bigg|_{V_{CBO}}$ in the presence of the Early effect.

A "good" dc transistor is normally defined as one for which $w_o/L_p \ll 1$ and the "low-frequency" range of transistor operation is the frequency region $f \ll f_\alpha$ where $f_\alpha \equiv D_p/\pi w_o^2$. The small argument ($|w_o/L_p^*| \ll 1$) expansions for the hyperbolic functions which are valid for a "good" dc transistor in its "low-frequency" range are

$$\coth \frac{w_o}{L_p^*} \approx \frac{L_p^*}{w_o} \left[1 + \frac{1}{3} \left(\frac{w_o}{L_p^*} \right)^2 \right]$$

and

$$\operatorname{csch} \frac{w_o}{L_p^*} \approx \frac{L_p^*}{w_o} \left[1 + \frac{1}{6} \left(\frac{w_o}{L_p^*} \right)^2 \right]^{-1}$$

The y-parameters for this case can be approximated as

$$y_{11} = g_n + g_e + j\omega C_{es} \quad (3.16)$$

$$y_{12} = -g_c \left[1 + j\omega \frac{\tau_B}{3} \right]^{-1} \quad (3.17)$$

$$y_{21} = -g_e \left[1 + j\omega \frac{\tau_B}{3} \right]^{-1} \quad (3.18)$$

and

$$y_{22} = g_c + j\omega C_{cs} \quad (3.19)$$

where we have defined

$$g_n \equiv \frac{qD_n}{L_n} \left. \frac{\partial F_n}{\partial V_{EB}} \right|_{V_{EBO}}, \quad (3.20)$$

$$g_e \equiv \frac{qD_p}{w_o} \left. \frac{\partial F_e}{\partial V_{EB}} \right|_{V_{EBO}}, \quad (3.21)$$

$$\tau_B \equiv \frac{1}{\omega_a} = \frac{w_o^2}{2D_p}, \quad (3.22)$$

$$C_{es} \equiv g_e \frac{2\tau_B}{3}, \quad (3.23)$$

$$g_c \equiv \frac{qD_p}{w_o} \left. \frac{\partial F_c}{\partial V_{CB}} \right|_{V_{CBO}} \quad (3.24)$$

and

$$C_{cs} \equiv g_c \frac{\tau_B}{3}. \quad (3.25)$$

In the y-parameter approximations, Eqs. 3.16 through 3.19, it has also been assumed that the emitter is very heavily doped such that $L_n^* = L_n$ and that terms of the order $(w_o/L_p)^2$ can be neglected in comparison with unity.

With the definitions of the circuit parameters, Eqs. 3.20 through 3.25, the y-parameter small-signal model can be configured as shown in Fig. 3.1. The base transport factor α_T in Fig. 3.1 is defined as the ratio of y_{21} to the minority carrier portion of y_{11} ; that is,

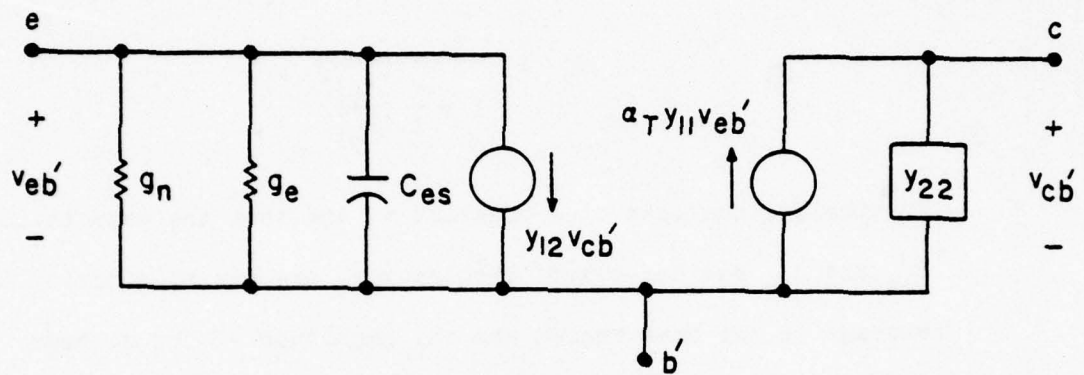


FIG. 3.1 SMALL-SIGNAL COMMON-BASE EQUIVALENT CIRCUIT FOR AN INTRINSIC DIFFUSION TRANSISTOR. ($y_{11} \approx g_n + g_e + j\omega C_{es}$, $y_{12} \approx -g_c$ AND $y_{22} \approx g_c + j\omega C_{cs}$)

$$\alpha_F \equiv \frac{y_{21}}{y_{11p}} \approx \frac{1}{\left[1 + \frac{1}{3} \left(\frac{w_0}{L_p}\right)^2 + j\omega \frac{2\tau_B}{3}\right] \left[1 + \frac{1}{6} \left(\frac{w_0}{L_p}\right)^2 + j\omega \frac{\tau_B}{3}\right]}$$

$$\approx \frac{\alpha_0}{1 + jf/f_\alpha} ,$$

where

$$\alpha_0 \equiv \frac{1}{1 + \frac{1}{2} \left(\frac{w_0}{L_p}\right)^2} .$$

Physically, the base time constant τ_B and thus the capacitances C_{es} and C_{cs} and the cutoff frequency f_α are due to minority carrier storage in the base region and the magnitude of the dc base transport factor α_0 is less than unity because of carrier recombination within the base region.

3.2.2 Narrow Base-Width Considerations. As the limiting value of zero base width is approached the elements of the small-signal model shown in Fig. 3.1 suffer the same fate as the dc emitter and collector currents of Eqs. 2.10 and 2.9; they grow without bound. Again this is not a physical result and again the fault lies in the assumption of a pure voltage dependency for the collector edge base region minority carrier boundary condition. If a voltage and current dependent boundary condition is assumed for the hole concentration at $x = w_0$, i.e., Eq. 2.11

$$F_c = F_c[V_{CBO}, J_p(w_0)] ,$$

then*

$$f_c \approx \left. \frac{\partial F_c}{\partial V_{CB}} \right|_{V_{CBO}} + \left. \frac{\partial F_c}{\partial J_p(w)} \right|_{J_{po}(w_o)} J_p(w_o) \quad (3.26)$$

Substituting this boundary value into Eq. 3.7 and solving for $J_p(w_o)$ yields

$$J_p(w_o) = \frac{\frac{qD_p}{L_p^*} \left[\left. \frac{\partial F_e}{\partial V_{EB}} \right|_{V_{EBO}} \operatorname{csch} \frac{w_o}{L_p^*} - \left. \frac{\partial F_c}{\partial V_{CB}} \right|_{V_{CBO}} \coth \frac{w_o}{L_p^*} \right]}{1 + \frac{qD_p}{L_p^*} \left. \frac{\partial F_c}{\partial J_p(w)} \right|_{J_{po}(w_o)} \coth \frac{w_o}{L_p^*}} \quad (3.27)$$

Similarly, when the new value for f_c is substituted into the hole-emitter current density expression Eq. 3.6, we obtain, in conjunction with Eq. 3.27,

$$J_p(0) = \frac{\frac{qD_p}{L_p^*} \left. \frac{\partial F_e}{\partial V_{EB}} \right|_{V_{EBO}} \left[1 + \frac{qD_p}{L_p^*} \left. \frac{\partial F_c}{\partial J_p(w)} \right|_{J_{po}(w_o)} \tanh \frac{w_o}{L_p^*} \right]}{\text{denom} - \frac{\frac{qD_p}{L_p^*} \left. \frac{\partial F_c}{\partial V_{CB}} \right|_{V_{CBO}} \operatorname{csch} \frac{w_o}{L_p^*}}{\text{denom}}} \quad (3.28)$$

where denom is the denominator of Eq. 3.27. The new values of the y-parameters are immediately obvious from Eqs. 3.27 and 3.28; namely,

$$y_{11} \equiv \frac{qD_n}{L_n^*} \left. \frac{\partial F_n}{\partial V_{EB}} \right|_{V_{EBO}} + \frac{y_{11p}^o \left[1 + \frac{qD_p}{L_p^*} \left. \frac{\partial F_c}{\partial J_p(w)} \right|_{J_{po}(w_o)} \tanh \frac{w_o}{L_p^*} \right]}{\text{denom}} \quad (3.29)$$

* Appendix A also contains a discussion of the evaluation of $\partial F_c / \partial J_p(w)$ when a current-dependent Early effect is present.

$$y_{12} \cong \frac{y_{12}^0}{\text{denom}} , \quad (3.30)$$

$$y_{21} \cong \frac{y_{21}^0}{\text{denom}} \quad (3.31)$$

and

$$y_{22} \cong \frac{y_{22}^0}{\text{denom}} , \quad (3.32)$$

where y_{ij}^0 signifies a previously defined value for the y-parameter y_{ij} , Eqs. 3.16 through 3.19, and y_{11p}^0 signifies the hole current portion of Eq. 3.16.

The simplest case which allows the analytical evaluation of Eqs. 3.29 through 3.32 and the only one which will be discussed in detail in this study is the coincidence of standard bias, $\exp(V_{CBO}/V_T) \ll 1$, and a level of injection for which $p_s \gg p_n$ but moderate enough such that the current dependent Early effect can be neglected. For this case, reference Eq. 2.12,

$$\left. \frac{\partial F_c}{\partial J_p(w)} \right|_{J_{po}(w_o)} \cong \frac{K}{qv_s} .$$

Thus for a "good" dc transistor in its "low-frequency" region

$$\text{denom} \cong 1 + \frac{D_p K}{v_s w_o} \left[1 + \frac{1}{3} \left(\frac{w_o}{L_p^*} \right)^2 \right] \quad (3.33)$$

which in the limit of very small base widths is the same term present in the denominator of the expression for the dc collector current density Eq. 2.13.

The only circuit elements in Fig. 3.1 which must be redefined such that the equivalent circuit is valid for all values of base width are the junction conductances g_e and g_c ; that is,

$$g_e \equiv \frac{g_e^0}{\text{denom}} \quad (3.34)$$

and

$$g_c \equiv \frac{g_c^0}{\text{denom}} \quad (3.35)$$

Now as $w_0 \rightarrow 0$ the elements and therefore the circuit currents do not grow in magnitude without bound and therefore the punch-through state, similar to the dc analysis, can be thought of as simply the limiting state, $w_0 = 0$.

3.2.3 The Complete Small-Signal Model. The small-signal circuit model of Fig. 3.1 is not a complete equivalent circuit model since it represents only the flow of carrier currents within the one-dimensional intrinsic or base-emitter region of the transistor. The terminal emitter current can be fully accounted for by adding a shunt emitter-base junction depletion-layer capacitance C_e across y_{11} (transit-time effects of carriers crossing the relatively narrow emitter-base junction depletion layer are ignored). The base terminal, the two-dimensional circuit contribution, can be represented to first order by adding a base lead series resistance r_b from the base terminal to the one-dimensional base position b' between the emitter and the collector. Finally, the total collector terminal current can be computed as follows: From Eq. 3.2 the total or terminal collector current density which is independent of position can be defined as

$$J_c = -J_p(x) - j\omega\epsilon E, \quad w_0 \leq x \leq w_c,$$

where the minus signs are due to the fact that the collector current is defined as positive into the collector. We integrate this equation over the collector-base depletion layer, $x = w_0$ to $x = w_0 + w_c$, and obtain

$$J_c = -\frac{1}{w_c} \int_{w_0}^{w_0+w_c} J_p dx + j\omega C_c v_{cb'} , \quad (3.36)$$

where C_c is the collector-base depletion-layer capacitance ϵ/w_c and

$$v_{cb'} \equiv - \int_{w_0}^{w_0+w_c} E dx .$$

Since the minority carrier current density at the collector edge of the base region $J_p(w_0)$ is also the initial or the injected particle current density for the collector-base depletion layer, the transit-time effects of holes crossing the relatively wide collector-base space-charge layer are all contained in the integral in Eq. 3.36 and can be expressed in a single term or transit-time factor Γ . That is,

$$J_c = -J_p(w_0)\Gamma + j\omega C_c v_{cb'} ,$$

where

$$\Gamma \equiv \frac{1}{w_c} \int_{w_0}^{w_0+w_c} \frac{J_p}{J_p(w_0)} dx .$$

The complete small-signal equivalent circuit can now be depicted as shown in Fig. 3.2.

One common approximation³³ for the transit-time factor Γ is derived by neglecting diffusion entirely and assuming that all the carriers in the depletion region drift at their saturated velocity v_s .

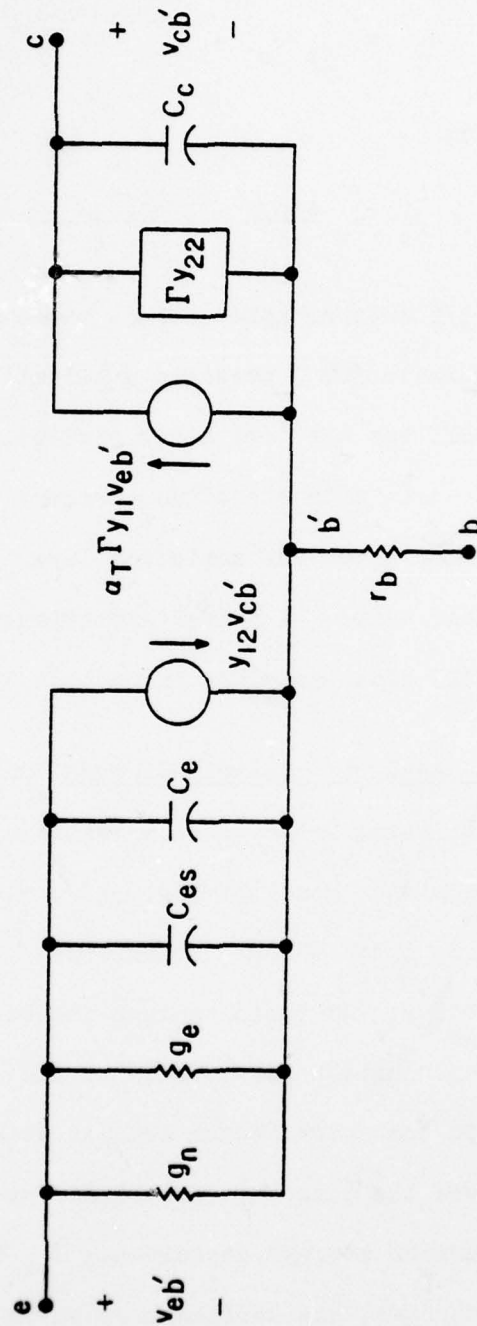


FIG. 3.2 COMPLETE COMMON-BASE EQUIVALENT CIRCUIT FOR DIFFUSION TRANSISTOR.

$$(y_{11} \approx g_n + g_e + j\omega C_{es}, y_{12} \approx -g_c, y_{22} \approx g_c + j\omega C_{cs})$$

The current density J_p can then be expressed as the space-charge current wave

$$J_p = J_p(w_0) e^{-j(\omega/v_s)(x-w_0)}$$

and thus Γ becomes

$$\Gamma_s = \frac{\sin \theta}{\theta} + j \frac{\cos \theta - 1}{\theta}, \quad (3.37)$$

the saturated drift approximation for Γ , where θ is the transit angle $\omega w_0/v_s$. This estimate for Γ predicts qualitative transit-time effects fairly well but its derivation obviously underestimates the actual carrier transit time since the carriers that are injected from the base region enter the depletion layer at velocities well below the saturated value. A better approximation of the Γ for a two-terminal BARITT diode is given in Section 3.4.

3.3 Small-Signal Analysis of Punch-Through Transistors

When the limiting value of zero base width $w_0 \rightarrow 0$ is approached, the diffusion transistor model of Fig. 3.2 evolves into the small-signal model of the punch-through transistor. Several circuit simplifications occur: At punch through the base region volume in which carrier recombination takes place shrinks to zero and therefore the base region dc transport factor becomes unity ($\alpha_0 = 1$). The same volume was the minority carrier storage region thus $f_\alpha \rightarrow \infty$ and the carrier storage capacitance C_{es} becomes negligible. Once into punch through, the defined base width is zero for all levels of punch-through bias, and the magnitude of the voltage dependent Early effect term $\partial w/\partial V_{CB}$ is zero by definition.

Thus the feedback and output admittance terms also disappear from the model. One last simplification can be realized if the relationship between the emitter electron and hole conductance terms g_n and g_e is explored. From Eqs. 3.20, 3.21, 3.33 and 3.34, we have in the punch-through state

$$\frac{g_n}{g_e} = \frac{J_{ne}}{J_{np}} = \frac{\frac{D_n}{L_n} \left. \frac{\partial F_n}{\partial V_{EB}} \right|_{V_{EBO}}}{\frac{v_s}{K} \left. \frac{\partial F_e}{\partial V_{EB}} \right|_{V_{EBO}}}$$

But from Eqs. 2.19 and 2.20 for all but extremely high levels of injection

$$\left. \frac{\partial F_n}{\partial V_{EB}} \right|_{V_{EBO}} = \frac{F_{no}}{V_T} \quad \text{and} \quad \left. \frac{\partial F_e}{\partial V_{EB}} \right|_{V_{EBO}} = \frac{F_{eo}}{V_T},$$

and the conductance ratio reduces to

$$\frac{g_n}{g_e} = \frac{J_{neo}}{J_{peo}} = \delta, \quad (3.38)$$

the ratio of dc electron and hole emitter currents. This ratio, defined as δ , can also be expressed in terms of the more common dc emitter efficiency, $\gamma_o = J_{peo}/J_{eo}$, as $\delta = (1 - \gamma_o)/\gamma_o$. The complete small-signal equivalent circuit for the punch-through transistor, with these simplifications, is shown in Fig. 3.3.

One important high-frequency parameter for any transistor structure is the base-resistance collector-base capacitance time constant³⁴ $r_b C_c$. A good estimate for the small-signal value of the base resistance r_b for no emitter crowding is to assume it to be

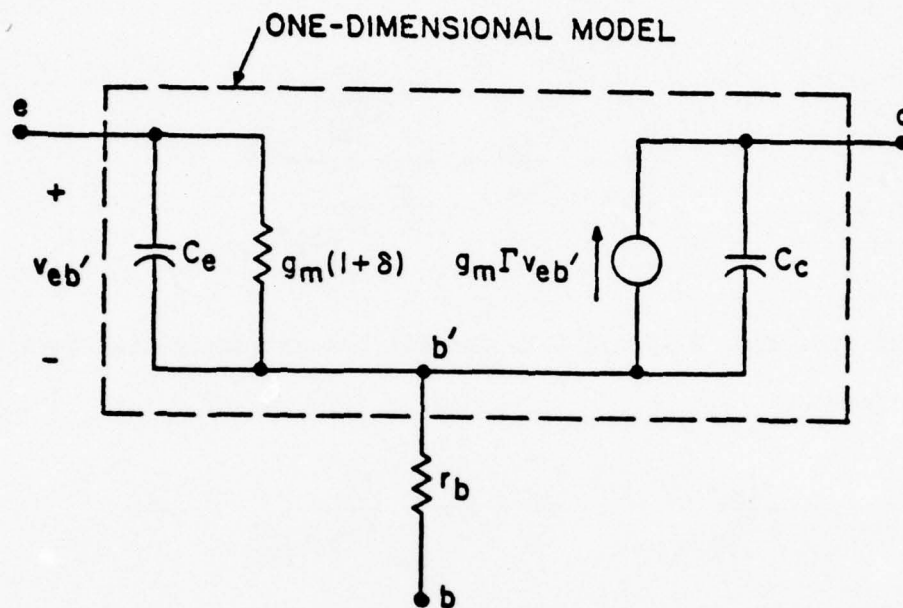


FIG. 3.3 SMALL-SIGNAL MODEL OF PUNCH-THROUGH TRANSISTOR.

equal to its dc value³⁵ R_B , Eq. 2.30. The low-level injection $r_b C_c$ time constant for the configuration of Fig. 1.2 can then be expressed as

$$r_b C_c = \frac{L_e^2}{\sqrt{\epsilon/(2qV_T \pi N_d)} 6u_n w_c} \quad (3.39)$$

It is obvious in Eq. 3.39 that in order to minimize $r_b C_c$ both N_d and w_c should be maximized. The maximum value of the product of N_d and w_c is limited by the onset of avalanche multiplication at the collector end of the collector-base space-charge region. That is, it must be true that

$$qN_d w_c / \epsilon \leq E_m ,$$

where E_m is the avalanche critical field intensity (approximately equal to 3×10^5 V/cm for holes in Si). A punch-through transistor constructed such that the critical field is nearly reached at its dc operating point will be termed a dc maximum power structure and the $r_b C_c$ time constants for three of these devices are plotted in Fig. 3.4 as a function of emitter stripe width. As can be seen, $r_b C_c$ values of less than a picosecond can easily be obtained for a wide range of base dopings and reasonable emitter widths.

The normalized real parts of the common-emitter output impedances for several dc maximum power structures are shown in Fig. 3.5 for $\Gamma = \Gamma_g$ and one particular base driving impedance (a resistive match at low frequencies). At very low frequencies the principal contribution to the output resistances comes from the space-charge resistances of the collector-base depletion layers.³⁶ At higher frequencies the depletion-layer transit-time effects are

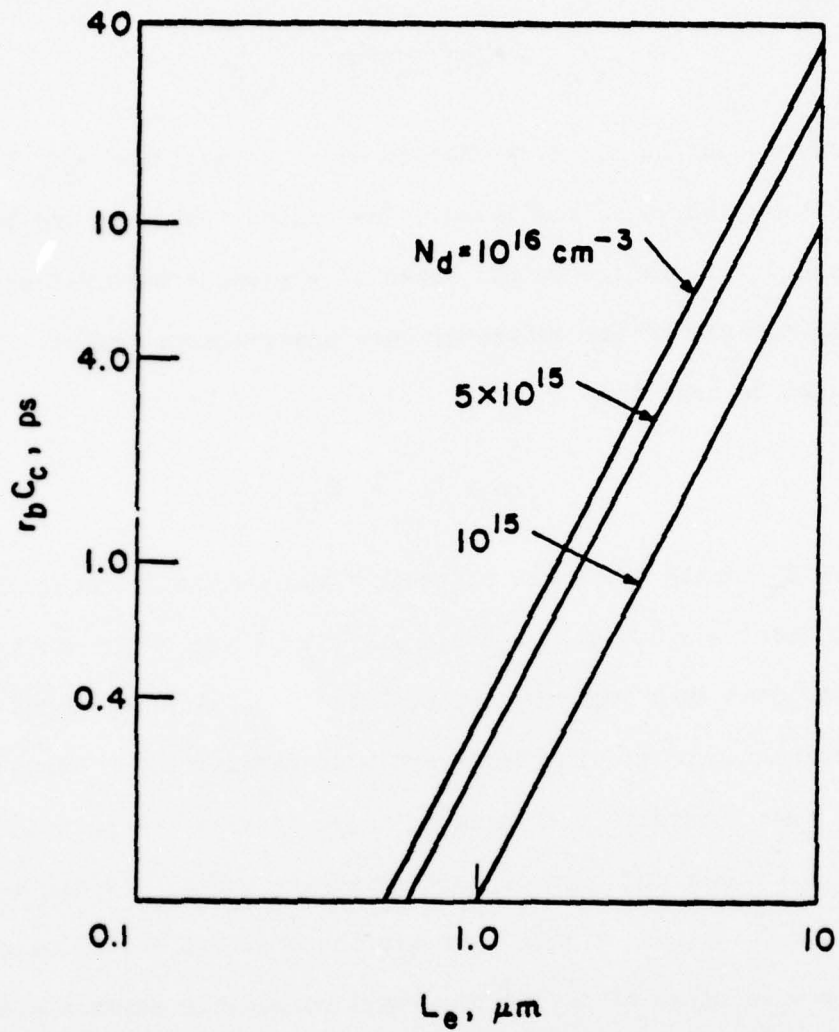


FIG. 3.4 BASE RESISTANCE-COLLECTOR CAPACITANCE TIME
CONSTANT FOR DC MAXIMUM POWER STRUCTURES.

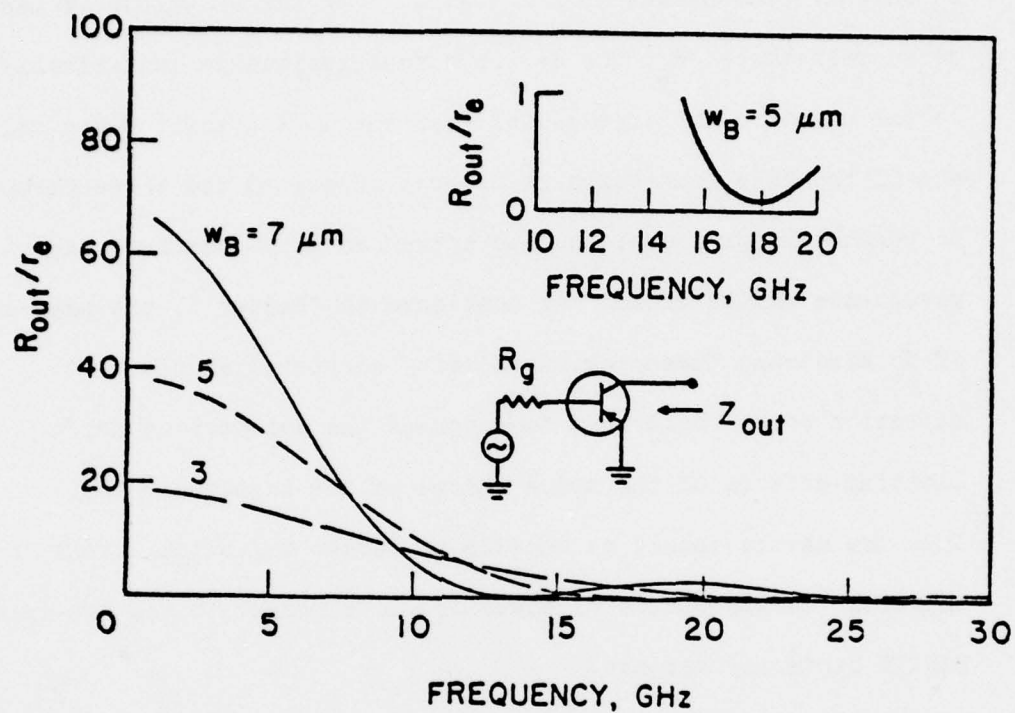


FIG. 3.5 COMMON EMITTER OUTPUT RESISTANCE FOR DC MAXIMUM POWER STRUCTURES. [$R_g = r_b + r_e$, $r_e = (1/g_e)$, $J_o = 100 \text{ A/cm}^2$, $C_e/C_c = 20$ AND $\delta = 0.01$]

clearly evident with the first dip in R_{out} occurring at a transit angle θ of approximately $3\pi/2$. An enlarged plot near the frequency of this transit angle for the 5- μ m device (w_c = base width) is shown in the insert to the figure. For larger values of base drive resistances R_g , the device output resistance can actually become negative for frequencies near the $3\pi/2$ transit angle value, and if the base connection is RF open circuited the three-terminal dc punch-through transistor can appear as a two-terminal negative resistance BARITT diode. As mentioned in Chapter I, the presence of dc electrons (base region majority carriers) at the injection point would tend to suppress the deleterious self-limiting effects of the space charge of the injected holes. Thus the device should be capable of larger injection levels and therefore larger output RF power levels compared to the two-terminal BARITT diode counterpart.

The unilateral gain U of an amplifying device is the maximum available gain of the structure after all internal feedback has been neutralized. It is the most indicative parameter of potential usefulness for an active device as it is independent of device orientation (common base, etc.). The unilateral gain as a function of frequency for the model of Fig. 3.3 can be expressed as³⁷

$$U = \frac{|\alpha|^2}{8\pi f r_b C_c \left(-\text{Im}(\alpha) + \frac{2\pi r_e C_c}{1 + 4\pi^2 f^2 (r_e C_e)^2} \right)},$$

where $r_e = [g_e(1 + \delta)]^{-1}$ and α is the common-base current gain

$$\alpha = \frac{g_e \Gamma_s}{g_e (1 + \delta) + j\omega C_e} .$$

Calculated unilateral gains for two dc maximum power punch-through transistors are shown in Fig. 3.6. Both structures show usable gain up to and past 10 GHz. The calculation of U was halted when a frequency was reached such that the imaginary part of α changed sign due to transit-time effects. At frequencies immediately above such a value the possibility of chip negative resistance exists and U no longer has any meaning. This does not indicate that the devices are unusable at these frequencies, only that stability may become the dominant circuit design concern. If the device is intended to function as an oscillator the presence of chip negative resistance may well add to its capabilities.

The experimental results presented in Chapter I for the low-frequency punch-through device proved that not only can transistors function in the punch-through mode but that they also show improved performance in this region of operation provided they are in the correct impedance environment. The theoretical and experimental results for the punch-through transistor that have been presented in this study must be considered to be preliminary and are far from exhaustive, but they do indicate the feasibility of the device.

3.4 Small-Signal BARITT Diode Analysis

3.4.1 Theory. Since the BARITT is basically an open-base punch-through transistor a first-order small-signal model for the device can be obtained directly from the punch-through transistor model of the previous section by simply eliminating the base region

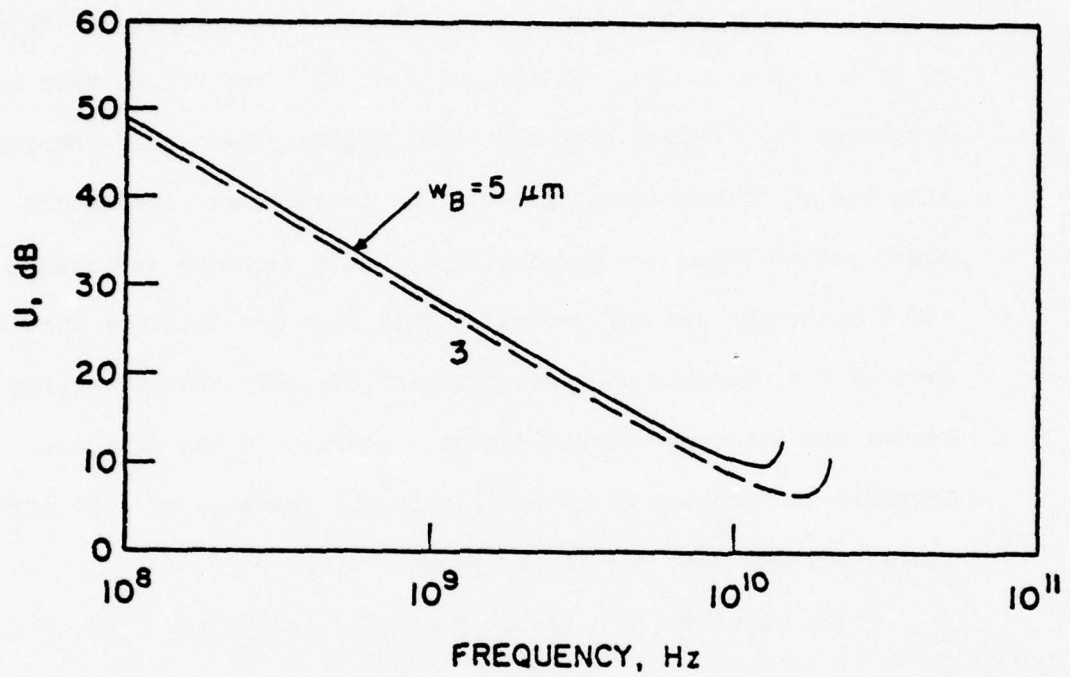


FIG. 3.6 UNILATERAL GAIN FOR DC MAXIMUM POWER STRUCTURES.

($L_e = 1 \mu m$, $J_o = 100 \text{ A/cm}^2$, $\delta = 0.01$ AND $C_e/C_c = 20$)

majority carrier circuit elements; namely r_o and δg_e . The impedance of the diode can then be expressed as the series combination of a forward-biased junction Z_F and the injection-current-dependent impedance of the back-biased junction Z_B . That is,

$$Z_d = Z_F + Z_B ,$$

where

$$Z_F = \frac{1}{g_e + j\omega C_e} \quad (3.40)$$

and

$$Z_B = \frac{1 - \Gamma_s M}{j\omega C_c} . \quad (3.41)$$

The complex quantity M is the ratio of the injected particle current to the total diode current, or in terms of the circuit elements of the forward-biased region

$$M = \frac{g_e}{g_e + j\omega C_e} . \quad (3.42)$$

This approach, modeling the diode as a forward-biased region in series with a reverse-biased saturated drift region, was first put forth by Weller³⁸ in his study of the MSM structure.

The method is similar to the calculation of the small-signal impedance of a Read-type IMPATT diode published by Gilden and Hines,³⁹ differing only in the physics of the injection mechanism.

The second-order small-signal BARITT diode model formulated in this study is an extension of Weller's work, retaining the simple description of the forward-biased region but expanding the treatment of the reverse-biased drift-diffusion region by assuming the region can be described as a perturbation of the single-carrier multisection dc model presented in Chapter II. Recall that in

the dc solution the low-field portion of the drift-diffusion region is divided into N one-dimensional lumps, Fig. 2.3. The dc minority carrier concentration within each lump is assumed to be constant over the extent of the lump, i.e., $p_{oi} = \text{constant}$, independent of x. The only additional assumptions, over those utilized in the dc study, needed to reduce the small-signal equations, Eqs. 3.1 through 3.4, to an analytically solvable set are the working hypotheses of constant values for D, v and μ within each lump. Since the actual values of the diffusion coefficient D, the dc drift velocity v, and the small-signal mobility μ all depend on the dc electric field E_0 which is a linear function of position within each lump, the realization of constant lump values for D, v and μ requires that these quantities be re-defined. After much experimentation the lump values for D, v and μ that have been chosen for use in this study are the spatial average values of each lump. That is,

$$v_i \equiv \langle v \rangle_i = \frac{1}{\Delta_i} \int_0^{\Delta_i} v \, dx_i$$

and so on. Simple integration yields

$$u_i = \frac{v_s}{E_i + E_s} \left[1 - \frac{E_{i-1}}{E_i - E_{i-1}} \left(\frac{E_i + E_s}{E_{i-1} + E_s} - 1 \right) \right],$$

$$v_i = v_s \left[1 - \frac{E_s}{E_i + E_{i-1}} \ln \left(\frac{E_i + E_s}{E_{i-1} + E_s} \right) \right]$$

and

$$D_i = \frac{V_T v_s}{E_i - E_{i-1}} \ln \left(\frac{E_i + E_s}{E_{i-1} + E_s} \right),$$

where

$$E_i = E_0(x = x_i) , \quad x_i = i\Delta , \quad i \leq N .$$

The resultant error introduced by the use of average values for the diffusion coefficient, the dc drift velocity, and the small-signal mobility, as with the error resultant from the previous dc analysis assumption of a constant lump minority carrier concentration, is expected to diminish as the number N of low-field lumped regions used in the model is increased.

The small-signal equations,* Eqs. 3.1, 3.3 and 3.4 can now be combined to form a linear, constant coefficient, homogeneous, ordinary differential equation for the minority carrier concentration p_i within each lump:

$$\left(D_i \frac{d^2}{dx^2} - v_i \frac{d}{dx} - \frac{1}{\epsilon} (\sigma_i + j\omega\epsilon) \right) p_i = 0 , \quad (3.43)$$

where $\sigma_i = qp_{0i}\mu_i$ is the minority carrier equivalent conductivity of each lump i , v_i is the constant drift velocity $\mu_i \langle E_0 \rangle_i$, and D_i is the constant diffusion coefficient μ_i/V_T . The secular equation for $\exp(\gamma x)$ solutions of Eq. 3.43 has roots

$$\gamma_i = \frac{1}{2D_i} [v_i \mp \sqrt{v_i^2 + 4D_i(\sigma_i + j\omega\epsilon)/\epsilon}] \quad (3.44)$$

which implies a forward and a reverse space-charge wave within each lump. Since the values of the parameters under the radical are all positive quantities the space-charge wave associated with the plus sign in Eq. 3.44 travels in the negative x -direction. The concept of

* Recombination lifetime τ_p for a single-carrier model is infinite by definition.

holes in effect diffusing back against a positive directed drift flow is physically unappealing except in a very small region near the injection point $x = 0$. We therefore neglect this portion of the solution in each lump; that is, all injected holes are assumed to be collected and

$$p_i(z) = p_i^0 e^{\gamma_i z},$$

where p_i^0 is the injected small-signal hole density for the i th lump, $\text{Im}(\gamma_i)$ is always a negative quantity and z is the local spatial variable. Substituting this solution back into the small-signal equations and solving for the particle current density, we obtain after some algebra

$$J_{pi}(z) = J_{pi}^0 e^{\gamma_i z} + \frac{J_t \sigma_i}{\sigma_i + j\omega\epsilon} \left(1 - e^{\gamma_i z} \right), \quad (3.45)$$

where again the 0 superscript indicates the injected or initial value. An equivalent circuit for each lump of the low-field region of the diode can be developed from Eq. 3.45 in a manner similar to the derivation of the collector-base depletion-layer model given in Section 3.2.3: The expression for the total current, Eq. 3.2, is averaged over the extent of each lump; that is,

$$J_t = J_{pi}^0 \frac{\frac{\Gamma_i}{\sigma_i(1 - \Gamma_i)}}{1 - \frac{\Gamma_i}{\sigma_i + j\omega\epsilon}} + \frac{j\omega C_i}{1 - \frac{\Gamma_i}{\sigma_i + j\omega\epsilon}} v_i,$$

$$J_t = J_{pi}^0 \Gamma_{mi} + Y_i v_i, \quad (3.46)$$

AD-A063 558

MICHIGAN UNIV ANN ARBOR ELECTRON PHYSICS LAB

F/G 9/5

FREQUENCY CONVERSION IN PUNCH-THROUGH SEMICONDUCTOR DEVICES.(U)

AUG 78 P J MCCLEER

DAA629-76-6-0232

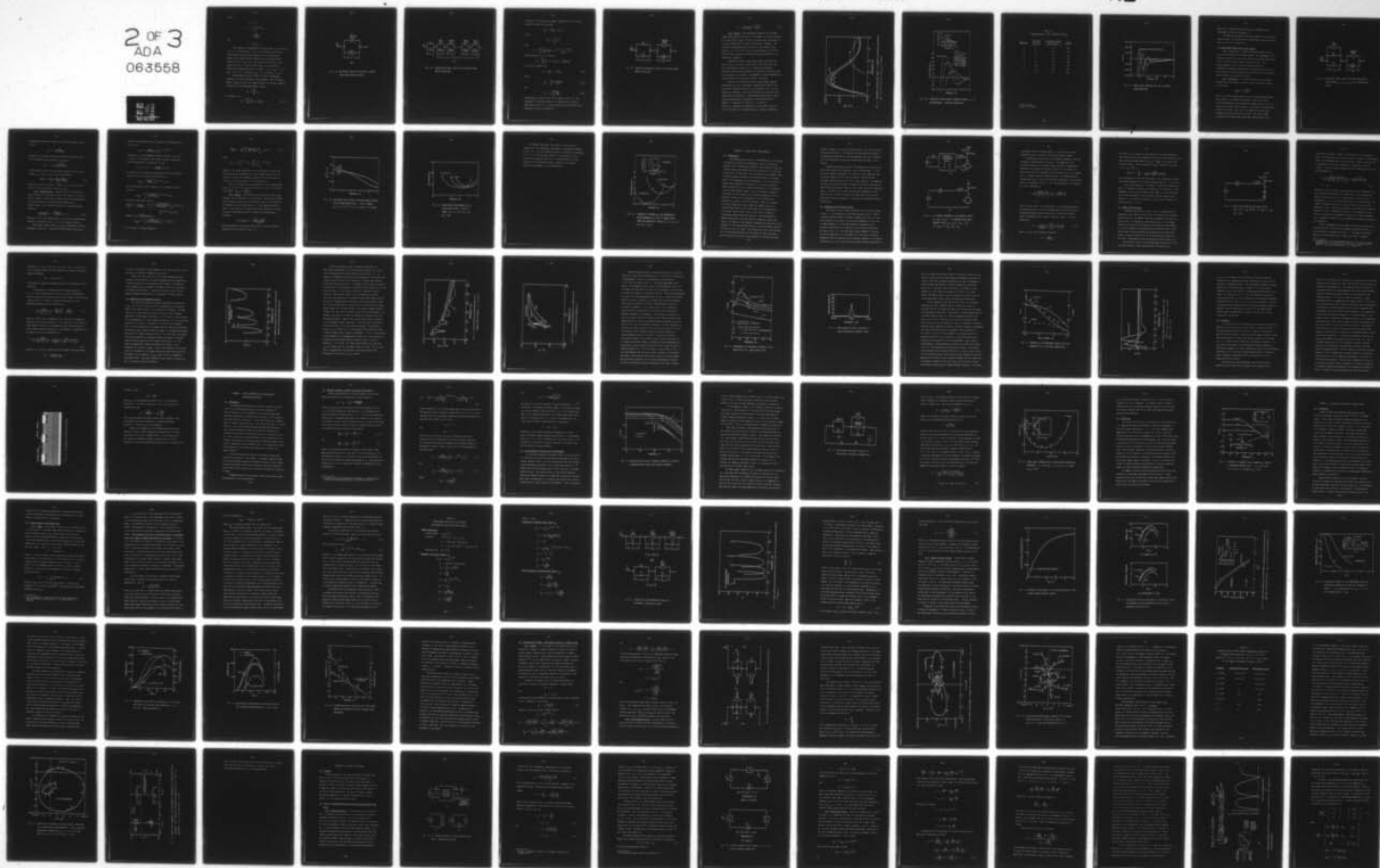
UNCLASSIFIED

TR-143

AR0-13853.2-EL

NL

2 OF 3
ADA
063558



where

$$C_i \equiv \epsilon/\Delta ,$$

$$\begin{aligned} \Gamma_i &\equiv \frac{1}{\Delta} \int_0^{\Delta} e^{\gamma_i z} dz \\ &= \frac{e^{\gamma_i \Delta} - 1}{\gamma_i \Delta} \end{aligned}$$

and

$$v_i \equiv \int_0^{\Delta} E_i dz .$$

This equation is represented by the equivalent circuit shown in Fig. 3.7a. The equivalent circuit for the entire diode can then be constructed as the series connection of the forward-biased region, the N lumped low-field regions, and the saturated drift region as shown in Fig. 3.7b. The saturated drift region can be treated as the $N + 1$ lump low-field region if the following modifications/simplifications are utilized: $v_{N+1} = (\langle v \rangle_{N+1} + v_s)/2$, $D_{N+1} = D(E_0 = E_s) = v_s V_T / (2E_s)$, $\Delta_{N+1} = w_c - w_s$ and $\sigma_{N+1} = \sigma_s \approx 0$.

The equivalent circuit of Fig. 3.7b can be considerably simplified by use of some rather tedious algebra: The total small-signal voltage v_B across the reverse-biased drift-diffusion region is the sum of all the lump small-signal voltages,

$$v_B = \sum_{i=1}^{N+1} v_i ,$$

but from Eq. 3.46

$$v_B = \sum_{i=1}^{N+1} \frac{1}{Y_i} (J_t - J_{pi}^0 \Gamma_{mi}) . \quad (3.47)$$

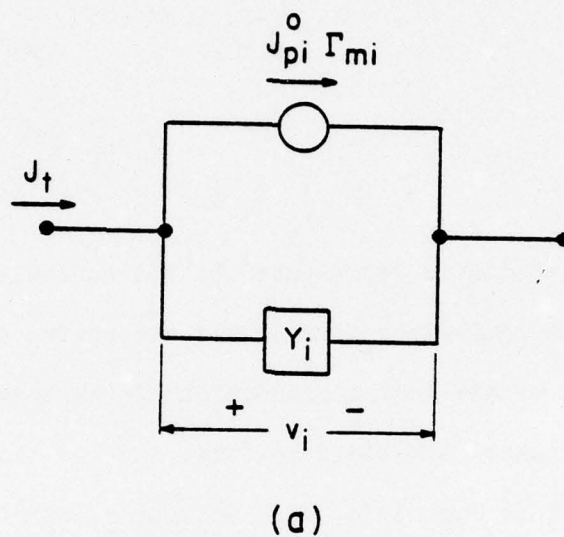


FIG. 3.7a EQUIVALENT CIRCUIT FOR i TH LUMP IN BARITT
DIODE DRIFT-DIFFUSION REGION.

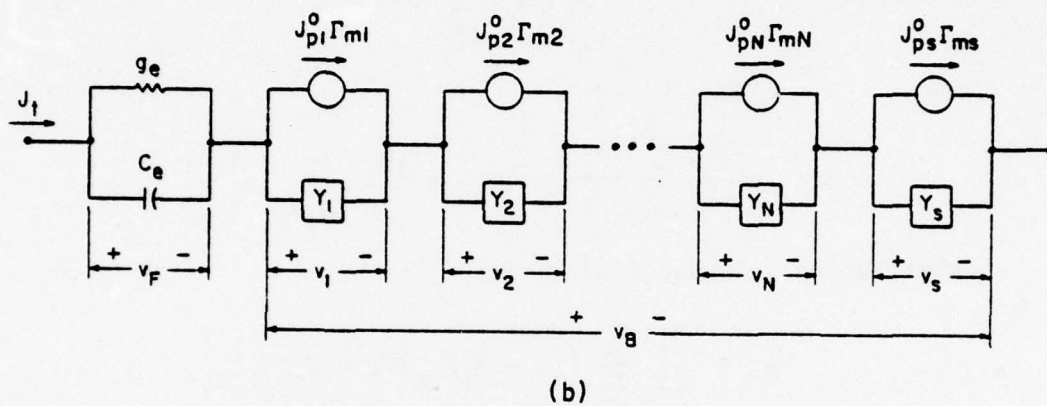


FIG. 3.7b COMPLETE EQUIVALENT CIRCUIT FOR THE SECOND-ORDER BARITT DIODE MODEL.

Using Eq. 3.45 we can form a general expression for the injected particle current into each lump:

$$J_{pi}^0 = J_{pi}^0 M_i + J_t N_i ,$$

where

$$M_i = \prod_{j=1}^{i-1} e^{\gamma_j \Delta}$$

and

$$N_i = \sum_{j=1}^{i-1} \left[\frac{\sigma_j}{\sigma_j + j\omega\epsilon} (1 - e^{\gamma_j \Delta}) \prod_{k=j+1}^{i-1} e^{\gamma_k \Delta} \right] .$$

Substituting into Eq. 3.47 yields

$$v_B = \sum_{i=1}^{N+1} \frac{1}{Y_i} [(1 - N_i \Gamma_{mi}) J_t - J_{pi}^0 M_i \Gamma_{mi}]$$

which can be expressed as

$$v_B = \frac{1}{Y_B} (J_t - J_{pi}^0 \Gamma_B) , \quad (3.48)$$

where

$$\frac{1}{Y_B} = \sum_{i=1}^{N+1} \frac{1 - N_i \Gamma_{mi}}{Y_i} \quad (3.49)$$

and

$$\Gamma_B = Y_B \sum_{i=1}^{N+1} \frac{M_i \Gamma_i}{j\omega C_i} . \quad (3.50)$$

The equivalent circuit for Eq. 3.48 is shown in Fig. 3.8. One advantage of this reduced form is its similarity to the first-order model of Eq. 3.41. By direct analogy the second-order diode impedance can thus be expressed as

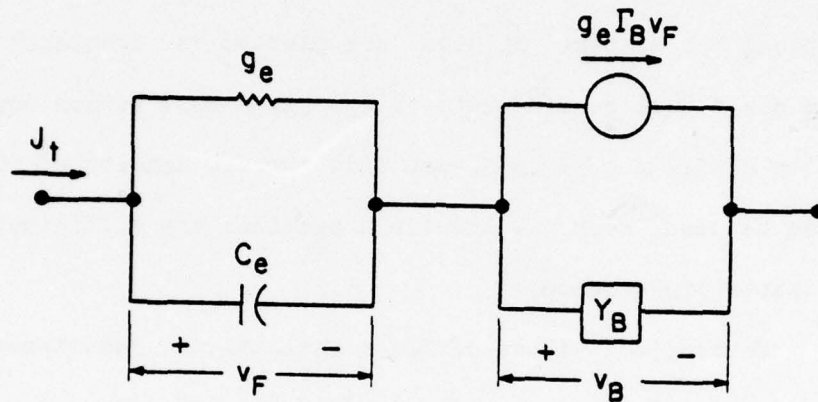


FIG. 3.8 SIMPLIFIED EQUIVALENT CIRCUIT FOR THE SECOND-ORDER BARITT DIODE MODEL.

$$Z_d = \frac{1}{g_e + j\omega C_e} + \frac{1 - M\Gamma_B}{Y_B} \quad (3.51)$$

3.4.2 Results. The convergence properties for the small-signal diode model as a function of the number of low-field sections N is demonstrated in Fig. 3.9 where the small-signal resistances of a typical X-band p^+np^+ Si diode are plotted vs. frequency. The diode has a base region width of $6.0 \mu m$, a base region doping density of $3.3 \times 10^{15} cm^{-3}$, and a dc current density of $50 A/cm^2$. As can be seen, even two low-field sections are sufficient for a reasonable convergence.

Theoretical values of diode small-signal resistances are given in Fig. 3.10 for the three p^+np^+ Si diode structures that were experimentally characterized by Snapp and Weissglas.¹⁰ The diode descriptions and the measured conductance values are given in the inserts to the figure. The agreement is quite acceptable and lends confidence to the overall accuracy of the model.

Finally, the theoretical values of small-signal negative resistances for four of the eight dc maximum power p^+np^+ Si diode structures, described in Table 3.1, are plotted in Fig. 3.11 as a function of frequency. The dc current density for each diode has been scaled from diode No. 1, approximately proportional to base region doping density, according to the scaling law given in Chapter I. Parameters for diode No. 1 are those of device No. 1 described in Reference 23. Also shown in Fig. 3.11 is the f^{-2} behavior of the maximum value of negative resistance.

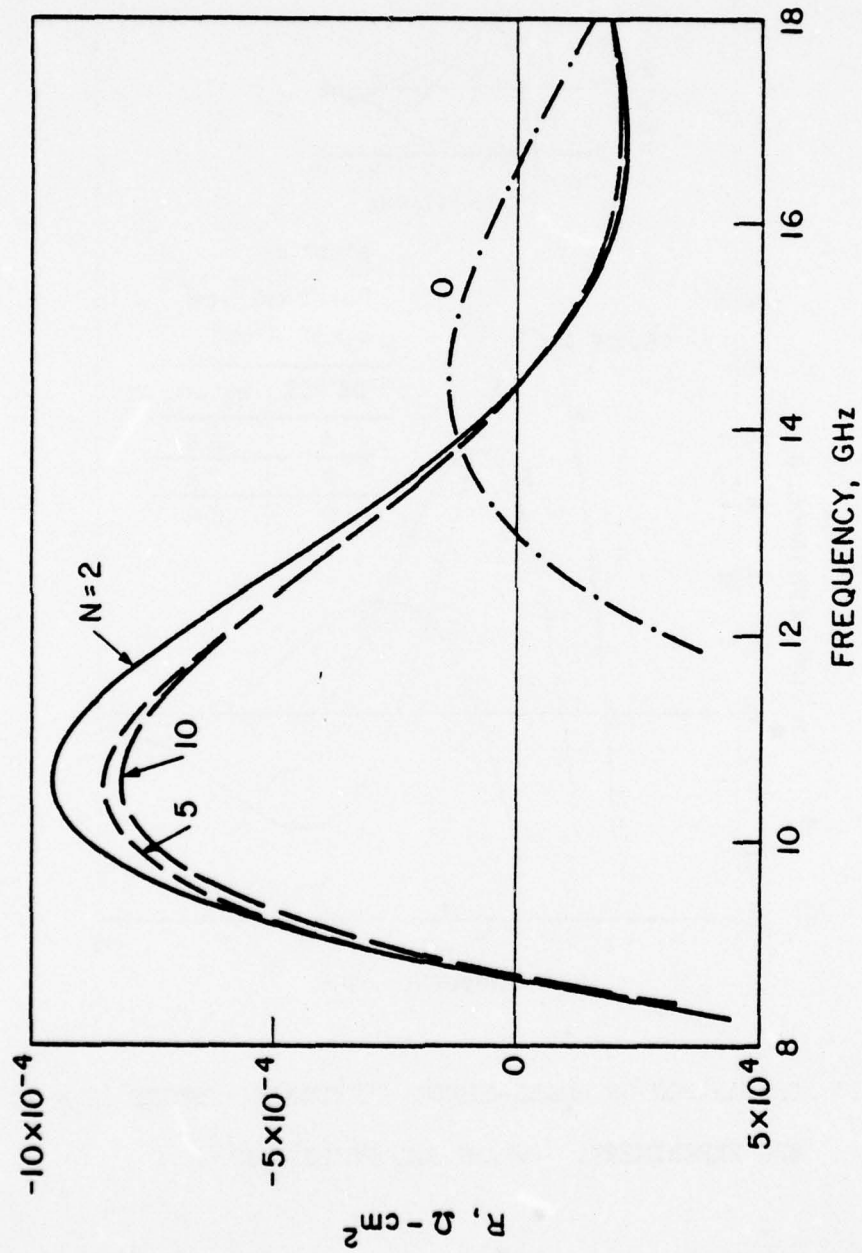


FIG. 3.9 CONVERGENCE OF SMALL-SIGNAL MODEL. (N = NUMBER OF LOW-FIELD REGION LUMPS).

($N_d = 3.3 \times 10^{15} \text{ cm}^{-3}$, $w_B = 6.0 \text{ } \mu\text{m}$, $J_o = 50 \text{ A/cm}^2$)

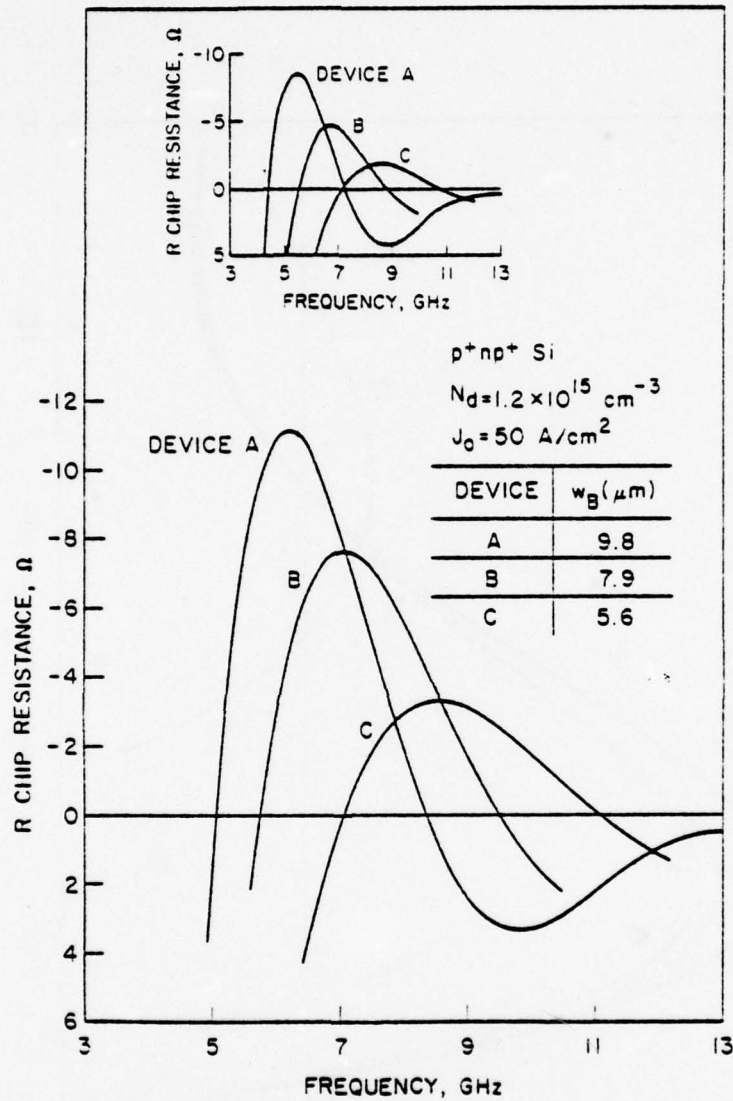


FIG. 3.10 COMPARISON OF SMALL-SIGNAL IMPEDANCE, THEORY ($N = 10$) AND EXPERIMENT. (SNAPP AND WEISSGLAS¹⁰)

Table 3.1

Dc Maximum Power* p^+np^+ Si BARITT Structures

<u>Device No.</u>	<u>Base Width w_B (μm)</u>	<u>Base Region Doping $N_d/10^{15}(cm^{-3})$</u>	<u>J_o (A/cm^2)</u>
1	6	3.3	260
2	5	4.0	320
3	4	5.0	400
4	3	6.6	520
5	2.5	8.0	630
6	2.0	9.9	780
7	1.5	13.0	1000
8	1.0	20.0	1600

* $wN_d \approx 20 \mu m \cdot cm^{-3}$.

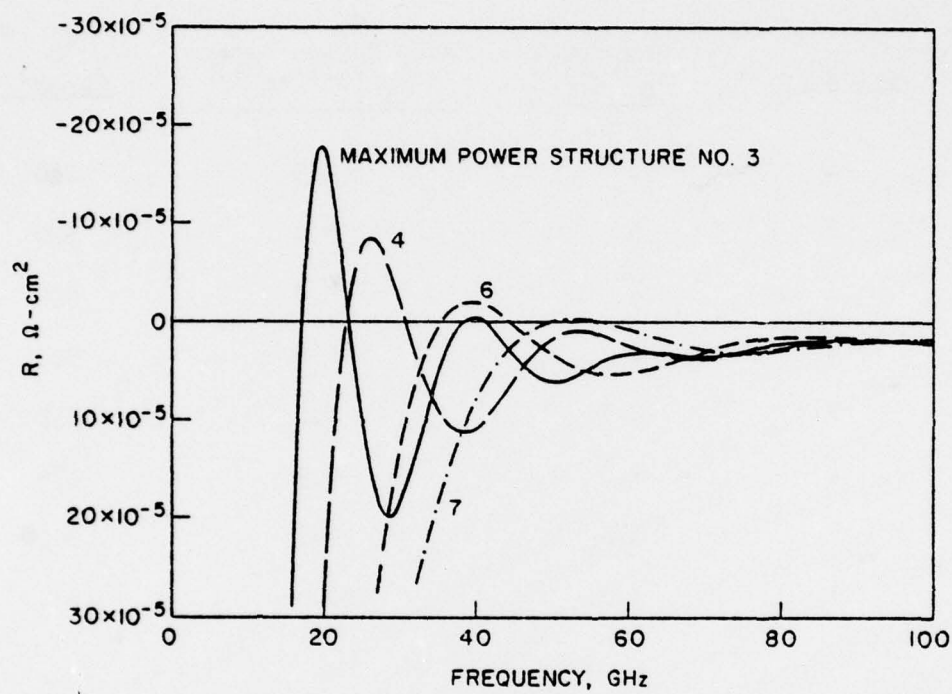


FIG. 3.11 SMALL-SIGNAL IMPEDANCE FOR FOUR DC MAXIMUM POWER STRUCTURES.

These eight dc maximum power structures are reexamined under large-signal conditions in Chapter VI.

The small-signal BARITT diode model presented in this section forms the basis for the detector and four-frequency mixer studies of Chapters IV and VII, respectively.

3.5 Small-Signal BARITT Diode Noise Analysis

Noise contributions to BARITT diode small-signal voltages and currents arise from two primary sources: the randomness of the injection process (shot noise) and the carrier velocity fluctuations within the drift-diffusion region (diffusion noise). The methods employed in this study for analyzing these two independent processes are extensions of the work of Haus et al.^{40,41} who considered a simplified MSM structure similar to the first-order model presented in the previous section.

3.5.1 Shot Noise. Dc currents injected across a forward-biased p-n junction exhibit a short-circuited noise power spectrum of the form⁴²

$$|J_{ns}|^2 = \frac{2qJ_0\Delta f}{A},$$

where J_0 is the dc current density, A is the cross-sectional diode area, and Δf is the observation bandwidth. This noise source can be incorporated into the second-order model of Fig. 3.8 by its inclusion as a shunt current generator J_{ns} across the forward-biased portion of the diode, Fig. 3.12. The open-circuit diode noise voltage can then be calculated as follows: The noise voltage v_{Fn} across the forward-biased region must produce particle and

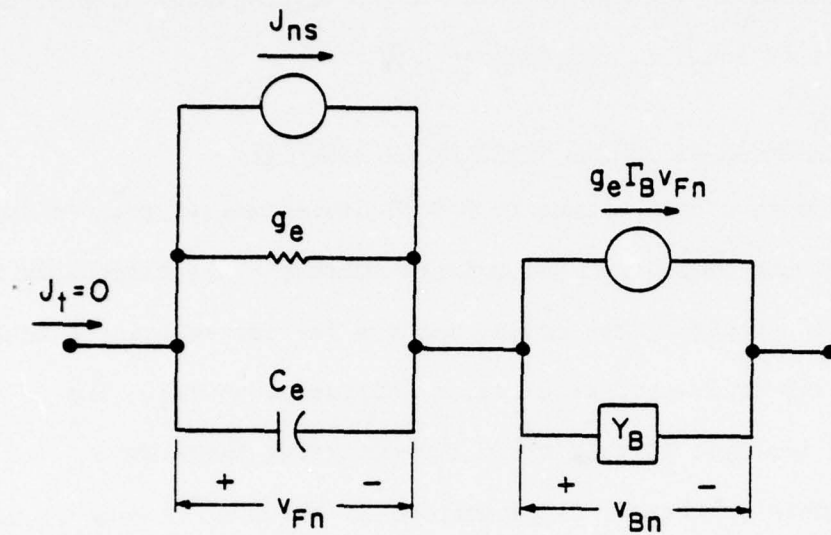


FIG. 3.12 EQUIVALENT CIRCUIT USED TO FIND THE OPEN-CIRCUIT
 NOISE VOLTAGE $v_{ns} = v_{Fn} + v_{Bn}$ DUE TO INJECTED SHOT
 NOISE.

displacement currents such that the total diode current is zero; that is,

$$v_{Fn} = - \frac{J_{ns}}{g_e + j\omega C_e} .$$

Similarly, the voltage across the drift-diffusion region v_{Bn} due to the injected particle current, $J_{ns} + g_e v_{Fn}$, is

$$v_{Bn} = - J_{ns} \frac{j\omega C_e \Gamma_B}{Y_B (g_e + j\omega C_e)} .$$

The mean square value of the total diode open-circuit shot noise voltage, $v_{ns} = v_{Fn} + v_{Bn}$, can then be expressed as

$$\overline{|v_{ns}|^2} = \overline{|J_{ns}|^2} \left| \frac{Y_B + j\omega C_e \Gamma_B}{Y_B (g_e + j\omega C_e)} \right|^2 . \quad (3.52)$$

The results given in Reference 41 neglect v_{Fn} and can be obtained from Eq. 3.52 by setting $\Gamma_B = \Gamma_s$ and $Y_B = j\omega C_e$.

3.5.2 Diffusion Noise. Several authors⁴³⁻⁴⁵ have shown that the noise due to dc carrier velocity fluctuations in a drift-diffusion region is distributed in nature and can be represented by a continuous series of uncorrelated small-signal noise current sources. The correlation function for these distributed sources is

$$\overline{J_{nd}(x) J_{nd}^*(x')} = \frac{4q^2 D p_o \Delta f}{A} \delta(x - x') , \quad (3.53)$$

where p_o is the dc hole concentration, D is the hole field-dependent diffusion coefficient, and $\delta(x - x')$ is the impulse function.

Over a small enough interval J_{nd} can be considered a constant, independent of position. The particle current density within this

interval can then be solved for, similar to the formulation of Eq. 3.45, as

$$J_p(z) = \frac{j\omega\epsilon}{\sigma + j\omega\epsilon} J_{nd}(x) \left(1 - e^{\gamma(z-x)}\right),$$

where again z is the independent spatial variable, $z \geq x$, and $\sigma = q\mu_0$. If the length of the interval is small enough such that it approaches the differential dx , then

$$J_p(z = x + dx) \approx - \frac{j\omega\epsilon\gamma}{\sigma + j\omega\epsilon} J_{nd}(x) dx.$$

The open-circuit differential voltage across the drift-diffusion region due to this one noise current source is

$$dv_{Bnd} = \frac{\gamma J_{nd}(x)}{\sigma + j\omega\epsilon} \int_x^w e^{\gamma(z-x)} dz dx.$$

Thus by superposition the voltage due to a continuum of noise sources is

$$v_{Bnd} = \int_0^w \frac{\gamma(x) J_{nd}(x)}{\sigma(x) + j\omega\epsilon} \int_x^w e^{\gamma(z-x)} dz dx$$

which has a mean square value of

$$\overline{|v_{Bnd}|^2} = \overline{v_{Bnd} v_{Bnd}^*} = \int_0^w \int_0^w \frac{|\gamma|^2 J_{nd}(x) J_{nd}^*(x')}{\sigma^2 + (\omega\epsilon)^2} \int_{x'}^w e^{\gamma^*(s-x')} ds \cdot \int_x^w e^{\gamma(z-x)} dz dx dx'.$$

Using Eq. 3.53, $\overline{|v_{Bnd}|^2}$ reduces to

$$\overline{|v_{Bnd}|^2} = \int_0^w \frac{4q^2 D p_0 |\gamma|^2}{[\sigma^2 + (\omega\epsilon)^2] A} \left| \int_x^w e^{\gamma z} dz \right|^2 dx$$

or, in terms of the lump boundaries,

$$\overline{|v_{Bnd}|^2} = \frac{4q^2}{A} \sum_{i=1}^{N+1} \frac{D_i P_{oi} |\gamma_i|^2}{\sigma_i^2 + (\omega \epsilon)^2} \int_{x_{i-1}}^{x_i} Q_i(x) dx, \quad (3.54)$$

where

$$Q_i(x) = \left| \int_x^{x_i} e^{\gamma_i z} dz + \sum_{j=i+1}^{N+1} \int_{x_{j-1}}^{x_j} e^{\gamma_j z} dz \right|^2.$$

Equation 3.54, though complicated, can be evaluated in closed form. The results given in Reference 42 can be obtained from Eq. 3.54 by using only one section, assuming a saturated drift velocity and no diffusion in the calculation of γ , and setting $\sigma = 0$.

Since no diffusion noise is associated with the forward-biased region of the diode, the open-circuit diffusion noise for the entire diode $\overline{|v_{nd}|^2}$ is equal to $\overline{|v_{Bnd}|^2}$.

3.5.3 Results. The computed mean square open-circuit noise voltages, shot and diffusion, for the typical X-band Si p^+np^+ BARITT diode discussed in Section 3.4.2 are shown in Fig. 3.13 as functions of frequency and bias current density. In the negative-resistance region of the diode, the two mean square noise voltages can be added (they are uncorrelated) and used to compute the noise measure of the diode:

$$\text{noise measure} \cong \frac{|v_{ns}|^2 + |v_{nd}|^2}{4|R_d|qV_T\Delta f}.$$

The noise measure of the X-band diode of Fig. 3.13 as a function of frequency and bias is shown in Fig. 3.14.

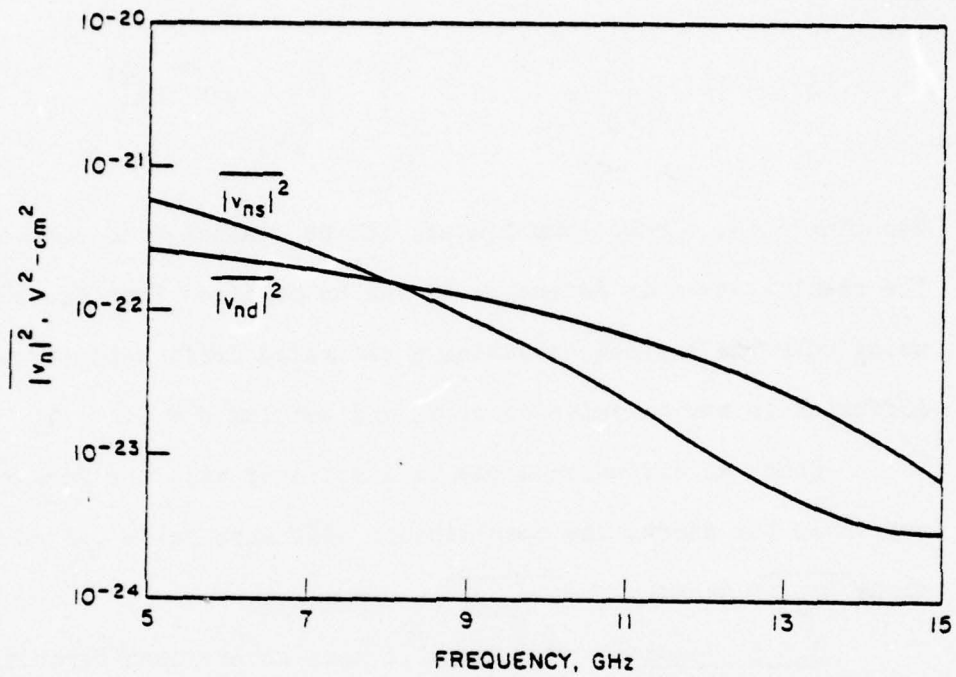


FIG. 3.13 SHOT NOISE AND DIFFUSION NOISE MEAN SQUARE VOLTAGES
FOR AN X-BAND BARITT DIODE. (p^+np^+ Si BARITT,
 $N_d = 3.3 \times 10^{15} \text{ cm}^{-3}$, $w_B = 6 \text{ } \mu\text{m}$ AND $J_o = 50 \text{ A/cm}^2$)

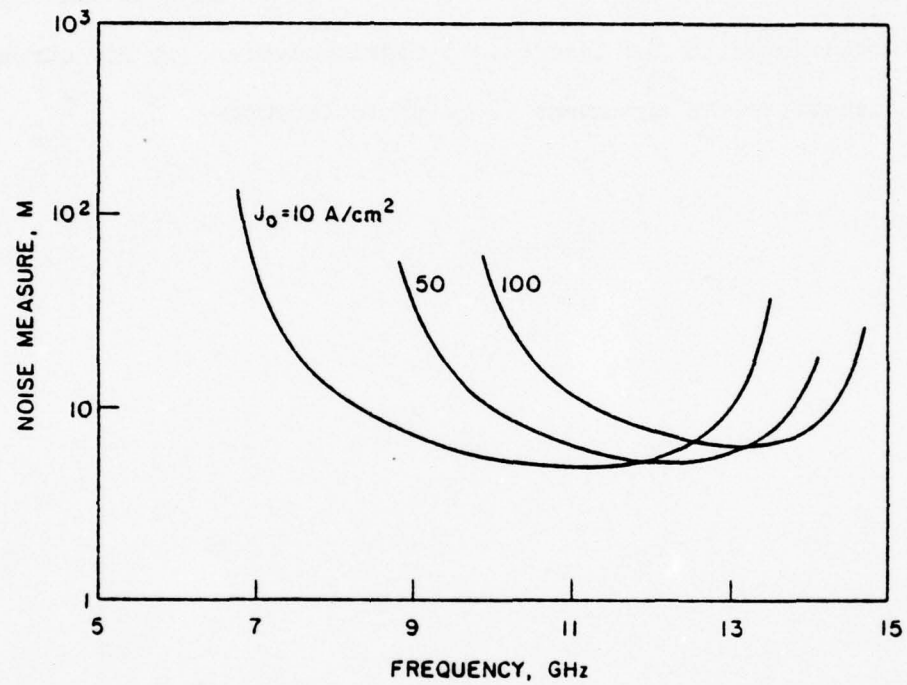


FIG. 3.14 SMALL-SIGNAL NOISE MEASURE FOR AN
X-BAND BARITT DIODE. (p^+np^+ Si
BARITT, $N_d = 3.3 \times 10^{15} \text{ cm}^{-3}$ AND
 $w_B = 6 \text{ } \mu\text{m}$)

The simple theoretical noise theory of this section is compared with the experimental measurements of Björkman and Snapp⁴⁶ in Fig. 3.15. As in the theoretical study of Sjölund,⁴⁷ a resistance of $1.5 \times 10^{-4} \Omega\text{-cm}^2$ has been assumed to be in series with R_d to account for substrate/contact loss. Diode heating has not been considered in the theoretical model; however, at low current densities the agreement is quite satisfactory.

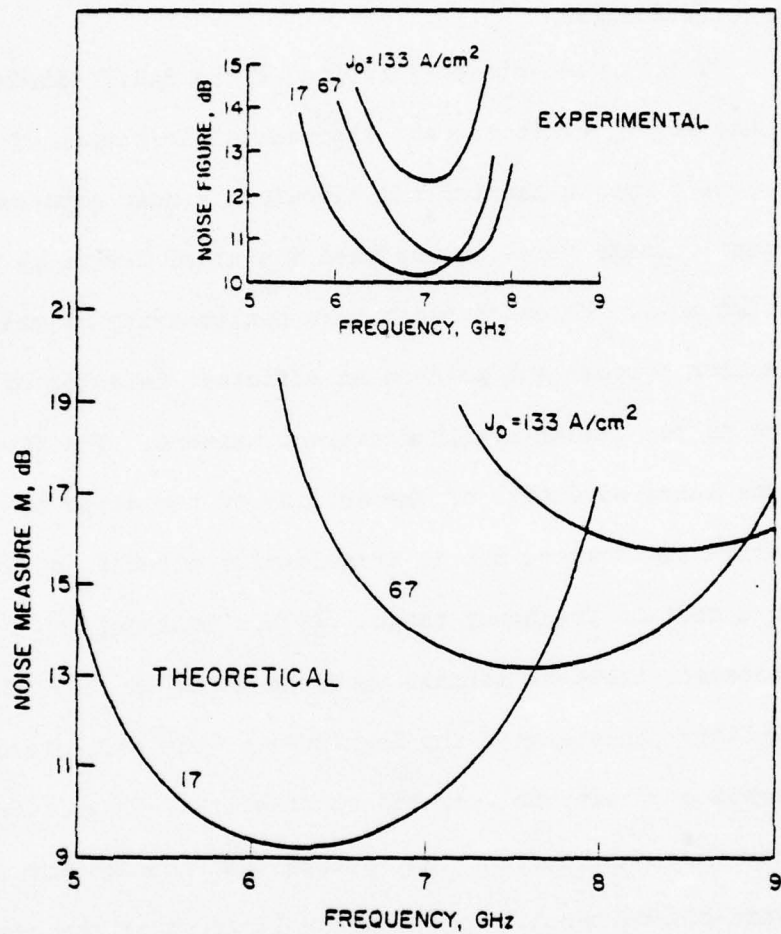


FIG. 3.15 COMPARISON OF THEORETICAL AND EXPERIMENTAL⁴⁵
 NOISE PROPERTIES OF A p^+np^+ Si BARITT DIODE.
 (SNAPP AND WEISSGLAS¹⁰ DEVICE B, $N_d = 1.2 \times 10^{15}$
 cm^{-3} , $w_B = 7.9 \text{ } \mu\text{m}$)

CHAPTER IV. BARITT DIODE VIDEO DETECTORS

4.1 Introduction

The forward-biased junction of the BARITT diode, as discussed in Chapter II, exhibits near exponential injection of minority carriers over its barrier and therefore a near exponential particle-current voltage relationship when the total device is in the punch-through mode. We can exploit this nonlinearity of the BARITT diode injection process and produce an efficient detector of microwave power in two fundamentally different manners. The first detection scheme takes advantage of the ability of the diode to present a negative resistance, due to transit-time effects, at its terminals over a certain frequency range. Within this region of negative resistance, incident signals upon the diode are amplified by the reflection process with the magnitude of the reflection gain determined by external circuit constraints. Thus it is possible to have the magnitude of the voltage that appears across the forward-biased portion of the diode larger than the magnitude of the incident signal itself. That is, the diode is capable of simultaneous amplification and detection. The second method of detection makes use of the fact that for frequencies higher than those in the region of diode negative resistance the real part of the impedance of the reverse-biased portion of the diode remains positive but falls to very low values. For certain bias levels the resistance of the reverse-biased region can fall below the series resistance which accounts for the loss in the substrate of the diode structure

making it appear that the reverse-biased region of the diode has been effectively shorted out. The detector as a whole then acts similar to an exponential diode detector with an extremely high cutoff frequency. Both of these methods of detection are discussed in detail in this chapter.

BARITT diode detectors differ from exponential diode, Schottky-barrier and point-contact detectors in the following ways: (1) they can attain negative resistance, (2) they do not have undepleted high resistivity regions, and (3) they are minority carrier devices, although recombination plays no role in their operation. The negative-resistance tunnel-diode detector can amplify and detect simultaneously and the back diode detector does not have a high resistivity undepleted region. However, both of these devices possess degenerately doped junctions which dictate untractable millimeter-wave device junction areas and thus are not compared to the high-frequency BARITT detectors studied here.

4.2 Exponential Diode Detector Theory

The detector circuit models considered in this study are shown in Figs. 4.1. The impedance transforming-resonating circuit, usually a two-port microwave cavity, is shown in general form, Fig. 4.1a, and can be characterized by any of its two-port parameters; in this case its ABCD parameters. At the diode terminals the generator and resonator-transformer can be replaced by their Thevenin equivalents as shown in Fig. 4.1b. The diode small-signal impedance is shown as the series combination of a resistance due to the loss in the diode undepleted layer and substrate and the parallel impedance of the barrier conductance, $g_b = I_o/V_T$, and the barrier depletion-layer capacitance, C_b .

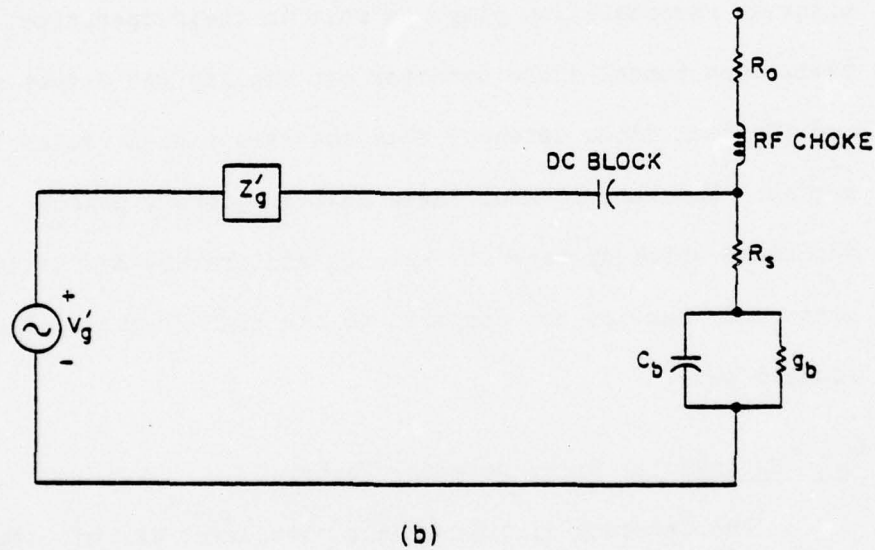
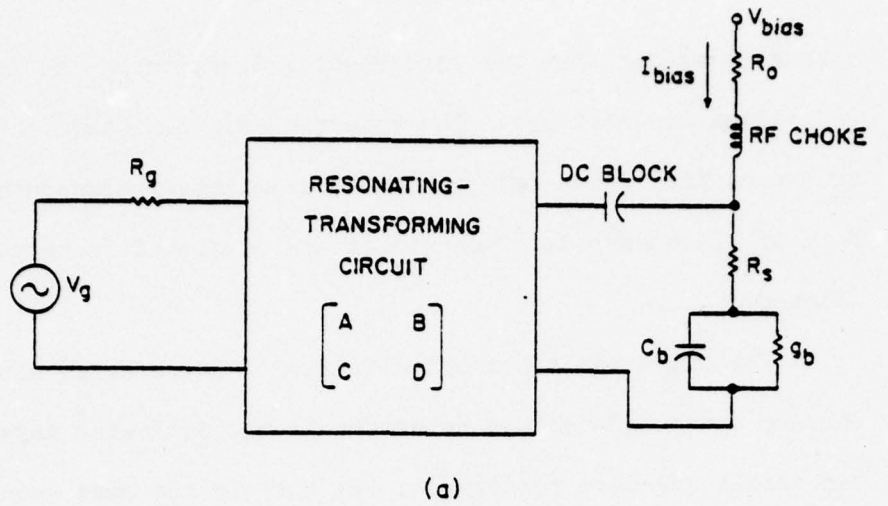


FIG. 4.1 (a) GENERAL EXPONENTIAL DIODE DETECTOR CIRCUIT

$$Z_b = (g_b + j\omega C_b)^{-1}. \quad (b) \text{ THEVENIN EQUIVALENT}$$

$$\text{DETECTOR CIRCUIT } V'_g = V_g / (A + CR_g), \quad Z'_g =$$

$$(B + DR_g) / (A + CR_g) \equiv R'_g + jX'_g.$$

A detectable rectified voltage signal V_R is read across the bias resistance R_0 due to the flow of rectified microwave current.

Rectification occurs due to the nonlinear exponential injection of majority carriers across the barrier. The magnitude of the rectified current can be determined analytically⁴⁸ by expanding the expression for the particle current injected over the barrier in a Taylor series about its quiescent value and extracting the dc component due to the small-signal RF voltage across Z_b . The maximum detected voltage sensitivity γ (V_R at loop resonance normalized to the available power of the generator with $R_0 \gg$ the video resistance of the diode R_V) can then be expressed as

$$\gamma = \frac{4R_s(R_s + R_b)}{|A + CR_s|^2(R'_s + R_s + R_b)} \cdot \frac{|Z_b|^2}{2V_T(R_s + R_b)}$$

$$\equiv \eta \cdot \gamma_m, \quad (4.1)$$

where the first term η is the efficiency of the transforming network in delivering power to the diode terminals and the second term γ_m is the maximum voltage detection sensitivity of the diode structure itself, independent of any circuit. Since $R_b = \text{Re}(Z_b)$ γ_m can be rewritten as

$$\gamma_m = \frac{R_s}{2V_T \left[g_b R_s (1 + g_b R_s) + (f/f_c)^2 \right]}, \quad (4.2)$$

where f_c is the cutoff frequency defined by

$$f_c = \frac{1}{2\pi C_b R_s};$$

note that f_c is a function of the bias point. An ideal exponential diode would have no series resistance and could be characterized by the ideal detected voltage sensitivity $\gamma_{mo} = (2V_T g_b)^{-1}$ on an equal bias current criterion. Thus a measure of detector ideality is the ratio of γ_m to γ_{mo} ; that is,

$$\text{Ideality} = \frac{\gamma_m}{\gamma_{mo}} = \frac{g_b R_s}{g_b R_s (1 + g_b R_s) + (f/f_c)^2}.$$

At an optimum bias current such that $g_b R_s = f/f_c$, neglecting the relatively weak dependence of C_b on bias, optimum ideality $= 1/[1 + 2(f/f_c)]$.

The cutoff frequency f_c is chosen as the principal theoretical basis for comparing the quality of exponential diode detectors. Other parameters such as noise equivalent power (NEP) in a 1-Hz video bandwidth, video resistance R_v , and square-law dynamic range are also important. In the main, the higher the device cutoff frequency, the better detector it will be.

4.3 BARITT Diode Detectors

A BARITT diode detector circuit, Fig. 4.2, differs from the exponential diode detector circuit only in its depiction of the semiconductor device. The BARITT diode series impedance is divided into three values: a resistance R_s representing the loss in the highly conductive substrate-contact regions of the diode, a forward-biased p-n junction impedance Z_F representing the injecting junction, and a diffusion-drift region impedance Z_B representing the transit-time effects of minority carrier flow in the reverse-biased junction of the diode. Displacement current reactances are also included in Z_B .

Rectification occurs in the forward-biased junction due to its nonlinear injection of base region minority carriers into the

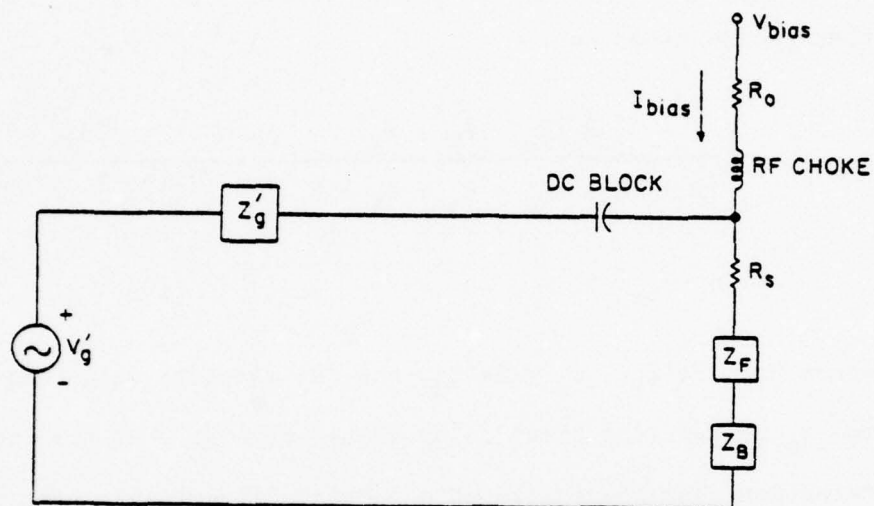


FIG. 4.2 BARITT DIODE DETECTOR EQUIVALENT CIRCUIT.

$$[V'_g = V_g / (A + CR_g) \text{ AND } Z'_g = (B + DR_g) / (A + CR_g)]$$

$$\equiv R'_g + jX'_g]$$

diffusion-drift region. Similar to the analysis of the exponential diode, the expression for the particle current through the forward-biased region can be expanded about its bias value in a Taylor series and the dc component due to the small-signal RF voltage across Z_F can be isolated. The loop resonance maximum detected voltage sensitivity can then be expressed as

$$\gamma = \frac{4R_g |R_s + R_F + R_B|}{|A + CR_g|^2 (R'_g + R_s + R_F + R_B)^2} \cdot \frac{|Z_F|^2}{2V_T |R_s + R_F + R_B|}$$

$$\equiv \eta \cdot \gamma_m, \quad (4.3)$$

where $R_F = \text{Re}(Z_F)$, $R_B = \text{Re}(Z_B)$ and the absolute value requirements in η and γ_m reflect the possibility of negative R_B . As the impedance and detection characteristics of a forward-biased p-n junction with no recombination, i.e., the forward-biased region of the BARITT diode, are formally the same as those of the majority carrier Schottky-barrier exponential diode, a functional explanation of the BARITT diode detector operation is this: a BARITT diode detector is an exponential diode detector in series with a dependent diffusion-drift region impedance* Z_B . In essence the behavior of Z_B determines the comparative usefulness of the detector.

The two fundamental modes of BARITT diode detector operation can now be identified. The first is the negative-resistance mode, $R_B < 0$, and the second is the passive mode, $R_B > 0$. The negative-resistance mode can be further quantified in terms of the level of negative

* The impedance of the reverse-biased portion of the diode is termed dependent since it is a function of the ratio of injected particle current to the total diode current, c.f., Chapter III.

resistance, i.e., $R_B < -(R_S + R_F)$, $-(R_S + R_F) < R_B < -R_S$, and so on, but our primary interest will be centered on the case of total diode negative resistance,

$$R_d = R_S + R_F + R_B < 0 .$$

The designation "negative-resistance mode" will be restricted to this case alone.

The expression for maximum detected voltage sensitivity, Eq. 4.3, can be specialized for each of the modes of BARITT diode detector operation into forms which are better suited to the individual characteristics of the mode. The maximum responsivity of the negative-resistance mode can be rewritten as

$$\gamma = \frac{4R_g |R_d|}{|A + CR_g|^2 (R'_g - R_d)^2} \cdot \left(\frac{R'_g - R_d}{R'_g + R_d} \right)^2 \cdot \frac{|Z_F|^2}{2V_T |R_d|} , \quad (4.4)$$

where the center term is recognized as the power gain of a negative-resistance reflection-type amplifier. The identities of the other two terms remain as before, the transforming circuit efficiency and the device maximum detection sensitivity. The responsivity expression for the passive mode can be manipulated into

$$\gamma = \frac{4R_g R_d}{|A + CR_g|^2 (R'_g + R_d)^2} \cdot \frac{R'_s}{2V_T [g_F R'_s (1 + g_F R'_s) + (f/f_{ce})^2]} , \quad (4.5)$$

where $R'_s = R_S + R_B$ and an effective cutoff frequency has been defined

$$f_{ce} \equiv \frac{1}{2\pi C_F (R_S + R_B)} .$$

Note that the effective cutoff frequency is not only a function of bias but also is a function of frequency, $R_B = R_B(f)$.

Again, the first term in Eq. 4.5 is the transforming circuit efficiency and the second is the device maximum detection sensitivity. In direct analogy with the exponential diode detector the effective cutoff frequency f_{ce} is chosen as the figure of merit for the passive mode BARITT diode detector. A sensitivity figure of merit for the negative-resistance mode detector is discussed in the next section.

4.4 Theoretical and Experimental Results

The theoretical negative-resistance mode detection idealities, γ_m/γ_{mo} , for four of the eight Si p⁺np⁺ dc maximum power structures of Table 3.1 are shown in Fig. 4.3 as a function of frequency. The bias conditions for each diode are as given in Table 3.1 and a minimum magnitude of diode negative resistance, $2 \times 10^{-6} \Omega\text{-cm}^2$, is the criterion for the determination of useful negative resistance ($10^{-3} \Omega\text{-cm}$ resistivity substrate, 10 μm thick). Presentation of the data in the format of Fig. 4.3 can be confusing for it appears that the ideality and therefore the detector quality improves toward the edges of the negative-resistance regions and with higher frequency devices. It is true that the ideality by definition behaves in this manner; however, the ability to produce stable reflection gain must also be taken into account, i.e., the larger the magnitude of negative resistance the better, in the determination of overall quality. Thus a better measure of the actual quality or usefulness of the negative-resistance mode detector would be the negative of the ideality, $-\gamma_m/\gamma_{mo}$, akin to the Q of a negative-resistance device. With this in mind, the lower values of ideality in Fig. 4.3 indicate the better detectors.

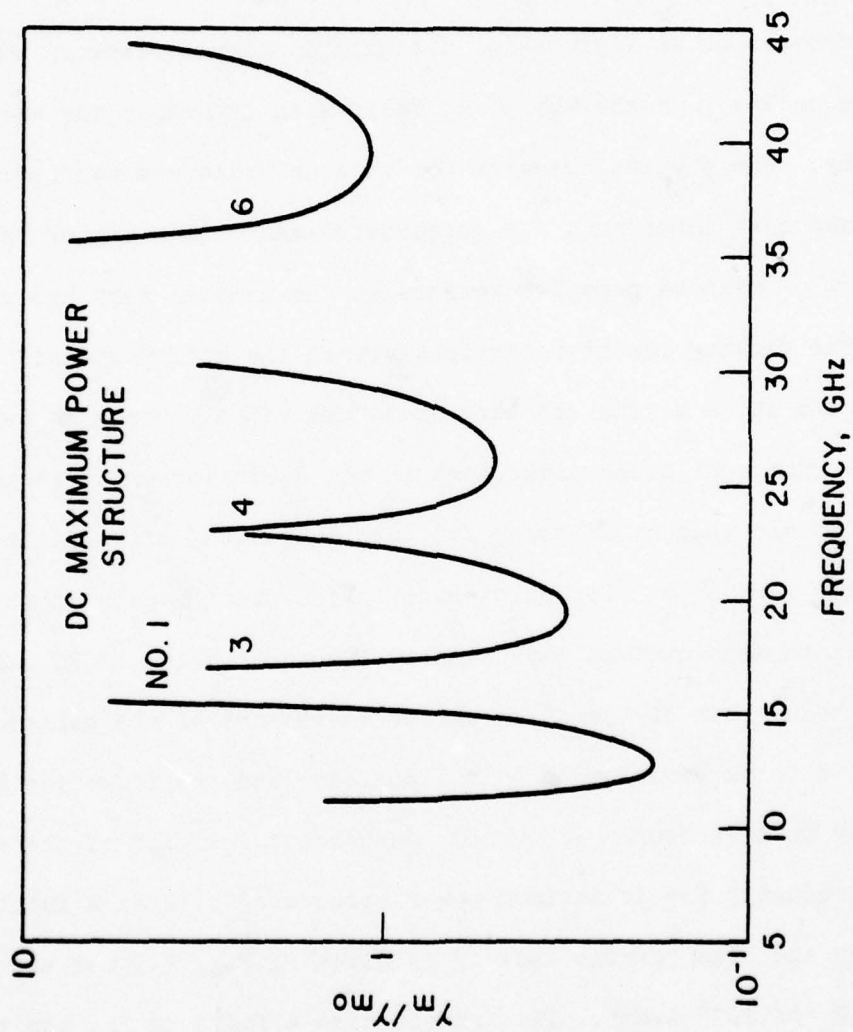


FIG. 4.3 NORMALIZED DETECTOR IDEALITIES FOR DC MAXIMUM POWER
STRUCTURE IN NEGATIVE-RESISTANCE REGIONS.

Beyond the frequency region of negative resistance the small-signal resistance of the diffusion-drift region R_B for four of the dc maximum power structures behave as shown in Fig. 4.4. In general, the magnitude of R_B falls with decreasing dc bias current and therefore the effective cutoff frequency of a passive mode detector using these devices would rise. To compare these structures as passive mode detectors on an even basis, a common dc current density of 50 A/cm² has been chosen. On the whole, R_B falls with frequency for each structure. The physical reasons for this decrease are twofold: First, and most important, for frequencies many times higher than the frequency of maximum negative resistance the induced terminal current due to the flowing minority carriers within the diffusion-drift region appears almost as a constant current to the rapidly changing terminal voltage. The real power dissipated in the diffusion-drift region, the average of the product of these two quantities, therefore falls with increasing frequency. Second, the diffusion-drift region is shunted by a displacement current capacitance. Once the value of R_B falls to a value below that of the fixed series resistance of the substrate contact, R_s , its effect on f_{ce} is diminished and the effective cutoff frequency becomes nearly frequency independent. A plot of the effective cutoff frequency for dc maximum power structure No. 2 as a function of frequency and bias current density is given in Fig. 4.5 for an assumed R_s of 10^{-6} Ω -cm². The transit-time effects on R_B , and thus f_{ce} , are clearly seen for the higher levels of dc bias. For all bias levels the magnitude of R_B eventually falls monotonically with frequency and its effect on f_{ce} is reduced.

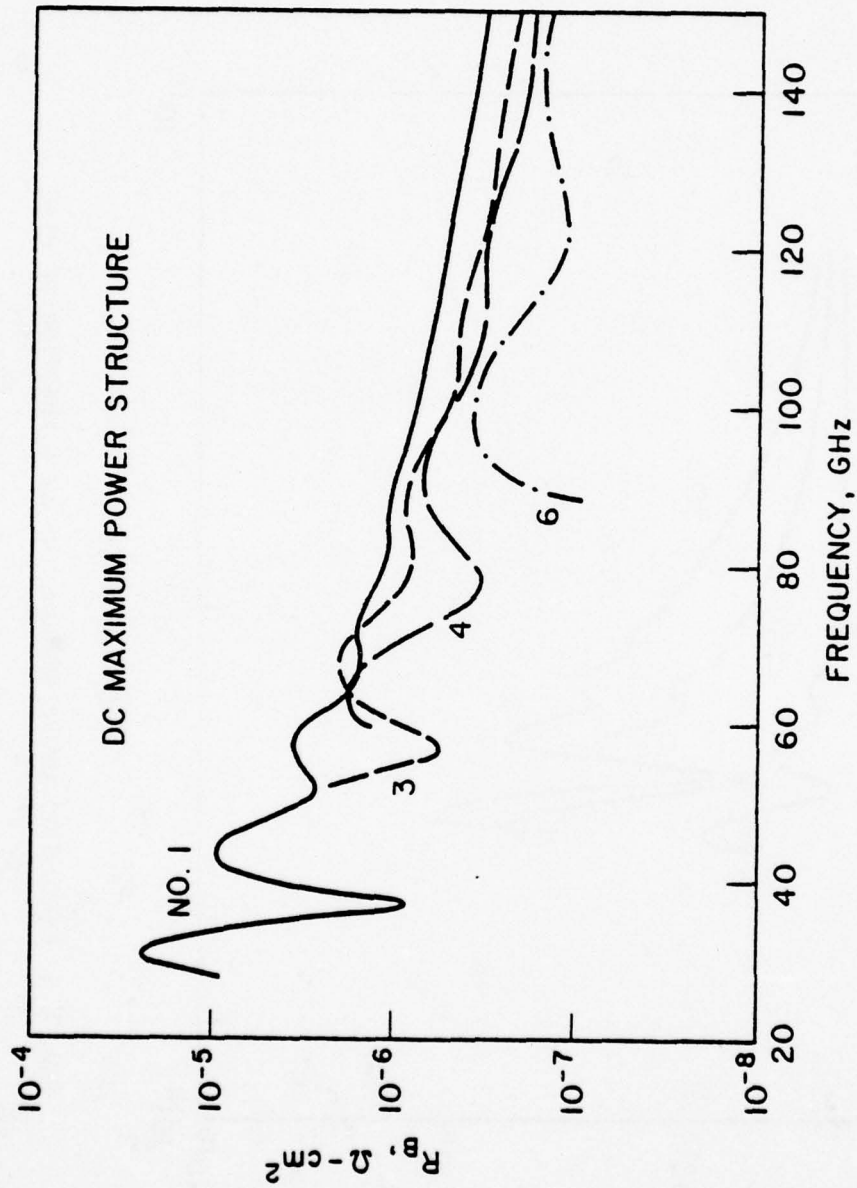


FIG. 4.4 DRIFT-DIFFUSION REGION RESISTANCES FOR DC
MAXIMUM POWER STRUCTURES. ($J_o = 50 \text{ A/cm}^2$)

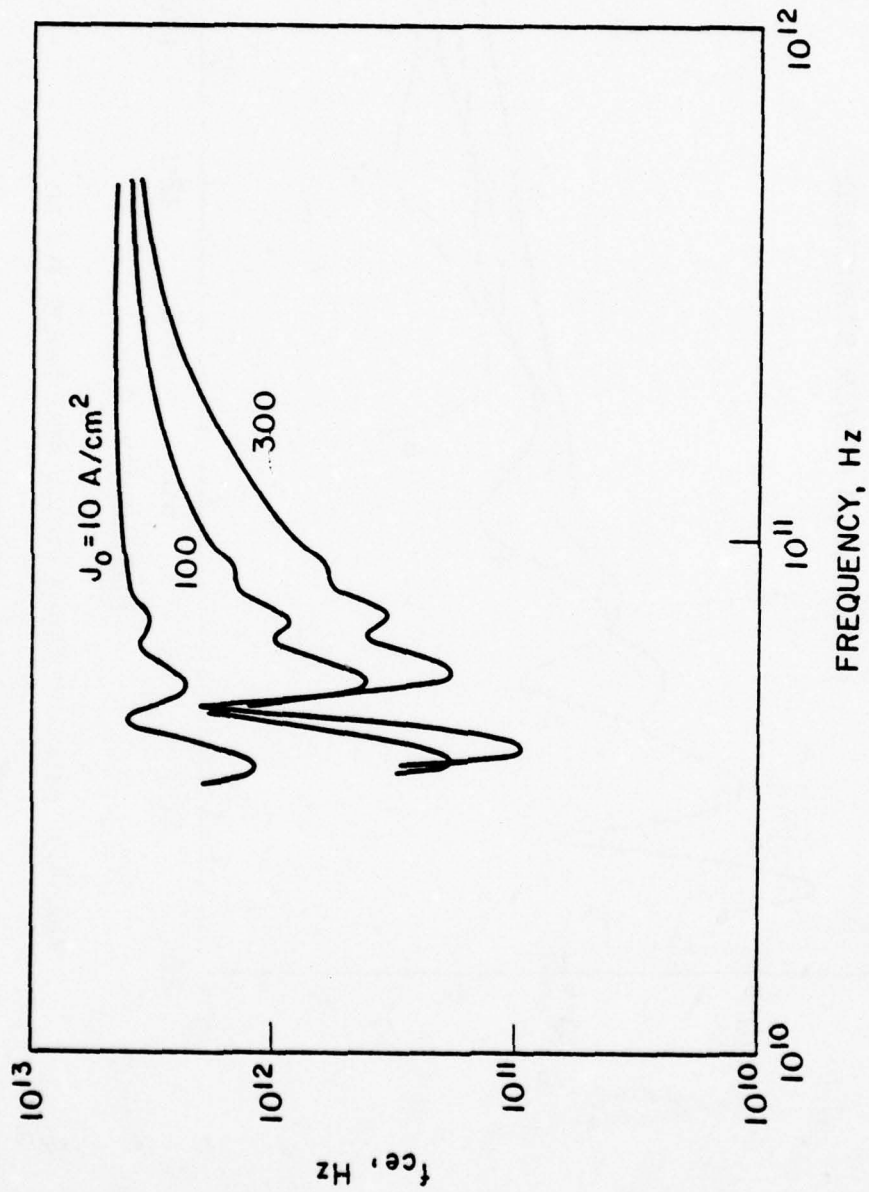


FIG. 4.5 EFFECTIVE CUTOFF FREQUENCIES AS A FUNCTION OF BIAS
FOR DC MAXIMUM POWER STRUCTURE NO. 2.

Measured maximum detected voltage sensitivities for a p^+np^+ Si diode with a base region doping density of $4 \times 10^{15} \text{ cm}^{-3}$, a base width of approximately $3 \text{ }\mu\text{m}$, and a one-dimensional junction area of $2 \times 10^{-5} \text{ cm}^2$ are shown in Fig. 4.6. The K-band measurements were made with the packaged diode placed in a WR-42 waveguide cavity with a resonant cap structure⁴⁹ such that with the addition of an E-H tuner the diode was capable of oscillation at 21 GHz. The Ka-band measurements were made with the same packaged diode placed in a similar WR-28 waveguide cavity with a resonant cap structure such that second-harmonic power could be extracted at 36 GHz. Second-harmonic operation is discussed in Chapter VI. Also shown in Fig. 4.6 are theoretical sensitivities for the same diode structure with the transformed generator impedance as a parameter. As predicted, the sensitivity within the negative-resistance region could be made arbitrarily high depending upon how close the equivalent generator impedance could be tuned to the total diode negative resistance. Since the resonant cap structure is a fairly high Q as well as a multiply resonant circuit, the E-H tuner was not maximally effective at each frequency in coupling generator power to the diode. To show the relatively narrow-band response of the detector circuit while the diode was in its negative-resistance region, a 100-MHz wide swept measurement was made around a center frequency of 20.5 GHz for a tuning that gave a midband response of $\gamma = 1.8 \times 10^5 \text{ mV/mW}$. As can be seen in Fig. 4.7 the 3-dB bandwidth was only about 10 MHz. Tuning for less midband gain gave a wider response curve, while tuning for a higher midband gain produced a narrower curve; a typical gain-bandwidth tradeoff. The NEP of the detector was also measured when the signal frequency

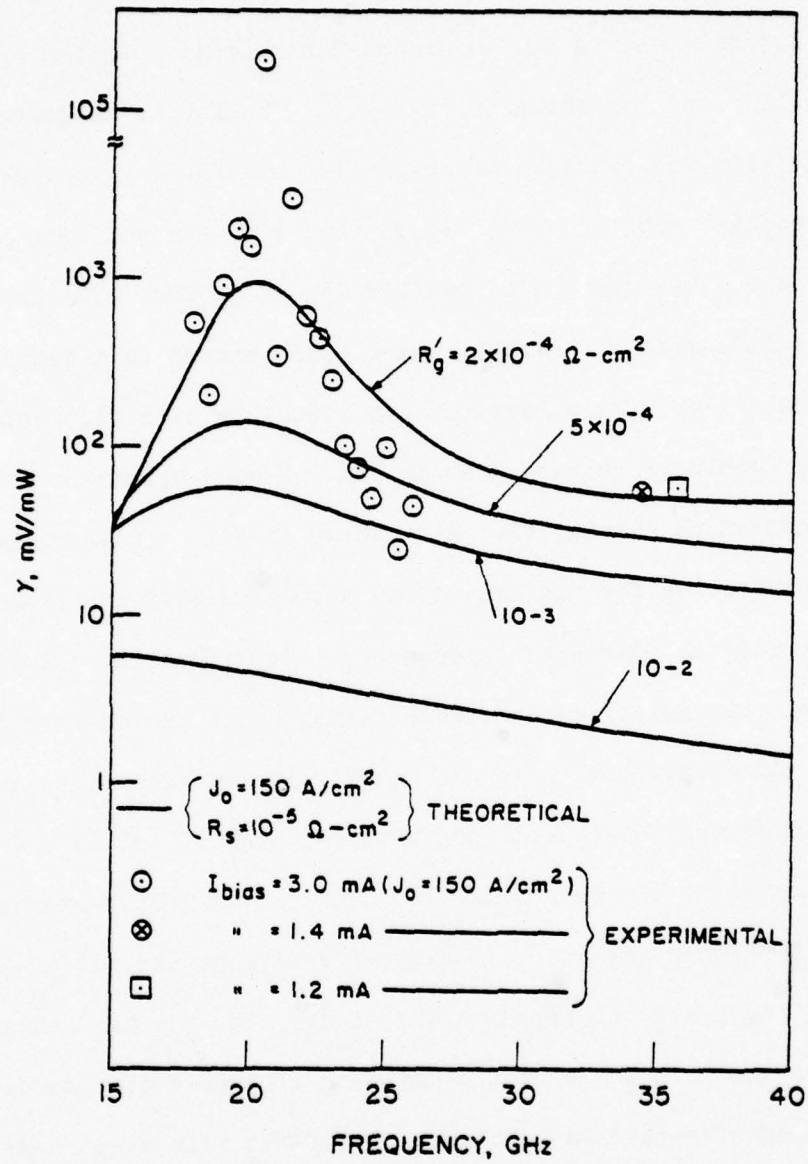


FIG. 4.6 EXPERIMENTAL AND THEORETICAL DETECTED VOLTAGE SENSITIVITY FOR A K-BAND BARITT DIODE.

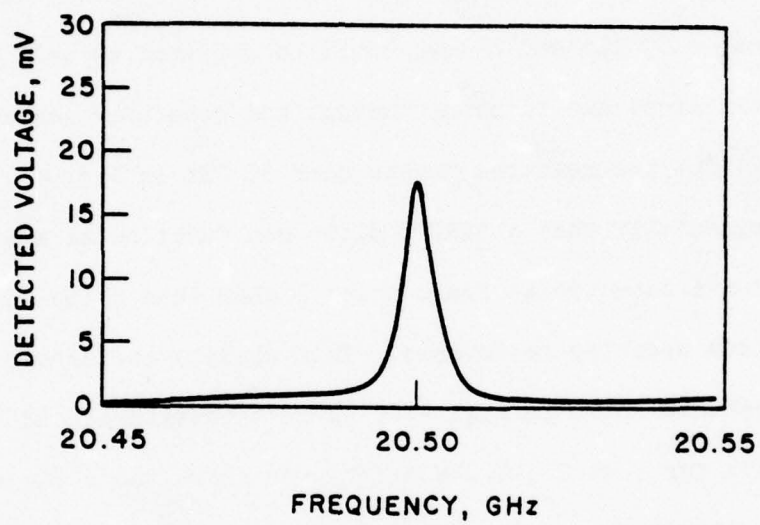


FIG. 4.7 SWEPT FREQUENCY DETECTOR RESPONSE IN
NEGATIVE-RESISTANCE FREQUENCY REGION.

was in the negative-resistance region of the diode. Similar to the detected voltage sensitivity measurements, seemingly arbitrarily low values of NEP could be measured depending upon one's willingness to accept narrower and narrower frequency response with increasing sensitivity. Typically, stable NEP values of -99 dBm at a video frequency of 1 kHz could be obtained at 20.5 GHz. Still lower values, -109 dBm and below, could be obtained as well but could not be maintained due to bias, tuning, and generator instabilities.

The two measured points near 35 GHz in Fig. 4.6 demonstrate experimentally that a BARITT diode can function as a sensitive microwave detector at frequencies higher than those within the region of diode negative resistance. This ability is further demonstrated by the results shown in Fig. 4.8. Here the measured and theoretical results for γ at 27.44 GHz and R_v are shown for a packaged X-band diode (similar to the one described in Fig. 4.9) mounted in the WR-28 waveguide cavity mentioned previously (different resonator cap diameter). The theoretical predictions for γ_m assume a series resistance of $10^{-5} \Omega\text{-cm}^2$, 10 μm of $10^{-2} \Omega\text{-cm}$ substrate; no attempt was made to estimate the device contact resistance. The transforming circuit efficiency was estimated by cavity Q measurements using a shorted diode package to be approximately 40 percent at a diode bias current of 100 μA . The measurement procedure was as follows: The one-port cavity parameter input coupling coefficient, β_1 , and intrinsic Q, Q_0 , of the cavity-diode mount with the shorted diode package in place were measured at the closest cavity resonant frequency that was higher than the resonant frequency of the cavity mount with the diode in place (less energy storage implies a higher resonant frequency). The loaded

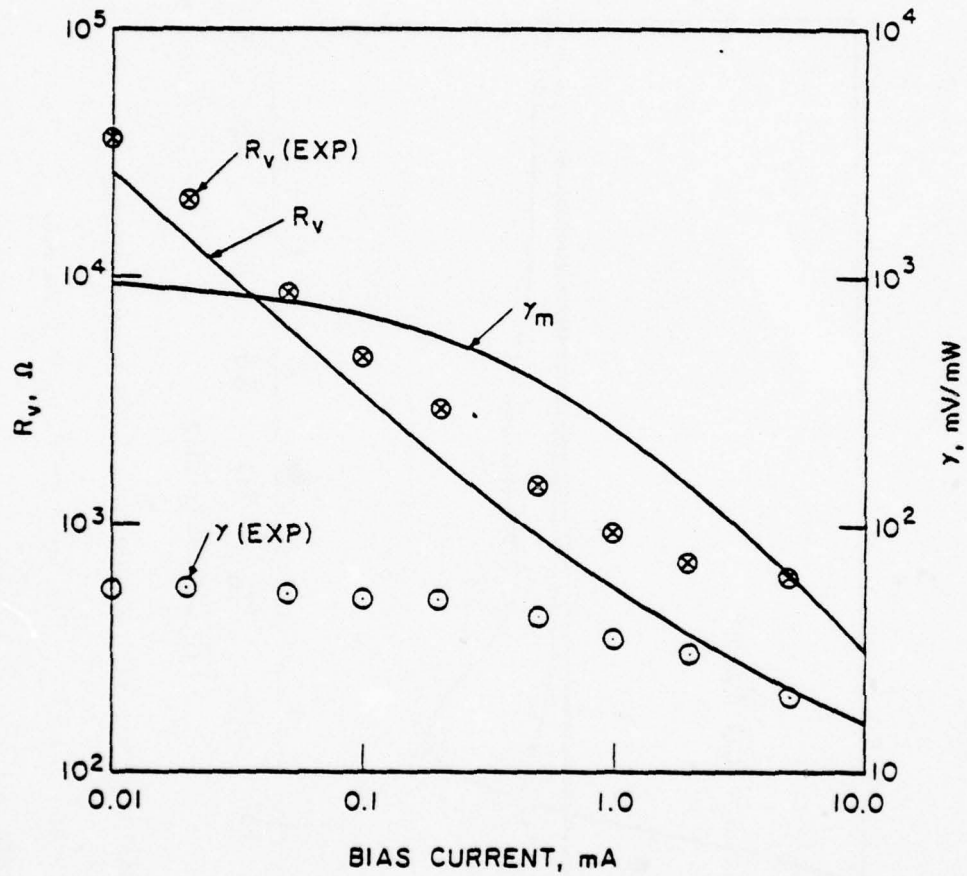


FIG. 4.8 THEORETICAL AND EXPERIMENTAL RESULTS FOR VIDEO DETECTION AT 27.44 GHz WITH X-BAND DIODE.

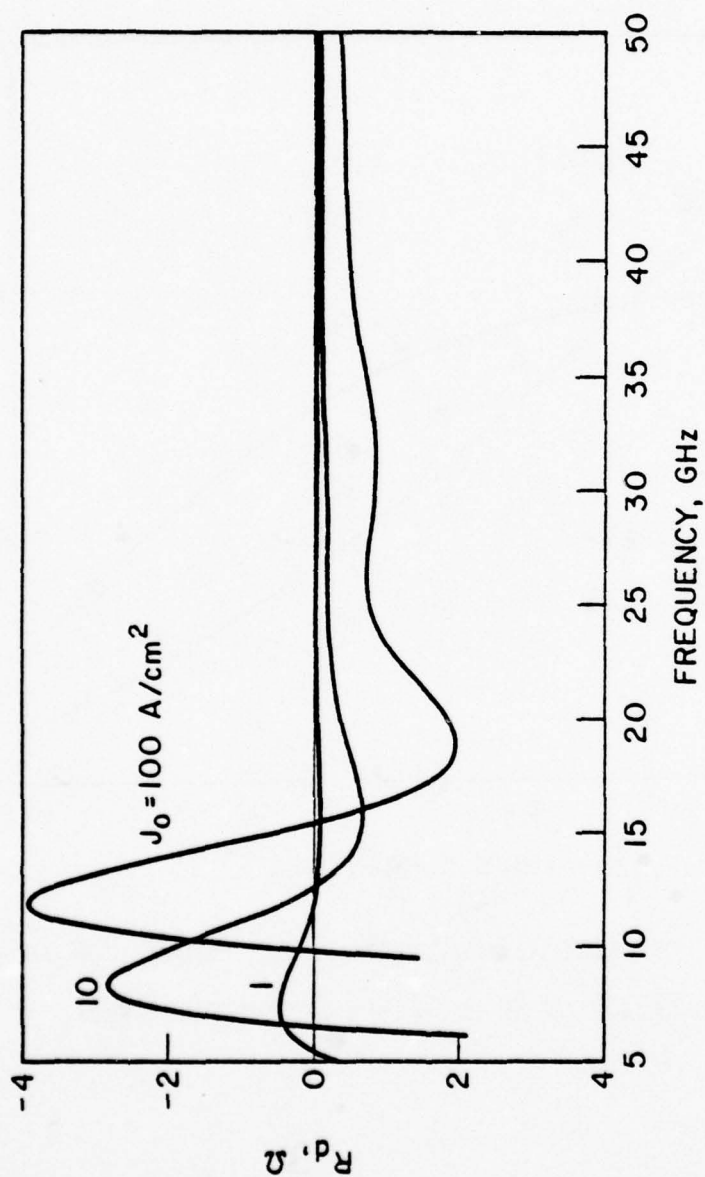


FIG. 4.9 SMALL-SIGNAL RESISTANCE OF X-BAND BARRITT DIODE.

($p^{+}np^{+}$, Si, $N_d = 2 \times 10^{15} \text{ cm}^{-3}$, $w_B = 5 \text{ } \mu\text{m}$ AND

AREA = $1.7 \times 10^{-4} \text{ cm}^2$)

Q , Q_L , of the two-port cavity mount with the diode in place was measured by the transmission method⁵⁰ using the diode itself as the detector of transmitted power. Since the change in resonant frequency between the two cases was small, 5 percent, it is a fairly good assumption that Q_0 and β_1 did not change appreciably between the two cases. Thus from $Q_L = Q_0 / (1 + \beta_1 + \beta_2)$ an estimate for the diode coupling coefficient, β_2 , can be obtained and the resonant transmission efficiency⁵⁰ $T(\omega_0) = 4\beta_1\beta_2 / (1 + \beta_1 + \beta_2)^2$ can be calculated. The poor coupling efficiency partially accounts for the discrepancy between the measured γ and the theoretical γ_m of Fig. 4.8; the remaining gap between theory and experiment is thought to be due to the contact resistance at the emitter.

4.5 Discussion

It has been shown both experimentally and theoretically that the BARITT diode can function as a useful detector of microwave power. In the negative-resistance mode the diode is capable of simultaneous amplification and detection, resulting in an extremely sensitive though narrow-band detector. However, the greatest potential of the diode lies in its passive mode of operation at millimeter wavelengths. For this mode the real part of the diffusion-drift region impedance is effectively averaged out at high frequencies and power can be efficiently transferred to the rectifying forward-biased junction. Theoretical cutoff frequencies exceeding 1000 GHz are predicted for Si one-dimensional p^+np^+ structures.

One obvious and simple improvement that could be made for detectors that are specifically intended for the passive mode of

operation is to fabricate the devices with a higher mobility substrate material such as n-type Si or GaAs (n^+pn^+ devices) and thus lower the substrate loss resistance R_s . The substrate could in principle be eliminated entirely by using an MSM structure, back-to-back Schottky barriers; although the control needed for the processing of the resulting wafers, 1 to 5 μm thick, may prove difficult. These improvements aside, a nagging question remains, "What is the validity of using predictions from a theory that considers only one-dimensional structures at millimeter wavelengths where circuit impedance level requirements would force device junction diameters to be comparable to the depleted base region thicknesses?" An accurate answer to this question awaits a complete two-dimensional analysis, but a reassuring counterquestion is this, "Why not make the devices two-dimensional in the first place?" Since we desire the real part of the impedance of the diffusion-drift region to be small for efficient passive mode operation, construction of a large area reverse-biased region can only help detector sensitivity. A proposed two-dimensional structure for passive mode BARITT diode detectors is shown in Fig. 4.10. This is the BARITT diode version of the "honeycomb" structure originally proposed for millimeter-wave Schottky-barrier detector and mixer diodes by Young and Irvin.⁵¹ For this device the effective collector diameter d_c will be larger than the actual diameter of the emitting junction d_E due to the two-dimensional spreading of the current in the reverse-biased region. Further current spreading will occur in the collector substrate region; resulting in the series resistance of the substrate being solely determined by the spreading resistance for values of effective collector diameters less than the substrate

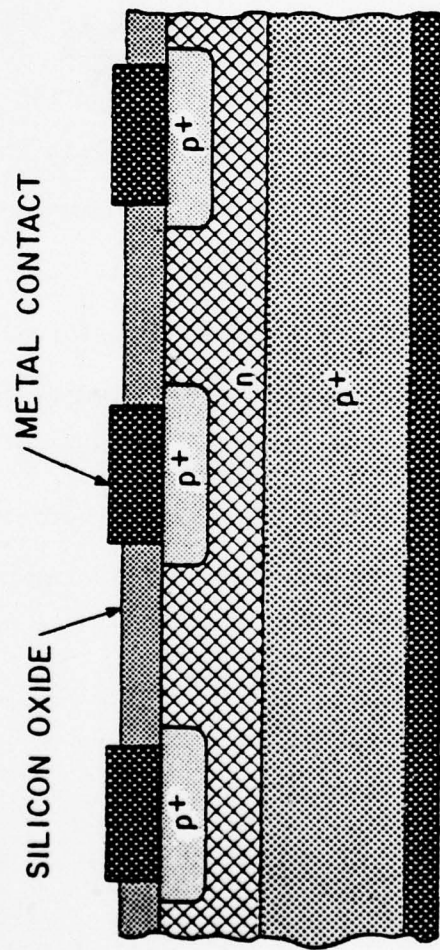


FIG. 4.10 TWO-DIMENSIONAL BARRITT DIODE STRUCTURE.

thickness. That is,

$$R_{sp} = \frac{\rho}{2d_C},$$

where R_{sp} is the spreading resistance⁵² and ρ is the substrate resistivity. Our previous calculation of R_s , for a given device junction area, was

$$R_s = \frac{\sigma w_B}{\pi(d_E/2)^2} = R_{sp} \frac{8w_B d_C}{d_E^2}$$

Thus, when d_E becomes less than w_B due to circuit impedance level constraints the previous estimate of R_s becomes exceedingly pessimistic if the device is two dimensional.

Based on the assumption of a two-dimensional passive mode detector, effective cutoff frequencies of greater than 10,000 GHz are envisioned for p^+np^+ Si BARITT diodes. Cutoff frequencies in this range would exceed the highest reported zero-bias cutoff frequencies for GaAs Schottky-barrier devices known to the author.^{53,54}

CHAPTER V. OPTICAL DETECTION WITH PUNCH-THROUGH
SEMICONDUCTOR DEVICES

5.1 Introduction

The open-base phototransistor has been in existence for some time and its operating characteristics are well understood.⁵⁵ However, operation of a phototransistor in the punch-through mode, essentially resulting in a BARITT diode structure, does not appear to have been previously considered. As the BARITT diode has a frequency region of negative resistance due to the transit-time delay of injected carriers, so too does the punch-through open-base phototransistor; thus, optically generated microwave currents can be amplified by choosing the proper load and placing the device in a resonant circuit. It is worth noting that a similar scheme of optical generation, low-frequency quantum gain and microwave negative-resistance amplification, could be implemented using an IMPATT diode but the comparatively lower noise properties of the BARITT diode suggest that it may be the superior detector.

A first-order theoretical model for the punch-through phototransistor is presented in this chapter. The highly simplified model for the punch-through transistor discussed in Section 3.3 and a single collector-base region optical current generator are used to describe the structure, and the results for one specific structure are presented in detail.

A suggested name for the open-base, transit-time, punch-through phototransistor is the "photo-BARITT."

5.2 Optically Generated Currents and Transit-Time Effects

Carrier pair generation by optical absorption can be mathematically stated by the conservation of photons equation,

$$G_n = G_p = \alpha \phi_0 e^{-\alpha x} \frac{\text{carriers}}{\text{cm}^3\text{-s}},$$

where G_n and G_p are the electron and hole density generation rates, α is the optical absorption coefficient and ϕ_0 is the magnitude of the photon density incidence rate at $x = 0$. If the optical generation takes place in a depleted region where, for simplicity, the carriers are assumed to drift at their saturated velocity v_s , then the following first-order nonlinear ordinary differential equations can be derived for the phasor electron and hole concentrations*

$$\left(\frac{d}{dx} - j \frac{\omega}{v_s} \right) n = \frac{-\alpha \phi_0}{v_s} e^{-\alpha x} \quad (5.1)$$

and

$$\left(\frac{d}{dx} + j \frac{\omega}{v_s} \right) p = \frac{\alpha \phi_0}{v_s} e^{-\alpha x}, \quad (5.2)$$

where ω is the modulation angular frequency of the incident light. These equations differ only in the sign of the drift velocity, i.e., the direction of drift, so a solution for one can be derived from the solution for the other by a simple sign change of v_s . The solution for either Eq. 5.1 or 5.2 is obtained by variation of parameters and can be expressed as

* We assume carrier pair generation throughout the depleted region rather than simple edge generation as assumed by Gärtner.⁵⁶

$$m(x) = \left[m(0) \pm \frac{\alpha \phi_0}{v_s \left(\alpha \mp j \frac{\omega}{v_s} \right)} \right] e^{\mp j(\omega/v_s)x} \mp \frac{\alpha \phi_0}{v_s \left(\alpha \mp j \frac{\omega}{v_s} \right)} e^{-\alpha x}, \quad (5.3)$$

where m represents n or p and the upper sign is for the hole solution. The depletion layer is assumed to extend from $x = 0$ to $x = w_c$ so the boundary conditions for optically generated electrons and holes which determine the constant in Eq. 5.3 are

$$n(w_c) = 0$$

and

$$p(0) = 0.$$

The solutions for electron and hole concentrations can now be substituted into the expressions for electron and hole saturated drift currents and spatially averaged over the depleted region to determine the induced terminal currents due to optical generation. The results are:

$$J_{nv} = \frac{\alpha q \phi_0}{\alpha + j(\omega/v_s)} \left[S(\alpha) - e^{-\alpha w_c} \Gamma_s(\omega) \right] \quad (5.4)$$

and

$$J_{pv} = \frac{\alpha q \phi_0}{\alpha - j(\omega/v_s)} \left[\Gamma_s(\omega) - S(\alpha) \right], \quad (5.5)$$

where

$$S(\alpha) = \frac{1 - e^{-\alpha w_c}}{\alpha w_c}$$

and

$$\Gamma_s(\omega) = \frac{1 - e^{-j(\omega/v_s)w_c}}{j(\omega/v_s)w_c} .$$

The term $S(\alpha)$ is the low-frequency collection efficiency, $1 - e^{-\alpha w_c}$, normalized to the optical absorption length of the depletion region, αw_c , and the complex transit-time factor, $\Gamma_s(\omega)$, is the same factor used in the simplified analysis of the collector-base space-charge layer in a transistor, Eq. 3.37. Plots of the magnitude of the total optical terminal current density for diode area A,

$$I_v = (J_{nv} + J_{pv})A ,$$

normalized to the incident available photogeneration current, $q\phi_0 A$, for several values of depletion-layer width, 0.7 μm wavelength light and $\alpha = 2 \times 10^3 \text{ cm}^{-1}$ (Reference 57), are given in Fig. 5.1 as a function of the optical modulation frequency. The transit-time rolloff effects are clearly evident.

5.3 Punch-Through Phototransistors--Photo-BARITTs

If the optical generation depletion region of the last section is identified as the collector-base space-charge region of a punch-through transistor (PTT), then the resulting structure can be termed a punch-through phototransistor. For a first-order analysis, it is assumed that the optical generation is solely confined to this same depletion layer. The relative widths of the collector-base and emitter-base depletion layers in a normal PTT structure and the short mean time to recombination in the highly doped emitter and collector undepleted bulk regions justify this assumption. Thus, we combine an

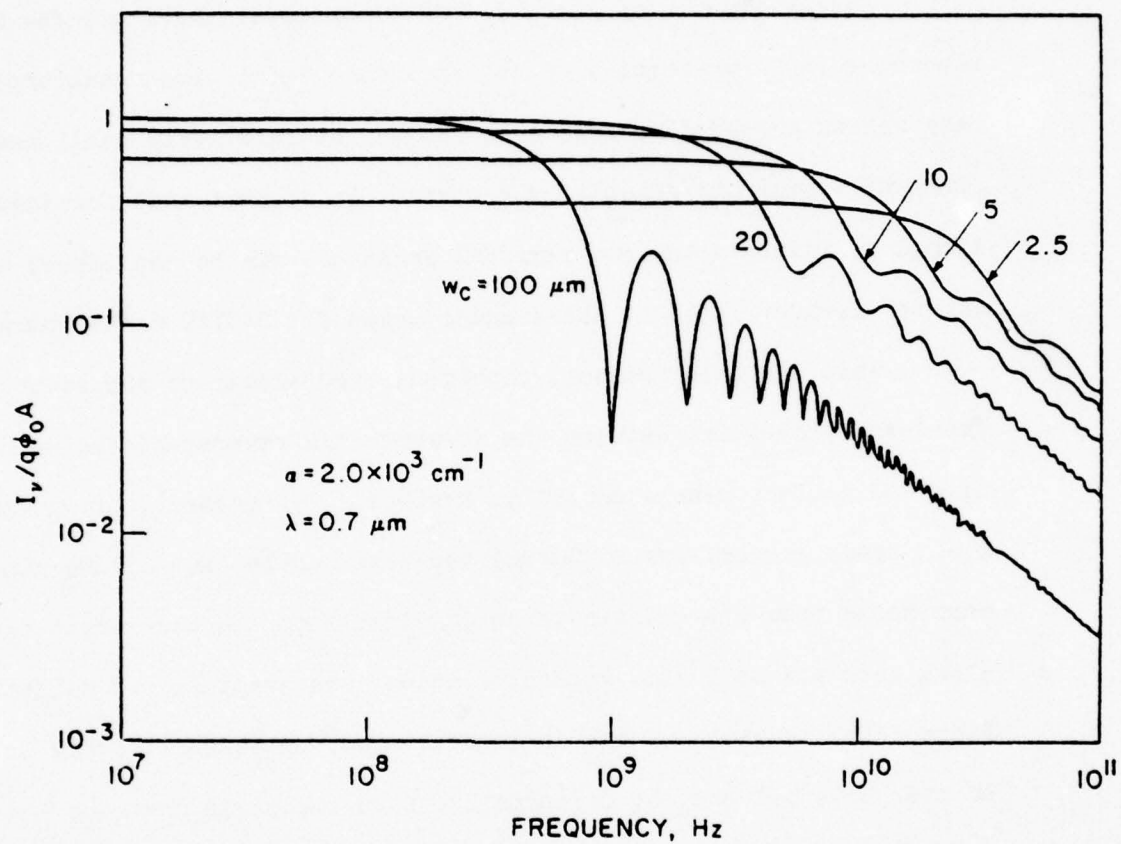


FIG. 5.1 DEPLETION-LAYER OPTICALLY GENERATED CURRENT AS A FUNCTION OF DEPLETION-LAYER WIDTH AND MODULATION FREQUENCY.

optical current generator and a PTT and arrive at the small-signal model shown in Fig. 5.2, where the symbols, except the optical current generator, all have the same meanings as introduced in Chapter III.

In the absence of light $J_v = 0$; therefore, there are few mobile electrons in a two-terminal p^+np^+ structure within the metallurgical base region except for those produced by the relatively small and constant leakage and generation process. It follows that for small-signal ac currents the two-terminal structure can be considered a single carrier device. This is the standard case for BARITT diode operation.

When light is present, photogenerated electrons are swept to the transition point between the forward- and reverse-biased emitter-base and collector-base depletion regions. The presence of electrons, i.e., space charge, lowers the emitter-base barrier and allows many more holes from the emitter to be injected into the base where they, along with the optically generated holes, are swept to the collector. Since δ is the ratio of the dc emitter electron current to the dc emitter hole current, it is normally quite small and thus the low-frequency quantum gain $(1 + \delta)/\delta$ is quite high. In the absence of an external base lead the only means available to increase δ is to increase the leakage or generation current or to optically dc bias the device with a constant light source.

The small-signal impedance Z_d of the punch-through photo-transistor for a one-dimensional two-terminal structure is identical with the small-signal impedance of the BARITT diode and can be derived using the fact that the total current through the device is independent of position and the fact that the conduction current within the collector-base depletion layer is a space-charge wave traveling at the saturated

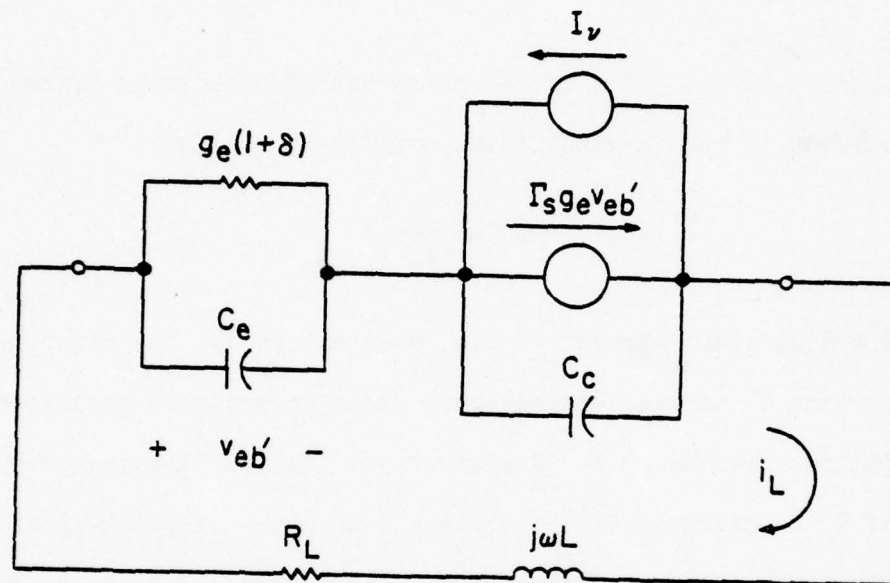


FIG. 5.2 SMALL-SIGNAL EQUIVALENT CIRCUIT FOR A PHOTO-BARITT INCLUDING A RESONANT LOAD.

drift velocity. The procedure parallels the derivation of the small-signal impedance of a Read-type IMPATT diode³⁹ and was given in detail in Chapter III. The resulting expression for Z_d is

$$Z_d = \frac{1}{g_e + j\omega C_e} + \frac{1 - M\Gamma_s(\omega)}{j\omega C_c}, \quad (5.6)$$

where M is the ratio of the hole conduction current to the total current in the forward-biased emitter-base diode:

$$M = \frac{g_e}{g_e + j\omega C_e}.$$

The equivalent circuit of Fig. 5.2, except for the light generation current I_v and the emitter-base diode conductance perturbation δ , follows from Eq. 5.6. A plot of the real (R) and imaginary (X) parts of Z_d is given in Fig. 5.3 for a 5- μ m wide collector-base depletion layer and bias conditions of $J_0 = 100$ A/cm² and $C_c/C_e = 0.05$. The device input resistance reaches its maximum negative value, -0.8×10^{-4} Ω -cm², at a frequency close to 17 GHz. Thus, to produce a reflection-type amplifier at this frequency, an inductive reactance of 5×10^{-3} Ω -cm² and a resistive load greater than 0.8×10^{-4} Ω -cm² are used as a series load for the phototransistor. The normalized magnitude of the load current i_L in Fig. 5.2, where

$$i_L = \frac{-[g_e(1 + \delta) + j\omega C_e] I_v}{\left\{ \delta g_e + [1 - \Gamma(\omega)]g_e - \omega^2 C_e C_c Z_L \right.} \quad (5.7)$$

$$\left. + j\omega\{C_e + [1 + g_e(1 + \delta)Z_L] C_c\} \right\}$$

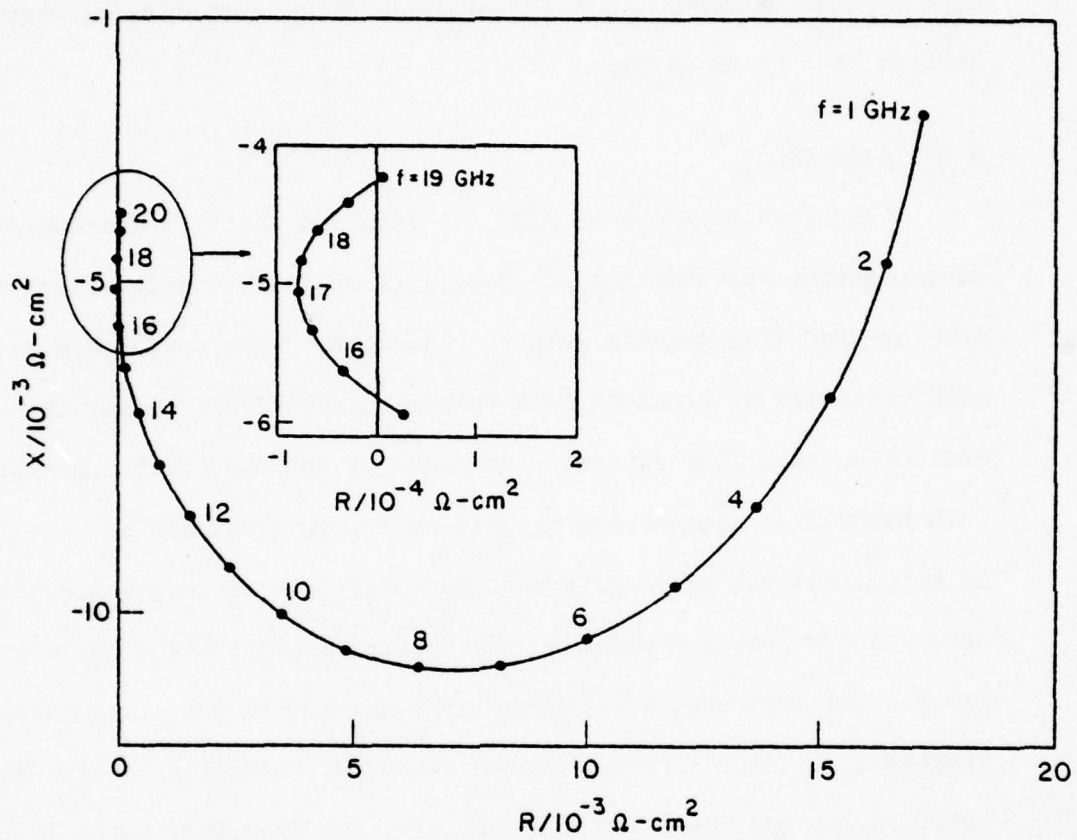


FIG. 5.3 SMALL-SIGNAL IMPEDANCE PLOT OF PUNCH-THROUGH TRANSISTOR STRUCTURE. ($J_0 = 100 \text{ A/cm}^2$, $\lambda = 0.7 \mu\text{m}$, $w_c = 5 \mu\text{m}$ AND $C_c/C_e = 0.05$)

for this particular diode, is plotted in Fig. 5.4 as a function of frequency with δ as a parameter. The insert in Fig. 5.4 shows an expanded scale for the negative-resistance region of the device and is a typical response curve for a singly tuned negative-resistance reflection-type amplifier.

5.4 Conclusions

The results shown in Fig. 5.4 indicate that the microwave gain of a negative-resistance photo-BARITT is relatively independent of the low-frequency quantum gain $(1 + \delta)/\delta$, but that comparable gain magnitudes can be attained by a proper choice of R_L . Since the reflection amplifier can be broadbanded by the use of filter-type loads, 3-dB bandwidths approaching or even exceeding 1 GHz can be envisioned. In actual devices the carriers do not drift at the scattering-limited saturation velocity throughout the entire collector-base depletion layer. The principal consequence of nonsaturated drift, as shown in Chapter III, is an increase in the effective electrical length of the drift region and therefore a lowering of the frequency range of the device small-signal negative resistance. This in no way alters the concept of negative-resistance amplification of optically generated signals but merely frequency translates its application.

In summary, a punch-through phototransistor structure has been proposed as a high-speed quantum-gain optical detector. Simple expressions have been derived which predict small-signal operation and specifically show negative-resistance, reflection-type amplification ability near the transit-time frequency.

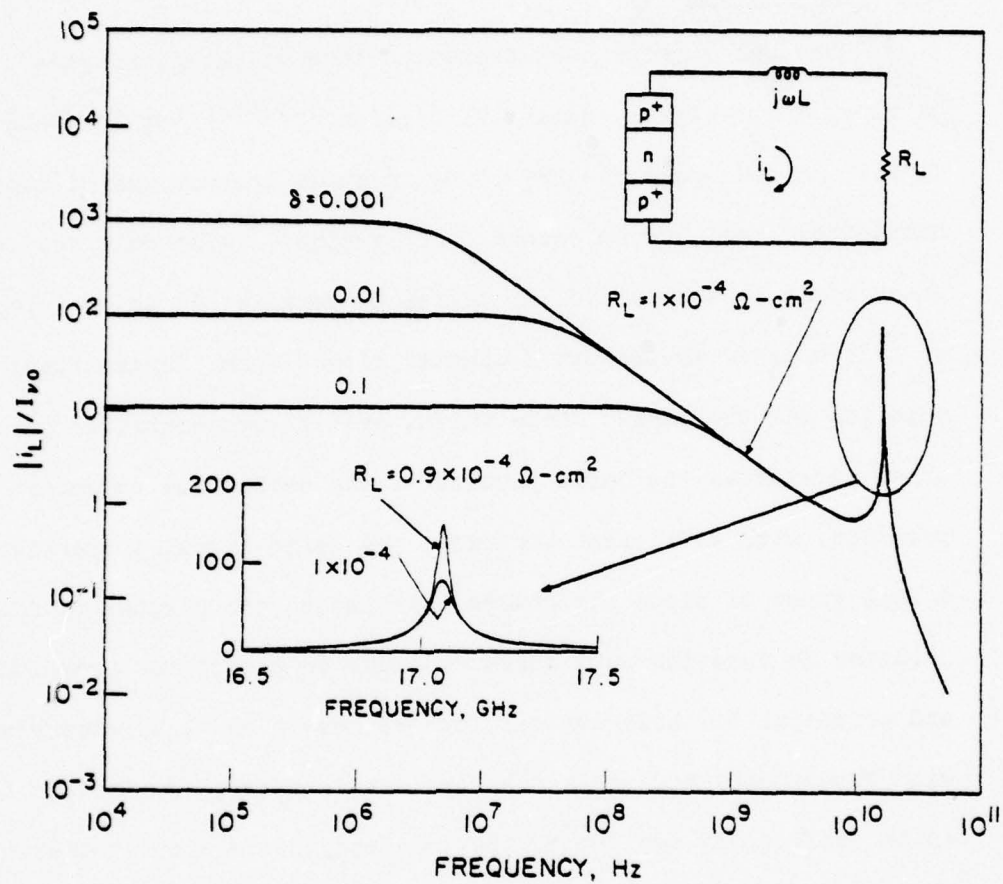


FIG. 5.4 MAGNITUDE OF DETECTED OPTICAL CURRENT AS A FUNCTION OF MODULATION FREQUENCY AND δ . ($J_0 = 100 \text{ A/cm}^2$, $\lambda = 0.7 \mu\text{m}$, $w_c = 5 \mu\text{m}$ AND $C_c/C_e = 0.05$)

CHAPTER VI. LARGE-SIGNAL ANALYSIS OF BARITT DIODES

6.1 Introduction

Several authors have presented sophisticated, single-carrier, large-signal, numerical studies^{1,23,58,59} of the BARITT diode. In each case the resulting computer program was of such complexity that, due to economic constraints, relatively few structures could be studied to any degree of detail. It is the purpose of this chapter to present a simple, closed-form, large-signal solution for the BARITT diode which, even though contrived in a sense, preserves the basic physics of the device and economically predicts, with sufficient accuracy, the large-signal properties of a full range of diode structures. It is not the purpose of this solution to function as a means to study in detail the properties and potential of these devices, but rather to show, by comparison with experiments and other theories, that it is of sufficient detail to be confidently applied to the frequency conversion studies of Chapter VII. The large-signal solution can be expressed in an equivalent circuit model form which follows from the small-signal investigations of Chapter III and in essence, with one very important exception, is a BARITT diode version of the large-signal IMPATT diode model presented by Mouthaan.⁶⁰

Single-frequency operation is first discussed. The model results are compared with experiment and another more complex theory, and the large-signal resistance and power capabilities of the maximum dc power structures of Table 3.1 are presented. A multifrequency study follows. A further justification of the method used in the

derivation of the single-frequency model is presented using a more correct two-frequency representation, and the possibility of second-harmonic power extraction is considered.

6.2 Single-Frequency Large-Signal Model

6.2.1 Theory. It was shown in the dc study of Chapter II and in the derivation of the small-signal BARITT diode model of Chapter III that for moderate levels of dc current density the injection of minority carriers and minority-carrier current into the base region of the punch-through diode is almost purely exponential in nature and depends only upon the value of the potential barrier presented to the emitting contact. That is, c.f., Eq. 2.23,

$$J(0) \propto \exp(V_F/V_T) ,$$

where $x = 0$ is the transition point between the reverse- and forward-biased regions of the diode and V_F is the applied portion of the total voltage across the forward-biased portion of the diode. If V_F is periodic with a fundamental angular frequency ω , then the current density $J(0)$ is also and can be expressed in the form of a complex Fourier series as*

$$J(0) = J_0 + \sum_{m=-\infty}^{\infty} \frac{\hat{J}_m}{2} e^{jm\omega t} \quad m \neq 0 , \quad (6.1)$$

where $\hat{J}_m = \hat{J}_{-m}^*$, as $J(0)$ must be a real quantity. Since the m th component of $J(0)$ is $2 \operatorname{Re} [(\hat{J}_m/2)e^{jm\omega t}]$, the quantity \hat{J}_m is the phasor representation of $J_m(0)$.

* In this chapter all complex quantities, except impedance and admittance terms, are denoted by " $\hat{}$ "; all terms without " $\hat{}$ " are real.

It is obvious that if the voltage across the forward-biased region of the diode varies in the large-signal sense then the extent of the forward-biased region itself must also vary in a large-signal manner. This behavior is borne out by the numerical studies of Kwok^{1,23} and Karasek.⁵⁸ The position of the injection point $x = 0$ is thus modulated by the driving voltage across the forward-biased region. This variation with drive is ignored entirely in the derivation of the analytic large-signal model of this chapter. To account for it would deprive the model of its simplicity, particularly in the representation of the forward-biased region, and to estimate it would require a detailed knowledge of space-charge layer behavior under forward bias. This problem did not arise in the small-signal study since the variation is a second-order correction and is lost in the linearization of the small-signal equations. However, under large-signal drive the variation results in yet another nonlinearity if the strict separation between the two regions is maintained. The approach taken here is to simply ignore the problem and await the results for justification.

For the purposes of this study an "average" forward-biased region width is defined as the distance given by the depletion approximation. That is,

$$w_e = \sqrt{\epsilon V_{Fto} / 2qN_d} ,$$

where V_{Fto} is the total dc voltage across the forward-biased region (V_{Fto} can be solved for once the level of RF drive and dc current density have been determined). With the width of the forward-biased region taken as a constant with respect to time, a forward-biased region space-charge capacitance C_F can be defined as was done in the small-signal model and the impedance of the forward-biased region at

$m\omega$ can be expressed as

$$Z_{Fm} = [(\hat{J}_m / \hat{V}_{Fm}) + j m \omega C_F]^{-1}, \quad (6.2)$$

where \hat{V}_{Fm} is the phasor voltage across the region at $m\omega$.

The reverse-biased region of the diode, as in the small-signal model, is divided into subregions. However, the number of subregions is restricted to two and the corresponding methods of current transport in each are assumed to be the limiting cases of pure diffusion (no drift) and saturated drift (little diffusion), respectively. These two limiting cases of current transport and their assignment to two separate regions represent the contrived nature of the model. Since in reality there is a continuous transition from the first method of current transport to the second in an actual diode drift-diffusion region, any absolute splitting of the regions of their occurrence must be construed as artificial. Nevertheless computational experience has yielded a suitable compromise for such a division of the reverse-biased region. To obtain the necessary phase retardation attributable to a region of pure diffusion, its length has been chosen to be equal to one third of the low-field region, i.e., the region in which the dc electric field is less than the saturation value E_s . To discount the resulting overestimate of diffusion attenuation, the real part of the diffusion region propagation coefficient has also been reduced by a factor of three. The criterion used to select these reduction factors was the closeness of match between the impedance-frequency results of the previously presented small-signal model and the present large-signal model when the large-signal equations were evaluated with small-signal drive. The method of analysis for the reverse-biased region follows closely that of the small-signal

model so in lieu of a detailed presentation the necessary equations are given in Table 6.1. Familiarity with the small-signal model will facilitate the translation of these equations to the complete single-frequency large-signal models shown in Fig. 6.1.

The Fourier coefficients of the injected minority-carrier current $J(0)$ are now developed. Since V_F is also periodic we have

$$V_F = V_{F0} + \sum_{m=-\infty}^{\infty} \frac{\hat{V}_{Fm}}{2} e^{jm\omega t}, \quad m \neq 0 \quad (6.3)$$

and by definition we have

$$\hat{J}_m = \frac{J_s}{2\pi} \int_0^{2\pi} e^{V_F/V_T} e^{-jm\omega t} d(\omega t) \quad (6.4)$$

Normally, in the large-signal analysis of diode structures, the magnitude of the RF voltage across the entire diode is specified (voltage drive). Here we follow Moutaen's method⁶⁰ and specify only the voltage across the injection region. We then solve for the voltage across the entire diode. In principle the two methods can be identical. Practically, however, at least for the frequency domain analysis presented here, there is an enormous difference between the two. We specify only a limited number of values for the harmonic content of V_F and assume the remaining values to be negligible. Obviously this is another simplifying assumption and it deserves some comment.

The BARITT diode is an inherently high Q structure. That is, it appears more reactive than resistive at frequencies within and beyond the negative-resistance region. This is evidenced by the negative-resistance region small-signal Q 's of the first four dc maximum power structures of Table 3.1 which are shown as a function of frequency in Fig. 6.2. In no case does the magnitude of the

Table 6.1

Large-Signal Equations for Uniformly
Doped BARITT Diode Diffusion-Drift Region

Region Definitions

Forward Biased $-w_e \leq x \leq 0$

Diffusion $0 \leq x \leq w_D$, $w_D = w_s/3$

$$w_s = \{\epsilon E_s / q[N_D + (KJ_o / 2qv_s)]\}$$

$$K = 1.15 \times 10^{10} / (N_d)^{0.57} \quad (\text{see Fig. 2.2})$$

Saturated Drift $w_D \leq x \leq w_c$

Impedance of Diffusion Region, Z_D

$$\hat{J}_p(x) = \hat{J}_p(0)e^{-\hat{\gamma}_D x}$$

$\hat{J}_p \rightarrow$ particle current phasor

$$\hat{\gamma}_D = \left(\frac{1}{3} + j\right) \sqrt{\omega / 2D_o}$$

$$D_o = \frac{V_T v_s}{E_s}$$

$$\hat{\Gamma}_D = \frac{1}{w_D} \int_0^{w_D} e^{-\hat{\gamma}_D x} dx$$

$$C_D = \epsilon / w_D$$

$$\hat{M}_F = \frac{G_{F1}}{G_{F1} + j\omega C_F}$$

$$Z_D = \frac{1 - \hat{M}_F \hat{\Gamma}_D}{j\omega C_D}$$

(cont.)

Table 6.1 (cont.)

Impedance of Saturated Drift Region, Z_s

$$\hat{J}_p(x) = \hat{J}_p(w_D) e^{-\hat{\gamma}_s(x - w_D)}$$

$$\hat{\gamma}_s = \frac{v_s - (v_s^2 + j\omega D_s)^{1/2}}{2D_s}$$

$$D_s = D_o/2$$

$$\hat{\Gamma}_s = \frac{1}{w_c - w_D} \int_0^{w_c - w_D} e^{-\hat{\gamma}_s(x - w_D)} dx$$

$$C_s = \epsilon / (w_c - w_D)$$

$$\hat{M}_D = \hat{M}_F e^{-\hat{\gamma}_D w_D}$$

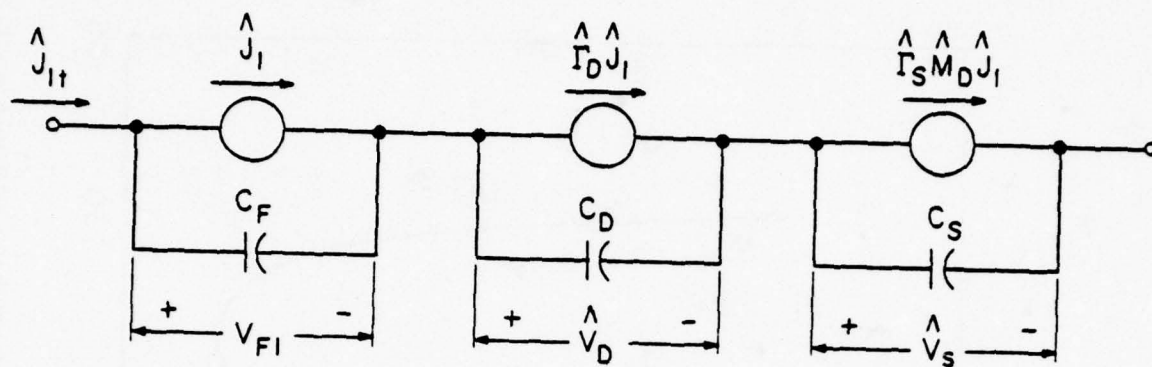
$$Z_s = \frac{1 - \hat{M}_D \hat{\Gamma}_s}{j\omega C_s}$$

Total Impedance of Reverse-Biased Region, Z_B

$$C_B = \frac{C_D C_s}{C_D + C_s}$$

$$\hat{\Gamma}_B = C_B \left(\frac{\hat{\Gamma}_D}{C_D} + \frac{\hat{M}_D \hat{\Gamma}_s}{C_s} \right)$$

$$Z_B = Z_D + Z_s = \frac{1 - \hat{M}_F \hat{\Gamma}_B}{j\omega C_B}$$



OR

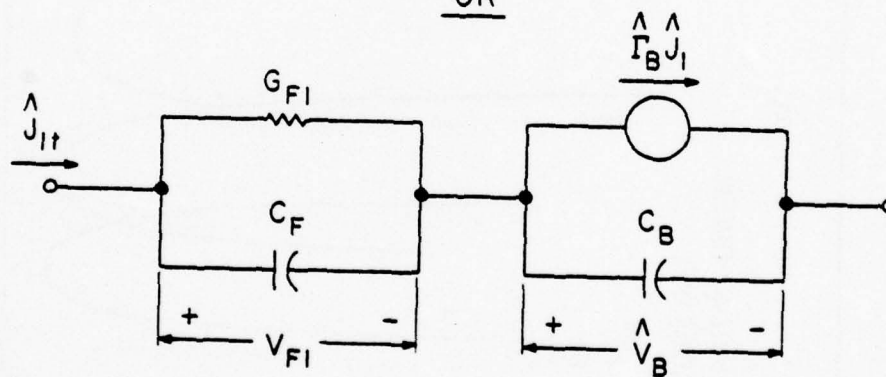


FIG. 6.1 LARGE-SIGNAL SINGLE-FREQUENCY MODELS FOR UNIFORMLY DOPED BARITT DIODES.

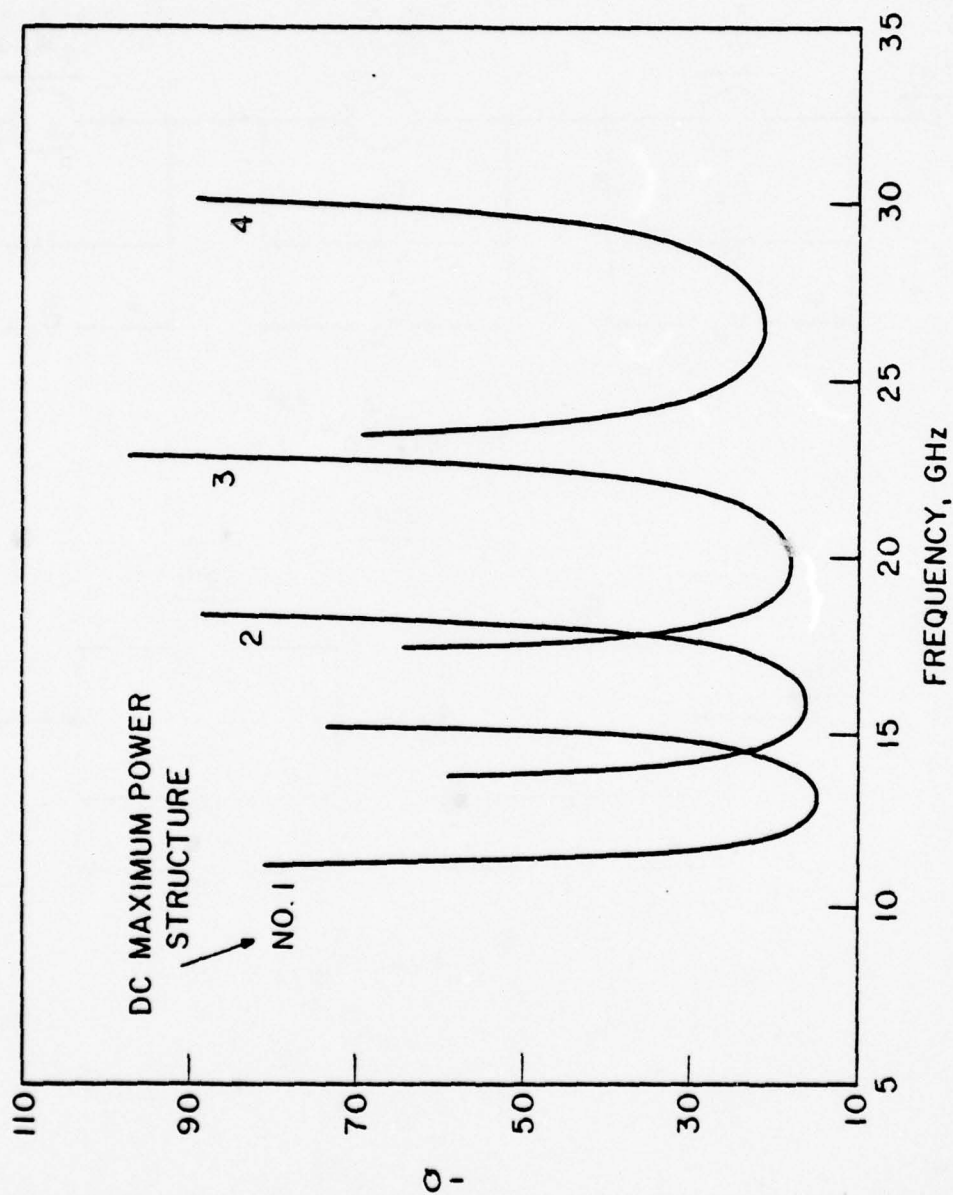


FIG. 6.2 SMALL-SIGNAL NEGATIVE-RESISTANCE REGION Q'S FOR THE FIRST FOUR DC MAXIMUM POWER STRUCTURES OF TABLE 3.1.

small-signal Q fall below a value of ten. Since the magnitudes of the values of large-signal Q 's exceed their small-signal counterparts it is clear that, for all levels of drive, the diode is predominantly an energy storage device. As shown experimentally by Snapp and Weissglas;¹⁰ theoretically by the reactance values which lead to Fig. 6.2; and intuitively by consideration of the parallel-plate nature of the depleted sandwich-like structure of the BARITT diode, the principle energy storage medium of the device is the parallel-plate "cold" capacitance of the depleted base region. That being the case, at any frequency within or above the region of negative resistance it must be true that

$$\frac{\hat{V}_F}{\hat{V}_{RF}} = \frac{C_d}{C_F}, \quad (6.5)$$

where C_d is the total diode "cold" capacitance and \hat{V}_{RF} is the voltage across the entire diode. The restriction of Eq. 6.5 obviously neglects all space-charge effects and its approximate nature will remain in effect as long as there is any particle current flow whatever. We will return to the consequences of this fact in Section 6.2.1 when the existence of a second-harmonic component in V_F is considered with the help of a two-frequency model. Accepting Eq. 6.5 for now and assuming circuit constraints limit the RF voltage across the entire diode to a single RF component, that of the fundamental, we can to the first order neglect the harmonic content of the voltage across the forward-biased region; that is,

$$V_F = V_{F0} + \text{Re} \left(\hat{V}_{F1} e^{j\omega t} \right). \quad (6.6)$$

If the phase of \hat{V}_{F1} is chosen as the phasor reference, then it can be

shown by using Eq. 6.4 that the phasor terms \hat{J}_m are all real and are given by⁶⁰

$$\hat{J}_m = J_m = \frac{2I_m \left(\frac{V_{F1}}{V_T} \right)}{I_0 \left(\frac{V_{F1}}{V_T} \right)} J_0, \quad (6.7)$$

where I_m is the modified Bessel Function of the first kind of order m and J_0 is the dc current density. A graph of the saturation characteristics of J_1/J_0 vs. V_{F1}/V_T is given in Fig. 6.3. The approximation of Eq. 6.7 will be used in all the single-frequency studies of this work.

6.2.2 Single-Frequency Results. X-band p^+np^+ Si devices measured by Kwok,¹ Nguyen-Ba,² and Kwok et al.⁶¹ ($1.7 \times 10^{15} \text{ cm}^{-3} \leq N_d \leq 2.5 \times 10^{15} \text{ cm}^{-3}$, $5.0 \text{ } \mu\text{m} \leq \text{Base width} \leq 6.2 \text{ } \mu\text{m}$, junction area = $2 \times 10^{-4} \text{ cm}^2$, $I_{\text{bias}} \leq 40 \text{ mA}$) produced a maximum power of approximately 25 mW and a maximum efficiency of approximately 1.7 percent in a waveguide mount at frequencies near 9.5 GHz. The single-frequency theoretical results for a similar device at a bias current of 40 mA are shown in Fig. 6.4. The performance agreement between theory and experiment is quite satisfactory but the model predicts a slightly higher optimum frequency of operation. Two factors are possible contributors to this discrepancy: (1) the waveguide cavity used in the experiment was designed for operation below 10 GHz and (2) the model does not account for self-heating effects. Overall, the model is thought to produce a useful description of RF performance.

Comparison of the theoretical predictions and measured results of Snapp and Weissglas's¹⁰ diode B are given in Figs. 6.5 and 6.6. The large-signal rectification and conductance-compression effects

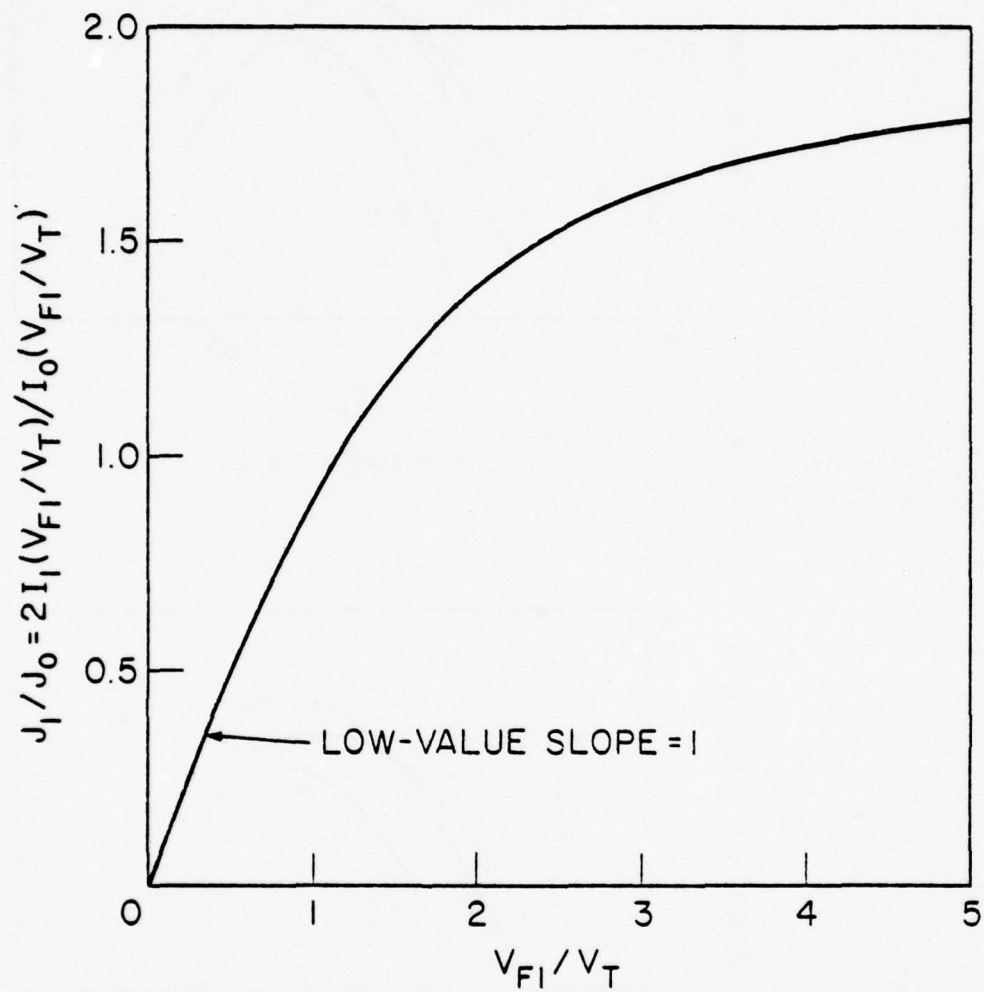
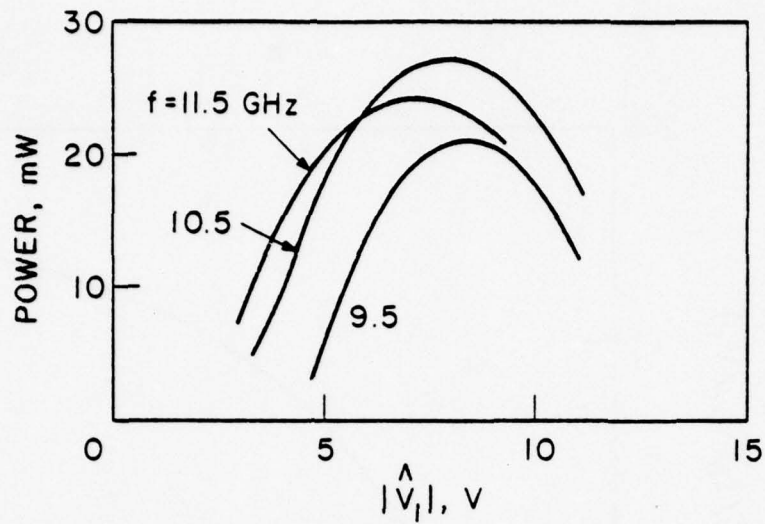
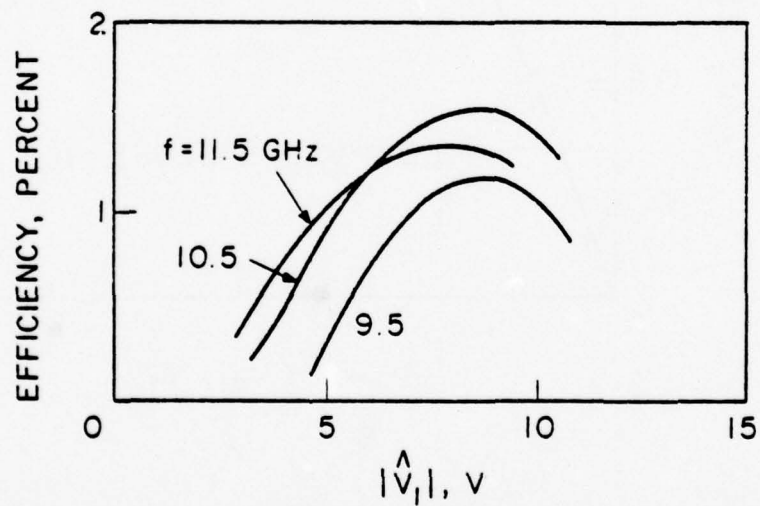


FIG. 6.3 SATURATION CHARACTERISTIC OF THE SINGLE-FREQUENCY LARGE-SIGNAL INJECTED PARTICLE CURRENT.



(a) POWER vs. $|\hat{V}_1|$



(b) EFFICIENCY vs. $|\hat{V}_1|$

FIG. 6.4 LARGE-SIGNAL POWER AND EFFICIENCY AS A FUNCTION OF DRIVE AND FREQUENCY FOR THE EXPERIMENTAL DEVICE OF KWOK,¹ NGUYEN-BA² AND KWOK ET AL.⁶¹

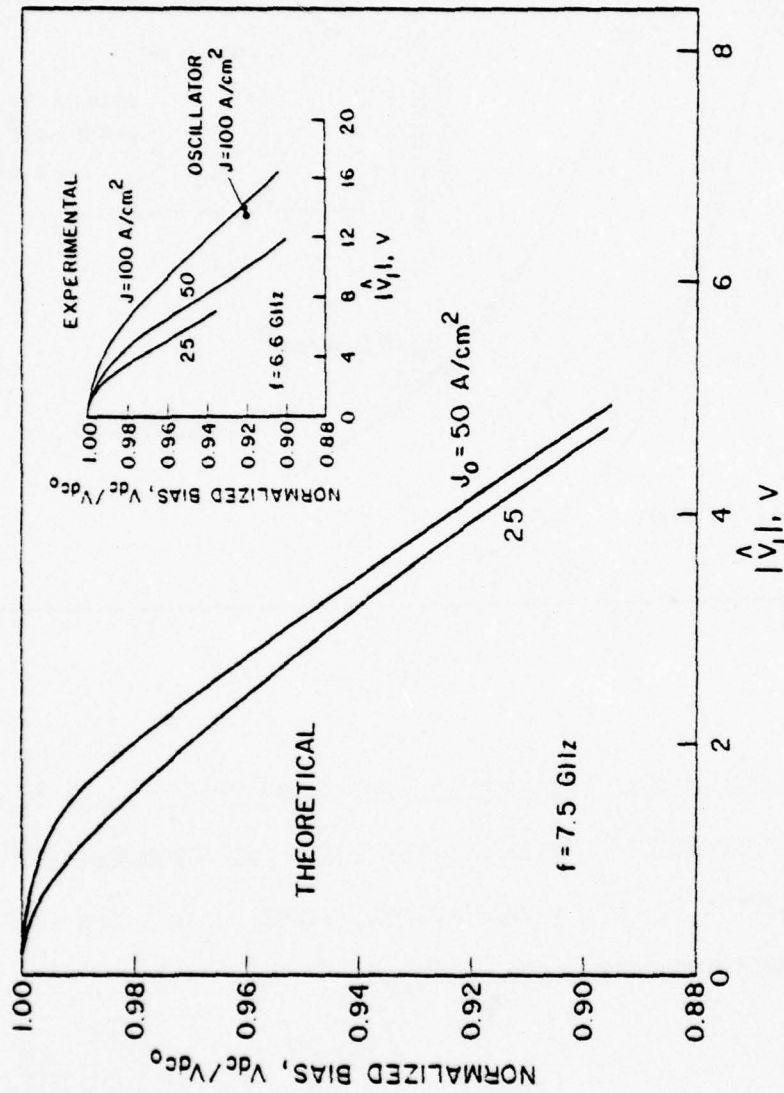


FIG. 6.5 LARGE-SIGNAL THEORETICAL AND EXPERIMENTAL VALUES FOR THE RECTIFICATION EFFECT FOR

SNAPP AND WEISSGLAS'S¹⁰ DIODE B. ($N_d = 1.2 \times 10^{15} \text{ cm}^{-3}$ AND BASE WIDTH = $7.9 \text{ } \mu\text{m}$)

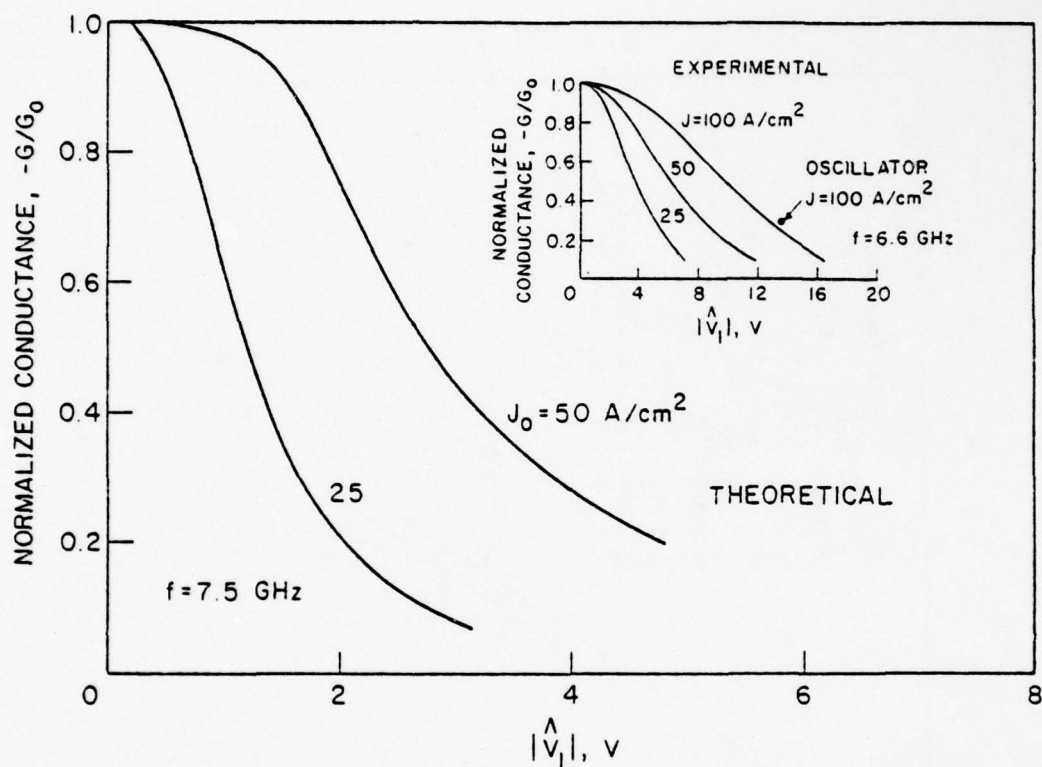


FIG. 6.6 LARGE-SIGNAL THEORETICAL AND EXPERIMENTAL VALUES FOR CONDUCTANCE COMPRESSION FOR SNAPP AND WEISSGLAS'S¹⁰ DEVICE B. (G_0 = SMALL-SIGNAL VALUE, $N_d = 1.2 \times 10^{15}$ cm⁻³ AND BASE WIDTH = 7.9 μ m)

are plotted as functions of RF drive and dc current density. Again, closest agreement between theory and experiment was found when theoretical results at a higher frequency (7.5 GHz theory, 6.6 GHz experiment) were compared with the published experimental data. A further point of divergence is the difference in the slopes between the theoretical and experimental curves (theoretical slope \approx twice the experimental slope) indicating that even though space-charge effects are partially accounted for within the model, the degree to which they are is evidently insufficient. However, qualitatively at least, the agreement remains more than satisfactory.

The final comparison to be presented is between the numerical-theoretical study of Kwok and Haddad^{1,23} and the present theory. Shown in Figs. 6.7 and 6.8 are two different sets of large-signal theoretical predictions for power density and efficiency for dc maximum power structure No. 1 as a function of drive and dc current density at a frequency of 10.5 GHz. The simple model predicts its maximum output power and efficiency at drive levels somewhat lower than those of the numerical study and this is consistent with the experimental results of Snapp and Weissglas. Also, the levels of output power and efficiency predicted by the simple model exceed those of Kwok, although not excessively. Overall, the agreement is more than adequate when consideration is given to the level of complexity inherent in each of the models.

For completeness, a compendium of theoretical results for the seven dc maximum power structures of Table 3.1 is given in Fig. 6.9. Plotted are the optimized maximum point values of device large-signal negative resistance and RF power density, maximized with

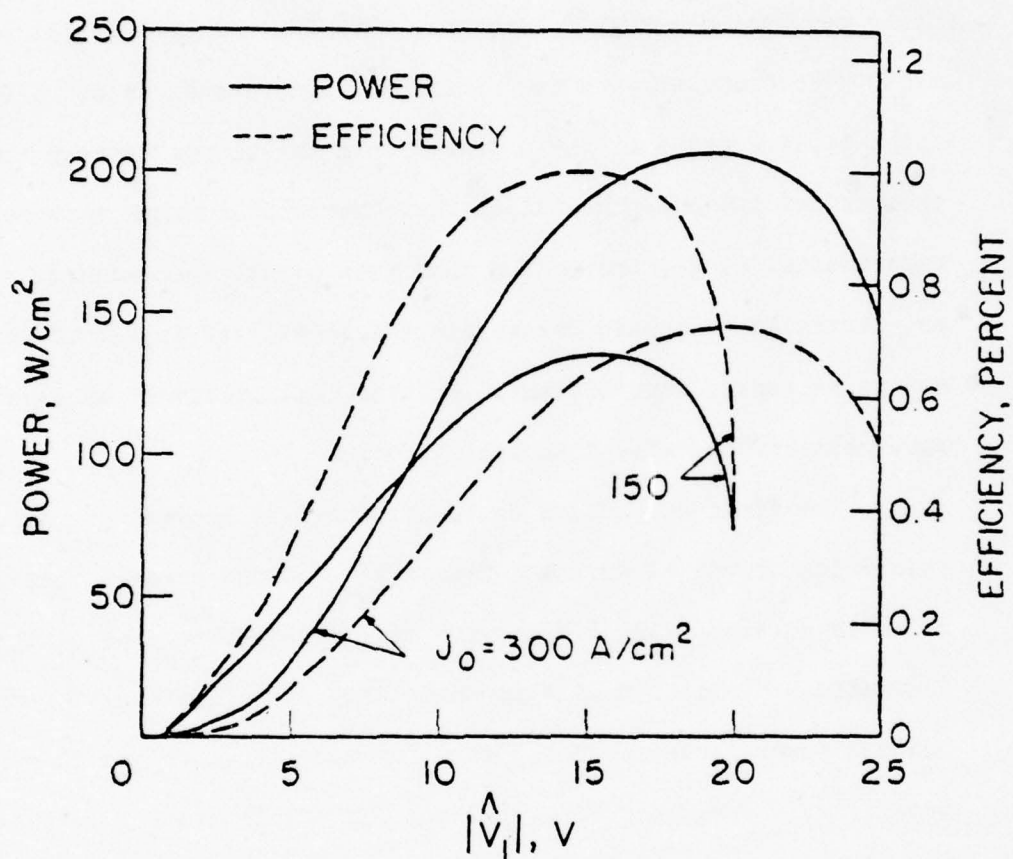


FIG. 6.7 THEORETICAL POWER OUTPUT AND EFFICIENCY VS. RF VOLTAGE AMPLITUDE FOR DC MAXIMUM POWER STRUCTURE NO. 1 AT 10.5 GHz. (KWOK AND HADDAD^{1,23})

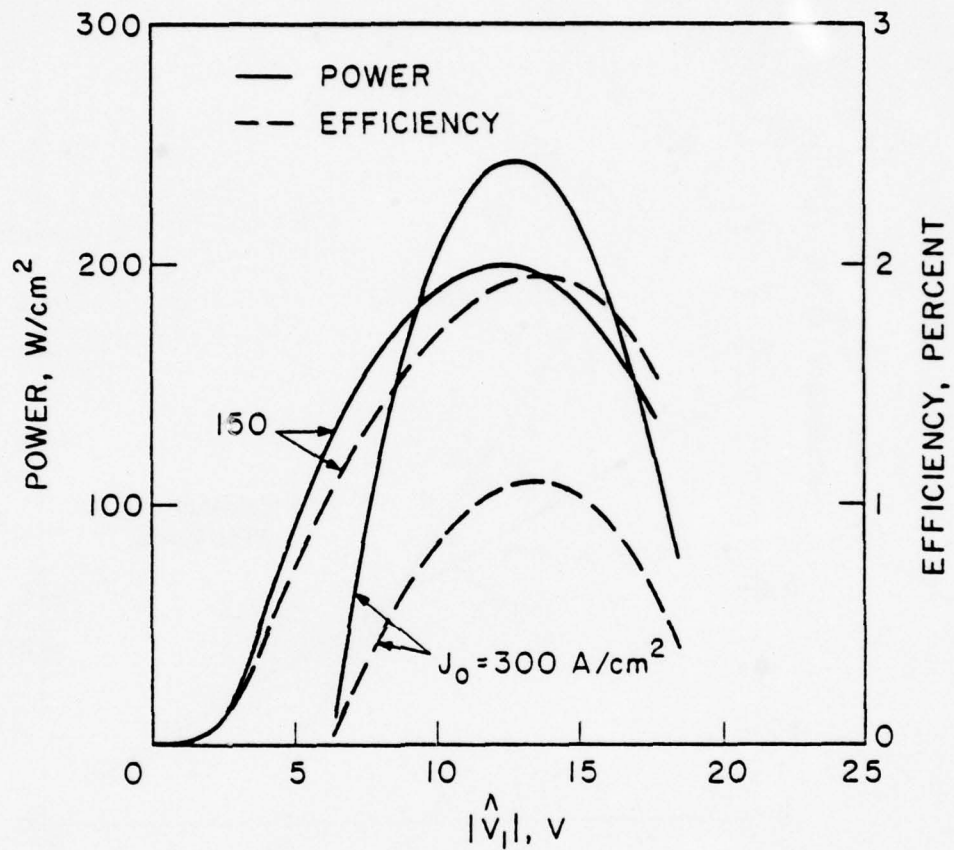


FIG. 6.8 SIMPLE-MODEL SINGLE-FREQUENCY LARGE-SIGNAL RESULTS
FOR DC MAXIMUM POWER STRUCTURE NO. 1 AT 10.5 GHz.

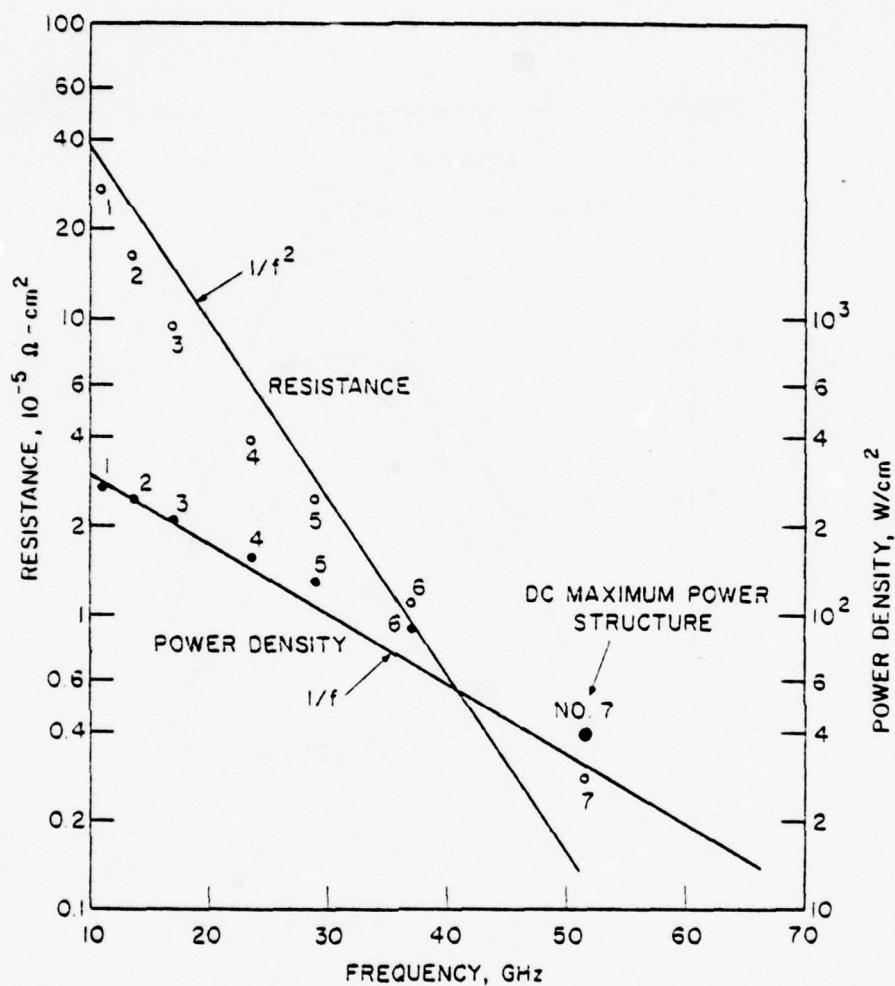


FIG. 6.9 OPTIMUM LARGE-SIGNAL VALUES FOR THE OUTPUT POWER DENSITY AND RESISTANCE OF THE DC MAXIMUM POWER STRUCTURES.

respect to frequency and drive. In general, the maximum power frequency for each device is approximately 90 percent of the frequency of maximum small-signal negative resistance, and the RF drive at maximum output power is approximately 15 percent of the dc bias voltage. Also depicted in Fig. 6.9 are $1/f$ and $1/f^2$ trajectories for normalized power and large-signal negative resistance. The inadequacy of the constant efficiency vs. frequency assumption (Chapter I) is obvious. A constant Pf^3 product is perhaps a better characterization.

The results shown in Fig. 6.9 foretell the difficulty of obtaining millimeter-wave RF power from the uniformly doped BARITT diode structure in the fundamental mode of operation. Normal fabrication procedures require that approximately 10 μm of heavily doped substrate be retained as either the emitter or collector bulk region to aid in device handling. For commercial p^+ Si substrates ($10^{-3} \Omega\text{-cm} \leq \text{resistivity} \leq 10^{-2} \Omega\text{-cm}$), this represents 10^{-6} to $10^{-5} \Omega\text{-cm}^2$ of series resistance that must be overcome before RF power can emanate from the complete diode structure, irrespective of circuit losses. Thus, a gray area of doubtful capability exists for p^+np^+ Si diodes beginning near 40 GHz. To surmount this difficulty, new fabrication procedures will have to be devised which eliminate the need for substrate foundations; new double-layer doping profiles^{2,62} will have to be developed which generate higher values of negative resistance or power will have to be harmonically extracted by circuit techniques. This last proposal is the subject of the remainder of this chapter.

6.3 Multifrequency Harmonic Large-Signal Operation of BARITT Diodes

6.3.1 Theory. If the voltage across the entire diode is not restricted to values of a single frequency but rather is allowed to contain harmonic values as well, then the possibility of harmonic power extraction exists. This phenomenon has been studied by several authors^{60,63-67} for the IMPATT diode, primarily as a means to improve fundamental output power through reactive harmonic terminations. This study, however, is intended more for the inverse case; that is, improved harmonic power output by reactively tuning the fundamental. For simplicity, only two-frequency operation is considered but the extension to more complicated cases should be obvious.

Allowing the voltage across the forward-biased region of the diode to contain two frequency components, in phasor space

$$\hat{V}_{F1} = V_{F1}$$

and

$$\hat{V}_{F2} = V_{F2} e^{j\psi},$$

we calculate the new fundamental and second-harmonic phasor components of $J(0)$, using Eq. 6.4, and obtain

$$\hat{J}_m = J_0 \frac{C_m + jS_m}{D_0}, \quad (6.8)$$

where $m = 1$ or 2 , J_0 is the dc current density,

$$J_0 = J_s e^{V_{F0}/V_T} D_0,$$

$$C_m = 2I_0 \left(\frac{V_{F2}}{V_T} \right) I_m \left(\frac{V_{F1}}{V_T} \right) + 2 \sum_{n=1}^{\infty} \left[I_{2n-m} \left(\frac{V_{F1}}{V_T} \right) + I_{2n+m} \left(\frac{V_{F1}}{V_T} \right) \right] I_n \left(\frac{V_{F2}}{V_T} \right) \cos n\psi,$$

$$S_m = 2 \sum_{n=1}^{\infty} \left[I_{2n-m} \left(\frac{V_{F1}}{V_T} \right) - I_{2n+m} \left(\frac{V_{F1}}{V_T} \right) \right] I_n \left(\frac{V_{F2}}{V_T} \right) \sin n\psi$$

and

$$D_o = I_o \left(\frac{V_{F1}}{V_T} \right) I_o \left(\frac{V_{F2}}{V_T} \right) + 2 \sum_{n=1}^{\infty} I_{2n} \left(\frac{V_{F1}}{V_T} \right) I_n \left(\frac{V_{F2}}{V_T} \right) \cos n\psi .$$

If we artificially split \hat{J}_1 and \hat{J}_2 into independent single-frequency terms and transadmittance cross-frequency terms, similar to the two-frequency circuit work of Brackett;^{65,67} that is,

$$\begin{aligned} y_{21} V_{F1} &\equiv \hat{J}_2 - \frac{2I_1 \left(\frac{V_{F2}}{V_T} \right) e^{j\psi}}{I_o \left(\frac{V_{F2}}{V_T} \right)} J_o \\ &\equiv \hat{J}_2 - G_{F2} V_{F2} e^{j\psi} \end{aligned}$$

and

$$\begin{aligned} y_{12} V_{F2} e^{j\psi} &\equiv \hat{J}_1 - \frac{2I_1 \left(\frac{V_{F1}}{V_T} \right)}{I_o \left(\frac{V_{F1}}{V_T} \right)} J_o \\ &\equiv \hat{J}_1 - G_{F1} V_{F1} , \end{aligned}$$

then the two-frequency large-signal equivalent circuit of Fig. 6.10 results. The transadmittance terms y_{12} and y_{21} are nonlinear functions of ω , V_{F1} , V_{F2} , ψ and the dc bias, while the independent in-phase conductance terms G_{F1} and G_{F2} are functions only of the drive level at their respective frequencies and the dc bias.

6.3.2 Two-Frequency Results. For exact results the two circuits of Fig. 6.10 must be solved simultaneously in conjunction with the external circuit loads since the two are coupled through the

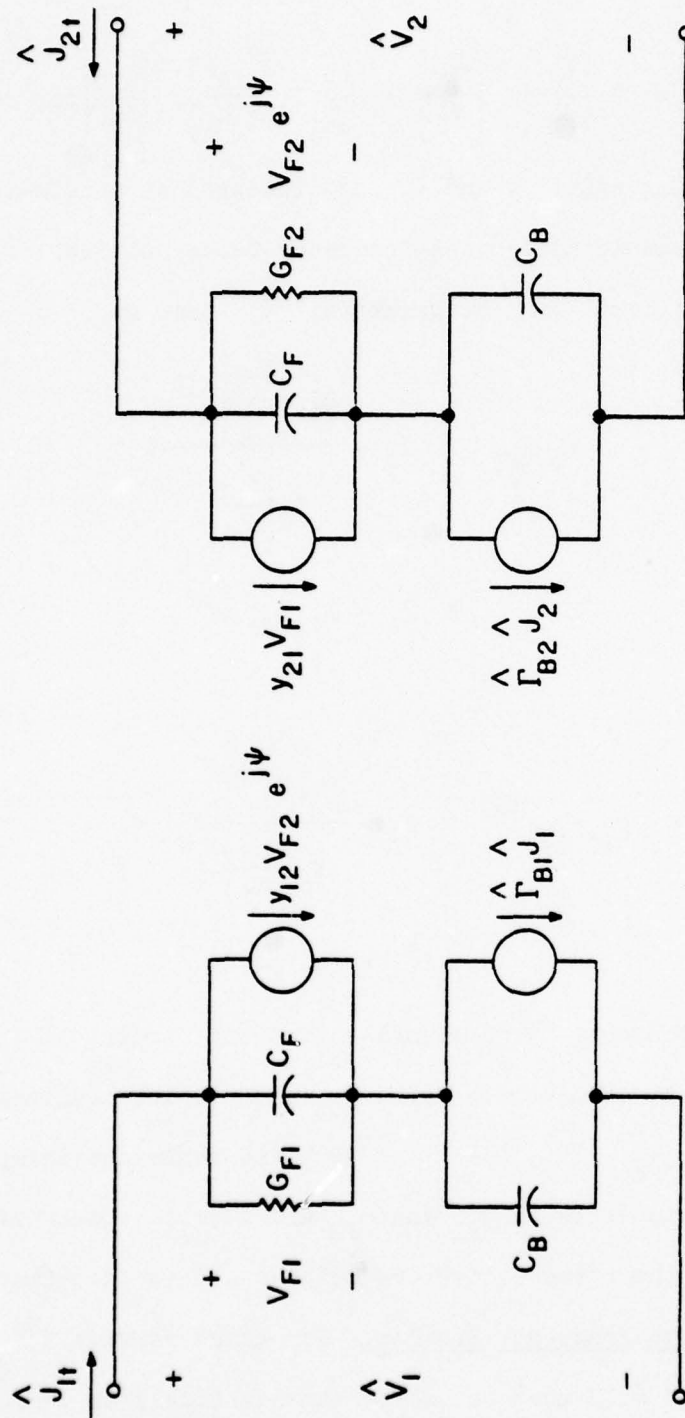


FIG. 6.10 TWO-FREQUENCY HARMONIC LARGE-SIGNAL EQUIVALENT CIRCUIT FOR THE BARRITT DIODE.

transadmittance terms. Such a procedure would prove very difficult as the active circuit elements are nonlinear functions of the forward-biased region driving voltages, and a complete solution would require a multivariable trial-and-error-type solution format. As an alternative, we choose to simply specify the two-drive components and their relative phase difference and to inspect the final results for evidence of physical realizability, i.e., for self-sustaining oscillations with passive loads the real parts of the total diode impedances at the fundamental and second harmonic must both be nonpositive.

The simplification invoked in Section 6.1 for a diode environment consisting of a singly resonant circuit; namely, the restriction of the time-varying portion of V_F to a single-frequency component, can now be re-examined in the light of the more exact two-frequency equivalent circuit of Fig. 6.10. The simplification can be thought of as a failure to include the effects of the $y_{12} V_{F2} e^{j\psi}$ current contribution to the particle current within the forward-biased region at the fundamental when the diode terminals are shorted at the second harmonic. The following specific case is examined. Figures 6.11 and 6.12 show impedance plane plots of

$$Z_2 = \frac{\hat{V}_2}{\hat{J}_{2t}}$$

for dc maximum power structure No. 3 at $V_{F1} = 0.4$ V and $f = 20$ GHz as a function of V_{F2} and ψ . As can be seen near the excitation point of $V_{F2} \approx 0.095$ V and $\psi \approx 320$ degrees, the second-harmonic impedance trajectory changes very rapidly and passes very close to the

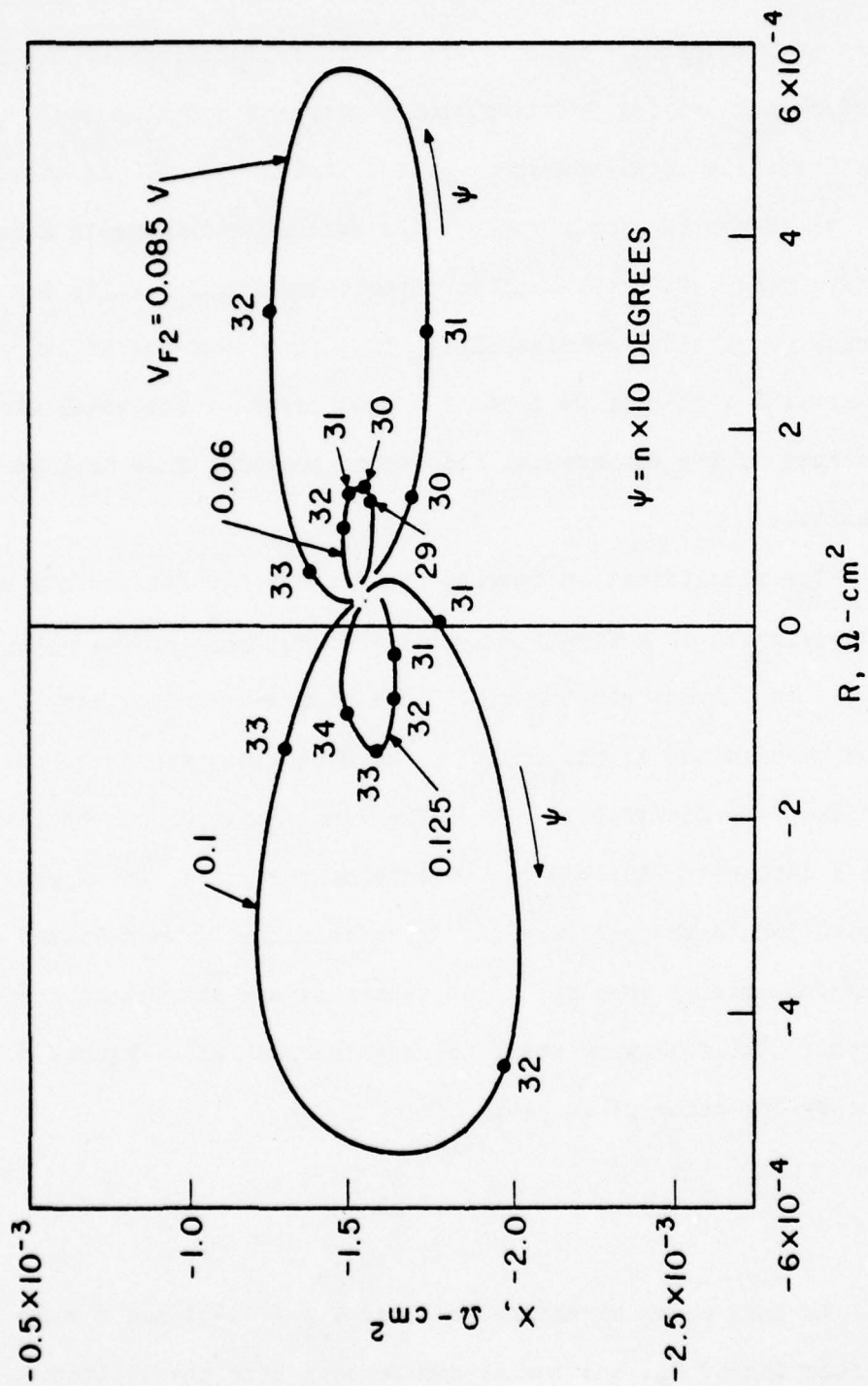


FIG. 6.11 LARGE-SIGNAL SECOND-HARMONIC IMPEDANCE FOR DC MAXIMUM POWER STRUCTURE NO. 3. ($V_{F1} = 0.4 \text{ V}$)

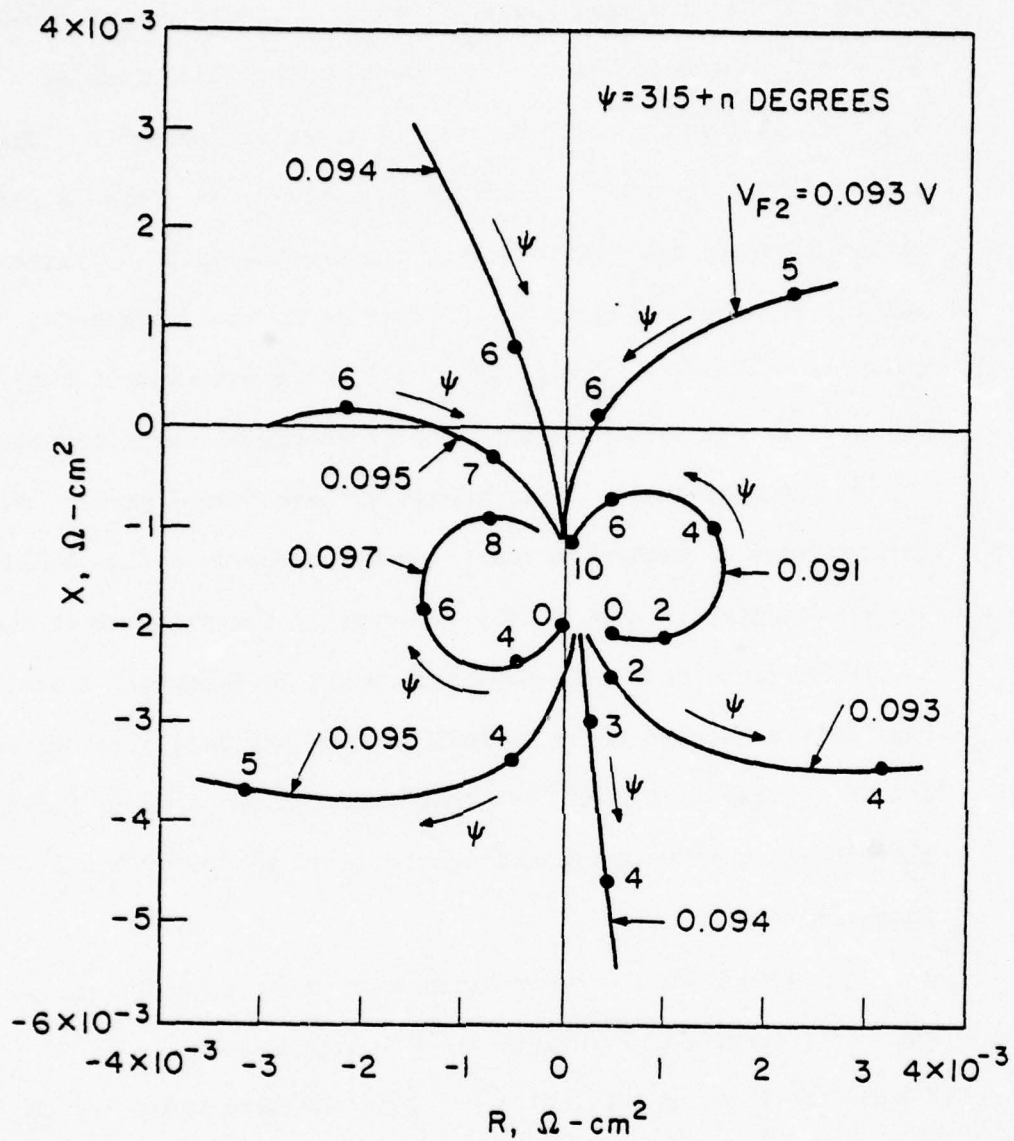


FIG. 6.12 LARGE-SIGNAL SECOND-HARMONIC IMPEDANCE FOR DC MAXIMUM POWER STRUCTURE NO. 3 NEAR SMALL VALUES OF \hat{V}_2 .
($V_{F1} = 0.4 \text{ V}$, NOTE SCALE CHANGE FROM FIG. 6.11)

origin of the impedance plane, $\hat{V}_2 = 0$. A comparison of two-frequency drive and single-frequency drive results for this diode at $V_{F2} = 0.093$ V and $\psi = 321$ degrees is given in Table 6.2. The results are not in disagreement to any appreciable extent, the largest variation being the difference in fundamental diode voltages V_{RF1} and the smallest being in the difference in the fundamental output power densities P_1 . Not given in the table but important to this argument is the fact that both the large-signal diode resistance and the fundamental output power change by less than 2 percent over the entire range of second-harmonic variation shown in Fig. 6.11. Thus the fundamental is only mildly affected by the presence of the second harmonic near this important point in parameter space. These results are thought to be typical for any proposed diode structure and it is therefore concluded that the single-frequency forward-biased region drive approximation is "good enough" for all single-frequency applications.

Second-harmonic power extraction using a BARITT diode was first reported by East et al.⁶⁸ A packaged K-band diode (p^+np^+ , Si, $N_d \approx 4 \times 10^{15}$ and base width ≈ 3 μ m) was placed in a Ka-band (WR-28) resonant cap waveguide mount such that guide power flow at the diode fundamental mode frequency was cut off. Power (0.2 to 1.6 μ W) was observed at 36 GHz when an E-H tuner was used to match the diode impedance to the guide impedance and the diode was biased between 200 and 600 A/cm². If losses are assumed low then such a diode must "see" almost a pure reactance at the fundamental frequency and the fundamental impedance locus must cross the imaginary axis at the same parameter point which corresponds

Table 6.2

Single-Frequency and Two-Frequency Large-Signal Results for
 Dc Maximum Power Structure No. 3 ($N_d = 5 \times 10^{15} \text{ cm}^{-3}$,
 Base Width = 4 μm , $J_0 = 400 \text{ A/cm}^2$, $V_{F1} = 0.4 \text{ V}$, $V_{F2} = 0.093 \text{ V}$,
 $\psi = 321 \text{ Degrees}$, Fundamental Frequency = 20 GHz)

<u>Parameter</u>	<u>Single-Frequency Value</u>	<u>Two-Frequency Value</u>
$R_1 \text{ } (\Omega\text{-cm}^2)$	-8.46×10^{-5}	-6.32×10^{-5}
$X_1 \text{ } (\Omega\text{-cm}^2)$	-3.08×10^{-3}	-3.09×10^{-3}
$R_2 \text{ } (\Omega\text{-cm}^2)$	--	3.12×10^{-4}
$X_2 \text{ } (\Omega\text{-cm}^2)$	--	1.20×10^{-4}
$P_1 \text{ } (\text{W/cm}^2)$	-108	-114
$P_2 \text{ } (\text{W/cm}^2)$	--	0.073
$V_1 \text{ } (\text{V})$	4.92	5.86
$V_2 \text{ } (\text{V})$	--	0.007

to a second-harmonic impedance of significant negative real part. The theoretical large-signal impedance plane plots, Z_1 and Z_2 , for this structure for one particular set of forward-biased region driving voltages, $V_{F1} = 0.3$ V and $V_{F2} = 0.1$ V, are given in Fig. 6.13. The parallel-plate "cold" capacitive reactances have been subtracted out of each locus such that the plots could be presented together. The points marked by squares in the figure are the single-frequency impedance values, i.e., $y_{12} = y_{21} = 0$, for the given drive levels. Note that oscillation is not possible at either frequency in the single-frequency case. The possibility of dual oscillation with no power delivered or absorbed at the fundamental is seen to exist at a second-harmonic drive relative phase angle of approximately -2.5 degrees. The second-harmonic predicted output power density at this point is 12 W/cm^2 which is two orders of magnitude larger than that measured (junction area $\approx 10^{-5} \text{ cm}^2$) so it is unlikely that the given drive parameters were those present in the experiment. The K-band diode package undoubtedly prevented an ideal match of the diode impedance at 36 GHz so the level of drive used in Fig. 6.12 is perhaps too high. Another possible set of impedance loci for smaller second-harmonic drive, $V_{F1} = 0.3$ V and $V_{F2} = 0.035$ V, is shown in Fig. 6.14. The second-harmonic output power density for this case is 0.4 W/cm^2 but the level of second-harmonic resistance, $\approx 10^{-6} \Omega\text{-cm}^2$ is too low for practical application. Lack of exact circuit characterization prevents any further definitive comparison between theory and experiment. In actuality, we do not wish to make such a comparison since it is not intended to portray these theoretical results as all inclusive or exact. Rather it is hoped

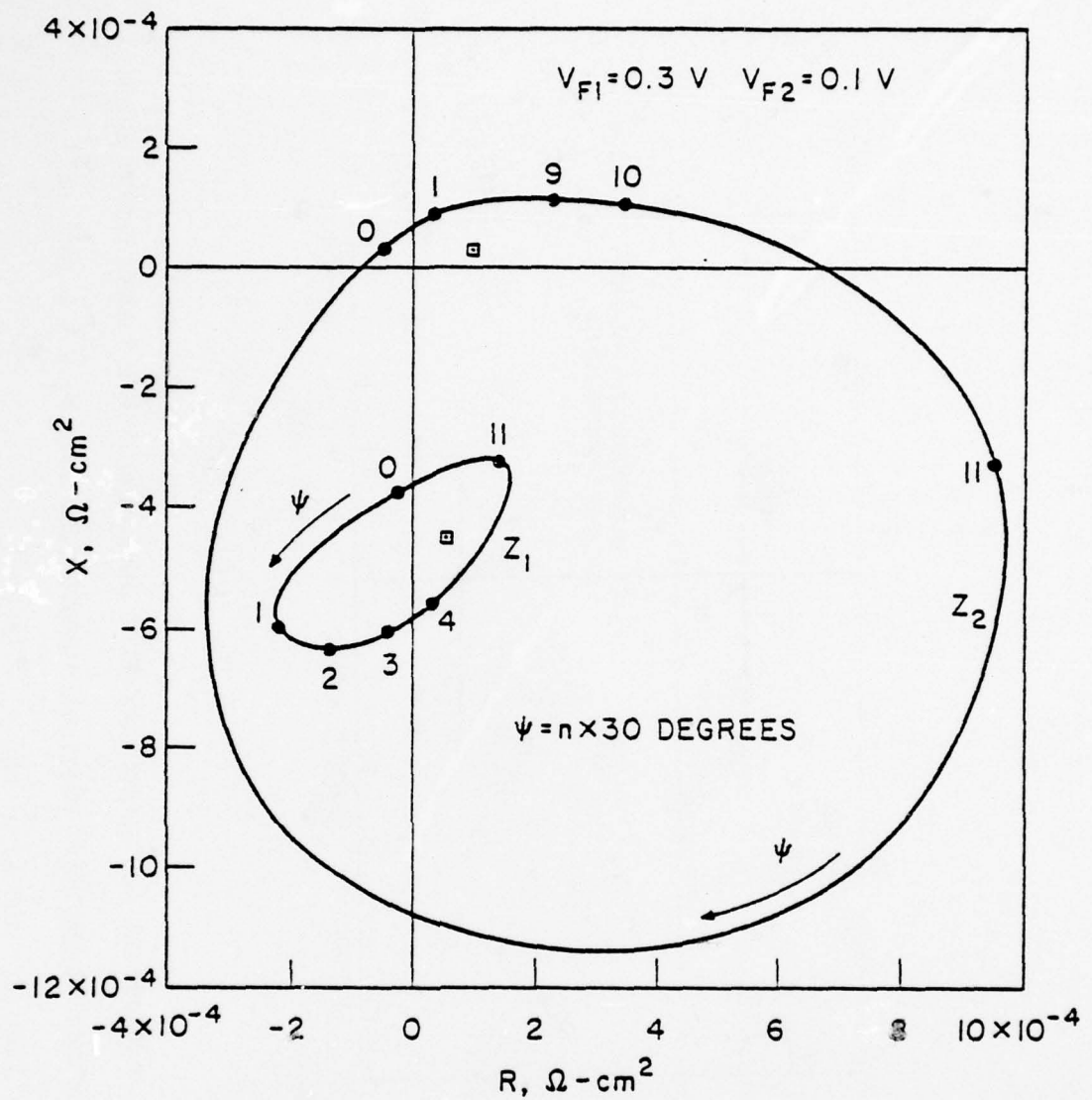


FIG. 6.13 LARGE-SIGNAL FUNDAMENTAL AND SECOND-HARMONIC IMPEDANCES
 FOR A K-BAND BARITT DIODE STRUCTURE. ("COLD" CAPACITIVE
 REACTANCES SUBTRACTED OUT, $N_d = 4 \times 10^{15} \text{ cm}^{-3}$, BASE
 WIDTH = 3 μm , $J_0 = 400 \text{ A/cm}^2$ AND $f_1 = 18 \text{ GHz}$)

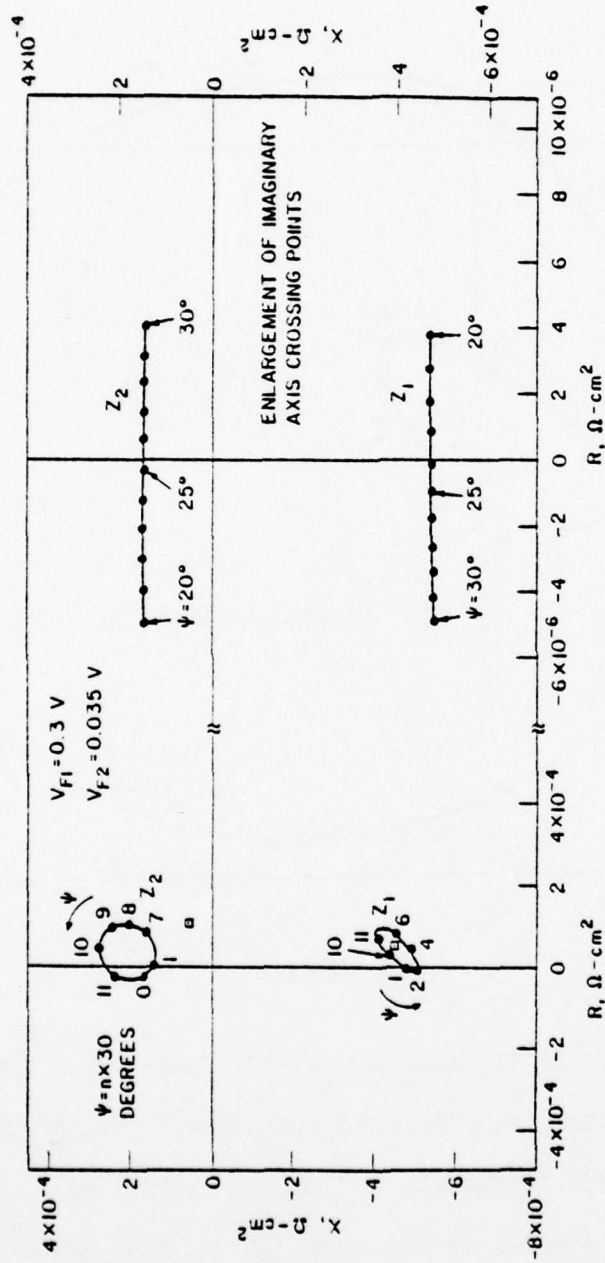


FIG. 6.14 LARGE-SIGNAL FUNDAMENTAL AND SECOND-HARMONIC IMPEDANCES FOR A K-BAND BARITT DIODE

STRUCTURE. ("COLD" CAPACITIVE REACTANCES SUBTRACTED OUT, $N_d = 4 \times 10^{15} \text{ cm}^{-3}$,

BASE WIDTH = $3 \text{ } \mu\text{m}$, $J_o = 400 \text{ A/cm}^2$ AND $f_1 = 18 \text{ GHz}$)

that the simple two-frequency theory will be recognized as a means to approximately predict possibilities or trends in the realm of millimeter-wave applications for the BARITT diode.

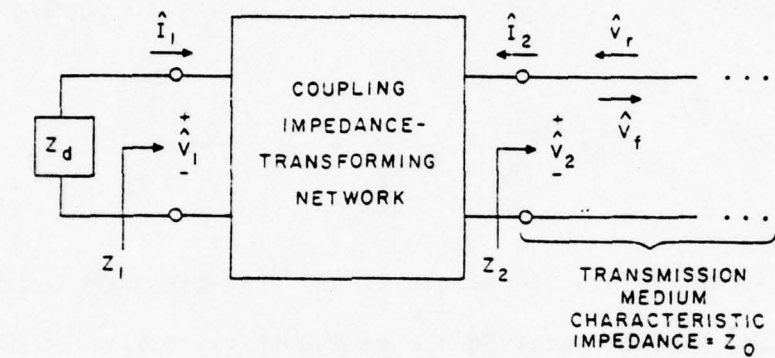
CHAPTER VII. BARITT DIODE MIXERS

7.1 Foreword

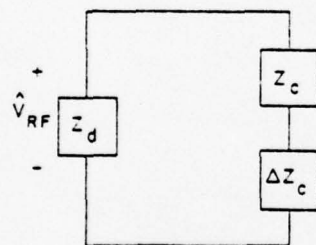
For the purposes of this study the subject of BARITT diode mixers is split into two principal subdivisions based on two distinctly different methods of analysis. The first method of analysis is based on low-level and near-frequency expansions of the voltage and current of an oscillating diode and is very similar to oscillator noise formulations. The second is based on classic small-signal expansions of a pumped conductance and is valid, in general, for any frequency range considered.

7.2 Very-Low Intermediate-Frequency Self-Oscillating BARITT Diode Mixers

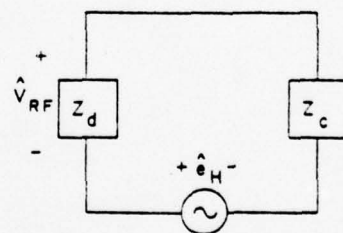
7.2.1 System Description. The equivalent circuits shown in Fig. 7.1 summarize the principles of an oscillating diode very-low intermediate-frequency receiver. The lossy coupling circuit, Fig. 7.1a, transforms (bilinear) the impedance "seen" at the input of the receiver transmission medium (waveguide, coaxial line, free-space, etc.) to levels comparable with the diode terminal impedance. The transmission medium can be any portion of the receiver in which the reverse traveling wave, with respect to the diode, consists only of the incoming "unknown" signal and does not contain any receiver-reflected diode power. The transforming-coupling network can be represented by any convenient set of two-port network parameters.



(a)



(b)



(c)

FIG. 7.1 (a) PHYSICAL CIRCUIT, (b) LOAD VARIATION MODEL AND (c) INJECTED SIGNAL MODEL.

In particular, for a Z-parameter representation of the coupling network, the input impedance "seen" from the diode terminals is

$$Z_1 = \frac{Z_{11}Z_2 + Z_{11}Z_{22} - Z_{12}^2}{Z_2 + Z_{22}} \quad (7.1)$$

For no incoming signal $Z_2 = Z_0$, the characteristic impedance of the transmission medium. However, with an incoming signal present* Z_2

becomes

$$Z_2 = -\frac{\hat{V}_2}{\hat{I}_2} = Z_0 \left(\frac{\hat{V}_f + \hat{V}_r}{\hat{V}_f - \hat{V}_r} \right),$$

where \hat{V}_f and \hat{V}_r are the values of the phasor forward and reverse traveling voltage waves in the medium at the output of the coupling network. If $|\hat{V}_r| \ll |\hat{V}_f|$ then

$$\begin{aligned} Z_2 &\approx Z_0 \left(1 + 2 \frac{\hat{V}_r}{\hat{V}_f} \right) \\ &\equiv Z_0 + \Delta Z_2 \end{aligned} \quad (7.2)$$

and

$$\begin{aligned} Z_1 &\approx Z_{10} + \left(\frac{Z_{12}}{Z_0 + Z_{22}} \right)^2 \Delta Z_2 \\ &\equiv Z_c + \Delta Z_c, \end{aligned} \quad (7.3)$$

* In this chapter, as in Chapter VI, RF phasor quantities are designated by " $\hat{}$."

where $Z_c = Z_{10}$ is obtained from Eq. 7.1 with $Z_2 = Z_o$. Equation 7.3 is in the form of the load-variation model suggested by Nagano and Akaiwa,⁶⁹ Fig. 7.1b. If ΔZ_1 is multiplied by the unperturbed ($Z_i = Z_c = Z_{10}$) value of diode current, then an equivalent voltage source \hat{e}_H can be defined and an injected-signal model¹³ results. Both methods of analysis, the load-variation model and the injected-signal model, are equivalent. However, the injected-signal model is chosen here as it can concurrently be used to study the oscillator noise properties by simply letting \hat{e}_H represent the intrinsic RF open-circuit noise voltage of the oscillating diode.

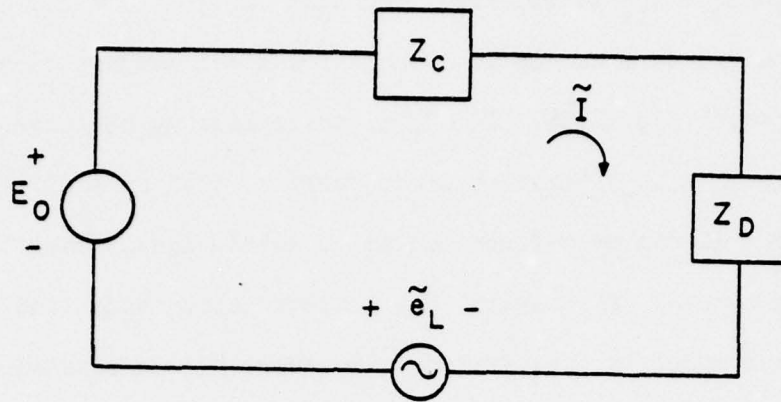
The notation* for the injected-signal mixer system studied here is given in Fig. 7.2. The two circuits symbolize the diode and its circuit environment at the two frequency regions of interest: RF (frequencies ω near the unperturbed, $\hat{e}_H = \hat{e}_L = 0$, oscillation frequency ω_o) and LF (low frequencies Ω near the bias frequency $\Omega_o = 0$, i.e., dc). The low-frequency voltage generator \hat{e}_L can either represent an external small-signal modulation source such as bias supply noise, or the open-circuit low-frequency intrinsic diode noise voltage, or both. The meanings of the remaining symbols in Fig. 7.2 are obvious from inspection.

The phasor equations that describe the coupling that exists between the LF and RF circuits are the LF Kirchhoff's voltage law,

$$E_o + \hat{e}_L = \tilde{I}(Z_C + Z_D) \quad , \quad (7.4)$$

and the RF voltage divider equation,

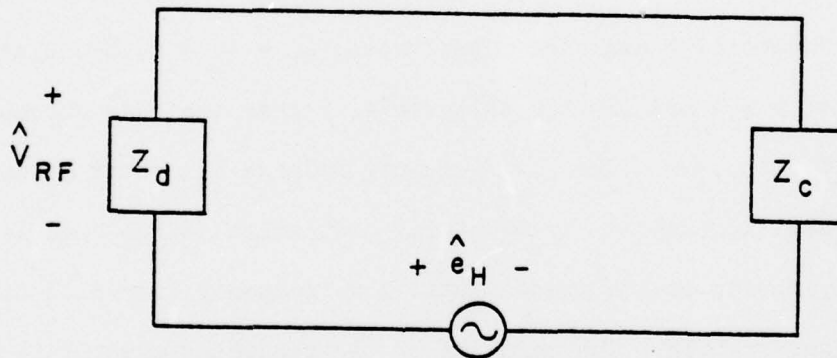
* Low-frequency phasor quantities are denoted by "-."



$$Z_D = Z_D(V_{RF}, I, \omega, \Omega)$$

FREQUENCY = Ω

BIAS, LF CIRCUIT



$$Z_d = Z_d(V_{RF}, I, \omega, \Omega)$$

FREQUENCY = ω

RF CIRCUIT

FIG. 7.2 LF AND RF COUPLED CIRCUIT MODELS. ($Z = R + jX$
FOR ALL IMPEDANCE QUANTITIES)

$$\hat{V}_{RF}(Z_c + Z_d) = \hat{e}_H Z_d \quad (7.5)$$

The two equations are coupled due to the nonlinearity of the diode impedance; that is,

$$Z_d = Z_d(V_{RF}, I, \omega, \Omega)$$

and

$$Z_D = Z_D(V_{RF}, I, \omega, \Omega) ,$$

where the functional dependence is understood to be nonlinear. Any small disturbance represented by \hat{e}_H or \hat{e}_L in either one or both of the loops will cause small changes in each of the four dependent variables, V_{RF} , I , ω and Ω , such that they vary about their unperturbed values, V_{RF_0} , I_0 , ω_0 and Ω_0 . For completeness, the next section contains a small-signal analysis⁷⁰ for such variations.

7.2.2 Perturbation Theory. Since it is assumed that the input RF signal is at a frequency very near the unperturbed oscillating frequency of the diode, the quasi-static approximation can be utilized. The LF Kirchhoff's voltage law equation and the RF voltage divider equation are each written at a single frequency, Ω_0 and ω_0 , respectively, but with the phasor quantities, amplitude and phase, understood to be slowly varying functions of time. As shown by Kurokawa⁷¹ there is one additional stipulation. At RF, letting

$$\hat{V}_{RF} = [V_{RFQ} + \delta V(t)]e^{j\Delta\phi(t)} ,$$

where δV and $\Delta\phi$ are small, we have

$$V_{RF}(t) = \text{Re}\left\{\hat{V}_{RF} e^{j\omega_0 t}\right\}$$

so

$$\frac{dv_{RF}}{dt} = \text{Re} \left[j \left(\omega_0 + \frac{d\Delta\phi}{dt} - j \frac{1}{V_{RF0}} \frac{d\delta V}{dt} \right) \hat{V}_{RF} e^{j\omega_0 t} \right]$$

Thus because of the quasi-static approximation (time-varying phasor quantities) any operation in phasor space that requires multiplication by ω must be carried out using

$$\begin{aligned} \omega &= \omega_0 + \frac{d\Delta\phi}{dt} - j \frac{1}{V_{RF0}} \frac{d\delta V}{dt} \\ &\equiv \omega_0 + \delta\omega - j \frac{1}{V_{RF0}} \frac{d\delta V}{dt} \end{aligned}$$

Similarly at baseband,

$$\tilde{I} = [I_0 + \delta I(t)] e^{j\Delta\psi(t)}$$

so

$$\begin{aligned} \Omega &= \Omega_0 + \frac{d\Delta\psi}{dt} - j \frac{1}{I_0} \frac{d\delta I}{dt} \\ &\equiv \Omega_0 + \delta\Omega - j \frac{1}{I_0} \frac{d\delta I}{dt} \end{aligned}$$

Expanding the LF loop equation in a Taylor series about its unperturbed operating point yields

$$\begin{aligned} \tilde{e}_L &= I_0 \left(\frac{\partial Z_D}{\partial V_{RF}} \Big|_0 - j \frac{1}{V_{RF0}} \frac{\partial Z_D}{\partial \omega} \Big|_0 \frac{d}{dt} \right) \delta V \\ &+ \left(Z_{T0} + I_0 \frac{\partial Z_D}{\partial I} \Big|_0 - j \frac{1}{I_0} \frac{\partial Z_T}{\partial \Omega} \Big|_0 \frac{d}{dt} \right) \delta I \\ &+ I_0 \frac{\partial Z_D}{\partial \omega} \Big|_0 \delta\omega + I_0 \frac{\partial Z_T}{\partial \Omega} \Big|_0 \delta\Omega \end{aligned} \quad (7.6)$$

It is physically reasonable and experimentally observed that since Ω is so low all quantities at baseband are approximately in phase, i.e., the imaginary portion of Eq. 7.6 is approximately equal to zero. This restriction implies the following: (1) $\Delta\psi(t) = 0$ and thus $\delta\Omega = 0$, (2) $X_D = X_C = 0$, (3) $\text{Im}(\tilde{e}_L) = 0$, and (4)

$$\frac{1}{V_{RF0}} \left. \frac{\partial R_D}{\partial \omega} \right|_0 \frac{d\delta V}{dt} = - \frac{1}{I_0} \left. \frac{\partial R_T}{\partial \Omega} \right|_0 \frac{d\delta I}{dt} .$$

Implication 4 can be identically satisfied if

$$\left. \frac{\partial R_D}{\partial \omega} \right|_0 = \left. \frac{\partial R_T}{\partial \Omega} \right|_0 = 0 .$$

The condition that the total baseband resistance is not a function of Ω easily follows from the previous acknowledgment that $X_T(\Omega) = 0$. However, the requirement that the active device not act as a discriminator is not so intuitive. Again, an experimental observation is invoked.

From the real part of Eq. 7.6 we have

$$\delta I = - \frac{I_0 \left. \frac{\partial R_D}{\partial V_{RF}} \right|_0 \delta V + I_0 \left. \frac{\partial R_D}{\partial \omega} \right|_0 \delta \omega}{R_{T0} + I_0 \left. \frac{\partial R_D}{\partial I} \right|_0} .$$

An experiment which enables a direct test of this expression is one in which the relative phase of a reflected portion, square-wave modulated, of an oscillator output is varied over at least 90 degrees.

The setup is shown in Fig. 7.3a. Varying the phase shifter causes the reflected portion of the total diode voltage to rotate around the reference diode output voltage phasor as shown in Fig. 7.3b. When the reflected portion of the total diode voltage is 90 degrees out of phase with the reference the diode is undergoing almost pure frequency modulation, i.e., $\delta V(t) = 0$. When the reflected portion is in phase or in antiphase with the reference the diode is being purely amplitude modulated, i.e., $\delta \omega = 0$. Thus a graph of the detected current δI vs. the relative phase shift of the medium would give an indication of the relative sensitivity of the diode to AM and FM modulation. Figure 7.3c shows such a plot for an oscillating X-band BARITT diode in a waveguide mount, obviously for this case one type of modulation is virtually undetectable. Since the rectification effect is known to exist; that is, $\partial R_D / \partial V_{RF} \neq 0$, it is concluded that $\partial R_D / \partial \omega \approx 0$ and that the diode is essentially an AM detector only. We will consider this result to be typical for all BARITT very-low IF mixers. Thus we are self-consistent with the observation that the baseband circuit exhibits negligible reactive effects. This consistency is not contained in the works of Nygren and Sjölund¹⁴ and Vlaardingerbroek.⁷⁰ However for reasons of simplicity they do discard the $\partial R_D / \partial \omega$ terms after obtaining a complete solution. The present work shows that neglecting this term is justifiable from the start.

One last assumption is in order. It is logical to assume that since $\partial Z_D / \partial \Omega \approx 0$ then $\partial Z_A / \partial \Omega$ is also negligible. The reasoning being that the functional dependence of the diode impedance on the various parameters of interest should be strongest for the particular

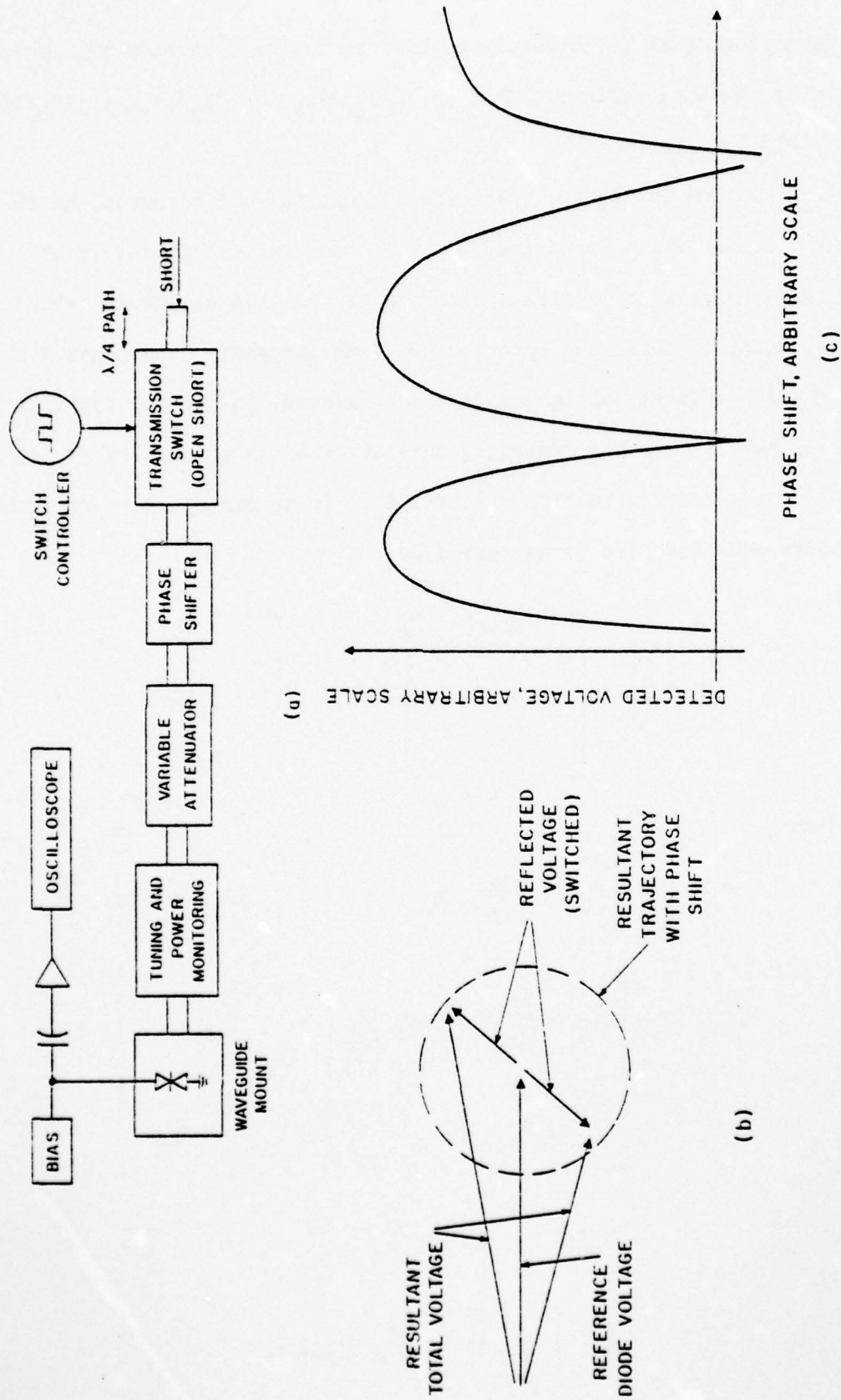


FIG. 7.3 MODULATION DETECTION SENSITIVITY EXPERIMENT. (a) TEST SETUP, (b) PHASOR DIAGRAM AND (c) EXPERIMENTAL RESULTS.

parameters that are directly applicable to the frequency region in which they are defined. That is, $|\partial Z_d / \partial V_{RF}| > |\partial Z_D / \partial V_{RF}|$, $|\partial Z_D / \partial I| > |\partial Z_d / \partial I|$, etc.

Subject to the preceding assumptions and observations the RF voltage divider equation, Eq. 7.5, can now be expanded in a first-order Taylor series similar to the LF loop equation. When the resultant is separated into its real and imaginary components a system of time differential equations can be formed, in conjunction with the real part of Eq. 7.6, relating the time-varying parameters δV , $\delta \omega$ and δI to the driving functions \hat{e}_H and \hat{e}_L . In matrix operator form these three equations can be expressed as

$$\left[M \left(\frac{d}{dt} \right) \right] \begin{bmatrix} \delta V(t) \\ \delta \omega(t) \\ \delta I(t) \end{bmatrix} = \begin{bmatrix} R_H(t) \\ X_H(t) \\ e_L(t) \end{bmatrix}, \quad (7.7)$$

where

$$M \left(\frac{d}{dt} \right) = \begin{bmatrix} R_{dv} + \frac{X_{tw}}{V_{RFO}} \frac{d}{dt} & R_{tw} & R_{dI} \\ X_{dv} - \frac{R_{tw}}{V_{RFO}} \frac{d}{dt} & X_{tw} & X_{dI} \\ I_O R_{Dv} & 0 & R_{To} + I_O R_{DI} \end{bmatrix},$$

$$R_H(t) = \text{Re} (Z_{do} \hat{e}_H / V_{RFO}),$$

$$X_H(t) = \text{Im} (Z_{do} \hat{e}_H / V_{RFO})$$

AD-A063 558

MICHIGAN UNIV ANN ARBOR ELECTRON PHYSICS LAB

F/G 9/5

FREQUENCY CONVERSION IN PUNCH-THROUGH SEMICONDUCTOR DEVICES.(U)

AUG 78 P J MCCLEER

DAA629-76-6-0232

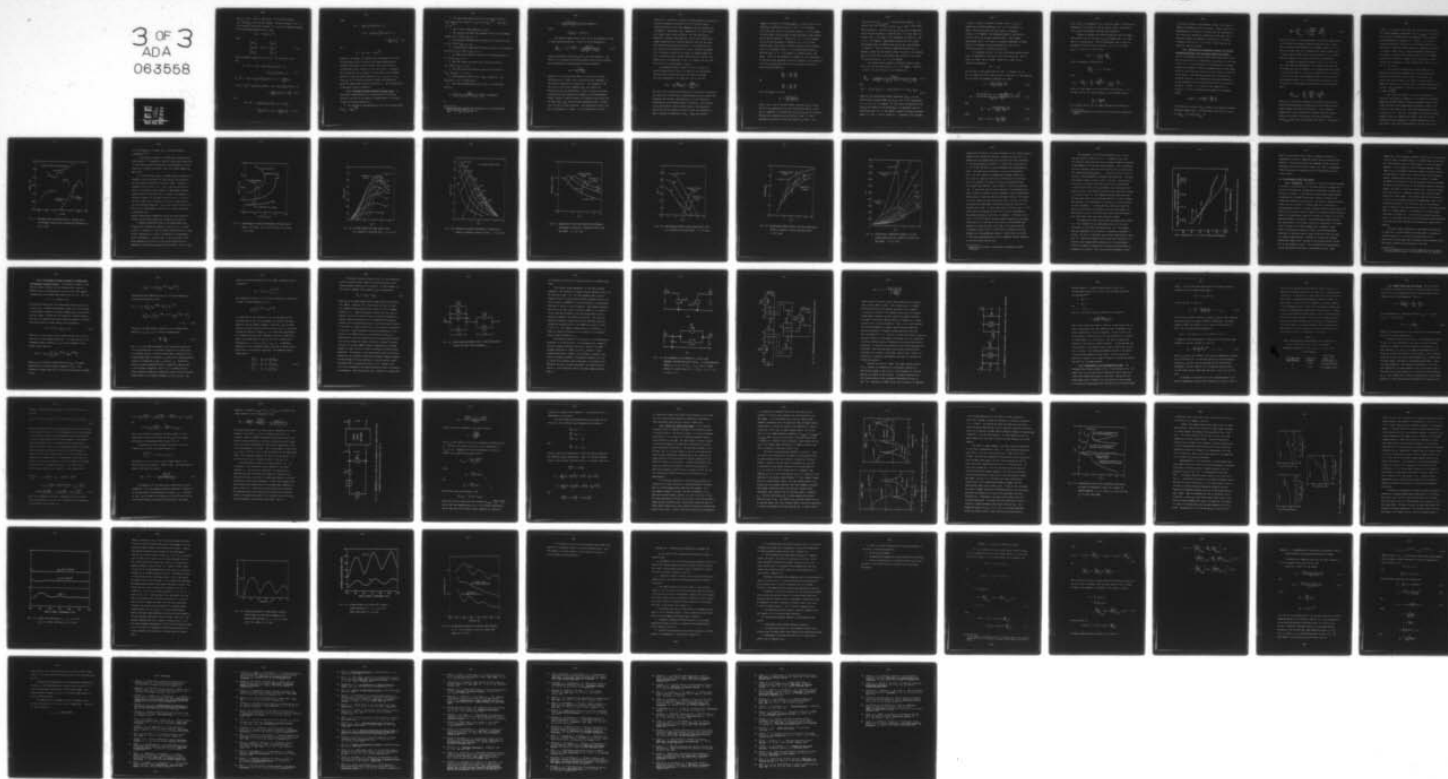
UNCLASSIFIED

TR-143

ARO-13853.2-EL

NL

3 OF 3
ADA
063558



and $e_L(t) = \tilde{e}_L(t)$, real by observation. The short-form notation $R_{dv} \rightarrow \partial R_d / \partial V_{RF}|_0$, etc., has been adopted. The matrix equation (Eq. 7.7) can be solved by the phasor technique, i.e., let the LF angular frequency of the time-varying quantities be α , then

$$\delta V(t) = \text{Re}[\delta \tilde{V}(\alpha) e^{j\alpha t}] .$$

Thus

$$\begin{bmatrix} \delta \tilde{V}(\alpha) \\ \delta \tilde{\omega}(\alpha) \\ \delta \tilde{I}(\alpha) \end{bmatrix} = [M(j\alpha)]^{-1} \begin{bmatrix} R_H(\alpha) \\ X_H(\alpha) \\ e_L(\alpha) \end{bmatrix} . \quad (7.8)$$

After considerable algebra the result, Eq. 7.8, can be put in the form

$$\begin{aligned} \delta \tilde{V} \cdot \det &= (R_{To} + I_O R_{DI}) |Z_H| |Z_{tw}| \sin(\theta_\omega - \theta_H) \\ &\quad + e_L |Z_{tw}| |Z_{dI}| \sin(\theta_I - \theta_\omega) , \quad (7.9) \end{aligned}$$

$$\begin{aligned} \delta \tilde{\omega} \cdot \det &= (R_{To} + I_O R_{DI}) |Z_H| \left[|Z_{dv}| \sin(\theta_H - \theta_v) + j \frac{\alpha}{V_{RF0}} |Z_{tw}| \right. \\ &\quad \cdot \cos(\theta_\omega - \theta_H) \left. \right] + I_O R_{Dv} |Z_H| |Z_{dI}| \sin(\theta_I - \theta_H) + e_L |Z_{dI}| \left[|Z_{dv}| \sin(\theta_v - \theta_I) \right. \\ &\quad \left. - j \frac{\alpha}{V_{RF0}} |Z_{tw}| \cos(\theta_\omega - \theta_I) \right] \quad (7.10) \end{aligned}$$

and

$$\begin{aligned} \delta \tilde{I} \cdot \det &= I_O R_{Dv} |Z_H| |Z_{tw}| \sin(\theta_H - \theta_\omega) + e_L |Z_{tw}| \\ &\quad \cdot \left[|Z_{dv}| \sin(\theta_\omega - \theta_v) + j \frac{\alpha}{V_{RF0}} |Z_{tw}| \right] , \quad (7.11) \end{aligned}$$

where

$$\begin{aligned} \det = & I_O R_{DV} |Z_{tw}| |Z_{dI}| \sin(\theta_I - \theta_\omega) \\ & + (R_{To} + I_O R_{DI}) |Z_{tw}| \left[|Z_{dv}| \sin(\theta_\omega - \theta_v) \right. \\ & \left. + j \frac{\alpha}{V_{RFO}} |Z_{tw}| \right] \quad (7.12) \end{aligned}$$

and

$$Z_H = R_H + jX_H = |Z_H| e^{j\theta_H}.$$

Equations 7.9 through 7.11 indicate that the presence of the disturbing signals \hat{e}_H and e_L induce slowly varying amplitude and frequency variations in the RF voltage across the diode and a low-frequency current variation in the bias circuit. In general, the RF variations can be thought of as the result of the combined effects of signal and image components at $\omega_o + \omega_{IF}$ and $\omega_o - \omega_{IF}$, where ω_{IF} is the difference frequency between the frequency of \hat{e}_H and the unperturbed oscillation frequency ω_o . This interpretation is developed further in Appendix B.

7.2.3 Perturbation Theory Discussion—Special Cases. To facilitate the specialization of the equations of the previous section to the case of the very-low IF downconverter it is helpful to make the following definitions:

1. The injected RF voltage generator due to the incoming signal is $\hat{e}_{Hs} = |\hat{e}_{Hs}| e^{j\theta_{Hs}}$.

2. The narrow-band representation* of the diode RF intrinsic open circuit noise voltage⁷² is $e_{Hn}(t) \equiv \text{Re}(\hat{e}_{Hn} e^{j\omega_o t})$, where $\hat{e}_{Hn} = e_n(t) e^{j\theta_n(t)}$.

3. The LF noise voltage generator $\equiv e_{Ln}(t)$.

4. The oscillator RF amplitude variation due only to the incoming signal is $\delta\tilde{V}_s \equiv \delta\tilde{V}(\hat{e}_H = \hat{e}_{Hs}, e_L = 0)$.

5. The oscillator RF amplitude fluctuation due to RF and LF noise is $\delta\tilde{V}_n \equiv \delta\tilde{V}(\hat{e}_H = \hat{e}_{Hn}, e_L = e_{Ln})$.

6. The oscillator RF amplitude fluctuation due only to the intrinsic RF noise is $\delta\tilde{V}_{Hn} \equiv \delta\tilde{V}(\hat{e}_H = \hat{e}_{Hn}, e_L = 0)$.

7. The bias current variation due only to the incoming signal is $\delta\tilde{I} \equiv \delta\tilde{I}(\hat{e}_H = \hat{e}_{Hs}, e_L = 0)$.

8. The bias current fluctuation due to RF and LF noise is $\delta\tilde{I}_n \equiv \delta\tilde{I}(\hat{e}_H = \hat{e}_{Hn}, e_L = e_{Ln})$.

9. The bias current fluctuation due only to the LF noise is $\delta\tilde{I}_{Ln} \equiv \delta\tilde{I}_{Ln}(\hat{e}_H = 0, e_L = e_{Ln})$.

10. The AM modulation sensitivity is $\tilde{M}_{AM} \equiv |Z_{dI}| \sin(\theta_I - \theta_\omega) / [|Z_{dv}| \sin(\theta_\omega - \theta_v) + j(\alpha/V_{Rfo}) |Z_{tw}|]$.

11. The coupling-transforming circuit, Fig. 7.1a, efficiency factor is

$$k \equiv \left| \frac{Z_o Z_{12}^2}{(Z_o + Z_{22})(Z_{11} Z_o + Z_{11} Z_{22} - Z_{12}^2)} \right| \quad (\text{Z-parameters})$$

or

* Mean square noise values⁷² are represented by the shortened form $|\hat{e}_{Hn}|^2 \equiv \{\text{Re}[\hat{e}_{Hn} \exp(j\omega_o t)]\}^2$, etc.

$$k \equiv \left| \frac{Z_o(AD - BC)}{(AZ_o + B)(CZ_o + D)} \right| \quad (\text{ABCD parameters}) ,$$

where

$$|\hat{e}_H/V_{RFO}| = k|2\hat{V}_r/\hat{V}_f| .$$

The detected signal-to-noise ratio can now be expressed in terms of these definitions and Eqs. 7.9 and 7.11 can be expressed as

$$\left(\frac{S}{N}\right)_{LF} = |\delta\tilde{I}_s|^2/|\delta\tilde{I}_n|^2 = \frac{g_m^2|\delta\tilde{V}_s|^2}{2g_m^2|\delta\tilde{V}_{Hn}|^2 + |\delta\tilde{I}_{Ln}|^2} , \quad (7.13)$$

where any correlation between \hat{e}_{Hn} and e_{Ln} has been neglected. The factor of two provides for the downconversion of both noise sidebands and a downconversion transconductance has been defined as

$$g_m \equiv \frac{I_{ODV}}{R_{TO} + I_{ODI}} .$$

Equation 7.13 is the principal result of the very-low IF mixer perturbation as it clearly shows the device-circuit dependence of the detected signal and the system noise. Most prominent is the fact that of the RF noise components only the intrinsic AM fluctuations $\delta\tilde{V}_{Hn}$ are downconverted. Thus, RF intrinsic frequency fluctuations do not influence the integrity of the downconverted signal. However, since both forms of RF intrinsic noise arise from the same source, \hat{e}_{Hn} , attaching mixer degradation purely to either AM or FM noise is truly artificial. The relationship is seen to be one of coincidence, not causal. It is interesting to note that

Gupta et al.¹³ arrived at a similar conclusion regarding the effects of oscillator frequency fluctuations on low IF self-oscillating doppler detectors but that they employed an entirely different set of arguments. Essentially, they reasoned that for short round-trip transit times, diode oscillators with the then typical measured FM spectral power densities did not have enough time to change frequencies with sufficient magnitude such that the resultant downconverted signal was affected. It is argued here that this criterion is too restrictive in that it precludes consideration of external sources for the origin of incoming signals and that it ignores the basic physical restriction which leads to the simple form of the denominator of Eq. 7.13; namely, that the diode does not act as a discriminator, or $R_{Dw} = 0$.

One seemingly apparent manner in which to optimize the detected signal-to-noise ratio is to minimize the low-frequency intrinsic noise contribution $\delta \tilde{I}_{Ln}$ by RF circuit techniques. After some manipulation, this term can be put in the form

$$\delta \tilde{I}_{Ln} = \frac{e_{Ln}}{R_{To} + I_o R_{DI}} \left(1 - \frac{g_m \tilde{M}_{AM}}{g_m \tilde{M}_{AM} + 1} \right).$$

The unity term in parentheses represents the bias current fluctuations that would flow if there were no downconversion while the second term represents the resultant canceling flow due to the closed-loop downconversion of upconverted current fluctuations. The loop gain is the downconversion transconductance times the AM modulation sensitivity and any increase in either of these two parameters is seen to diminish the magnitude of $\delta \tilde{I}_{Ln}$. Nygren and Sjölund¹⁴

suggested one method of increasing \tilde{M}_{AM} , to circuit tune for very large \tilde{M}_{AM} by operating such that $\theta_\omega - \theta_V \approx 0$ or 180 degrees. As is shown later this is a false goal since $\theta_I \approx \theta_V + 180$ degrees for most diodes, thus \tilde{M}_{AM} cannot be made arbitrarily large independent of system stability. Tuning for $\theta_\omega - \theta_V \approx 0$ or 180 degrees would force the determinant of matrix M, Eq. 7.12, to become extremely small which implies quiescent operation near an unstable point in the impedance plane, i.e., non-small-signal operation. The proof that $\theta_I \approx \theta_V + 180$ degrees for a BARITT diode is very simple. Since, by the assumptions of Chapter VI, the nonlinearity of the total diode impedance is entirely contained in the conductance G_F of the forward-biased region, the two partial derivatives in question can be written as.

$$\frac{\partial Z_d}{\partial V_{RF}} = \frac{\partial Z_d}{\partial G_F} \frac{\partial G_F}{\partial V_{RF}}$$

and

$$\frac{\partial Z_d}{\partial I} = \frac{\partial Z_d}{\partial G_F} \frac{\partial G_F}{\partial I}$$

Also from Chapter VI we have

$$G_F = I_1 \frac{2I_1(V_{F1}/V_T)}{V_{F1} I_0(V_{F1}/V_T)},$$

where I_0 and I_1 are the modified Bessel functions and V_{F1} is that portion of V_{RF} appearing across the forward-biased region. Since V_{F1} is a magnitude, the quotient $2I_1(V_{F1}/V_T)/I_0(V_{F1}/V_T)$ is a positive monotonically increasing function with V_{F1} , slope < 1 , which saturates at the value two for high levels of V_{F1} drive. It is

clear that $\partial G_F / \partial V_{F1} \big|_I = \text{const}$ is real and always negative. It is equally clear that $\partial G_F / \partial I \big|_{V_{F1}} = \text{const} \rightarrow V_{RF} = \text{const}$ is also always real but positive. Finally, since V_{RF} and V_{F1} are both magnitudes and as such are related by a positive ratio, it is seen that it is exactly true, to the extent of the assumptions of Chapter VI, that $\theta_V = \theta_I + 180$ degrees. Experimental evidence that this tuning relationship holds for IMPATT diodes as well has been presented by Peterson.⁷³ Thus the method of Nygren and Sjölund will, in general, produce just the opposite effect for which it was intended; \tilde{M}_{AM} will in fact tend to zero rather than infinity if the circuit is tuned such that $\theta_V - \theta_\omega = 0$ or 180 degrees.

As a special case we examine the detected signal-to-noise ratio with this new stipulation, $\theta_V = \theta_I + 180$ degrees. Equations 7.12 and 7.13 can now be put in the following form:

$$\left(\frac{S}{N}\right)_{LF} = \frac{\beta^2 |\hat{e}_{Hs}|^2}{2\beta^2 |\hat{e}_{Hn}|^2 + [(v_{RF0}^2/v_c^2) \sin^2 \xi + \alpha^2 |Z_{tw}/Z_{do}|^2] \overline{e_{Ln}^2}} \quad (7.14)$$

and

$$\det = \beta |Z_{tw}| [|Z_{dI}| \sin \xi + (1/g_m) (|Z_{dv}| \sin \xi + j(\alpha |Z_{tw}|/v_{RF0}))], \quad (7.15)$$

where β is the rectification effect coefficient $I_O R_{Dv}$, v_c is the device-circuit tuning voltage $|Z_{do}|/|Z_{dv}|$, and ξ is the tuning angle $\theta_V - \theta_\omega = \theta_I - \theta_\omega + 180$ degrees. As can be seen, optimization of the $(S/N)_{LF}$ with respect to the tuning angle ξ is impossible since the obvious solution, $\xi = 0$ or 180 degrees, implies an unstable operating point, i.e., $\det \rightarrow 0$ for low values of α . Cognizant of this dilemma,

we choose to define a "heuristic optimum" value of $(S/N)_{LF}$ by maximizing the system determinant, Eq. 7.15, with respect to ξ . Again, the obvious solution for this course is orthogonal tuning, $\xi = \pm 90$ degrees. The backhanded aspect of this choice is that the $(S/N)_{LF}$ is actually minimized when $\xi = \pm 90$ degrees. Nevertheless, as Eq. 7.14 cannot be optimized independent of system stability, orthogonal tuning is maintained not only to be a satisfactory goal but a desirable one as well.

It is apparent from Eq. 7.14 that the detected signal-to-noise ratio is independent of the value of the bias resistor R_C . Thus to study the common case of constant current bias, a bias circuit variation is defined as

$$\delta \tilde{V}_C = R_C \delta \tilde{I}$$

and the limit of the system equations, Eqs. 7.9 through 7.11, as $R_C \rightarrow \infty$ is taken. This is the case studied by Gupta et al.¹³ The equations for the RF and LF incremental components now become

$$\delta \tilde{V} = \frac{|\hat{e}_H| v_c \sin(\theta_\omega - \theta_H)}{V_{RFO} \cdot \text{detc}}, \quad (7.16)$$

$$\delta \tilde{\omega} = \frac{|\hat{e}_H| |Z_{do}| \left[\sin(\theta_H - \theta_v) + j \frac{\alpha}{V_{RFO}} \left| \frac{Z_{tw}}{Z_{dv}} \right| \cos(\theta_\omega - \theta_H) \right]}{V_{RFO} |Z_{tw}| \cdot \text{detc}} \quad (7.17)$$

and

$$\delta \tilde{V}_G = e_L + \frac{\beta v_c |\hat{e}_H| \sin(\theta_H - \theta_\omega)}{V_{RFO} \cdot \text{detc}}, \quad (7.18)$$

where

$$\text{detc} = \sin \xi + j \frac{\alpha}{V_{RFO}} \left| \frac{Z_{tw}}{Z_{dv}} \right|. \quad (7.19)$$

Since $(S/N)_{LF}$ is independent of R_C it does not change. The particular advantage for this method of bias is clearly evident, upconversion of the diode low-frequency noise has been eliminated.*

Finally, we estimate the corner frequency at which the imaginary portion of $\sin \xi + j(\alpha/V_{RFO})|Z_{tw}/Z_{dv}|$ becomes equal to the real part for a typical diode. From the experimental data of Snapp and Weissglas¹⁰ for their Diode B (see Fig. 6.6) at $J_0 = 50 \text{ A/cm}^2$, $V_{RFO} = 5 \text{ V}$ and $f_0 = 6.6 \text{ GHz}$, we have

$$|Z_{dv}| \approx - \frac{1}{(\omega_0 C_d)^2} \left. \frac{\partial G_d}{\partial V_{RF}} \right|_0 ,$$

where from graphical differentiation

$$\left. \frac{\partial G_d}{\partial V_{RF}} \right|_0 \approx - 1.4 \times 10^{-4} \text{ mho/V} .$$

Also,

$$|Z_{tw}| \approx \left. \frac{\partial X_t}{\partial \omega} \right|_0 = \frac{2R_c}{\omega_0} \cdot \frac{\omega_0 \left. \frac{\partial X_t}{\partial \omega} \right|_0}{2R_c} \approx \frac{1}{(\omega_0 C_d)^2} \cdot \frac{2G_d}{\omega_0} \cdot Q_L ,$$

where Q_L is the loaded Q of the oscillator circuit and $G_d \approx - 7.2 \times 10^{-4} \text{ mho}$. Thus at the corner frequency α_c for orthogonal tuning

$$\frac{\alpha_c}{2\pi} \approx \frac{3.2 \text{ GHz}}{Q_L} .$$

For a typical value of $Q_L = 25$ (again estimated from Reference 10)

* Current fluctuations in the bias source can still be upconverted however.

this corner frequency is approximately 120 MHz. This result is deemed as representative for most diodes. Further, since all the measurements for the very-low IF mixers that are considered in this study are at modulation frequencies of less than 1 MHz, we can safely neglect any imaginary contributions to the phasor incremental terms in Eqs. 7.16 through 7.19 and consider all quantities real and in phase.

7.2.4 Theoretical and Experimental Results for Very-Low Intermediate-Frequency Self-Oscillating BARITT Diode Mixers.

Very-low intermediate-frequency negative-resistance mixers can be easily characterized in an experimental setup similar to that shown in Fig. 7.3a. At any particular diode operating point the phase shifters are adjusted to produce a maximum detected voltage signal across the diode terminals (detected current through the diode for a Gunn device). This procedure ensures pure AM modulation as discussed previously. The transmission medium path attenuation is then increased until the downconverted signal is just equal to the noise. From Eq. 7.17 we have for this condition, i.e., $(S/N)_{LF} = 1$, and for low modulation frequencies and orthogonal tuning,

$$\beta^2 |\hat{e}_{Hs}|^2 = 2\beta^2 |\hat{e}_{Hn}|^2 + \frac{V_{RFO}^2}{V_c^2} e_{Ln}^2.$$

We can express this value of \hat{e}_{Hs} in terms of the measurable minimum detectable signal (MDS) to the measurable carrier power (C) ratio as $|\hat{e}_{Hs}|_{\min} = 2k V_{RFO} |\hat{V}_r / \hat{V}_f|_{\min}$ or

$$\frac{\text{MDS}}{C} = \left| \frac{\hat{V}_r}{\hat{V}_f} \right|_{\min}^2 = \frac{1}{k^2} \left[\frac{|\hat{e}_{Hn}|^2}{2V_{Rfo}^2} + \frac{\overline{e_{Ln}^2}}{4\beta^2 v_c^2} \right] \quad (7.20)$$

This ratio, MDS/C is of prime importance in radar-type applications, as it indicates the maximum allowable system path loss or range. While in receiver-type applications the primary interest is in the value of the MDS only, for it represents the receiver sensitivity. It follows that the MDS/C ratio for a given value of C is a useful means for comparison for various device-circuit combinations.

An important consequence inherent in Eq. 7.20 is the fact that, other than the determination of the amplitude of the diode RF voltage drive and the presence of the coupling efficiency factor k, the device-RF-circuit interaction is manifest only in its effect on the LF noise term. The dependence of MDS/C on the RF noise is one of proportionality to the intrinsic-device noise alone. This is contrary to the measurable double-sideband AM-noise-to-carrier ratio,

$$\left(\frac{N}{C} \right)_{\text{AM,DSB}} = \frac{2v_c^2}{V_{Rfo}^2} \cdot \frac{|\hat{e}_{Hn}|^2}{V_{Rfo}^2} + \frac{M_{\text{AM}} \overline{i_{Bn}^2}}{V_{Rfo}^2},$$

where i_{Bn} is the current fluctuation in the bias source in which both the device-RF-circuit interaction and the intrinsic-RF-device noise determine the total RF contribution. Thus in theory it appears that it may be possible for the MDS/C ratio for certain devices and circuits to be actually less than the measured $(N/C)_{\text{AM,DSB}}$ ratio, even for noiseless bias supplies. In practice,

however, to the author's knowledge, this has never been observed. The closest agreement between MDS/C and $(N/C)_{AM,DSB}$ for any device has been with the BARITT diode (see References 2 and 11 and the noise measurements in Reference 74). Figure 7.4 is a plot of measured X-band MDS/C values¹¹ for four different BARITT diode structures, a commercial IMPATT diode and a commercial Gunn diode vs. their RF output powers. Clearly the BARITT structures are all superior in terms of MDS values and the 16-V and 50-V BARITT structures are superior in terms of path loss as well. These results can be explained, at least qualitatively, with the aid of Eq. 7.20 as follows:

1. The intrinsic RF open-circuit noise voltage for the BARITT and the Gunn are comparable since they both arise substantially from diffusion noise sources. The intrinsic RF open-circuit noise voltage for an IMPATT is several orders of magnitude higher since it results from the avalanche multiplication process. Thus the IMPATT is inferior on an equal RF drive basis in terms of $[\hat{e}_{Hn}]^2$.

2. The Gunn diode appears to be a poor downconverter a posteriori and suffers in comparison to the BARITT and the IMPATT. Nagano and Akaiwa⁶⁹ measured conversion sensitivity values for an X-band Gunn which can be approximately expressed in terms of the notation of this study as δv_c . They found maximum values of δv_c of less than 0.6 V. This is to be compared with values of several hundred or more for a BARITT or an IMPATT. Thus the LF noise contribution is more dominant in the MDS/C expression for the Gunn device. Also, the "corner frequency" for the $1/f$ LF noise

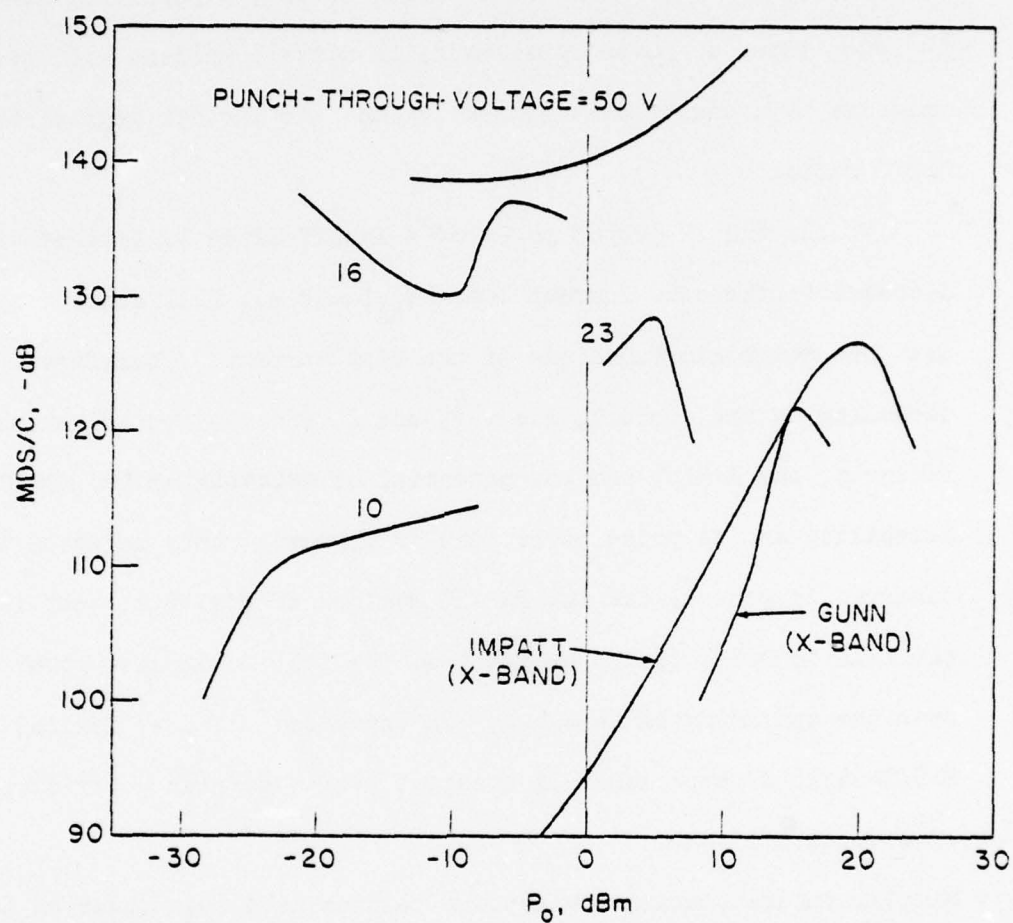


FIG. 7.4 MEASURED MINIMUM DETECTABLE SIGNAL TO CARRIER RATIOS
FOR DIFFERENT X-BAND DEVICES (ADOPTED FROM REFERENCE 11).
($f_m = 10$ kHz)

of a Gunn appears to be higher than its IMPATT and BARITT counterparts.⁷⁵⁻⁷⁷

3. The LF noise voltage of an IMPATT varies inversely with bias current.^{78,79} Therefore at lower RF output power levels--due to lower input dc power levels--the LF noise component will rise, relative to a higher bias current value, and further degrade the MDS/C ratio.

4. As the RF output power of a BARITT diode is lowered via a decrease in the bias current both $|\hat{e}_{Hn}|$ and e_{Ln} fall since they are both monotonic functions of the bias current. Therefore, depending on the circuit, i.e., v_c and k , and the rectification factor β , the BARITT has the potential of maintaining its MDS/C capability as its prime power (dc) is lowered. This behavior is observed in general for the BARITT devices of Fig. 7.4; that is, the fall in MDS/C is not as great as the fall in carrier power over the operating range shown. In one case, the 16-V device, the MDS/C ratio is approximately constant over a carrier power drop of more than 15 dB.

Similar substantiating comparative results have been observed at K-band¹² and at very-low modulation frequencies at X-band.⁸⁰

A detailed theoretical study of the K-band BARITT diode structure first presented in Chapter VI (see Fig. 6.13) is given in Figs. 7.5 through 7.9. All the results presented are at a single RF drive frequency of 21.3 GHz to correspond to the experimental study of Reference 12. Shown in Fig. 7.5 is an R-X plot of the diode impedance as a function of bias current density and the magnitude of the RF drive voltage across the diode. The two tuning

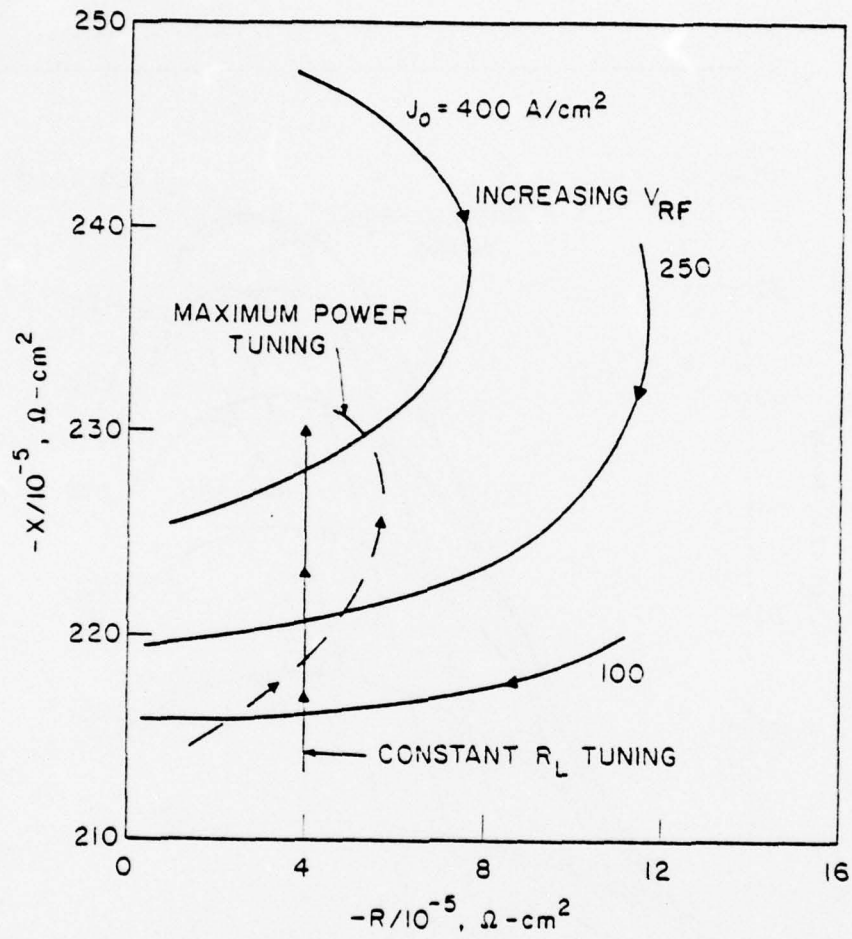


FIG. 7.5 LARGE-SIGNAL R-X TUNING TRAJECTORIES FOR K-BAND BARITT DIODE. (Si, p^+np^+ , $N_d = 4 \times 10^{15} \text{ cm}^{-3}$, $w_B = 3.0 \text{ } \mu\text{m}$ AND $f = 21.3 \text{ GHz}$)

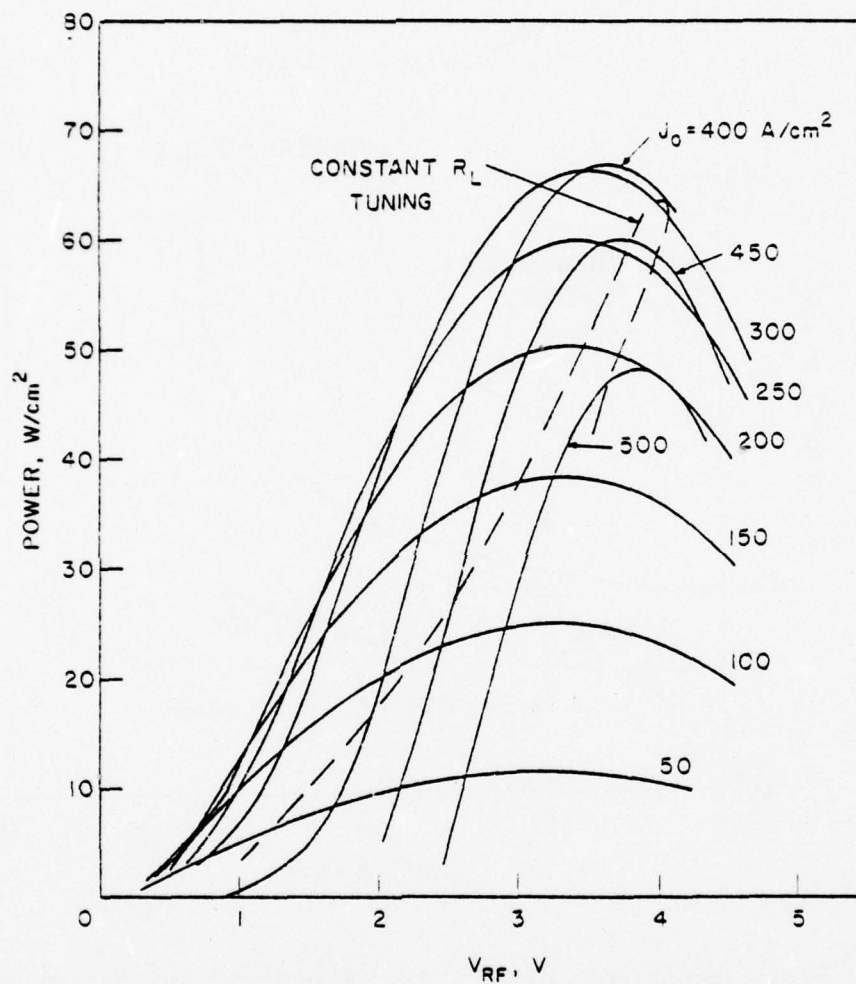


FIG. 7.6a RF OUTPUT POWER FOR K-BAND BARITT DIODE
AS A FUNCTION OF DRIVE AND BIAS. ($f = 21.3$ GHz)

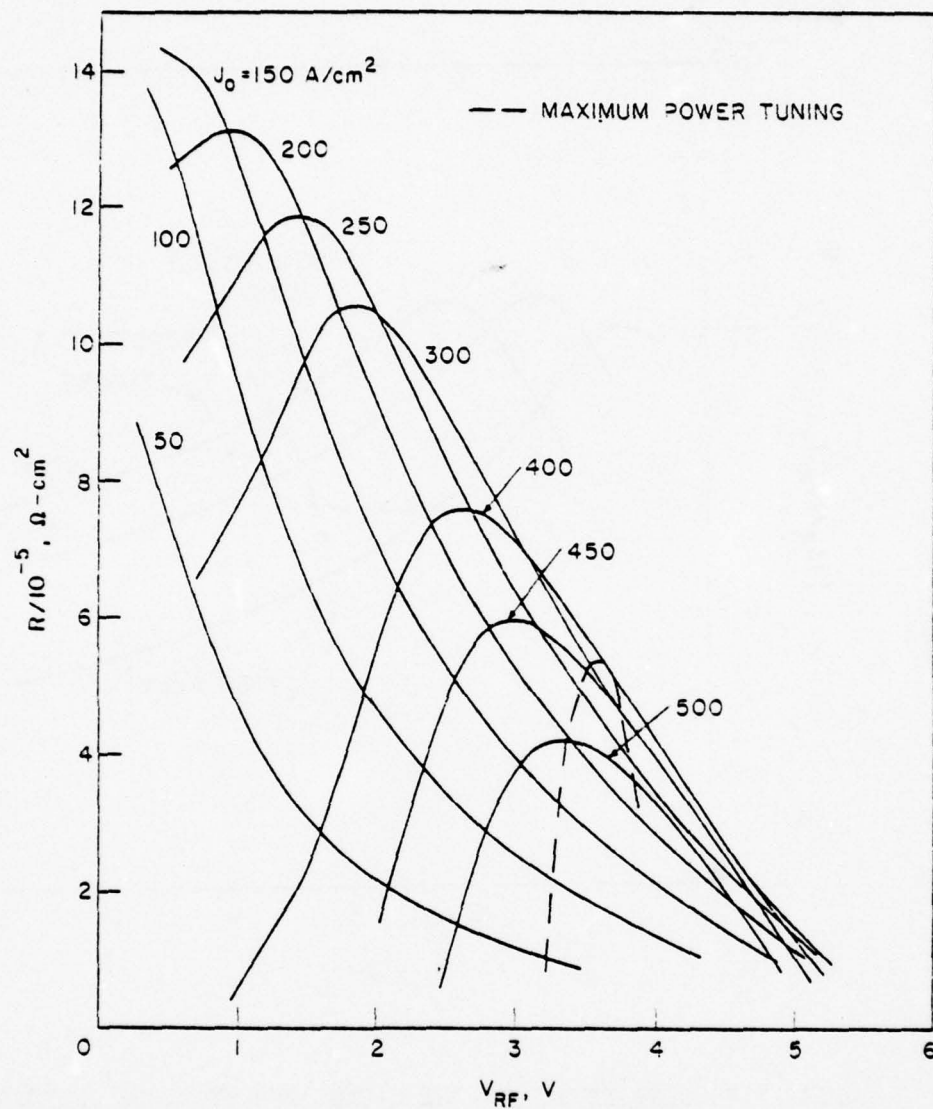


FIG. 7.6b LARGE-SIGNAL NEGATIVE RESISTANCE OF K-BAND BARITT
DIODE AS A FUNCTION OF DRIVE AND BIAS. ($f = 21.3 \text{ GHz}$)

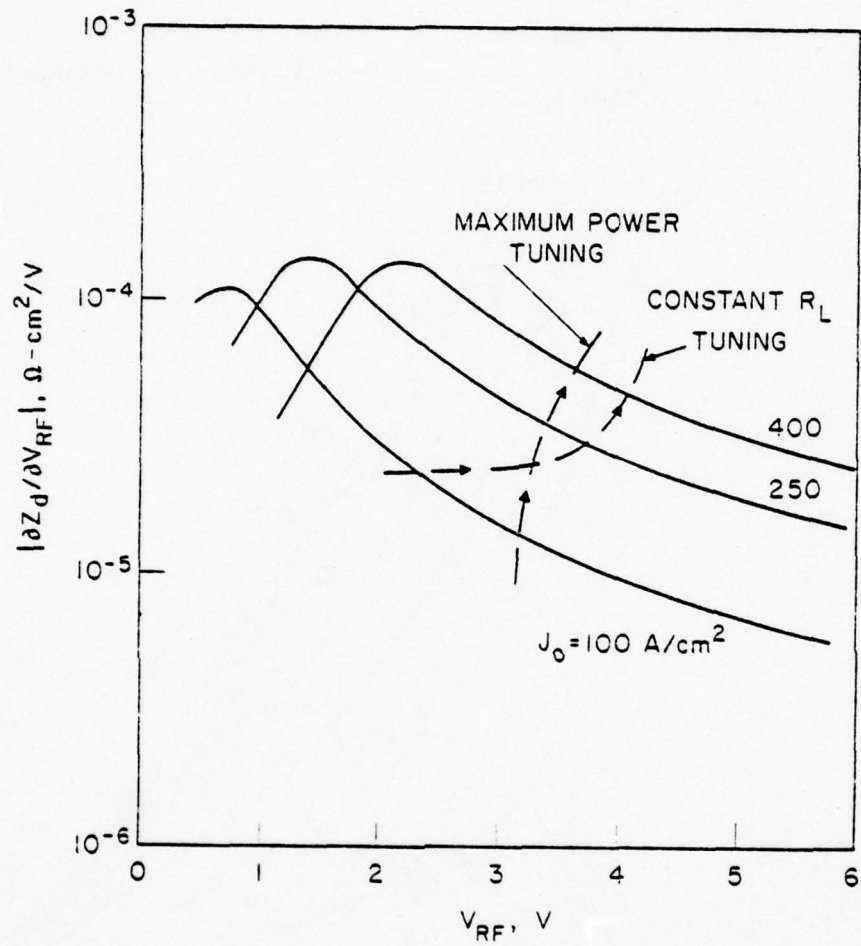


FIG. 7.7 SENSITIVITY OF THE K-BAND BARITT DIODE IMPEDANCE WITH RESPECT TO DRIVE AS A FUNCTION OF DRIVE, BIAS AND TUNING. ($f = 21.3 \text{ GHz}$)

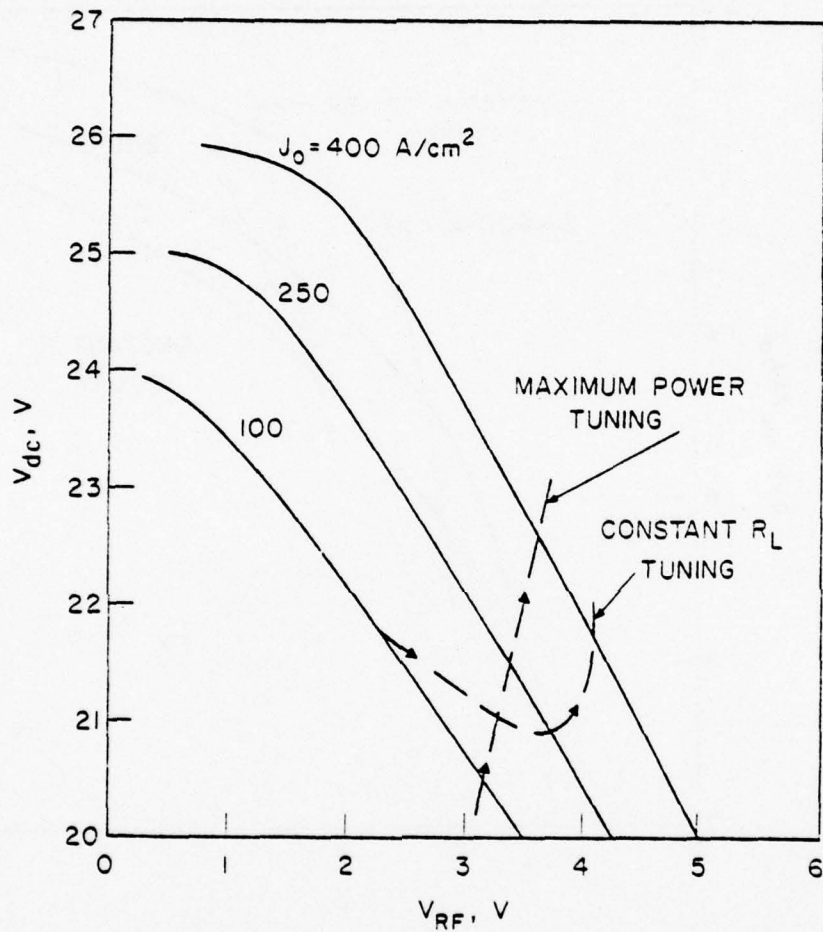


FIG. 7.8a RECTIFICATION EFFECT FOR THE K-BAND BARITT DIODE
AS A FUNCTION OF BIAS AND TUNING. ($f = 21.3$ GHz)

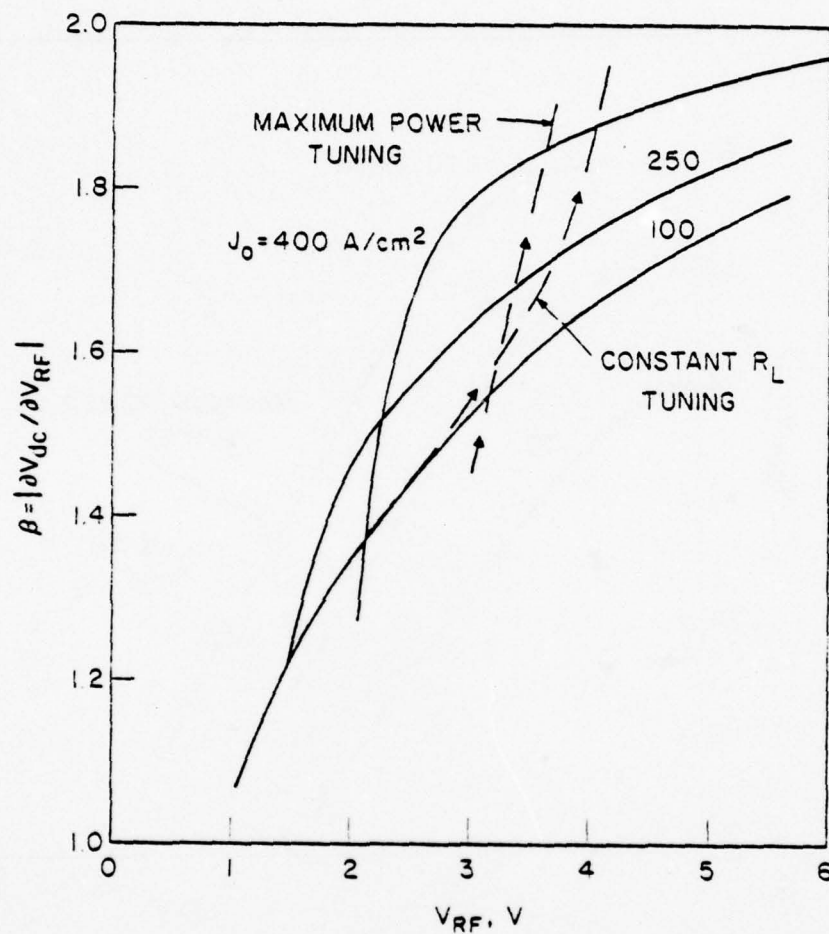


FIG. 7.8b RECTIFICATION EFFECT FACTOR β FOR THE K-BAND BARITT DIODE AS A FUNCTION OF DRIVE, BIAS AND TUNING.
($f = 21.3 \text{ GHz}$)

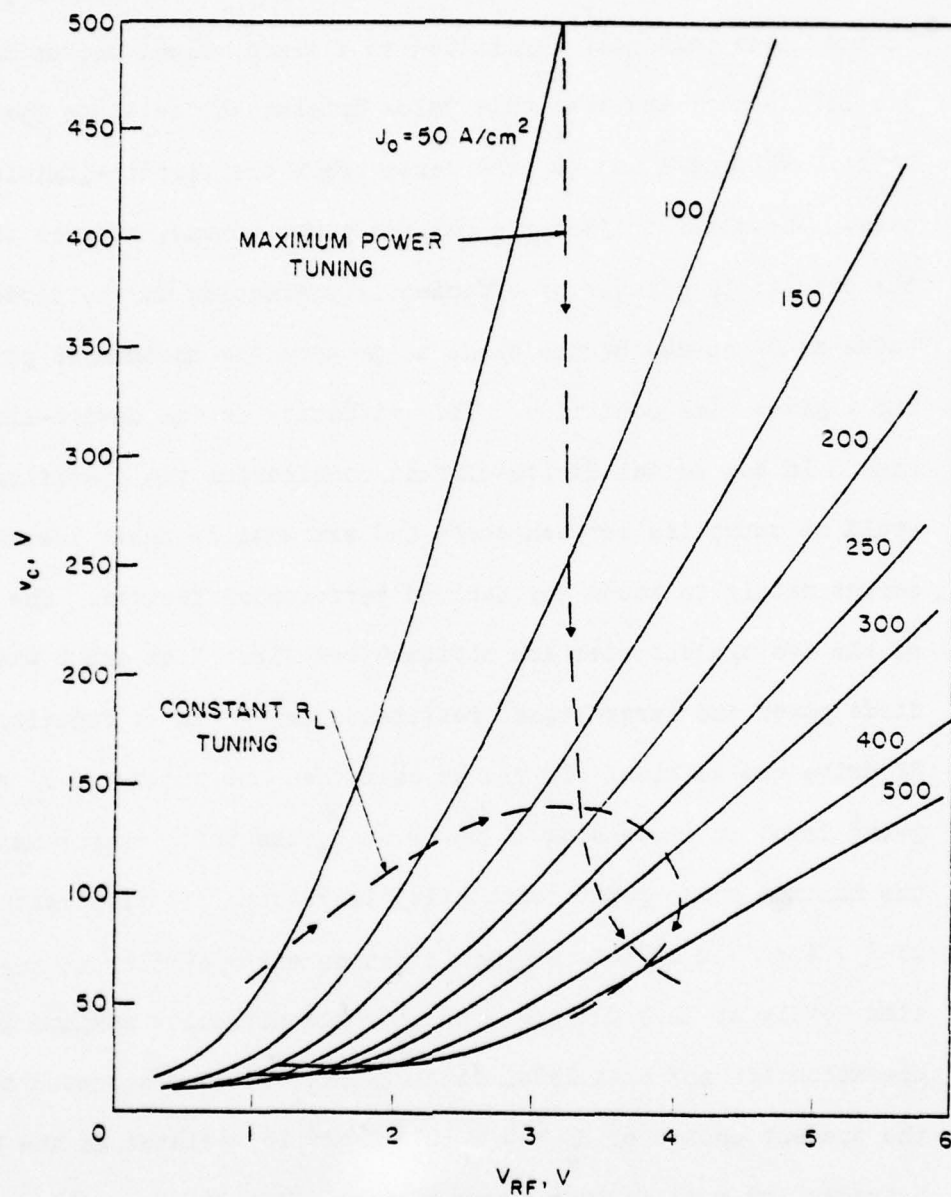


FIG. 7.9 DEVICE-CIRCUIT INTERACTION VOLTAGE V_c FOR THE K-BAND BARITT DIODE AS A FUNCTION OF DRIVE, BIAS AND TUNING. ($f = 21.3$ GHz)

trajectories indicated in the figure represent the two limiting cases of device-circuit interaction. One case, constant R_L tuning ($R_L = R_c$), assumes that the minimum practical* resistance that can be presented to the diode terminals is limited to a fixed value, chosen here as $4 \times 10^{-5} \Omega\text{-cm}^2$, and that this value determines the diode operating point. This case can be considered to be the circuit-limiting case. The other trajectory, maximum power tuning, assumes that the circuit is capable of efficiently presenting to the diode any value of R_L needed by the diode to produce its maximum RF power for a given bias condition. This situation is the device-limiting case. In any actual device-circuit combination the operating point would no doubt lie between these two extremes so their identification serves mainly to bound any derived performance factors. The origins of the two trajectories are obvious from Figs. 7.6a and b where the diode power and large-signal resistance are given as functions of RF drive and dc bias. It can be seen that the choice of $R_L = 4 \times 10^{-5} \Omega\text{-cm}^2$ leads to increasing RF power with bias until approximately the maximum power point (with bias) is reached. A different choice of R_L , i.e., $6 \times 10^{-5} \Omega\text{-cm}^2$, would not permit operation at the higher bias levels at 21.3 GHz and in fact would not allow maximum power operation for any bias level at 21.3 GHz. It is also noted that the present choice of $R_L \geq 4 \times 10^{-5} \Omega\text{-cm}^2$ is violated at the bias extremes for pure maximum power tuning. Clearly then, the choice of the actual operating point will be a compromise process depending on both the circuit and the bias.

* Practical in the sense of maintaining a reasonable coupling efficiency.

The dependence of the system determinant $|Z_{dv}|$ on drive, bias and tuning is shown in Fig. 7.7. In general, $|Z_{dv}|$ falls with diode RF output power and thus the system becomes more sensitive to disturbances as the diode RF power decreases. This is desirable since for constant current bias the LF device noise is removed from the upconversion-downconversion loop and its effect in the LF circuit is thus diminished by increased loop sensitivity. The diode rectification effect is shown in Figs. 7.8a and b. The rectification factor β is seen to less than double over the entire range of the plot and as such can be considered a very weak function of bias and tuning. The theoretical device-circuit interaction voltage v_c is shown in Fig. 7.9. The comparison between these values and the Gunn diode values of βv_c mentioned previously is most striking. Also apparent is the desirability of operation in a device-limited circuit environment. Of course practical limitations govern the extent or even prevent the existence of any such environment for a given actual circuit so the trend toward better MDS/C performance with lower prime (bias) power must eventually reverse.

To complete the K-band device study the measured MDS values¹² in a 1-Hz bandwidth for an experimental version of the diode (chip area $\approx 2 \times 10^{-5} \text{ cm}^2$) are shown in Fig. 7.10. The maximum path loss capability for this device at a modulation frequency of 10 kHz, $\sim 117 \text{ dB}$, is 30 dB worse than the best X-band measured value, Fig. 7.4. Since the difference in RF output power between the two diodes at their optimum MDS/C operating points is approximately 15 dB it is logical to assume that the K-band diode performance is hindered by its circuit. Also, the theoretical maximum RF output

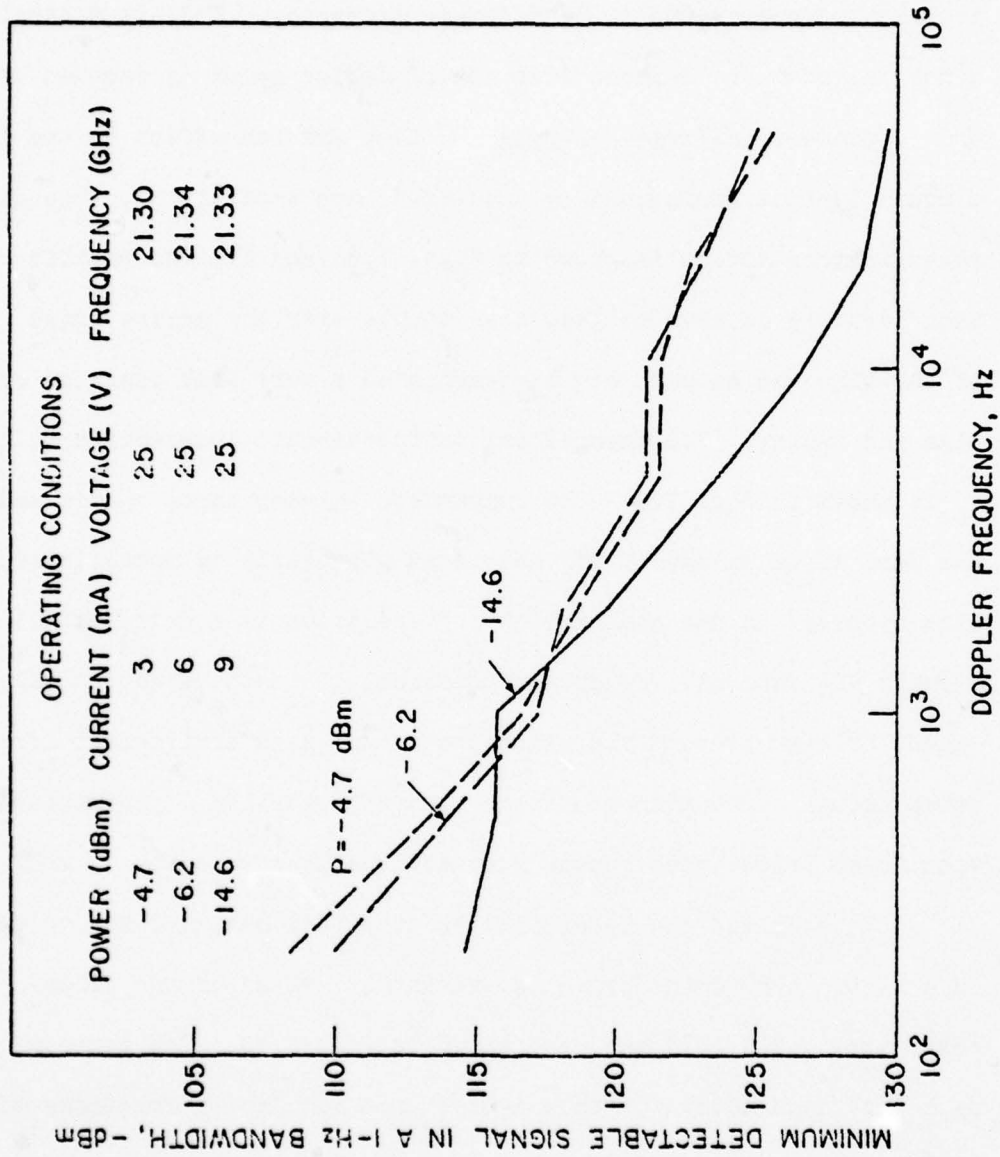


FIG. 7.10 K-BAND BARTLETT DIODE DOPPLER DETECTOR SENSITIVITY.

power for this device over its region of negative resistance is approximately an order of magnitude higher than that observed experimentally. Given the relatively close agreement between theory and experiment for RF output power at X-band, this level of disagreement further reinforces the supposition that the experimental device is circuit limited.

7.3 Four-Frequency BARITT Diode Mixers

7.3.1 Introduction. The analysis of very-low IF mixers presented in Section 7.2 was restrictive in the sense that both the amplitude of the diode RF perturbation voltage and the intermediate frequency were required to be small. In this section a general small-signal analysis is presented for the BARITT diode mixer in which the value of the intermediate frequency is unrestricted. The method of analysis follows closely the work of Hines¹⁵ on IMPATT diodes and is essentially a straightforward extension of classic nonlinear resistive mixer theory.^{81,82} Similar to the detector study of Chapter IV the particle current injection region (the forward-biased region of the diode) is assumed to be the only nonlinear element of the device. The forward-biased region displacement capacitance at first glance could also be considered to be pumped, since the extent of the region changes with the pumping voltage. However, considering the diode as a whole, the total displacement capacitance is fixed and does not vary with RF drive since the diode is a punch-through structure. Therefore if we define an "average" forward-bias region width, the phase of the injected particle current will on the average be correct. This is definitely an approximation, but one that greatly facilitates a closed-form solution. Hines

assumed that actual frequency conversion occurs only in the nonlinear injection region (avalanche region) of an IMPATT diode and that the drift region serves only as a linear parasitic (active or passive) impedance. This is similar to the two-frequency harmonic large-signal study of Mouthaan⁶⁰ discussed in Chapter VI except that only the pump signal is assumed to be large while the other perturbing signals, nonharmonically related, are all assumed to be small.

The IMPATT diode frequency conversion analysis of Evans and Haddad⁸³ considered the entire diode to be the nonlinear frequency converting element, the effect of which was a restriction of their closed-form analytical solutions to frequency regions which resulted in small diode drift transit angles. The approach taken here, ala Hines, is to solve for the frequency converting transadmittance terms of the forward-biased region of the diode, much like the two-frequency study of Chapter VI, and then include the effect of the diffusion-drift region in a manner similar to the derivation of the small-signal diode model of Chapter III. A coupled three-frequency equivalent circuit is thus formed from which the conversion and noise properties* of any specified mixer network can be determined by simple circuit analysis.

Two basic modes of operation for the BARITT diode mixer can be identified: an active mode in which pump power is supplied by the diode itself, i.e., the self-oscillating mixer, and a passive mode in which pump power is supplied from an external source. Both modes of operation are discussed in this work.

* The IF is assumed to be of sufficient magnitude such that noise contributions of the pump (i.e., oscillator noise) are negligible.

7.3.2 The Frequency Conversion Process in a BARITT Diode and Frequency Converter Circuits. As developed in Chapter II the particle current injected into the diffusion-drift region of a BARITT diode is a near exponential function of the total applied voltage across the forward-biased region; that is, c.f., Eq. 2.23,

$$J(t) = J_s \exp[V_F(t)/V_T] .$$

The applied voltage across the forward-biased region consists of a dc portion V_{F0} , a large-signal pumping voltage $V_p(t)$, and a number of small-signal information carrying voltages $\sum_n v_{Fn}(t)$ arising from the input signal or signals and the subsequent conversion process. Since all the information carrying voltages are assumed to be small, the injected particle current density can be expanded as

$$J(t) = J_p(t) \left(1 + \frac{1}{V_T} \sum_n v_{Fn}(t) \right) , \quad (7.21)$$

where $J_p(t)$ is that portion of the injected current that is due to the dc bias and the pumping signal only. For a periodic $V_p(t)$ with fundamental angular frequency ω_p , $J_p(t)$ can be expressed by its complex Fourier series as

$$J_p(t) = J_{dc} + \frac{1}{2} \sum_{m=1}^{\infty} \left(\hat{J}_{pm} e^{jm\omega_p t} + \hat{J}_{pm}^* e^{-jm\omega_p t} \right) ,$$

where J_{dc} is the diode dc current density and \hat{J}_{pm} is the phasor representation of the mth harmonic component of $J_p(t)$. The information voltage terms of Eq. 7.21 can also be written in complex form as

$$\sum_n v_{Fn}(t) = \frac{1}{2} \sum_n \left(\hat{v}_{Fn} e^{j\omega_n t} + \hat{v}_{Fn}^* e^{-j\omega_n t} \right).$$

Substituting these expressions into Eq. 7.21 and performing the indicated multiplication yields

$$\begin{aligned} J(t) = & J_{dc} + \frac{1}{2} \sum_{m=1}^{\infty} \hat{J}_{pm} e^{jm\omega_p t} + \frac{g_e}{2} \sum_n \hat{v}_{Fn} e^{j\omega_n t} \\ & + \frac{1}{2} \sum_{m=1}^{\infty} y_m \sum_n \left(\hat{v}_{Fn} e^{j(m\omega_p + \omega_n)t} + \hat{v}_{Fn}^* e^{j(m\omega_p - \omega_n)t} \right) \\ & + c. c. , \quad (7.22) \end{aligned}$$

where g_e is the small-signal conductance of the forward-biased region ($g_e = J_{dc}/V_T$), y_m is a defined transadmittance,

$$y_m = \frac{g_e}{2} \cdot \frac{\hat{J}_{pm}}{J_{dc}}, \quad (7.23)$$

and c. c. is the complex conjugate of all the previous quantities on the right-hand side of the equation except the dc current term. It is evident from Eq. 7.22 that a small-signal voltage across the forward-biased region at frequency ω_n gives rise to injected particle currents at frequencies ω_n , $m\omega_p + \omega_n$ and $m\omega_p - \omega_n$. Hines¹⁵ convenient and simple numbering system is adopted for keeping track of the different frequencies. That is, it is assumed that the lowest frequency information voltage which exists across the forward-biased region is at an angular frequency ω_0 with $\omega_0 \leq \omega_p/2$. The

injection currents associated with this signal voltage are then at frequencies

$$\omega_k = |k|\omega_p \pm \omega_0 \begin{cases} + \rightarrow k \geq 0 \\ - \rightarrow k < 0 \end{cases}.$$

The information portion of $J(t)$ can now be expressed in complex form in terms of these frequencies ω_k , i.e.,

$$\frac{1}{2} \sum_k \left(\hat{J}_k e^{j\omega_k t} + \hat{J}_k^* e^{-j\omega_k t} \right).$$

If coefficients of like exponentials on the left-hand side and right-hand side of Eq. 7.22 are equated, two infinite rank matrix equations, one the complex conjugate of the other, can be formed relating the phasor injected particle currents \hat{J}_k due to the phasor information carrying voltages \hat{V}_{Fk} . As a first-order approximation it is assumed that only three information carrying voltages exist across the forward-biased region and that these voltages are at frequencies ω_0 , $\omega_1 = \omega_p + \omega_0$ and $\omega_{-1} = \omega_p - \omega_0$. A completely deterministic 3 by 3 submatrix equation can then be extracted from either one of the full matrix equations. The submatrix equation chosen here is

$$\begin{pmatrix} \hat{J}_{-1}^* \\ \hat{J}_0 \\ \hat{J}_1 \end{pmatrix} = \begin{pmatrix} g_e^* & y_1^* & y_2^* \\ y_1 & g_e & y_1^* \\ y_2 & y_1 & g_e \end{pmatrix} \begin{pmatrix} \hat{V}_{F-1}^* \\ \hat{V}_{F0} \\ \hat{V}_{F1} \end{pmatrix}. \quad (7.24)$$

The particle injection currents of Eq. 7.24 are transported across the diffusion-drift region of the diode and give rise to induced terminal currents at the collector. At each frequency ω_k , the collector terminal total current \hat{J}_{tk} can be expressed as

$$\hat{J}_{tk} = \hat{\Gamma}_{Bk} \hat{J}_k + Y_{Bk} \hat{V}_{Bk} \quad , \quad (7.25)$$

where \hat{V}_{Bk} is the small-signal phasor voltage across the diffusion-drift region. Equation 7.25 in conjunction with Eqs. 3.48 and 3.51 suggests the equivalent circuit of Fig. 7.11 for an example frequency of ω_1 . Similar equivalent circuits hold at ω_0 and ω_{-1} . External circuits and sources at each of the three frequencies of interest complete the description of the BARITT diode frequency converter and a simultaneous solution of the three coupled circuits is required for a complete description of the conversion properties of the diode. Hines¹⁵ presented closed-form expressions for the solution of an IMPATT version of this problem but they are so cumbersome that only after numerous restricting simplifying assumptions can any insight be obtained from them. Peterson⁸⁴ obtained solutions for the same IMPATT problem by expressing the coupling between the three circuits in terms of equivalent two-port network parameters. This results in one large coupled circuit which can be analyzed by any convenient linear network analysis computer program. The disadvantage of such an approach is that any possible insight obtainable from a closed-form solution is lost. However, this loss is far outweighed by the speed and ease with which the analysis is implemented. The second course, that of Peterson, is chosen here

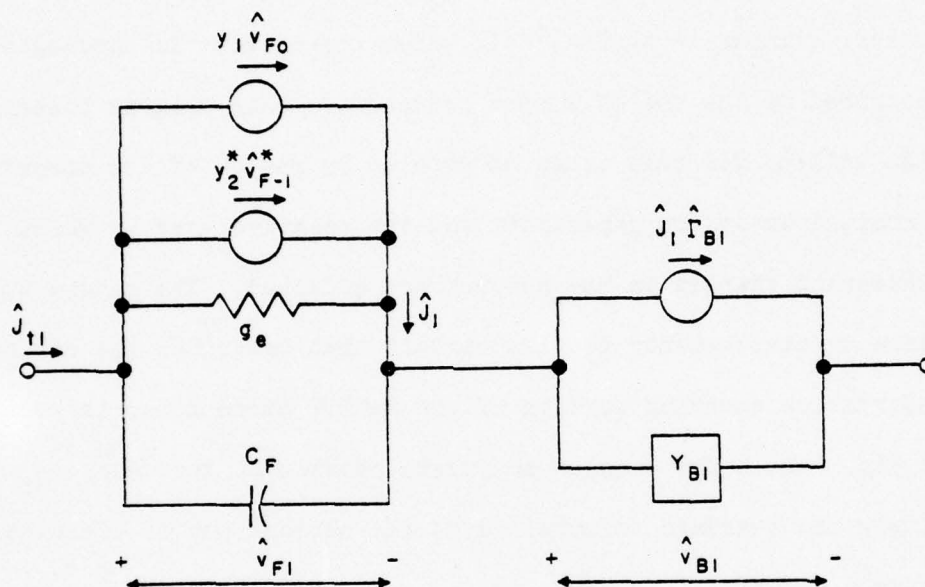
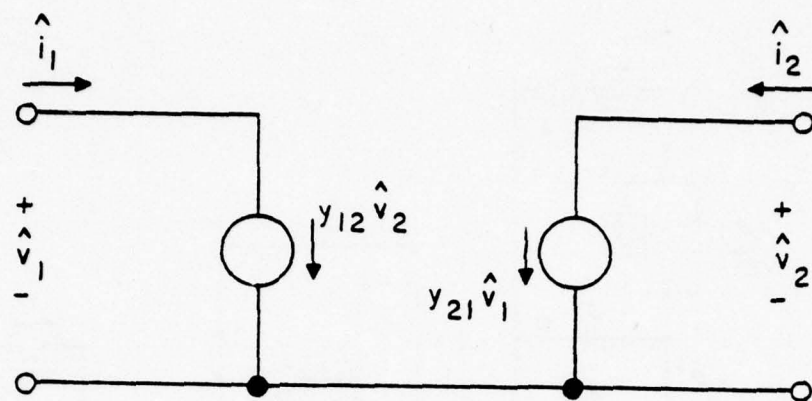


FIG. 7.11 SMALL-SIGNAL EQUIVALENT CIRCUIT OF THE PUMPED BARITT DIODE AT THE INPUT SIGNAL FREQUENCY ω_1 .

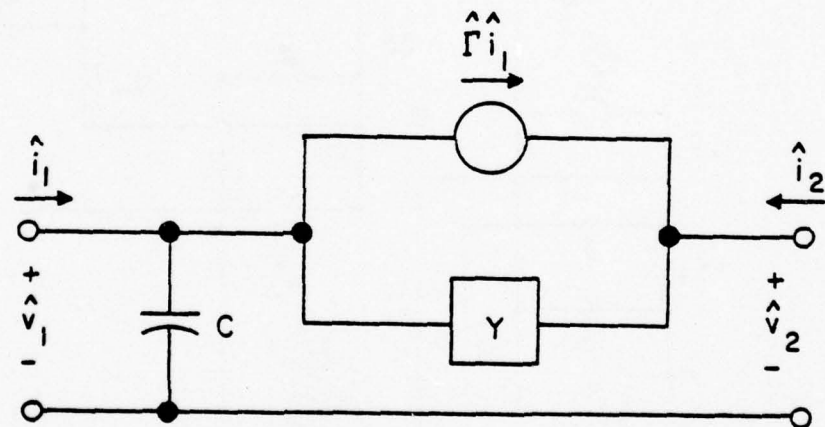
as the method of solution for coupled networks of the BARITT diode mixer.

The two-port network parameters, in this case the ABCD parameters, that describe the coupled circuits typified by Fig. 7.11 are depicted in Fig. 7.12. The ABCD parameters were chosen to enable the use of a linear circuit analysis program written by the author, similar to MARTHA,⁸⁵ in which the network is topologically described by the use of wiring operators. This program possesses a high utility for this class of problem by reason of its powerful circuit description capability and the relative ease by which subsequent changes in the network are affected. The single but large three-frequency coupled circuit that describes the entire information carrying portion of the BARITT diode mixer is shown in Fig. 7.13. The complex conjugate network at frequency ω_{-1} is simply the standard formulation of the network but is evaluated using a negative frequency, $-\omega_{-1}$.

The principal interest of this section is the downconversion properties of the BARITT diode. For this application, signals in the input frequency network, either the ω_1 network [an upper-sideband downconverter (USBDC)] or the ω_{-1} network [a lower-sideband downconverter (LSBDC)], are converted to signals in the other two frequency networks. The desired conversion is to the ω_0 circuit so a conversion gain (power gain) of the mixer can be defined as the ratio of power delivered to the external circuit load at ω_0 to the available power of the input signal generator. That is,



(a)



(b)

FIG. 7.12 ABCD PARAMETERS OF TWO ELEMENTS OF A BARITT DIODE

FREQUENCY CONVERTER EQUIVALENT CIRCUIT. (a) TRANSADMITTANCE

NETWORK ($A = D = 0$, $B = 1/y_{21}$, $C = y_{12}$) AND (b) LINEAR

PORTION OF A BARITT DIODE [$A = 1 + (j\omega C/Y)$, $B = (1 - r)/Y$,

$C = j\omega C$, $D = 1$].

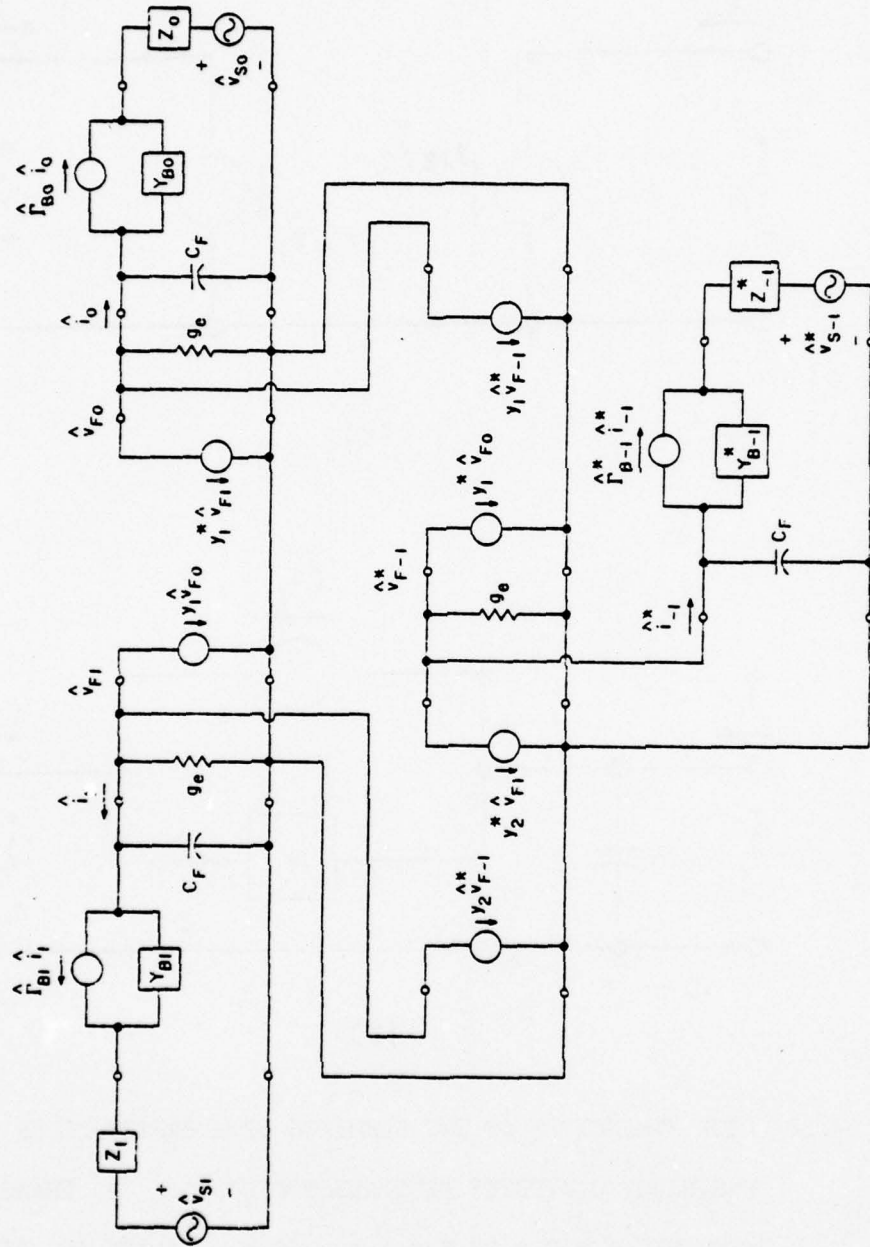


FIG. 7.13 COMPLETE BARITT DIODE FREQUENCY CONVERTER EQUIVALENT CIRCUIT.

$$\text{Gain} = \text{PG} = \frac{\frac{1}{2} |\hat{i}_o|^2 \text{Re}(Z_o)}{\frac{1}{8} \frac{|\hat{v}_{s\pm 1}|^2}{\text{Re}(Z_{\pm 1})}},$$

where the use of the plus or minus signs depends on the particular type of mixer, USBDC or LSBDC. The conversion gain of a BARITT diode downconverter can be greater than unity for two reasons:

(1) Injection currents at one frequency which result from forward-biased region voltages at another induce both terminal resistive (in phase) currents and terminal reactive (90 degrees out of phase) currents due to transit-time effects. Thus, at the diode terminals the structure appears as a pumped complex nonlinear admittance. The gain properties of a pumped nonlinear admittance have been well documented.^{86,87} (2) Also, due to transit-time effects, there are frequency regions of diode negative resistance which can be employed to produce conversion gain by combined reflection-type amplification and mixing. In any particular application the two gain phenomena are coincident; since they both result from transit-time effects and no attempt will be made to individually identify them. Rather, the possibility of conversion gain greater than unity is considered as a stability question.

Consider the case of a USBDC. The image frequency network, the ω_{-1} network, is terminated with the external impedance Z_{-1}^* . Thus from the signal ω_1 and the IF ω_o diode terminals the converter appears as a simple two-port network. A suitable description for this reduced network is the y-parameter representation shown in Fig. 7.14. Obviously the LSBDC circuit can be studied in a completely

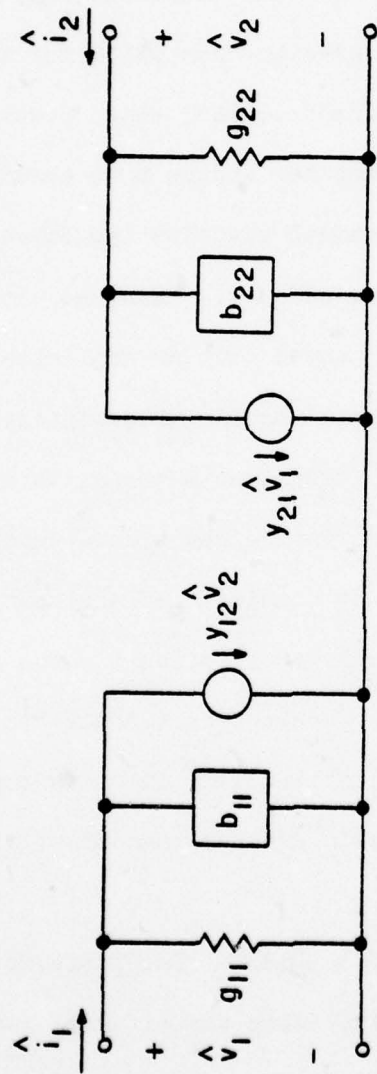


FIG. 7.14 y -PARAMETERS FOR A REDUCED FREQUENCY CONVERTER NETWORK (IMAGE PORT TERMINATED).

analogous manner. A linear two-port network is said to be unconditionally stable if all three of the following conditions are satisfied:^{88,89}

$$1. \quad g_{11} > 0 ,$$

$$2. \quad g_{22} > 0$$

and

$$3. \quad 0 \leq C < 1 ,$$

where C is the Linvill stability factor⁸⁸ and is given by

$$C = \frac{|y_{21} y_{12}|}{2g_{11}g_{22} - \text{Re}(y_{21}y_{12})} .$$

When C falls outside the range of condition 3 there exists a set of passive terminations such that either the input conductance or the output conductance, or both, are negative. If one or more of the three stability conditions are not met the downconverter is capable of infinite gain, i.e., oscillation. This does not degrade the potential of the diode as a useful converter. It only requires that care be taken in the external circuit design to ensure that oscillation is avoided. The ultimate performance indicator of any mixer is its noise performance or noise figure. In this context, the question of whether or not a mixer is capable of a power gain greater than unity is a secondary concern.

7.3.3 Determination of the Transadmittance Terms. The

transadmittance terms y_m present in Eq. 7.24 and defined in Eq. 7.23 depend only on the dc bias and the large-signal pump voltage $V_p(t)$ across the forward-biased region of the diode. Drawing from the large-signal study of Chapter VI we can identify the pump voltage as the specified large-signal drive voltage across the forward-biased

region. For the first-order approximation of a single sinusoidal voltage across the forward-biased region,

$$V_p(t) = V_{F1} \cos \omega_p t ,$$

we have (see Eqs. 6.4 and 6.7)

$$y_m = \frac{g_e}{2} \frac{2I_m(V_{F1}/V_T)}{I_o(V_{F1}/V_T)} , \quad m = 1, 2, \dots \quad (7.26)$$

In this case the phasor injection currents \hat{J}_{pm} are all real quantities since the choice of the phase reference (time origin), the phase of pumping voltage, has resulted in $J_p(t)$ being an even function of time. For the second-order approximation

$$V_p(t) = V_{F1} \cos(\omega_p t + \phi) + V_{F2} \cos(2\omega_p t + 2\phi + \psi) ,$$

a fundamental and second-harmonic voltage drive with arbitrary phase reference ϕ , we have, from Eqs. 6.4 and 6.8,

$$y_m = \frac{g_e}{2} \frac{C_m + jS_m}{D_o} e^{jm\phi} , \quad m = 1, 2 , \quad (7.27)$$

where C_m , S_m and D_o are defined in the equations immediately following Eq. 6.8 in Chapter VI. In this case, given that the relationships between V_{F1} , V_{F2} and ψ are not arbitrary but are device-circuit determined, it is not clear nor is it necessarily possible that ϕ (a time origin) can be chosen such that both y_1 and y_2 will be pure real.

An example of the sensitivity of the transadmittances to the order of approximation used in their calculation is shown in Table 7.1.

The first- and second-order approximation values for the y_m of a K-band diode examined previously (see Table 6.2), dc maximum power structure No. 3, are given for a particular set of drive conditions that produce a negligible second-harmonic terminal voltage. As can be seen, a choice of $\phi = -24.2$ degrees as the phase reference of the fundamental drive voltage in the two-frequency pumping case results in transadmittance terms that are easily within 4 percent of the single-frequency pumping values. Thus, the single-frequency values are entirely adequate. These results are deemed typical for all device-circuit configurations which limit the voltage across the diode terminals to a single frequency value (considering the pump signal only) and as such the first-order approximation will be exclusively used in the remainder of this study.

Table 7.1

First- and Second-Order Approximations for a K-Band Diode

$$(N_d = 5 \times 10^{15} \text{ cm}^{-3}, w_B = 4 \text{ } \mu\text{m}, J_0 = 400 \text{ A/cm}^2,$$

$$\text{Fundamental Frequency} = 20 \text{ GHz}, V_{F1} = 0.4 \text{ V}, V_{F2} = 0.093 \text{ V},$$

$$\psi = 321 \text{ Degrees})$$

<u>Transadmittance Term (mho/cm²)</u>	<u>First-Order Value</u>	<u>Second-Order Value x e^{-mφ} m = 1 or 2</u>
y_1	1.935	1.915 /24.2 Degrees
y_2	1.750	1.689 /49.2 Degrees

7.3.4 BARITT Diode Mixer Noise Figure. The noise figure of a network is defined as the ratio of the input signal-to-noise ratio to the output signal-to-noise ratio when the input noise is thermal noise at room temperature. That is,

$$NF = \frac{(S/N)_{in}}{(S/N)_{out}} = \frac{S_{in}}{S_{out}} \cdot \frac{N_{out}}{N_{in}} .$$

If a network gain G is identified such that $S_{out} = G \cdot S_{in}$ and $N_{out} = G \cdot N_{in} + N_e$ then

$$NF = 1 + \frac{N_e}{G \cdot N_{in}} , \quad (7.28)$$

where N_e is the excess noise at the output due to the network alone and N_{in} is the input thermal noise.

The excess noise at the IF port of the downconverter circuit of Fig. 7.13 can be determined by the use of the noise theories developed in Chapter III and the principle of superposition. At each frequency ω_0 , ω_1 and ω_{-1} the signal voltage generator is replaced by the diode open-circuit noise voltage \hat{V}_{ni} due to diffusion noise, and a shunt shot noise current generator \hat{I}_{ni} is added across the small-signal conductance of the forward-biased region. Since the noise properties of any network are unaffected by the output port termination, one simple measure of the output excess noise is the open-circuit noise voltage ($Z_o = \infty$) across the diode terminals at ω_0 . This voltage can be found by considering each noise voltage generator or noise current generator separately and adding all the

results. The excess noise voltage at the IF port will then be of the form

$$\hat{v}_{ne,o} = T_{10} \hat{v}_{n1} + T_{-10} \hat{v}_{n-1} + \hat{v}_{no} + Z_{10} \hat{i}_{n1} + Z_{-10} \hat{i}_{n-1} + Z_{oo} \hat{i}_{no} , \quad (7.29)$$

where the transfer terms T_{ij} and Z_{ij} are each found from the solution of the circuit of Fig. 7.13 for a voltage input at the diode terminals or a current input across the forward-biased junction, at frequency ω_i , and a voltage output at the IF diode terminals. The diffusion noise contributions to Eq. 7.29 arise from the diffusion-drift region of the diode which, in our approximate analysis, is unpumped. Thus they remain uncorrelated for any level of mixer operation. However the shot noise contributions to Eq. 7.29 are directly determined by the pumping level, the large-signal injected particle current, and can thus be expected to exhibit deterministic in-phase properties since the pumping is periodic. With these facts in mind the output excess noise voltage has a mean square value of

$$\begin{aligned} \overline{|\hat{v}_{ne,o}|^2} &= |T_{10}|^2 \overline{|\hat{v}_{n1}|^2} + |T_{-10}|^2 \overline{|\hat{v}_{n-1}|^2} + \overline{|\hat{v}_{no}|^2} \\ &+ |Z_{10}|^2 \overline{|\hat{i}_{n1}|^2} + |Z_{-10}|^2 \overline{|\hat{i}_{n-1}|^2} + |Z_{oo}|^2 \overline{|\hat{i}_{no}|^2} \\ &+ 2\text{Re}(Z_{10}^* Z_{oo} \overline{\hat{i}_{n1} \hat{i}_{no}^*} + Z_{-10}^* Z_{oo} \overline{\hat{i}_{n-1} \hat{i}_{no}^*} + Z_{10}^* Z_{-10} \overline{\hat{i}_{n1} \hat{i}_{n-1}^*}) . \quad (7.30) \end{aligned}$$

Kim,⁹⁰ in an extension of Strutt's fundamental work,¹⁶ has shown that the correlation of the shot noise components can be expressed, in the notation of this study, as

$$2 \operatorname{Re} (Z_{10} Z_{00}^* \overline{\hat{I}_{n1} \hat{I}_{no}^*} + Z_{-10} Z_{00}^* \overline{\hat{I}_{n-1} \hat{I}_{no}^*}) = \frac{2qJ_{p1}}{A} \operatorname{Re} [(Z_{10} + Z_{-10}) Z_{co}^*]$$

and

$$2 \operatorname{Re} (Z_{10} Z_{-10}^* \overline{\hat{I}_{n1} \hat{I}_{n-1}^*}) = \frac{2qJ_{p2}}{A} \operatorname{Re} (Z_{10} Z_{-10}^*) ,$$

where a unit observation bandwidth has been assumed, A is the cross-sectional area of the diode, and the J_{pm} are the Fourier coefficients of the pumping current density, Eq. 6.7.

The open-circuit noise voltage at the IF port due to the thermal noise from the input signal generator is

$$\overline{|\hat{V}_{ng,o}|^2} = 4qV_T \operatorname{Re} (Z_{\pm 1}) |T_{\pm 10}|^2 ,$$

where again the use of the plus or minus signs depends on the particular mixer configuration, USBDC or LSBDC. The downconversion excess noise figure now becomes

$$NF_e = NF - 1 = \frac{\overline{|\hat{V}_{ng,o}|^2}}{4qV_T \operatorname{Re} (Z_{\pm 1}) |T_{\pm 10}|^2} . \quad (7.31)$$

The expression for the excess noise figure bears a strong resemblance to the noise measure expression presented in Chapter III. If the small-signal diode resistance at frequency $\omega_{\pm 1}$ is defined as $R_{d\pm 1}$ and an excess noise voltage at the IF port due to all the noise sources except the diffusion noise voltage at the signal

frequency is defined as $\hat{v}_{nex,o} = \hat{v}_{ne,o} - \hat{v}_{n\pm 1} T_{\pm 10}$, the excess noise figure expression can be rearranged to yield

$$NF_e = \frac{|R_{d\pm 1}|}{\text{Re}(Z_{\pm 1})} \cdot \frac{|\hat{v}_{n\pm 1}|^2}{4qV_T |R_{d\pm 1}|} + \frac{|\hat{v}_{nex,o}|^2}{4qV_T \text{Re}(Z_{\pm 1}) |T_{\pm 10}|^2}$$

The second multiplicand in the first term is recognized as the noise measure of the diode at $\omega_{\pm 1}$ due to diffusion noise alone. In frequency regions of negative resistance the diffusion noise is the dominant noise contribution to the diode open-circuit noise voltage and the diffusion noise measure is very close to being equal to the total noise measure of the diode. Thus for any number of cases [high $T_{\pm 10}$, $|R_{d\pm 1}| > \text{Re}(Z_{\pm 1})$, etc.] it may be possible for the excess noise figure to be numerically smaller than the diode noise measure. One such theoretical case is examined in detail in Section 7.3.5.

The downconverter excess noise figure defined in Eq. 7.31 is dependent on the equivalent source impedance at the signal frequency $\omega_{\pm 1}$. One can easily determine⁹¹ the optimum source impedance such that the excess noise figure is a minimum if the total excess noise of the diode is transformed through the converter network and is artificially assigned to a shunt noise current source and a series noise voltage source at the signal input terminals as shown in Fig. 7.15. Since all the noise sources of the diode are now represented as noise sources at the now noise-free converter network, the excess noise figure of the converter can be found just from a knowledge of these noise sources alone. That is,

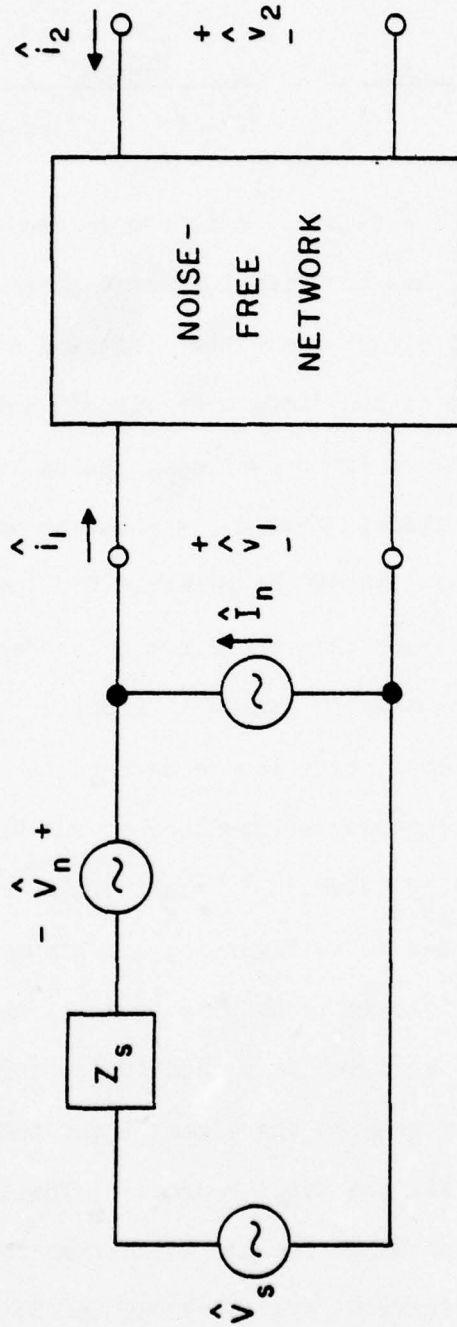


FIG. 7.15 REPRESENTATION OF A LINEAR TWO-PORT NETWORK WITH ALL INTERNAL NOISE SOURCES EXPRESSED AS EQUIVALENT INPUT NOISE SOURCES \hat{V}_n AND \hat{I}_n .

$$NF_e = \frac{|\hat{V}_{nu}|^2 + |Z_Y + Z_s|^2 |\hat{I}_n|^2}{4qV_T R_s},$$

where a correlation impedance Z_Y has been defined as

$$Z_Y = \frac{\overline{\hat{V}_n \hat{I}_n^*}}{|\hat{I}_n|^2}$$

and \hat{V}_{nu} is that portion of \hat{V}_n which is completely uncorrelated with \hat{I}_n . Obviously, the correct choice for X_s for a minimum NF_e is $X_{s,opt} = -X_Y$. Minimizing the resulting expression for NF_e with respect to R_s leads to the optimum choice⁹¹

$$R_{s,opt} = \left(\frac{R_u + G_n R^2}{G_n} \right)^{1/2},$$

where

$$R_u = \overline{|\hat{V}_{nu}|^2} / 4qV_T$$

and

$$G_n = \overline{|\hat{I}_n|^2} / 4qV_T.$$

The optimum excess noise figure is then

$$NF_{e,opt} = 2G_n (R_Y + R_{s,opt}).$$

Since there are four quantities that determine $NF_{e,opt}$, $\overline{|\hat{V}_{nu}|^2}$, $\overline{|\hat{I}_n|^2}$ and the real and imaginary parts of Z_Y , four different measurements must be made with four different source impedances to completely

determine the optimum source impedance. One satisfactory set of measurements is as follows:

The output open-circuit mean-square noise voltages at the IF port for four different source impedances are denoted as

$$\overline{v_s^2} \rightarrow Z_s = 0 ,$$

$$\overline{v_o^2} \rightarrow Z_s = \infty ,$$

$$\overline{v_R^2} \rightarrow Z_s = R_{st}$$

and

$$\overline{v_x^2} \rightarrow Z_s = jX_{st} ,$$

where R_{st} and X_{st} are arbitrary but finite test source resistance and reactance values, respectively. Then, for the ABCD representation of the noiseless converter network, it is easily shown that

$$|\hat{i}_n|^2 = |C|^2 \overline{v_o^2} ,$$

$$R_Y = \frac{1}{2R_{st}} \left(|A + CR_g|^2 \overline{v_R^2} - |A|^2 \overline{v_s^2} - R_g^2 |C|^2 \overline{v_o^2} \right) ,$$

$$X_Y = \frac{1}{2X_{st}} \left(|A + jCX_g|^2 \overline{v_x^2} - |A|^2 \overline{v_s^2} - X_g^2 |C|^2 \overline{v_o^2} \right)$$

and

$$|\hat{v}_{nu}|^2 = |A|^2 \overline{v_s^2} - |C|^2 |Z_Y|^2 \overline{v_o^2} .$$

All theoretical excess noise figure values presented in this study will be optimized values computed by numerically performing the above experiment using the noise theory of Chapter III.

7.3.5 Results for BARITT Diode Mixers. One of the most intriguing forms of a BARITT diode mixer is the self-oscillating or autodyne version. The diode is placed in a circuit environment which allows it to oscillate in its negative-resistance region, thus providing its own pump. The input signal is usually coupled to the diode by means of the same medium through which the pump power flows away from the diode. The principal advantage of the autodyne mixer is its utter simplicity and for this reason alone there has been considerable interest shown in the literature for tunnel diode,^{90,92,93} Gunn diode,^{94,95} bipolar transistor,⁹⁶ and FET^{97,98} versions of the converter. The particular BARITT diode structure chosen for study here as a self-oscillating mixer is Snapp and Weissglas's Diode B¹⁰ since it appears to be by far the most characterized BARITT structure, both theoretically and experimentally.

It is virtually impossible to discuss every possible configuration for a mixer structure, so several parameters throughout most of the self-pumping mixer study are held constant. The self-pumped frequency is chosen to be near the midpoint of the negative-resistance region, see Fig. 3.10, and is held at 7.5 GHz. The image termination is chosen to be an open. This choice prevents image frequency diffusion noise currents from flowing but does not hinder image frequency shot noise currents through the forward-biased region of the diode. A short or any finite pure reactive termination

at the image diode terminals would allow both forms of noise currents to flow and would therefore not be as effective as an open image. It is conceivable that a specific complex image impedance termination could be chosen such that the image forward-biased region is effectively shorted, thus negating the frequency conversion of both forms of image frequency noise. The correct choice for this image termination impedance is $Z_{\text{image}} = (\Gamma_{B,\text{image}} - 1) / Y_{B,\text{image}}$ where Γ_B and Y_B are as given in the small-signal model of Chapter III. However there are frequency regions where the real part of this needed image termination is a negative quantity and does not represent a realizable passive load.

The first converter property examined is stability. Since the diode is self-oscillating, one expects to find regions around the pump frequency where the converter is potentially unstable. Figures 7.16a and b show the stability parameters g_{11} , g_{22} and C as functions of input signal frequency for the diode biased at $J_{\text{dc}} = 50 \text{ A/cm}^2$ and for two different levels of pumping: weak pumping, $V_p/V_T = 1$, and strong pumping, $V_p/V_T = 10$, where V_p is the magnitude of the assumed single-frequency (7.5 GHz) pumping voltage across the forward-biased region. The weak pumping values of g_{11} and g_{22} are only slightly different from their unpumped, uncoupled, small-signal counterparts and the potentially unstable region corresponds almost exactly with the frequency region of negative g_{11} . The more interesting case of strong pumping shows greatly modified values of g_{11} . The values of g_{22} are also altered but not to the same degree, and a far different range of potential instability is evident as compared to the weak pumping case. A unique feature

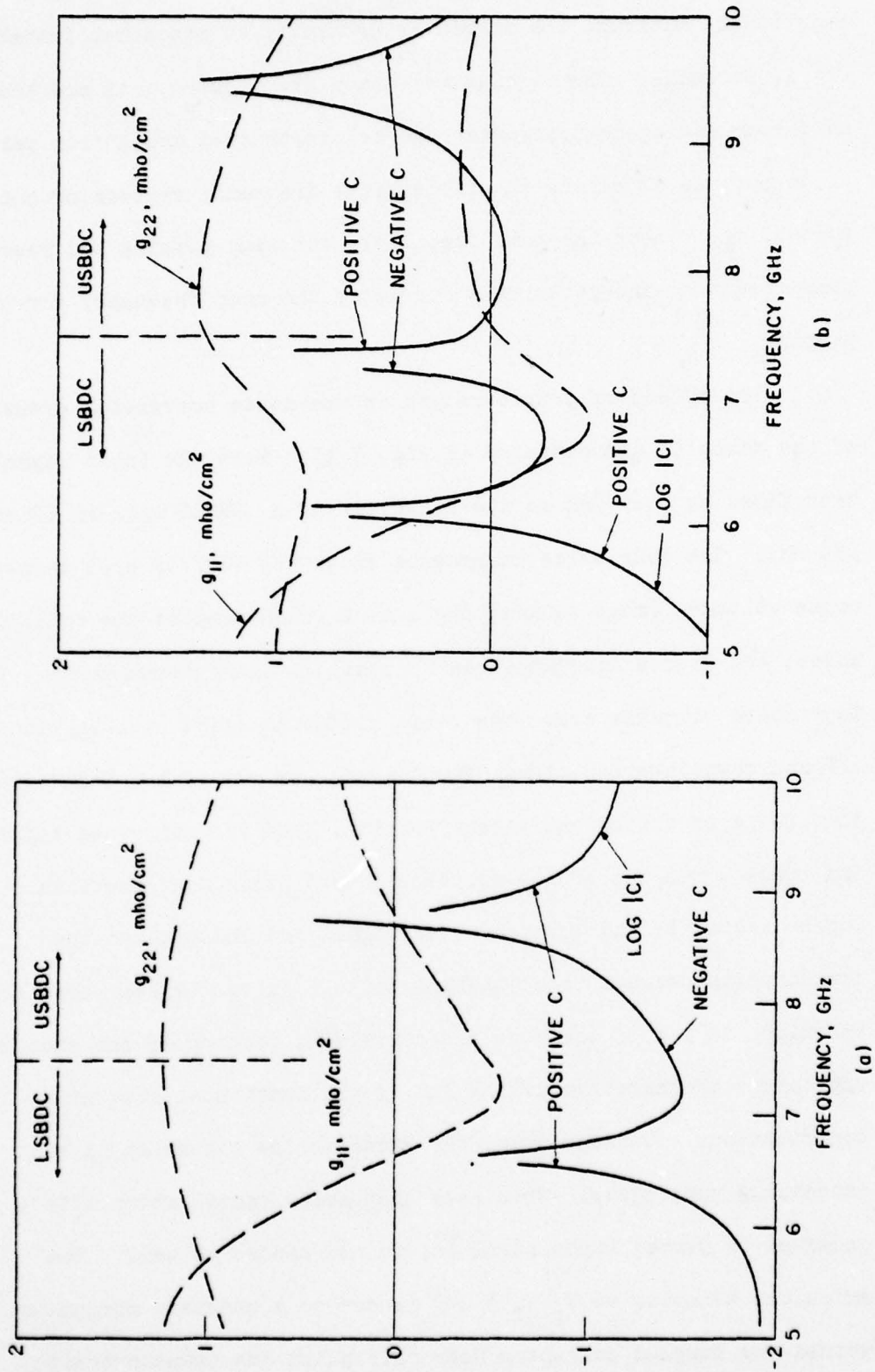


FIG. 7.16 STABILITY PARAMETERS FOR SNAPP AND WEISSGLAS'S DIODE B. (a) WEAK PUMPING, $V_p/V_T = 1$ AND (b) STRONG PUMPING, $V_p/V_T = 10$. ($f_p = 7.5$ GHz, OPEN IMAGE, $J_0 = 50$ A/cm²)

of the strong pumping case is the region of absolute stability near 8 GHz, although its margin or proximity to potential instability, $C > 1$, is small. The conclusions drawn from these plots are that a self-oscillating downconverter can be constructed using this particular diode but, as expected, it will exhibit frequency regions of potential gain instability: near the pump frequency for weak pumping and near the pump frequency and relatively far above the pump frequency for strong pumping.

The effect of pump strength on the noise conversion properties of the diode is demonstrated in Fig. 7.17. Here the input signal has been fixed at 7.65 GHz so the converter is a USBDC with an IF of 150 MHz. The four noise components shown are four IF port open-circuit noise voltages (mean square) the sum of which compose the total IF noise; the source impedance has been set at its optimum value. The four noise voltages are: the total diffusion noise contribution (IF and downconverted signal frequency), the sum of the individual shot noise contributions (open-circuit IF and downconverted signal and image), the sum of the correlated shot noise contributions (open-circuit IF and downconverted signal and image), and the downconverted signal input thermal noise. As can be seen the harder the diode is pumped the more the correlated portion of the shot noise approaches the negative of the sum of the individual shot noise contributions. Consequently, the excess noise figure falls with increasing pump power. This same shot noise cancellation effect is observed in pumped exponential and tunnel diodes as well. The anomalous behavior at $V_p/V_T \approx 2.7$ is due to a resonant phenomenon within the coupled circuit. Near this point the downconversion

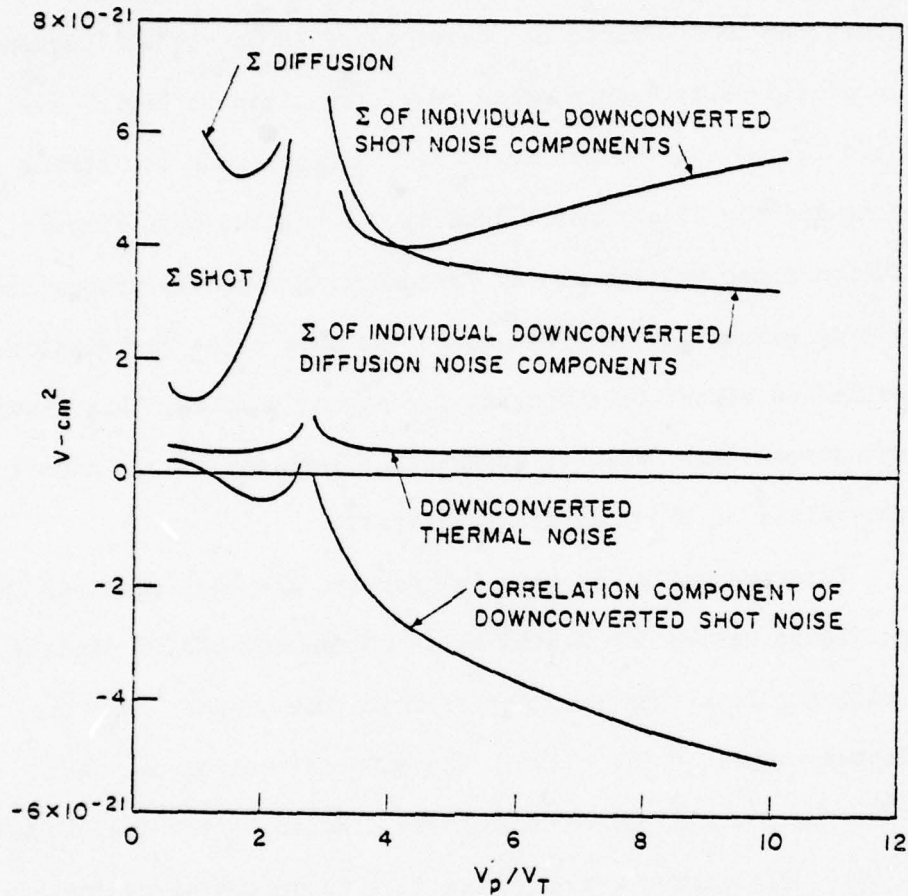


FIG. 7.17 DOWNCONVERTED NOISE VOLTAGE COMPONENTS (MEAN SQUARE)
FOR SNAPP AND WEISSGLAS'S DIODE B AS A FUNCTION OF
PUMPING STRENGTH. ($J_0 = 50 \text{ A/cm}^2$, $f_s = 7.65 \times 10^9 \text{ GHz}$,
 $f_p = 7.5 \text{ GHz}$, OPEN IMAGE)

voltage gain rises to very high values and the entire circuit is very sensitive to changes of any sort.

Finally, the optimum excess noise figure values for USBDC applications of the diode as functions of input signal frequency, dc current density, and pumping level are given in Fig. 7.18a, b and c. The lowest values of NF_e are seen to occur for strong pumping and low bias current density. Since the open-circuit diffusion noise voltage at any frequency is directly proportional to the dc current density and since the shot noise correlation-cancellation effect is strongest for strong pumping, this trend is not surprising. What is surprising, perhaps, is the magnitude of the values of NF_e that are predicted.

Experimentally, in this laboratory, the best measured SSB noise figure values for X-band self-oscillating BARITT diode mixers are slightly less than an order of magnitude greater than the predicted values of Fig. 7.18. The experimental diodes were $p^{+}np^{+}$ uniformly doped Si devices similar to the one shown in Fig. 1.1. The diodes were mounted in a converted waveguide crystal detector unit with a slide-screw or E-H tuner placed in front of the mount to provide concurrent mechanical tuning of resonant frequency and impedance matching, both for the oscillator and the input signal. When this assembly was used in conjunction with a circulator to isolate the input noise source (noise tube), total receiver double-sideband noise figures (IF amplifier contribution ≈ 1.5 dB) of 22 dB and above were routinely measured for an IF of 30 MHz. Raising the IF to 144 MHz and adding a second tuner in

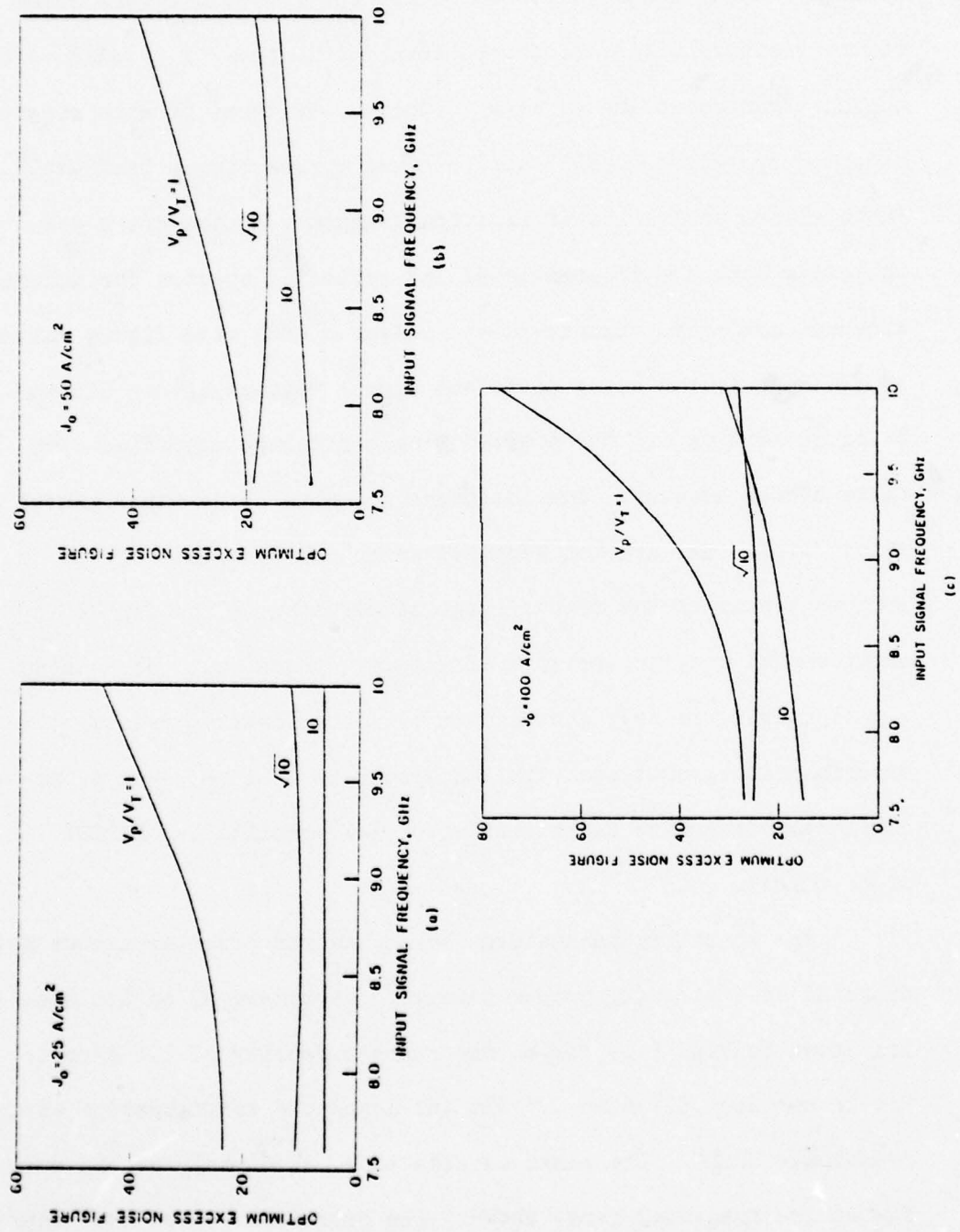


FIG. 7.18 OPTIMUM EXCESS NOISE FIGURES FOR SNAPP AND WEISSGLAS'S DIODE B. (USBDC, $f_p = 7.5 \text{ GHz}$, OPEN IMAGE)

series with the first to enable double tuning produced total receiver single-sideband noise figures (IF contribution ≈ 4 dB) of 13.7 to 15 dB. Double tuning can only be termed a headache as inordinate amounts of time are required to attain the lowest possible noise figure readings since all four mechanical degrees of freedom of the tuning arrangement are strongly coupled. Evidence of true single-sideband operation (USBDC) was obtained by sweeping a low-level input signal across the oscillating frequency of the diode and observing both the downconverted and reflected spectra for undesired sideband activity. Nguyen-Ba^{2,11} measured DSB noise figure values of 12 dB at X-band using different higher voltage diodes and an IF of 30 MHz. He did not attempt single-sideband operation with these diodes however. One hesitates to quote these experimental values since they are not accompanied by any detailed circuit information as to the actual image termination or the degree of input signal coupling network efficiency, therefore, there is no way of knowing if they are optimum or not. Clearly, precise experimental circuit analysis and synthesis will be required to completely determine the potential of self-oscillating BARITT diode mixers.

The stability parameters for dc maximum power structure No. 2 operated as a strongly pumped passive mode mixer, 40 to 100 GHz, are shown in Fig. 7.19 for a bias current density of 100 A/cm². The IF has been fixed at 1.5 GHz and again the configuration is an open image USBDC. The mixer is seen to be absolutely stable over the entire frequency range shown. The principal reason that the diode mixer is no longer active is that the frequency region of

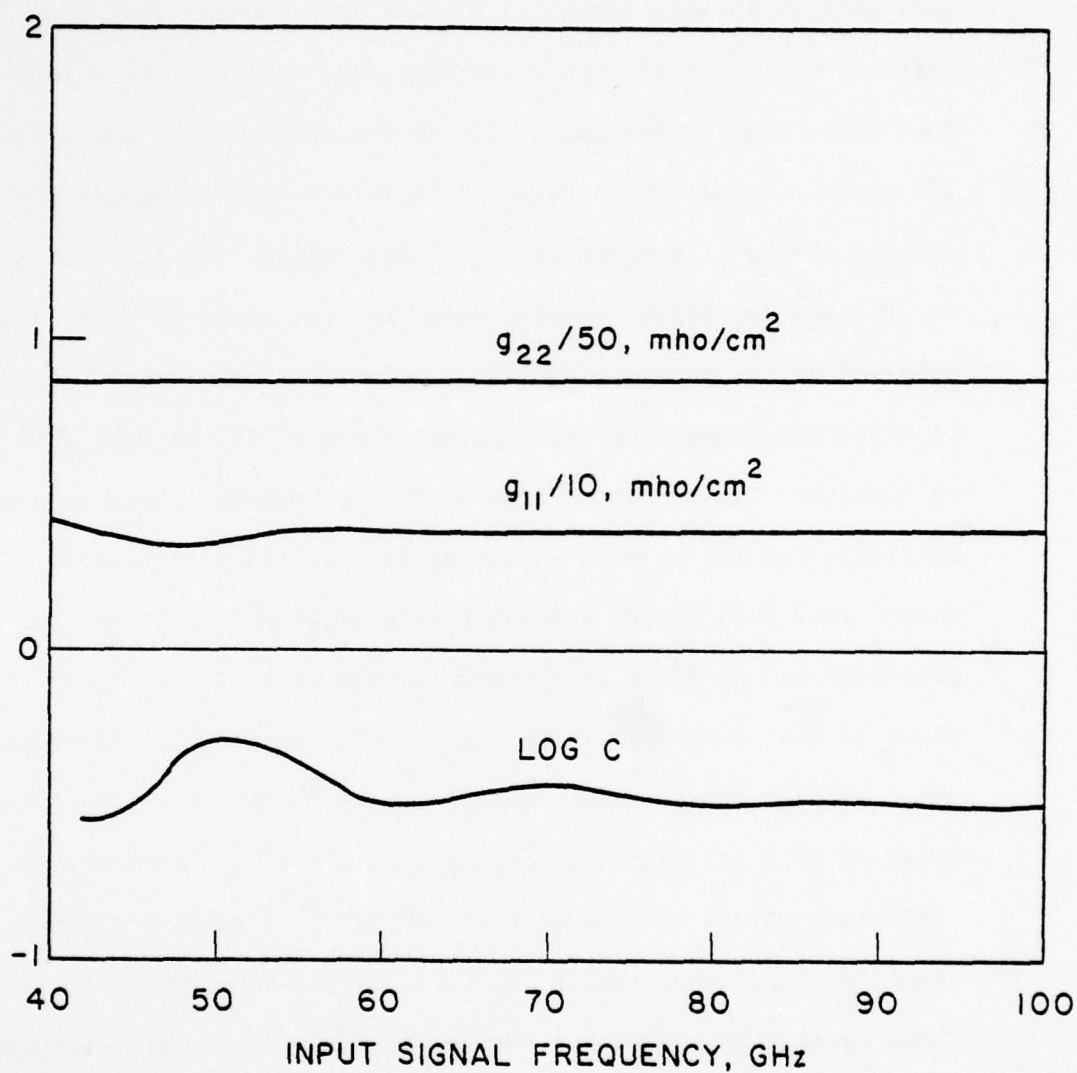


FIG. 7.19 MAXIMUM POWER STRUCTURE NO. 2. ($J_o = 100 \text{ A/cm}^2$,
 $V_p/V_T = 10$, USBDC, OPEN IMAGE, IF = 1.5 GHz)

negative resistance is well below the frequency range considered so that all "active" transit-time effects are averaged out by the multiple RF period transit-time diffusion-drift region. Transit-time effects however are still present in this same region's open-circuit diffusion noise voltage, Fig. 7.20, so it is expected that the excess noise figure will show some frequency variation. The optimum excess noise figure as a function of frequency and pumping strength is shown in Fig. 7.21. Again, the best values for NF_e are for strong pumping when the shot noise is effectively canceled out by strong correlation effects. The primary obstacle to achieving these very encouraging values of NF_e at millimeter wavelengths will be the efficiency of the optimum source impedance matching-coupling network, diode series resistance included. The needed real part of the optimum source impedance that must be presented to the diode at the signal terminals for $V_p/V_T = 10$ is shown in Fig. 7.22. These values are all, gratefully, above any worst case substrate loss resistance, see Section 6.2.2, and at least an order of magnitude higher than the diode large-signal resistance values that would be presented to a pumping signal (pumping signal such that $V_p/V_T = 10$) at the same frequency. These large-signal pump resistances as well as the small-signal at the same frequency resistances are also shown in Fig. 7.22. The external pumping power that is needed to produce $V_p/V_T = 10$ for this diode averages approximately 20 W/cm^2 over the frequency range of 40 to 100 GHz, thus pumping network efficiency should not be a major problem as this represents a minimal amount of pumping power.

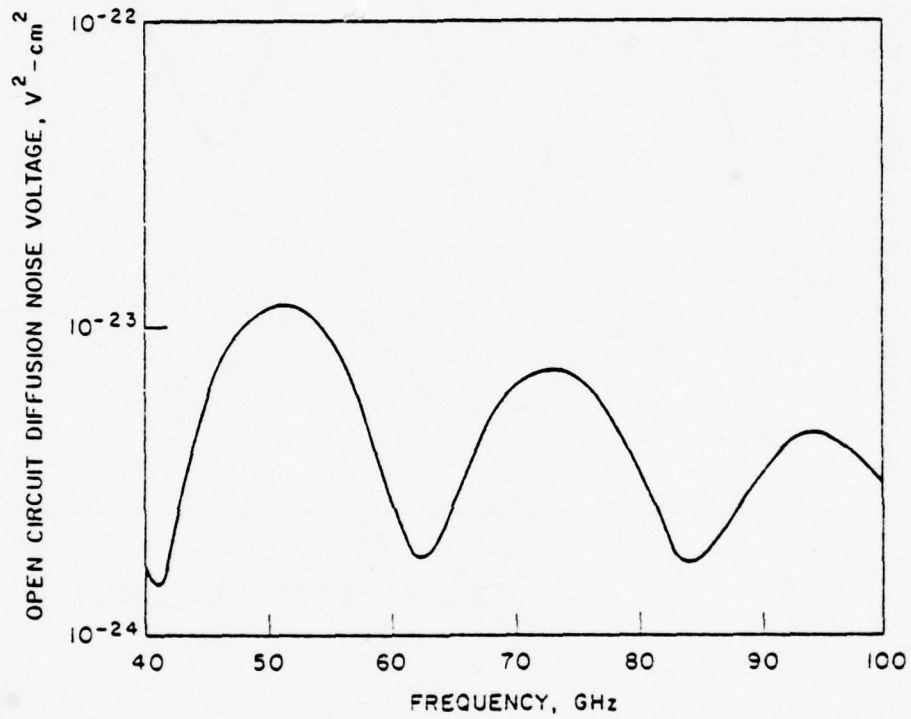


FIG. 7.20 TRANSIT-TIME EFFECTS ON OPEN-CIRCUIT DIFFUSION NOISE VOLTAGE AT INPUT SIGNAL FREQUENCY OF DC MAXIMUM POWER STRUCTURE NO. 2. ($J_0 = 100 \text{ A/cm}^2$, $V_p/V_T = 10$, USBDC, IF = 1.5 GHz)

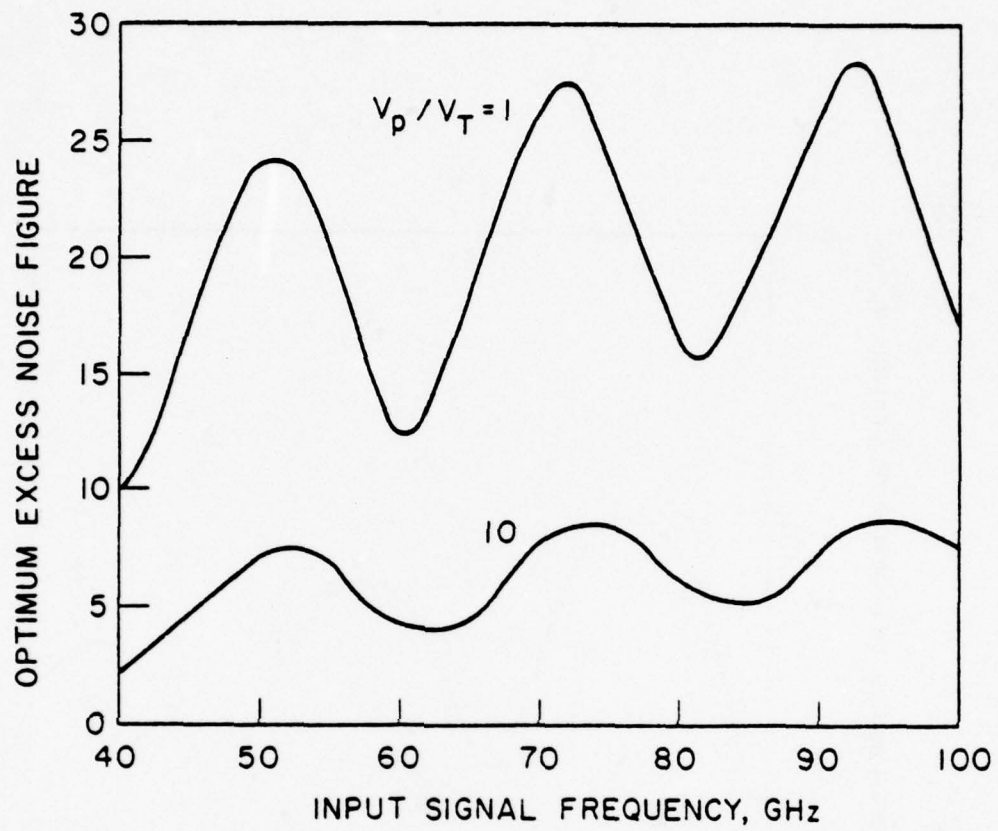


FIG. 7.21 OPTIMUM EXCESS NOISE FIGURE FOR DC MAXIMUM
POWER STRUCTURE NO. 2. ($J_0 = 100 \text{ A/cm}^2$,
USBDC, OPEN IMAGE, $IF = 1.5 \text{ GHz}$)

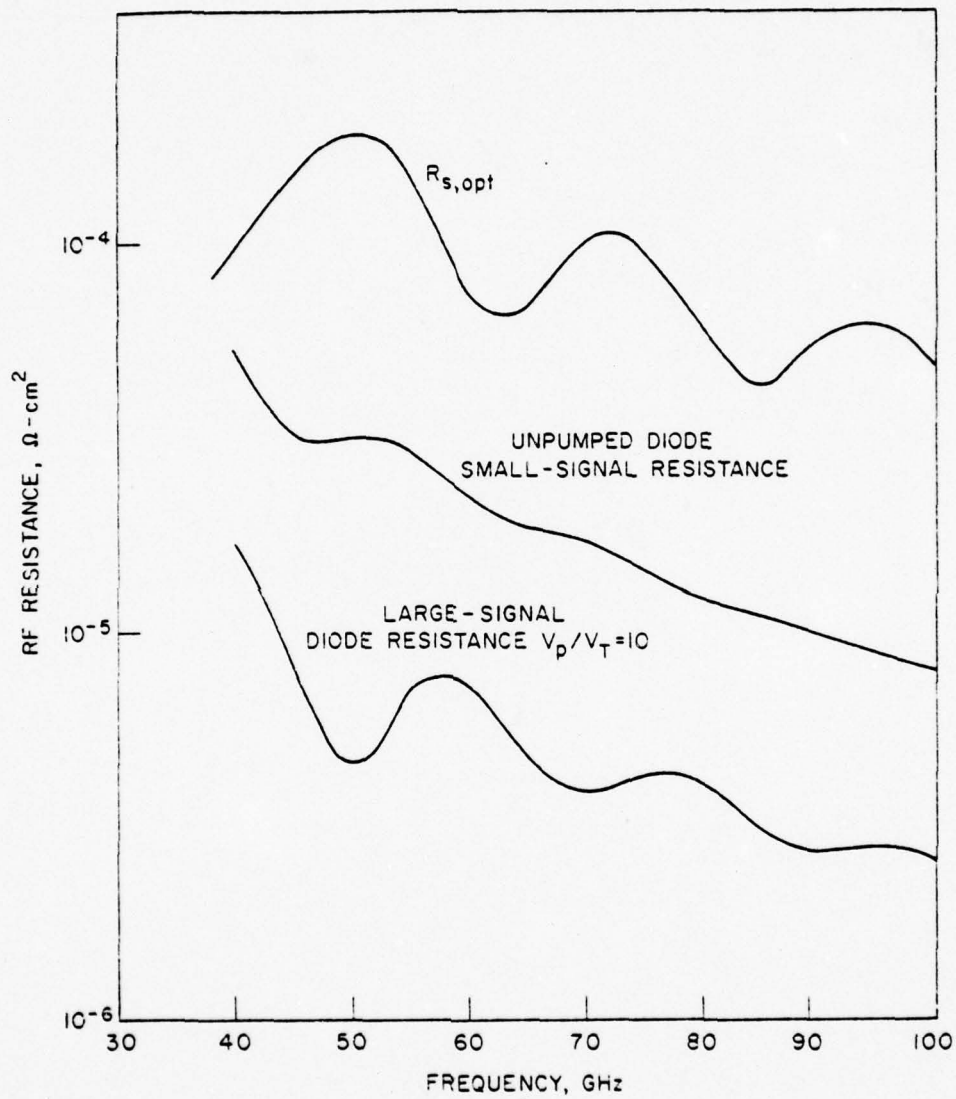


FIG. 7.22 RF RESISTANCE VALUES FOR DC MAXIMUM POWER STRUCTURE
 NO. 2. ($J_o = 100 \text{ A/cm}^2$, $V_p/V_T = 10$, USBDC, OPEN
 IMAGE, IF = 1.5 GHz)

It is concluded that both active and passive mode BARITT diode mixers hold considerable promise as low-noise downconverters. Much work remains to be done, however, for both modes, principally in circuit design and characterization.

CHAPTER VIII. CONCLUSIONS AND SUGGESTIONS FOR FURTHER WORK

In the course of this dissertation the author has sought to establish that:

1. The BARITT diode and the punch-through transistor can both be derived from standard bipolar junction transistor theory providing the correct collector-base minority carrier concentration boundary condition is employed (Chapters II and III).

2. Transistor "action" continues into the punch-through mode of operation and in fact improves frequency-response-wise (Chapters I through III).

3. The BARITT diode has two useful modes of video detector operation: an active mode in which the nonlinear negative resistance of the structure is used to simultaneously amplify and detect signals and a passive mode in which the parasitic impedance of the diffusion-drift region falls with frequency thereby improving the rectifying efficiency of the entire diode (Chapter IV).

4. The BARITT diode can be a very sensitive high-speed optical detector in two frequency regions: before transit-time rolloff and within the diode negative-resistance region (Chapter V).

5. Fundamental frequency RF power production by uniformly doped BARITT diodes is limited to frequencies below approximately 40 GHz (Chapters III and VI).

6. RF power can be extracted from harmonic operation of BARITT diodes if the fundamental is also excited (Chapter VI).

7. The minimum detectable signal-to-carrier ratio of a very-low IF BARITT diode mixer can be comparable to or below the measurable AM double-sideband noise-to-carrier ratio (Chapter VII).

8. The ultimate excess noise figure limitation of a general BARITT diode mixer, oscillation noise aside, is the ratio of the signal frequency diffusion-drift region diffusion noise to the input thermal noise of the signal source impedance and that this optimum ratio approaches small values for strong pumping and low bias currents (Chapter VII).

Hopefully, the methods and assumptions used in the derivations of these results have led to a further understanding of punch-through device operation and the results themselves will stir renewed activity in the general area of punch-through semiconductor devices.

In addition to the actual fabrication of millimeter-wave BARITT diode devices and microwave versions of punch-through transistors and photo-BARITTs, numerous areas of supplemental research and study are suggested by either the methods of analysis used in this work or their attendant results. A few of the most conspicuous are:

1. Two-dimensional effects (emitter crowding, undepleted base bulk regions, etc.) in punch-through transistors.
2. Transit-time frequency operation of punch-through transistors.
3. Large-signal punch-through transistor operation.
4. Two-dimensional effects in a two-dimensional BARITT diode structure used for passive-mode video detection and passive-mode mixing.
5. Measurement of RF series resistance due to substrate and contact loss in a BARITT diode.

6. Study of injection response time (assumed instantaneous in this study) in punch-through devices.
7. Noise in photo-BARITTs.
8. Subharmonically pumped self-oscillating BARITT diode mixers.
9. Detailed characterization of existing BARITT diode detector and mixer circuits particularly at millimeter and submillimeter wavelengths.

APPENDIX A. VOLTAGE AND CURRENT EARLY EFFECT

For a pnp transistor structure under normal forward biasing, the hole concentration and the hole current density at a point near the collector edge $x = w$ of the base region can be expressed as*

$$p(x,t) = p_0(x) + p_1(x,t)$$

and

$$J_p(x,t) = J_{p0}(x) + J_{p1}(x,t)$$

If

$$\begin{aligned} w &= w[V_{CB}, J_p(w)] \\ &= w_0 + \left. \frac{\partial w}{\partial V_{CB}} \right|_{V_{CB0}} V_{CB1} + \left. \frac{\partial w}{\partial J_p(w)} \right|_{J_{p0}(w)} J_{p1}(w) \\ &\equiv w_0 + w_1, \end{aligned} \tag{A.1}$$

then

$$\begin{aligned} p(w,t) &= p_w \approx p(w_0,t) + \left. \frac{\partial p}{\partial x} \right|_{w_0} w_1 \\ &= p_0(w_0) + p_1(w_0,t) + \left. \frac{\partial p}{\partial x} \right|_{w_0} w_1 \end{aligned} \tag{A.2}$$

* In this Appendix quantities with a "0" subscript denote dc values and quantities with a "1" subscript represent small-signal time-varying values.

and

$$J_p(w, t) = J_p(w_0, t) + \left. \frac{\partial J_p}{\partial x} \right|_{w_0} w_1 = J_{p0}(w_0) + J_{p1}(w_0, t) + \left. \frac{\partial J_p}{\partial x} \right|_{w_0} w_1 \quad (A.3)$$

But

$$\left. \frac{\partial J_p}{\partial x} \right|_{w_0} w_1 = \left. \frac{\partial J_{p0}}{\partial x} \right|_{w_0} w_1 + \left. \frac{\partial J_{p1}}{\partial x} \right|_{w_0} w_1 = 0$$

since the second term is of second order and the derivative portion of the first term is negligible when the major share of the dc current throughout the transistor is composed of hole current. Thus for

$$\begin{aligned} F_w &= F_w[V_{CB}, J_p(w)] \\ &\approx F_w[V_{CB0}, J_{p0}(w)] \\ &\quad + \left. \frac{\partial F_w}{\partial V_{CB}} \right|_{V_{CB0}} V_{CB1} + \left. \frac{\partial F_w}{\partial J_p(w)} \right|_{J_{p0}(w)} J_{p1}(w) \quad (A.4) \end{aligned}$$

we have from Eq. A.2

$$p_1(w_0, t) = p(w, t) - p_0(w_0) - \left. \frac{\partial p}{\partial x} \right|_{w_0} w_1$$

or, substituting the results of Eqs. A.1, A.3 and A.4, .

$$\begin{aligned}
 p_1(w_0, t) &= \left(\frac{\partial F_w}{\partial V_{CB}} \Big|_{V_{CB0}} - \frac{\partial p}{\partial x} \Big|_{w_0} \frac{\partial w}{\partial V_{CB}} \Big|_{V_{CB0}} \right) V_{CB1} \\
 &+ \left(\frac{\partial F_w}{\partial J_p(w)} \Big|_{J_{p0}(w_0)} - \frac{\partial p}{\partial x} \Big|_{w_0} \frac{\partial w}{\partial J_p(w)} \Big|_{J_{p0}(w_0)} \right) J_{p1}(w_0) \\
 &\equiv \left(\frac{\partial F_w}{\partial V_{CB}} \Big|_{V_{CB0}} \right)' V_{CB1} + \left(\frac{\partial F_w}{\partial J_p(w)} \Big|_{J_{p0}(w_0)} \right)' J_{p1}(w_0) .
 \end{aligned}$$

APPENDIX B. AN INTERPRETATION OF THE AM AND FM MODULATION OF THE RF
VOLTAGE ACROSS AN OSCILLATING DIODE VERY-LOW IF MIXER

For modulation frequencies well below the corner frequency α_c ,
all low-frequency phasor quantities are real.

Equations 7.16 and 7.17 then become

$$\delta V(t) = \frac{\hat{z}_H \sin(\omega_i t + \theta_d - \theta_\omega)}{|Z_{dv}| \sin \xi} \quad (B.1)$$

and

$$\delta \omega(t) = \frac{-Z_H \sin(\omega_i t + \theta_d - \theta_v)}{|Z_{tw}| \sin \xi}, \quad (B.2)$$

where

$$Z_H = \frac{|\hat{e}_H|}{V_{RF_0}} |Z_{do}|,$$

$$Z_{do} = |Z_{do}| e^{j\theta_d},$$

ω_i is the IF, the arbitrary phase of \hat{e}_H has been chosen as π , and the remaining symbols are as defined in Section 7.2. One interpretation of the AM and FM modulation described by Eqs. B.1 and B.2 is as follows: Visualize a reference phasor \hat{U}_0 at the unperturbed RF frequency ω_0 and two additional small magnitude phasors \hat{U}_1 and \hat{U}_2 at $\omega_0 + \omega_i$ and $\omega_0 - \omega_i$, counterrotating about the tip of \hat{U}_0 . The total phasor \hat{U} is the vector sum of the three; that is,

$$\hat{U} = U_0 + U_1 e^{j(\omega_i t + \phi_1)} + U_2 e^{-j(\omega_i t - \phi_2)} \quad , \quad (B.3)$$

where U_1 and $U_2 \ll U_0$. It can be shown, after some tedious algebra, that this phasor notation represents the AM and FM modulation of Eqs. B.1 and B.2, i.e.,

$$|\hat{U} - U_0| \rightarrow \delta V(t)$$

and

$$\frac{d}{dt} \angle \hat{U} - \omega_i \rightarrow \delta \omega(t) \quad ,$$

when the phasor quantities are identified as

$$U_1 = \frac{V_m}{2} [u(1 + \sqrt{1 - v^2})]^{1/2} \quad , \quad (B.4)$$

$$U_2 = \frac{V_m}{2} v \left(\frac{u}{1 + \sqrt{1 - v^2}} \right)^{1/2} \quad (B.5)$$

and

$$\phi_1 + \phi_2 = \tan^{-1} \left(\frac{2\sqrt{R}}{R - 1} \sin \xi \right) \quad , \quad (B.6)$$

where

$$R \equiv \frac{\omega_i |Z_{t\omega}|}{V_{RF0} |Z_{dv}|} \quad ,$$

$$u \equiv \frac{R + 1}{R} \quad ,$$

$$v \equiv \frac{R - 1}{R + 1} \sec(\phi_1 + \phi_2)$$

and

$$V_m \equiv \frac{Z_H}{|Z_{dv}| \sin \xi} \quad .$$

Since only the sum of the relative phases of \hat{U}_1 and \hat{U}_2 need be known, either ϕ_1 or ϕ_2 can be set to zero and the other can be determined from Eq. B.6.

The physical interpretation of this three-phasor representation is that U_0 is the unperturbed diode voltage and that either \hat{U}_1 or \hat{U}_2 is the voltage across the diode due to the incoming signal. The remaining phasor voltage, \hat{U}_1 or \hat{U}_2 , is the induced image signal due to the conversion process.

The simplest case to examine is that of orthogonal tuning. For this restriction $\sin \xi = 1$ and U_1 and U_2 become equal. Equations B.4 and B.5 reduce to

$$U_1 = U_2 = \frac{V_m}{2} \sqrt{(R+1)/R} .$$

LIST OF REFERENCES

1. Kwok, S. P., "Properties and Potential of BARITT Devices," Technical Report No. 133, Electron Physics Laboratory, The University of Michigan, Ann Arbor, December 1974.
2. Nguyen-Ba, H., "Properties and Applications of BARITT Devices," Technical Report No. 137, Electron Physics Laboratory, The University of Michigan, Ann Arbor, July 1977.
3. McCleer, P. J., Jackson, T. N. and Haddad, G. I., "Operation of Transistors in the Punch-Through Mode," Proc. Sixth Biennial Cornell Conf. on Active Microwave Semiconductor Devices and Circuits, Ithaca, NY, pp. 305-313, August 1977.
4. Thornton, R. D., et al., Characteristics and Limitations of Transistors; Semiconductor Electronics Education Committee, Vol. 1, John Wiley and Sons, Inc., New York, 1964.
5. Shockley, W., "Negative Resistance Arising from Transit Time in Semiconductor Diodes," Bell System Tech. J., vol. 33, No. 4, pp. 799-826, July 1954.
6. Sze, S. M., Coleman, D. J., Jr. and Loya, A., "Current Transport in Metal-Semiconductor-Metal (MSM) Structures," Solid-State Electronics, vol. 14, No. 12, pp. 1209-1218, December 1971.
7. Coleman, D. J., Jr. and Sze, S. M., "A Low-Noise Metal-Semiconductor-Metal (MSM) Microwave Oscillator," Bell System Tech. J. (Brief), vol. 50, No. 5, pp. 1695-1699, May-June 1971.
8. Sze, S. M. and Ryder, R. M., "Microwave Avalanche Diodes," Proc. IEEE, vol. 59, No. 8, pp. 1140-1154, August 1971.
9. Stewart, J.A.C., "p⁺-n-p⁺ BARITT-Diode Design," Electronics Letters, vol. 11, No. 19, pp. 460-461, September 18, 1975.
10. Snapp, C. P. and Weissglas, P., "On the Microwave Activity of Punchthrough Injection Transit-Time Structures," IEEE Trans. on Electron Devices, vol. ED-19, No. 10, pp. 1109-1118, October 1972.
11. East, J. R., Nguyen-Ba, H. and Haddad, G. I., "Design, Fabrication, and Evaluation of BARITT Devices for Doppler System Applications," IEEE Trans. on Microwave Theory and Techniques, vol. MTT-24, No. 12, pp. 943-948, December 1976.
12. East, J. R., McCleer, P. J. and Haddad, G. I., "K-Band BARITT Doppler Detectors," 1977 IEEE MTT-S Int. Microwave Symp. Digest, San Diego, CA, pp. 88-91, June 1977.

13. Gupta, M. S., Lomax, R. J. and Haddad, G. I., "Noise Considerations in Self-Mixing IMPATT Diode Oscillators for Short-Range Doppler Radar Applications," IEEE Trans. on Microwave Theory and Techniques, vol. MTT-22, No. 1, pp. 37-43, January 1974.
14. Nygren, T. and Sjöblund, A., "Sensitivity of Doppler Radar and Self-Detecting Diode Oscillators," IEEE Trans. on Microwave Theory and Techniques, vol. MTT-19, No. 12, pp. 906-910, December 1971.
15. Hines, M. E., "Large-Signal Noise, Frequency Conversion, and Parametric Instabilities in IMPATT Diode Networks," Proc. IEEE, vol. 60, No. 12, pp. 1534-1548, December 1972.
16. Strutt, M.J.O., "Noise Figure Reduction in Mixer Stages," Proc. IRE, vol. 34, No. 12, pp. 942-950, December 1946.
17. Shockley, W., "The Theory of p-n Junctions in Semi-Conductors and p-n Junction Transistors," Bell System Tech. J., vol. 28, No. 3, pp. 435-489, July 1949.
18. Matz, A. W., "A Modification of the Theory of the Variation of Junction Transistor Current Gain with Operating Point and Frequency," J. Electronics and Control, vol. 7, No. 2, pp. 133-152, August 1959.
19. Kirk, C. T., "A Theory of Transistor Cutoff Frequency (f_T) Falloff at High Current Densities," IRE Trans. on Electron Devices, vol. ED-9, No. 3, pp. 164-174, March 1962.
20. Middlebrook, R. D., "Effects of Modified Collector Boundary Conditions on the Basic Properties of a Transistor," Solid-State Electronics, vol. 6, No. 6, pp. 573-588, November-December 1963.
21. Sah, C. T., Noyce, R. N. and Shockley, W., "Carrier Generation and Recombination in p-n Junctions and p-n Junction Characteristics," Proc. IRE, vol. 45, No. 9, pp. 1228-1243, September 1957.
22. Chu, J. L., Persky, G. and Sze, S. M., "Thermionic Injection and Space-Charge-Limited Current in Reach-Through p⁺np⁺ Structures," J. Appl. Phys., vol. 43, No. 8, pp. 3510-3515, August 1972.
23. Kwok, S. P. and Haddad, G. I., "Power Limitations in BARITT Devices," Solid-State Electronics, vol. 19, No. 9, pp. 795-807, September 1976.
24. Persky, G., "Thermionic Saturation of Diffusion Currents in Transistors," Solid-State Electronics, vol. 15, No. 12, pp. 1345-1351, December 1972.
25. Berz, F., "Diffusion Near an Absorbing Boundary," Solid-State Electronics, vol. 17, No. 12, pp. 1245-1255, December 1974.

26. Wang, S., Solid-State Electronics, McGraw-Hill Book Co., Inc., New York, p. 269, 1966.
27. Sah, C. T., "The Spatial Variation of the Quasi-Fermi Potentials in p-n Junctions," IEEE Trans. on Electron Devices, vol. ED-13, No. 12, pp. 839-846, December 1966.
28. Middlebrook, R. D., An Introduction to Junction Transistor Theory, John Wiley and Sons, Inc., New York, 1957.
29. Sze, S. M., Physics of Semiconductor Devices, Wiley-Interscience, New York, 1969.
30. Hauser, J. R., "The Effects of Distributed Base Potential on Emitter-Current Injection Density and Effective Base Resistance for Stripe Transistor Geometries," IEEE Trans. on Electron Devices, vol. ED-11, No. 5, pp. 238-242, May 1964.
31. Early, J. M., "Design Theory of Junction Transistors," Bell System Tech. J., vol. 32, No. 6, pp. 1271-1312, November 1953.
32. Early, J. M., "Effect of Space-Charge Layer Widening in Junction Transistors," Proc. IRE, vol. 40, No. 11, pp. 1401-1406, November 1952.
33. Early, J. M., "P-N-I-P and N-P-I-N Junction Transistor Triodes," Bell System Tech. J., vol. 33, No. 3, pp. 517-533, May 1954.
34. Watson, H. A. (Ed.), Microwave Semiconductor Devices and Their Circuit Applications, McGraw-Hill Book Co., Inc., New York, 1969.
35. Gray, P. E., et al., Physical Electronics and Circuit Models of Transistors; Semiconductor Electronics Education Committee, Vol. 2, John Wiley and Sons, Inc., New York, 1964.
36. Shockley, W. and Sze, S. M., "Unit-Cube Expression for Space Charge Resistance," Bell System Tech. J., vol. 46, No. 5, pp. 837-842, October 1966.
37. Sze, S. M., Physics of Semiconductor Devices, Wiley-Interscience, New York, p. 292, 1969.
38. Weller, K. P., "Small-Signal Theory of a Transit-Time Negative-Resistance Device Utilizing Injection from a Schottky Barrier," RCA Rev., vol. 32, No. 3, pp. 372-382, September 1971.
39. Gilden, M. and Hines, M. E., "Electronic Tuning Effects in the Read Microwave Avalanche Diode," IEEE Trans. on Electron Devices, vol. ED-13, No. 1, pp. 169-175, January 1966.
40. Haus, H. A., Statz, H. and Pucel, R. A., "Noise Measure of Metal-Semiconductor-Metal Schottky-Barrier Microwave Diodes," Electronics Letters, vol. 7, No. 22, pp. 667-669, 4 November 1971.

41. Statz, H., Pucel, R. A. and Haus, H. A., "Velocity Fluctuation Noise in Metal-Semiconductor-Metal Diodes," Proc. IEEE, vol. 60, No. 5, pp. 644-645, May 1972.
42. van der Ziel, A., "Theory of Shot Noise in Junction Diodes and Junction Transistors," Proc. IRE, vol. 43, No. 11, pp. 1639-1646, November 1955.
43. Beatie, R. N., "A Lumped Model Analysis of Noise in Semiconductor Devices," IRE Trans. on Electron Devices, vol. ED-6, No. 2, pp. 133-140, April 1959.
44. Shockley, W., Copeland, J. A. and James, R. P., "The Impedance Field Method of Noise Calculation in Active Semiconductor Devices," in Quantum Theory of Atoms, Molecules, and the Solid State, Löwdin, Per-Olov (Ed.), Academic Press, Inc., New York, 1966.
45. van der Ziel and van Vliet, "H.F. Thermal Noise in Space-Charge Limited Solid State Diodes--II," Solid-State Electronics, vol. 11, No. 4, pp. 508-509, April 1968.
46. Björkman, G. and Snapp, C. P., "Small-Signal Noise Behavior of Companion p⁺-n-p⁺ and p⁺-n-v-p⁺ Punchthrough Microwave Diodes," Electronics Letters, vol. 8, No. 20, pp. 501-503, 5 October 1972.
47. Sjöblund, A., "Small-Signal Noise Analysis of p⁺np⁺ BARITT Diodes," Electronics Letters, vol. 9, No. 1, pp. 2-4, 11 January 1973.
48. Cowley, A. M. and Sorensen, H. O., "Quantitative Comparison of Solid-State Microwave Detectors," IEEE Trans. on Microwave Theory and Techniques, vol. MTT-14, No. 12, pp. 588-602, December 1966.
49. Misawa, T. and Kenyon, N. D., "An Oscillator Circuit with Cap Structures for Millimeter-Wave IMPATT Diodes," IEEE Trans. on Microwave Theory and Techniques, vol. MTT-18, No. 11, pp. 969-970, November 1970.
50. Ginzton, E. L., Microwave Measurements, McGraw-Hill Book Co., Inc., New York, 1957.
51. Young, D. T. and Irvin, J. C., "Millimeter Frequency Conversion Using Au-n-Type GaAs Schottky Barrier Epitaxial Diodes with a Novel Contacting Technique," Proc. IEEE (Correspondence), vol. 53, No. 12, pp. 2130-2131, December 1965.
52. Clifton, B. J., Lindley, W. T., Chick, R. W. and Cohen, R. A., "Materials and Processing Techniques for the Fabrication of High Quality Millimeter Wave Diodes," Proc. Third Biennial Cornell Conf. on High Frequency Generation and Amplification: Devices and Applications, Ithaca, NY, pp. 463-475, 1971.

53. McColl, M., Hodges, D. T. and Garber, W. A., "Submillimeter-Wave Detection with Submicron-Size Schottky-Barrier Diodes," IEEE Trans. on Microwave Theory and Techniques, vol. MTT-25, No. 6, pp. 463-467, June 1977.
54. Schneider, M. V. and Carlson, E. R., "Notch-Front Diodes for Millimeter-Wave Integrated Circuits," Electronics Letters, vol. 13, No. 24, pp. 745-747, 24 November 1977.
55. Shockley, W., Sparks, M. and Teal, G. K., "p-n Junction Transistors," Phys. Rev., vol. 83, No. 1, pp. 151-162, July 1, 1951.
56. Gärtner, W. W., "Depletion-Layer Photoeffects in Semiconductors," Phys. Rev., vol. 116, No. 1, pp. 84-87, October 1, 1959.
57. Dash, W. C. and Newman, R., "Intrinsic Optical Absorption in Single-Crystal Germanium and Silicon at 77°K and 300°K," Phys. Rev., vol. 99, No. 4, pp. 1151-1155, August 15, 1955.
58. Karasek, M., "Large-Signal Analysis of the Silicon pnp-BARITT Diode," Solid-State Electronics, vol. 19, No. 7, pp. 625-631, July 1976.
59. Kwarada, K. and Mizushima, Y., "Large-Signal Analysis of Negative-Resistance Diode Due to Punch-Through-Injection and Transit-Time Effect," Japanese J. Appl. Phys., vol. 12, No. 3, pp. 423-433, March 1973.
60. Mouthaan, K., "Characterization of Nonlinear Interactions in Avalanche Transit-Time Oscillators, Frequency Multipliers, and Frequency Dividers," IEEE Trans. on Microwave Theory and Techniques, vol. MTT-18, No. 11, pp. 853-862, November 1970.
61. Kwok, S. P., Nguyen-Ba, H. and Haddad, G. I., "Properties and Potential of BARITT Devices," Presented at the 1974 Int. Solid-State Circuits Conf., Philadelphia, PA, February 1974.
62. Nguyen-Ba, H. and Haddad, G. I., "Effects of Doping Profile on the Performance of BARITT Devices," IEEE Trans. on Electron Devices, vol. ED-24, No. 9, pp. 1154-1163, September 1977.
63. Blue, J. L., "Approximate Large-Signal Analysis of IMPATT Oscillators," Bell System Tech. J., vol. 48, No. 2, pp. 383-396, February 1969.
64. Schroeder, W. E. and Haddad, G. I., "Effect of Harmonic and Subharmonic Signals on Avalanche-Diode Oscillator Performance," IEEE Trans. on Microwave Theory and Techniques (Correspondence), vol. MTT-18, No. 6, pp. 327-331, June 1970.
65. Brackett, C. A., "Characterization of Second-Harmonic Effects in IMPATT Diodes," Bell System Tech. J., vol. 49, No. 8, pp. 1777-1810, October 1970.

66. Brackett, C. A., "Peak AC Voltage Limitations in Second-Harmonically Tuned IMPATT Diodes," IEEE Trans. on Microwave Theory and Techniques, vol. MTT-18, No. 11, pp. 992-993, November 1970.
67. Brackett, C. A., "Circuit Effects in Second-Harmonic Tuning of IMPATT Diodes," IEEE Trans. on Electron Devices, vol. ED-18, No. 3, pp. 147-150, March 1971.
68. East, J. R., McCleer, P. J. and Haddad, G. I., "K-Band BARITT Doppler Detectors," Presented at the 1977 IEEE Int. Microwave Symp., San Diego, CA, June 1977.
69. Nagano, S. and Akaiwa, Y., "Behavior of Gunn Diode Oscillator with a Moving Reflector as a Self-Excited Mixer and a Load Variation Detector," IEEE Trans. on Microwave Theory and Techniques, vol. MTT-19, No. 12, pp. 906-910, December 1971.
70. Vlaardingerbroek, M. T., "Theory of Oscillator Noise," Electronics Letters, vol. 7, No. 21, pp. 648-650, 21 October 1971.
71. Kurokawa, K., "Some Basic Characteristics of Broadband Negative Resistance Oscillator Circuits," Bell System Tech. J., vol. 48, No. 6, pp. 1937-1955, July-August 1969.
72. Thaler, H., Ulrich, G. and Weidmann, G., "Noise in IMPATT Diode Amplifiers and Oscillators," IEEE Trans. on Microwave Theory and Techniques, vol. MTT-19, No. 8, pp. 692-705, August 1971.
73. Peterson, D. F., "A Device Characterization and Circuit Design Procedure for Realizing High-Power Millimeter-Wave IMPATT-Diode Amplifiers," IEEE Trans. on Microwave Theory and Techniques, vol. MTT-21, No. 11, pp. 681-689, November 1973.
74. Fikart, J. L., "AM and FM Noise of BARITT Oscillators," IEEE Trans. on Microwave Theory and Techniques, vol. MTT-22, No. 5, pp. 517-523, May 1974.
75. Haddad, G. I., "Microwave Semiconductor Devices, Circuits, and Applications," Summer Course Notes, The University of Michigan, Ann Arbor, July 1976.
76. Ohtomo, M., "Experimental Evaluation of Noise Parameters in Gunn and Avalanche Oscillators," IEEE Trans. on Microwave Theory and Techniques, vol. MTT-20, No. 7, pp. 425-437, July 1972.
77. Gnerlich, H. R. and Ondria, J., "A New Look at Noise in Transferred Electron Oscillators," IEEE Trans. on Microwave Theory and Techniques, vol. MTT-25, No. 12, pp. 977-981, December 1977.

78. Hines, M. E., "Noise Theory for the Read Type Avalanche Diode," IEEE Trans. on Electron Devices, vol. ED-13, No. 1, pp. 158-163, January 1966.
79. Gummel, H. K. and Blue, J. L., "A Small-Signal Theory of Avalanche Noise in IMPATT Diodes," IEEE Trans. on Electron Devices, vol. ED-14, No. 9, pp. 569-580, September 1967.
80. Iijima, Y., East, J. R. and Haddad, G. I., "Solid-State Devices for Low-Frequency Doppler Detectors," IEEE Trans. on Microwave Theory and Techniques (Tech. Note), vol. MTT-26, No. 2, pp. 132-133, February 1978.
81. Peterson, L. C. and Llewellyn, F. B., "The Performance and Measurement of Mixers in Terms of Linear-Network Theory," Proc. IRE, vol. 33, No. 7, pp. 458-476, July 1945.
82. Torrey, H. C. and Whitmer, C. A., Crystal Rectifiers, McGraw-Hill Book Co., Inc., New York, 1948.
83. Evans, W. J. and Haddad, G. I., "Frequency Conversion in IMPATT Diodes," IEEE Trans. on Electron Devices, vol. ED-16, No. 1, pp. 78-87, January 1969.
84. Peterson, D. F., "Circuit Conditions to Prevent Second-Subharmonic Power Extraction in Periodically Driven IMPATT Diode Networks," IEEE Trans. on Microwave Theory and Techniques, vol. MTT-22, No. 8, pp. 784-790, August 1974.
85. Penfield, P., Jr., MARTHA Users Manual, The MIT Press, Cambridge, 1971.
86. Edwards, C. F., "Frequency Conversion by Means of a Nonlinear Admittance," Bell System Tech. J., vol. 35, No. 6, pp. 1403-1416, November 1956.
87. Becker, L. and Ernst, R. L., "Nonlinear-Admittance Mixers," RCA Rev., vol. 25, No. 4, pp. 662-691, December 1964.
88. Linvill, J. G. and Gibbons, J. F., Transistors and Active Circuits, McGraw-Hill Book Co., Inc., New York, 1961.
89. Rollett, J. M., "Stability and Power-Gain Invariants of Linear Twoports," IRE Trans. on Circuit Theory, vol. CT-9, No. 1, pp. 29-32, March 1962.
90. Kim, C. S., "Tunnel-Diode Converter Analysis," IEEE Trans. on Electron Devices, vol. ED-8, No. 9, pp. 394-405, September 1961.
91. Haus, H. A., et al, "Representation of Noise in Linear Twoports," Proc. IRE, vol. 48, No. 1, pp. 69-74, January 1960.

92. Barber, M. R., "A Numerical Analysis of the Tunnel-Diode Frequency Converter," IEEE Trans. on Microwave Theory and Techniques, vol. MTT-13, No. 5, pp. 663-670, September 1965.
93. Pucel, R. A., "Theory of the Esaki Diode Frequency Converter," Solid-State Electronics, vol. 3, No. 3/4, pp. 167-207, November-December 1961.
94. Lazarus, M. J., Cheung, K. Y. and Novak, S., "Improved mm-Wave Gunn Mixer Receivers," Microwave J., vol. 20, No. 3, pp. 43-47, March 1977.
95. Albrecht, P. and Bechteler, M., "Noise Figure and Conversion Loss of Self-Excited Gunn-Diode Mixers," Electronics Letters, vol. 6, No. 11, pp. 321-322, 28 May 1970.
96. van der Ziel, A. and Okamoto, M., "Noise in Common-Base Transistor Mixers with HF Feedback from the Output," IEEE J. of Solid-State Circuits, vol. SC-3, No. 3, pp. 303-304, September 1968.
97. Pucel, R. A., Massé, D. and Bera, R., "Integrated GaAs FET Mixer Performance at X-Band," Electronics Letters, vol. 11, No. 9, pp. 199-200, 1 May 1975.
98. Pucel, R. A., Massé, D. and Bera, R., "Performance of GaAs MESFET Mixers at X-Band," IEEE Trans. on Microwave Theory and Techniques, vol. MTT-24, No. 6, pp. 351-360, June 1976.